School of Ocean and Earth Science and Technology
Hawai'i Natural Energy Institute

UNIVERSITY of HAWAI'I® MĀNOA

September 29, 2017

Ms. Kathryn D. Parks
Office of Naval Research
Seattle Regional Office
300 Fifth Avenue, Suite 710
Seattle WA 98104

Re: Final Technical Report: APRISES11: Grant N00014-12-1-0496

Dear Ms. Parks,

Enclosed you will find a copy of the Final Technical Report for the subject grant, titled Asia Pacific Research Initiative for Sustainable Energy Systems 2011 (APRISES11). Also enclosed is a completed Standard Form 298.

The DD 882 Report of Inventions and Subcontracts was sent earlier by our Office of Research Services to appropriate parties.

Sincerely,

Richard E. Rocheleau
Principal Investigator

Attachments: Final Technical Report
SF 298

c: Office of Naval Research (Report + SF298)
ONR Regional Office Seattle-N63374 (Report + SF425)
Defense Technical Information Center (Report + SF 298)✓
Naval Research Laboratory, Code 5596 (Report only)
D. Oride
ORS

17-131

1680 East-West Road, POST 109, Honolulu, Hawai'i 96822
Telephone: (808) 956-8890 Fax: (808) 956-2336
An Equal Opportunity/Affirmative Action Institution

REPORT DOCUMENTATION PAGE

Form Approved
OMB No. 0704-0188

The public reporting burden for this collection of information is estimated to average 1 hour per response, including the time for reviewing instructions, searching existing data sources, gathering and maintaining the data needed, and completing and reviewing the collection of information. Send comments regarding this burden estimate or any other aspect of this collection of information, including suggestions for reducing the burden, to Department of Defense, Washington Headquarters Services, Directorate for Information Operations and Reports (0704-0188), 1215 Jefferson Davis Highway, Suite 1204, Arlington, VA 22202-4302. Respondents should be aware that notwithstanding any other provision of law, no person shall be subject to any penalty for failing to comply with a collection of information if it does not display a currently valid OMB control number.
PLEASE DO NOT RETURN YOUR FORM TO THE ABOVE ADDRESS.

1. REPORT DATE *(DD-MM-YYYY)*	2. REPORT TYPE	3. DATES COVERED *(From - To)*
29/09/2017	Final Technical Report	01/05/12 - 30/06/17

4. TITLE AND SUBTITLE
Final Technical Report
Asia Pacific Research Initiative for Sustainable Energy Systems 2011 (APRISES11)

5a. CONTRACT NUMBER

5b. GRANT NUMBER
N00014-12-1-0496

5c. PROGRAM ELEMENT NUMBER

6. AUTHOR(S)
Rocheleau, Richard, E; St-Pierre, Jean; Cooney, Michael J; Turn, Scott, Q; Yu, Jian;Yoza, Brandon, A; Hihara, Lloyd, H; Masutani, Stephen, M; Cross, Patrick; Busquet, Severine; Ewan, James, "Mitch"; Maskrey, James, A.; Thomas, Don; Hashimoto, Andrew; Gaillard, Nicolas; Zinner, Stuart; Eldred, Michael

5d. PROJECT NUMBER
15PR214-61-00

5e. TASK NUMBER

5f. WORK UNIT NUMBER

7. PERFORMING ORGANIZATION NAME(S) AND ADDRESS(ES)
Hawaii Natural Energy Institute, University of Hawaii at Manoa
1680 East West Road, POST109
Honolulu, Hawaii 96822

8. PERFORMING ORGANIZATION REPORT NUMBER

9. SPONSORING/MONITORING AGENCY NAME(S) AND ADDRESS(ES)
Office of Research Services, University of Hawaii at Manoa
2440 Campus Road, Box 368
Honolulu, Hawaii 96822-2234

10. SPONSOR/MONITOR'S ACRONYM(S)
ONR

11. SPONSOR/MONITOR'S REPORT NUMBER(S)

12. DISTRIBUTION/AVAILABILITY STATEMENT
Approved for Public Release; Distribution is Unlimited

13. SUPPLEMENTARY NOTES

14. ABSTRACT
The focus of APRISES11 was to develop, test, and evaluate distributed energy systems using Hawaii as a model to address integration of emerging technologies in Hawaii and throughout the Pacific Region, including: fuel cell testing and evaluation; synthetic fuels processing and production; biomass; biofuel corrosion; extraction and stability of seabed methane hydrates; and alternative energy systems for electric power generation, energy efficiency, and secure-smart microgrids, including ocean energy, grid-scale battery energy storage, hydrogen fueling, building energy efficiency test platforms, energy efficiency technologies, and development of several microgrid test projects.

15. SUBJECT TERMS
Fuel cells, biofuels, biomass, biofuel corrosion, synthetic fuels, alternative energy, methane hydrates, renewable energy, ocean thermal energy conversion, OTEC, wave energy, ocean energy, battery energy storage, microgrids, power grid integration, photovoltaic, PV, energy efficiency, energy test platforms, hydrogen, hydrogen fueling, geothermal resource.

16. SECURITY CLASSIFICATION OF:			17. LIMITATION OF ABSTRACT	18. NUMBER OF PAGES	19a. NAME OF RESPONSIBLE PERSON
a. REPORT	b. ABSTRACT	c. THIS PAGE			Richard E. Rocheleau
					19b. TELEPHONE NUMBER *(Include area code)*
U	U	U	UU	187	(808) 956-8346

INSTRUCTIONS FOR COMPLETING SF 298

1. REPORT DATE. Full publication date, including day, month, if available. Must cite at least the year and be Year 2000 compliant, e.g. 30-06-1998; xx-06-1998; xx-xx-1998.

2. REPORT TYPE. State the type of report, such as final, technical, interim, memorandum, master's thesis, progress, quarterly, research, special, group study, etc.

3. DATE COVERED. Indicate the time during which the work was performed and the report was written, e.g., Jun 1997 - Jun 1998; 1-10 Jun 1996; May - Nov 1998; Nov 1998.

4. TITLE. Enter title and subtitle with volume number and part number, if applicable. On classified documents, enter the title classification in parentheses.

5a. CONTRACT NUMBER. Enter all contract numbers as they appear in the report, e.g. F33315-86-C-5169.

5b. GRANT NUMBER. Enter all grant numbers as they appear in the report. e.g. AFOSR-82-1234.

5c. PROGRAM ELEMENT NUMBER. Enter all program element numbers as they appear in the report, e.g. 61101A.

5e. TASK NUMBER. Enter all task numbers as they appear in the report, e.g. 05; RF0330201; T4112.

5f. WORK UNIT NUMBER. Enter all work unit numbers as they appear in the report, e.g. 001; AFAPL30480105.

6. AUTHOR(S). Enter name(s) of person(s) responsible for writing the report, performing the research, or credited with the content of the report. The form of entry is the last name, first name, middle initial, and additional qualifiers separated by commas, e.g. Smith, Richard, J, Jr.

7. PERFORMING ORGANIZATION NAME(S) AND ADDRESS(ES). Self-explanatory.

8. PERFORMING ORGANIZATION REPORT NUMBER. Enter all unique alphanumeric report numbers assigned by the performing organization, e.g. BRL-1234; AFWL-TR-85-4017-Vol-21-PT-2.

9. SPONSORING/MONITORING AGENCY NAME(S) AND ADDRESS(ES). Enter the name and address of the organization(s) financially responsible for and monitoring the work.

10. SPONSOR/MONITOR'S ACRONYM(S). Enter, if available, e.g. BRL, ARDEC, NADC.

11. SPONSOR/MONITOR'S REPORT NUMBER(S). Enter report number as assigned by the sponsoring/ monitoring agency, if available, e.g. BRL-TR-829; -215.

12. DISTRIBUTION/AVAILABILITY STATEMENT. Use agency-mandated availability statements to indicate the public availability or distribution limitations of the report. If additional limitations/ restrictions or special markings are indicated, follow agency authorization procedures, e.g. RD/FRD, PROPIN, ITAR, etc. Include copyright information.

13. SUPPLEMENTARY NOTES. Enter information not included elsewhere such as: prepared in cooperation with; translation of; report supersedes; old edition number, etc.

14. ABSTRACT. A brief (approximately 200 words) factual summary of the most significant information.

15. SUBJECT TERMS. Key words or phrases identifying major concepts in the report.

16. SECURITY CLASSIFICATION. Enter security classification in accordance with security classification regulations, e.g. U, C, S, etc. If this form contains classified information, stamp classification level on the top and bottom of this page.

17. LIMITATION OF ABSTRACT. This block must be completed to assign a distribution limitation to the abstract. Enter UU (Unclassified Unlimited) or SAR (Same as Report). An entry in this block is necessary if the abstract is to be limited.

FINAL TECHNICAL REPORT

Asia Pacific Research Initiative for Sustainable Energy Systems

Office of Naval Research

Grant Award Number N00014-12-1-0496

For the period May 1, 2012 to June 30, 2017

HNEI
Hawai'i Natural Energy Institute
University of Hawai'i at Mānoa

September 2017

Table of Contents

EXECUTIVE SUMMARY 3

Task 1. PROGRAM MANAGEMENT AND OUTREACH 5

Task 2. FUEL CELL SYSTEMS 5

2.1 Fuel Cell Systems: Development and Testing 6

2.2 Support for Big Island Fuel Cell Electric Buses 56

Task 3. ALTERNATE FUELS 59

3.1 Methane Hydrates 60

3.2 Technology for Synthetic Fuels Production 73

3.3 Sustainable Biomass 96

3.4. Low Cost Materials for Solar Fuels Production 100

3.5 Hydrogen Fuel Production 101

Task 4. OCEAN ENERGY 106

4.1 OTEC Heat Exchanger Development and Testing 107

4.2 Wave Energy Testing 108

TASK 5. GEOTHERMAL RESOURCE ASSESSMENT 109

Task 6. MICROGRIDS/GRID INTEGRATION 115

6.1 Solar Hydrogen at Marine Corps Base Hawaii 115

6.2 Secure Microgrids 125

6.3 Grid Integration at Community College Sites 175

Task 7. ENERGY EFFICIENCY 178

Final Technical Report
Asia Pacific Research Initiative for Sustainable Energy Systems
Grant Award Number N00014-12-1-0496
May 1, 2012 to June 30, 2017

EXECUTIVE SUMMARY

This report summarizes work conducted under Grant Award Number N00014-12-1-0496, the Asia Pacific Research Initiative for Sustainable Energy Systems 2011 (APRISES11), , funded by the Office of Naval Research (ONR) to the Hawaii Natural Energy Institute (HNEI) of the University of Hawaii at Manoa (UH). The overall objective of the APRISES11 effort was to develop, test, and evaluate distributed energy systems using Hawaii as a model to address integration of emerging technologies in Hawaii and throughout the Pacific Region. APRISES11 encompassed fuel cell testing and evaluation including technologies developed at the Naval Research Laboratory (NRL); synthetic fuels processing and production to accelerate the use of liquid biofuels for Navy needs; the extraction and stability of seabed methane hydrates; and alternative energy systems for electric power generation, energy efficiency, and secure-smart microgrids. Testing and evaluation of alternative energy systems includes work on Ocean Thermal Energy Conversion (OTEC), grid-scale battery energy storage, support for hydrogen fuel operations at the Marine Corps Base Hawaii and on the Island of Hawaii, building energy efficiency test platforms, end-use high value energy efficiency technologies, and development of several microgrid test projects

Under Task 1, Program Management, HNEI managed the program, developed and monitored partner and subcontract agreements, and developed outreach materials for both technical and non-technical audiences. HNEI continued to collaborate closely with ONR and NRL to identify high-priority areas requiring further detailed evaluation and analysis.

Under Task 2, Fuel Cell Systems, , HNEI conducted testing and evaluation of single cells, stacks and balance of plant components to support NRL efforts to develop fuel cell powered UAVs; to improve understanding of contamination mechanisms, assess the tolerance of alternate catalysts to contaminants, and, development of contaminant mitigation techniques. Support to NRL including validation of the impedance-based NRL battery state of health diagnostic method with a battery pack. Under Task 2, HNEI also designed, built and commissioned an air filter test station that is being used to test and evaluate filtration materials and designs for fuel cell demonstration buses in the harsh atmosphere of Hawaii Volcanoes National Park.

Efforts under Task 3, Alternative Fuels, focused on the development, testing and evaluation of alternative fuels and technologies included activities in the areas of Methane Hydrates, Technology for Synthetic Fuels Production, Sustainable Biomass, Low-cost Material for Solar Fuels Production, and Hydrogen Fuel Production. Methane hydrates efforts focused on hydrate stability and related environmental issues; hydrogen fuel storage in binary hydrates; and promoting international research collaborations. Technology for Synthetic Fuels Production included efforts in Hydrogen Production for Fuel Cell Applications, Evaluation of Second Generation Biofuels, Novel Solvent Based Extraction of Bio-oils and Protein from Oil-Bearing Biomass, Biochemical Conversion of Synthesis Gas into Liquid Fuels, Bio-contamination of Fuels, Biofuel Corrosion Control, and Waste Management Using the Flash-Carbonization™ Process.

Task 4, Ocean Energy work included continued development and testing of cost effective heat exchangers for Ocean Thermal Energy Conversion (OTEC) under a subaward to Makai Ocean Engineering; and technology support of wave energy testing at the Navy's Wave Energy Test Site (WETS), off Marine Corps Base Hawaii (MCBH).

The objective of Task 5, Geothermal Resource Assessment, was to perform preliminary surveys on DOD lands in Hawaii to assess their potential for hosting a geothermal resource, using audio-magnetotelluric survey methods.

Task 6, Microgrids/Grid Integration included efforts on developing Solar Hydrogen at Marine Corps Base Hawaii, a range of projects to develop, test and evaluate cost effective Secure Microgrids along with the enabling technology, and Grid Integration at a Community College, focused on integration of renewable energy generation and related technologies.

Task 7 comprised three projects relating to Energy Efficiency in buildings. This instrumenting and monitoring zero energy research platforms and existing, conventional classrooms to determine comparative performance in energy, indoor environmental quality, and comfort. Desiccant dehumidification was examined as a means to improve comfort at lower energy expense, and the applicability of ceiling fans to low energy thermal comfort.

This report provides detail of the work that has been accomplished under each of these tasks, along with summaries of task efforts that are detailed in journal and other publications, including reports, conference proceedings and presentations. Publications produced through these efforts are listed and available on HNEI's website at http://www.hnei.hawaii.edu/publications/project-reports#APRISES11.

Task 1. PROGRAM MANAGEMENT AND OUTREACH

This program-wide task provided management and coordination of all research, test, development and evaluation efforts under APRISES11. Partner and subcontract agreements were developed and monitored, and outreach materials for both technical and non-technical audiences were developed. In close collaboration with ONR, high-priority areas requiring further detailed evaluation and analysis were identified. Partners, outreach materials and high-priority areas requiring further are included in the specific tasks below.

Task 2. FUEL CELL SYSTEMS

Work under Task 2 included continuation of fuel cell testing and evaluation, continued development of new diagnostic techniques. An air filter test station was designed, built and commissioned to field testing of FC-electric buses and development of contaminant mitigation. Under Task 2, testing of single cell Li-ion batteries was also expanded.

Fuel cell stacks and humidifiers were tested in support of NRL UAV system development. Significant efforts continued to be devoted to the impact of contaminants on fuel cells. The distributed effects of contamination along the fuel cell stacking direction (cell number) was demonstrated with an organic airborne contaminant and mechanistic explanations were formulated. The sensitivity of alternative catalysts that do not contain precious metals, to several common inorganic air contaminants, was evaluated to clarify catalyst replacement options. A mathematical model for a fuel cell contaminated with carbon monoxide in the hydrogen stream was validated for concentrations closer to the international standard requirement using segmented cell data to capture local variations across the cell active area, and to predict performance losses. To determine the existence of mass transport losses associated with contaminant adsorption on materials that modify their hydrophobic properties, the quantity of product water in the fuel cell air compartment was measured at NIST using neutron imaging. The efficiency of a fuel cell stack compatible performance recovery method, based on the circulation of nitrous oxide to oxidize contaminants irreversibly adsorbed on the catalyst surface, was also investigated. An impedance model containing mass transport parameters was developed as a first step toward the cross-validation of an HNEI developed method to separate reactant mass transfer coefficients into fundamental contributions for cell design optimization purposes. HNEI verified the state of health diagnostic based on single frequency impedance developed by NRL for lithium ion batteries.

An air filter test station was designed, built and commissioned to evaluate options for fuel cell demonstration buses that will be exposed in the field to high levels of atmospheric sulfur dioxide during field tests at Volcano National Park.

Support for Big Island Fuel Cell Buses, subtask 2.2, entailed converting fossil-fueled internal combustion engine powered shuttle buses to battery-fuel cell hybrids fueled by hydrogen. Under other funding, these buses will be operated in harsh environments with elevated levels of SO_2 to demonstrate and evaluate fuel cell and filtration performance.

The following provides more detail on each of these subtasks.

2.1 Fuel Cell Systems: Development and Testing

Work performed under previous ONR awards focused on the understanding, performance, and durability of fuel cell systems subject to harsh environments, and issues associated with UUV and UAV fuel cell systems. Efforts to develop new fuel cell diagnostics for improved understanding were also continued. Additionally, HNEI provided testing services to NRL in support of their activities to explore the potential of 3D printing and metal stamping for fuel cell bipolar plates. A fuel cell stack with an integrated humidifier was also selected and characterized as an alternative to off-the-shelf humidifiers. Work under APRISES11 continued and extended these efforts to batteries for hybrid power systems.

Many aspects of fuel cell contamination were investigated because little or no information was available to anticipate issues, failures, maintenance needs and technology improvement options. These aspects include the performance loss distribution in a stack (cell to cell variations), the tolerance of alternate catalysts based on iron, the predictive mathematical modeling of performance losses for low contaminant concentrations, the impact of contaminants on product water management within a cell, and the recovery of performance losses in a stack. Fuel cell technology has partially focused on operation at high current densities and decreases in costly platinum catalyst loadings to meet commercialization cost targets. Under these design parameters, performance losses associated with reactant mass transfer are exacerbated, which have stimulated research in the measurement of mass transfer coefficients for cell design optimization. Battery state of health diagnostics with a minimal system complexity and cost are needed to minimize the occurrence of failures. However, the applicability of single frequency impedance measurements to battery packs, which simplifies excitation signal generation, data acquisition and treatment, has not been evaluated.

A more detailed description of all these contributions follows below.

NRL support

The potential of 3D printing, also known as additive manufacturing (AM), was explored by NRL to evaluate the possibility of simplifying the manufacture of metallic bipolar plates (BPP). Additive manufacturing for fuel cell components is a recent trend due to its ability to create metal parts with complex geometries, such as the internal passages of coolant flow fields inside bipolar plates, with a relatively short lead time. Single piece metallic bipolar plates could lead to a significant reduction in the number of parts and assembly complexity of fuel cell stacks. In addition, multiple flow field designs could be created during a single run, highlighting rapid prototyping capabilities.

NRL's overall goal was to evaluate whether 3D printed metallic bipolar plates could match the performance of existing technologies, i.e. graphite composites and stamped metallic bipolar plates, for use in ultra-lightweight fuel cells. Using the 3D-printing method of direct metal laser sintering (DMLS), NRL designed and built 21 cm^2 titanium-alloy bipolar plates with embedded flow channels that were subsequently polished to the appropriate roughness and coated with a conductive corrosion barrier. During the research and development cycle, NRL delivered four stack builds using these plates to HNEI for testing and evaluation, i.e. a 10 cell stack (Figure 2.1.1), an 8 cell stack, a 40 cell stack (after flight testing) with standard bolt compression (Figure 2.1.1), and another 13 cell stack with NRL's newly developed spot welded titanium strap compression system. The strap compression technique aimed to reduce the weight of the end

plates and compression rods typically used in fuel cell applications not requiring ultra-light weight. In addition, HNEI also tested a Protonex 60 cell 1.5 kW test system to provide comparison data with tests performed on a brassboard at NRL and humidifier performance evaluations as part of the balance of plant development.

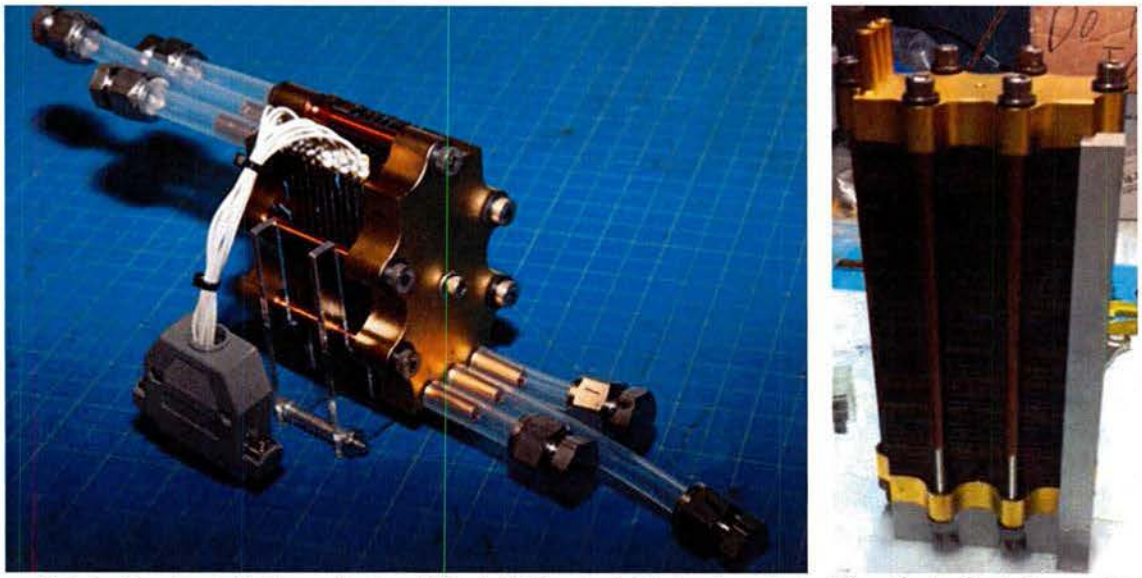

Figure 2.1.1. Pre-installation photo of first 3-D printed bipolar plate 10 cell stack delivered to HNEI with standard endplate/bolt combination for stack compression (left). 40 cell stack photo (right).

For the 3D printed stack evaluations, HNEI developed a short testing program for each stack build aimed at determining the performance under typical fuel cell conditions, for comparison with standard plate designs, and a sequence of in situ individual cell diagnostics to evaluate the cell to cell variability and uniformity to determine any inconsistencies due to the 3D printed plate design and/or manufacturing. As part of the diagnostic test development, HNEI was able to optimize an existing single cell experimental method to evaluate individual cell hydrogen crossover and electrical shorting, reducing the experiment completion time from 45 minutes to 7 minutes per cell or from 30 to 4.6 h per 40 cell stack.

Previous work by NRL demonstrated that a single-cell fuel cell made from the 3D-printed bipolar plates performed well compared to standard parts.[1,2] However the 8, 10, and 40 cell fuel cell stack power as tested at HNEI was over 20 % less than expected due to performance losses induced by the inadequate flatness of several of the BPPs. This cell-to-cell mismatch led to high contact resistance in several of the cells, as well as caused electrical shorting from pinching on parts of the membrane/electrode assembly. NRL was able to correlate white light prolifometry data with in situ cell diagnostic data taken at HNEI for plates demonstrating poor performance.[3-5]

HNEI also noted that the observed poor performance and instability at higher current densities may be a by-product of the plate design iterations. Early single cell 3D printed designs by NRL used straight parallel flow channels with embedded straight parallel coolant channels where a temperature differential from inlet to outlet is maintained to limit condensation downstream in the flow-field channels. Subsequent design iterations by NRL lead to adapting a serpentine flow field design while maintaining straight, parallel embedded coolant channels. This could have resulted in condensation of water in the downstream section of the flow field that is passing the cooler section of the coolant channel inlet due to the serpentine design. However without in situ

water content analysis, such as that provided by neutron imaging or residence time distribution methods, this hypothesized effect could not be verified.

NRL concluded that DMLS clearly showed the benefit of being able to make complex flow fields and hollow parts with no welds and is useful for prototyping flow fields in single cells or short stacks. However, NRL also concluded more work is needed toward reducing the weight and increasing the flatness of BPPs made by DMLS before they can be used in larger stacks. A summary of the test plan, diagnostic method development and key results from testing and evaluation of the four stack builds delivered to HNEI are presented below. Further details of this work by NRL and HNEI has been documented in 4 publications, 1 conference proceeding, and 1 magazine article.[1-6] As new approaches to 3D printing of metals are developed, such as those recently developed in 2017 by Desktop Metals Inc,[7] revisiting the production of bipolar plates by 3D printing may be prudent.

All fuel cell experiments were performed at HiSERF using the in-house designed 5 kW test stand. An Agilent 4338B AC milliohm meter was used for high frequency resistance (HFR) measurements and a Solartron 1287 Potentiostat/Galvanostat was used for membrane/electrode assembly (MEA) diagnostics, i.e. hydrogen crossover (H2X), shorting resistance (SHORT), and cyclic voltammetry (CV) for determination of electrochemical surface area (ECSA) experiments. A novel in-house multi-cell electrochemical impedance spectroscopy (EIS) based on National Instruments CDAQ signal conditioning modules was also used for evaluation of the 8 cell stack to help diagnose mass transport issues observed. All HFR, H2X, SHORT, and ECSA measurements were performed sequentially from cell 1 to the last cell, using a 4-wire system that was changed manually by test operators after each cell diagnostics experiment. The 3D printed plate design has unused square holes at the end of each cell which were used to make connections for the 4-wire measurements, as shown in Figure 2.1.2. The unused holes were also used for cell voltage measurements, also shown in Figure 2.1.2.

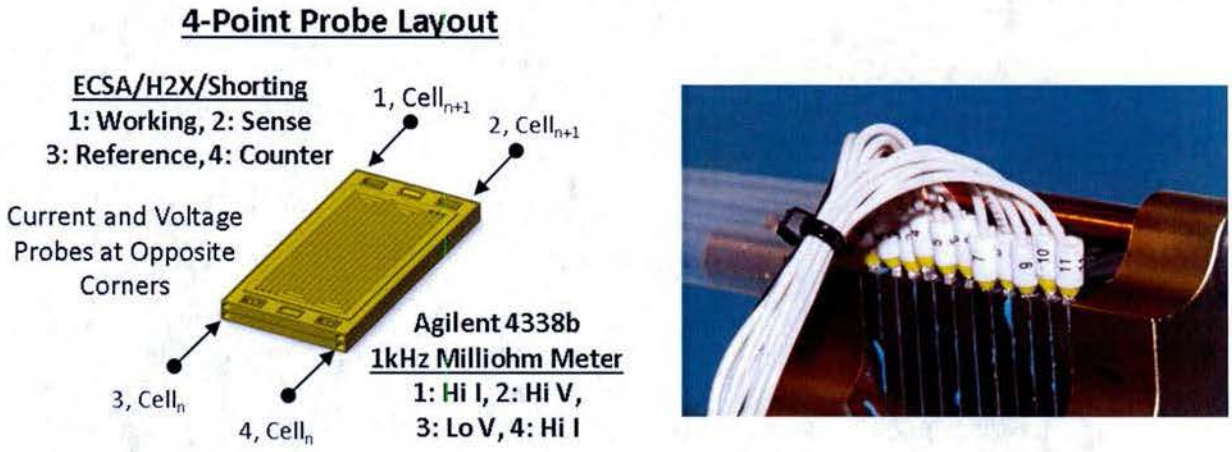

Figure 2.1.2. Layout of 4-Wire probe for individual cell measurements (left). Cell voltage monitoring connections on 10 cell stack (right).

For all experiments performed, the stack was operated in a Z-flow configuration with the reactants in co-flow mode. The anode and cathode gas inlets are located at opposite sides of the top of the positive endplate and the outlets at the bottom of the negative endplate. The coolant inlet and outlet was opposite to that of the gas flow, with the inlet and outlet located at the negative and positive endplate, respectively. For all experiments the coolant was controlled at a

constant flow rate of 2 LPM with inlet temperature control and no back pressure.**Error! Reference source not found.** Figure 2.1.3 shows the port orientation and flow paths for the reactant gases and coolant. From Figure 2.1.3, bottom, the downstream portion of the reactant flow paths coincide with the inlet of the coolant, which may lead to detrimental condensation of water in the reactant flow paths, as mentioned previously, due to the lower temperature at the coolant inlet vs. outlet and the higher water content from water generated by the fuel cell reactions in the downstream portion of the flow paths.

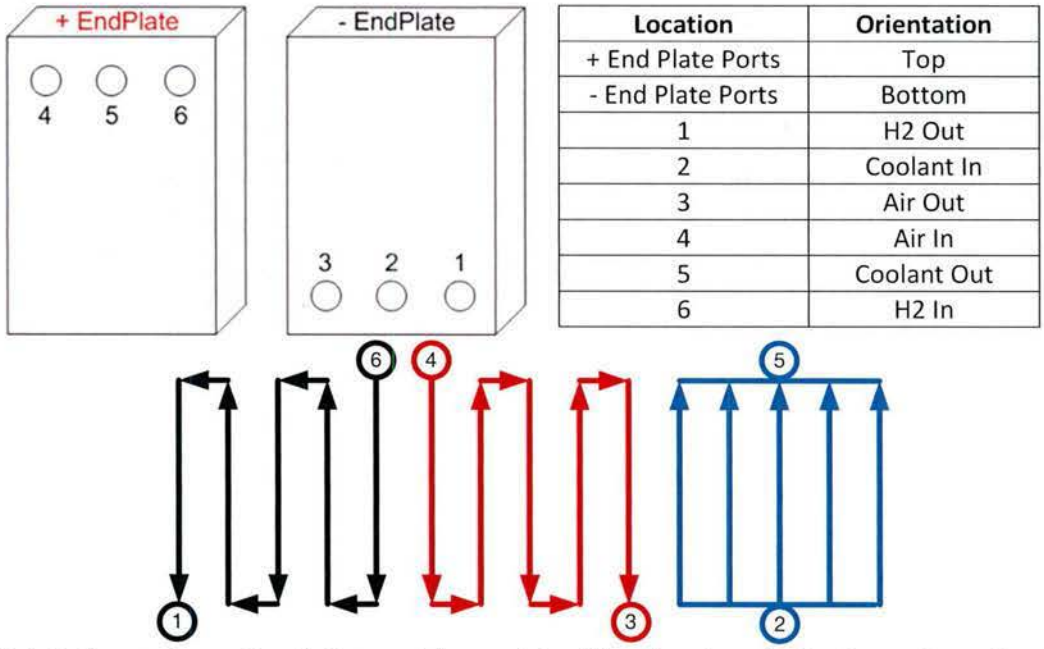

Location	Orientation
+ End Plate Ports	Top
- End Plate Ports	Bottom
1	H2 Out
2	Coolant In
3	Air Out
4	Air In
5	Coolant Out
6	H2 In

Figure 2.1.3. Front view of end plates with port identification (top, left). Port orientation for co-flow reactants, counter-flow coolant (top, right). Serpentine reactant and straight parallel coolant flow paths labeled with anode = black, cathode = red, and coolant = blue (bottom).

A limited set of diagnostic tests was agreed upon between NRL and HNEI to provide sufficient information for comparison data and diagnose any major issues with the plate design. A summary of these experiments, test conditions, and test profiles is provided in Table 2.1.1.

As mentioned previously and described in Table 2.1.1, most researchers to date have used a simple, slow potentiodynamic scan for measuring the shorting resistance and equivalent hydrogen crossover currents. However these scans take approximately 45 minutes per cell which is not practical for measuring multiple cells in a fuel cell stack, particularly without an automated multiplexer for switching the cell measurement points. CV scans for ECSA typically take about 5 minutes per cell for small cells. To reduce the time to make individual H2X, SHORT, and ECSA measurements, a ramp and hold method was developed and tested so that all 40 cells can be tested in one working day with a technician switching the 4-point cell measurement connections manually. Only two points are needed to calculate a slope, thus a two-step sequence was developed, whereby first ramping at 5 mV sec^{-1} from open circuit to 0.35 V and holding for 3 minutes while averaging the last 15 seconds of the hold to obtain the current at 0.35 V. Then another ramp at 5 mV sec^{-1} is initiated from 0.35 to 0.5 V again holding for 3 minutes and averaging the last 15 seconds of the hold to obtain the current at 0.5 V. The slope can then be calculated using the current/voltage (IV) data of the two points to provide the shorting resistance. The equivalent hydrogen crossover current can then be obtained using the short resistance corrected current at 0.5 V. The method schematic and validation of the ramp and hold method vs

the scanning method are provided in Figure 4, with data recorded on cell 8 from the 8 cell stack tests which showed an excessively large electrical short.

Table 2.1.1. Summary of experimental diagnostics.

Experiment	**Test Conditions**	**Test Profile**
H_2/Air Polarization with 1 kHz HFR and multi-cell EIS from 0.1 Hz to 10 kHz performed at 0.8 A/cm^2 on selected stacks	60 °C, 100 % RH, 2/2 Stoichiometry, Ambient Back Pressure	Condition at 0.8 A/cm^2 for >10 min, ramp to 1 A/cm^2, perform descending steps to OCV with flows constant below 0.4 A/cm^2, extend hold time (~30 min) to allow for HFR measurements, average data last 30 seconds of hold.
Cathode Stoichiometry Sweep at 0.8 A/cm^2 to Evaluate mass transport losses	60 °C, 100 % RH, 2/Variable Stoichiometry, Ambient Back Pressure	Condition at 0.8 A/cm^2 for >10 min, Increase cathode flows to equivalent stoichiometry of 3, change flows in 0.2 increments every 5 minutes down to 1.3 stoichiometry
Short Resistance and Hydrogen Crossover (Long Method: Potentiodynamic) (Short Method: Ramp and Hold)	30 °C, 100 % RH, 0.25 SLPM/cell H_2, 0.25 SLPM/cell N_2, Ambient Back Pressure	Potentiodynamic: 0.1 mV/sec scan From 0.1 to 0.5 V vs. reference Ramp and hold: OCV to 0.35 V to 0.5 V vs. reference Ramp rate: 5 mV/sec, Hold time: 3 min Average data last 15 s of hold. Short Resistance = dV/di (0.5 V, 0.35 V) H_2 Xover = short corrected i @ 0.5 V (Ramp and Hold was a newly protocol developed)
Cyclic Voltammetry for Electrochemical Surface Area Determination	30 °C, 100 % RH, 0.25 SLPM/cell H_2, 0.1 SLPM/cell N_2, Ambient Back Pressure	CV Scan @ 20 mV/sec Scan Range: 0.06-0.6 V vs. reference, 3 cycles Short corrected V vs. I data before integration of H_2 adsorption and desorption regions for surface area estimations

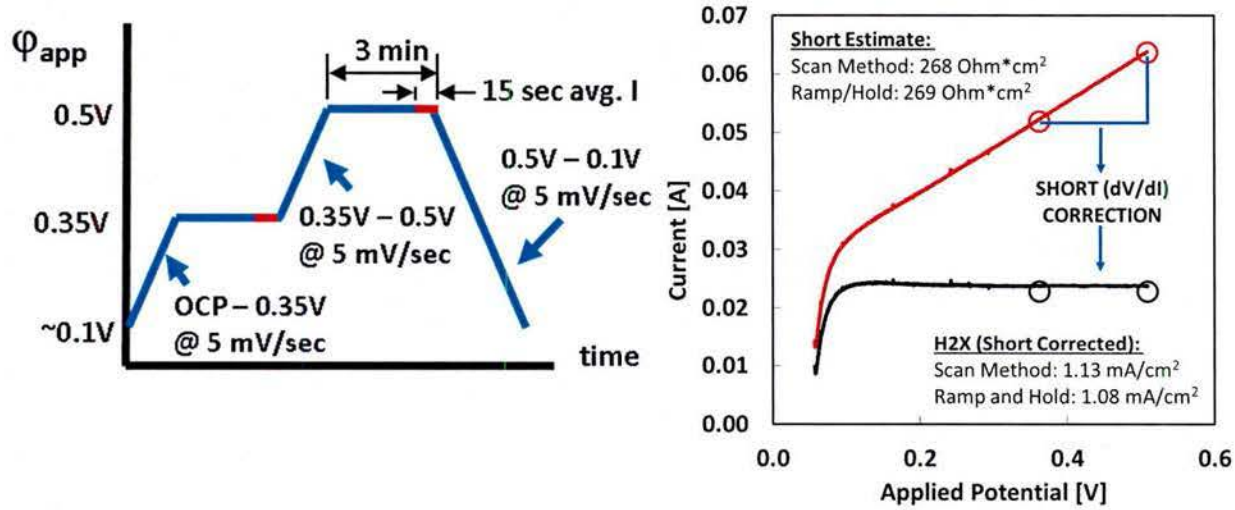

Figure 2.1.4. Schematic of ramp and hold shorting resistance/hydrogen crossover diagnostic method (left). Comparison/validation data using the 45 minutes potentiodynamic scan method vs. the 7 minute ramp and hold two point method (right).

A 10 cell stack was the first 3D printed stack build delivered to HNEI in July 2013. NRL indicated that they built both a 10 cell and a 32 cell stack (not tested by HNEI) simultaneously. However the 10 cell stack was made with "B-grade" plates which were qualitatively selected based on their less than flat appearance. The MEAs utilized for this test were GORE 5715 Series with 0.1/0.4 mg Pt cm^{-2} platinum loadings on the anode and cathode, respectively. The only experiments performed on this stack were the air polarization curve with HFR measurements, anode ECSA, and cathode ECSA MEA diagnostics. Figure 5, top, left displays the averaged polarization curve data, while Figure 5, top, right shows the corresponding HFR measurements. Figure 5, bottom, left presents the time series data during the polarization curve and Figure 5, bottom, right displays the ohmic-corrected polarization curve data. From the time series data plot, cell 3 was observed to drop off at 400 mA cm^{-2}, possibly due to insufficient water clearing with the lower flow rates, however cell voltages were relatively stable at higher current densities. Cell 4 losses were found to increase with increasing current density indicating ohmic loss related issues, and cell 10 had a lower open circuit voltage than all other cells possibly indicating higher hydrogen crossover or an electrical short. From the averaged polarization curve data, HFR measurements confirmed cell 4 losses were predominantly ohmic losses, with the adjacent cells 3 and 5 having the next highest HFR magnitude. The ECSA measurements (not shown) indicated no loss of active area and the surface area calculations for all 10 cells on both the anode and the cathode were within expectations for new GORE 5715 electrodes (~70-80 m^2 g of Pt). Cell 10 did show a slight increase in current with increasing voltage during the ECSA tests indicating a possible electrical short, which correlates with the lower open circuit voltage. Thus for all future ESCA and H2X measurements, evaluation of the electrical shorting was deemed necessary to correct the scan IV data results prior to calculating the ECSA and H2X magnitudes. A Quality Assurance/Quality Control (QA/QC) procedure was also recommended to NRL using an Alternating Current (AC) milliohm meter to measure the HFR under ambient temperature conditions with hydrogen and nitrogen on the anode and the cathode, respectively, following the initial stack build to validate the HFR and compression characteristics. This would enable NRL, who has limited test stand capabilities, the ability to identify whether the flatness of the plates was causing an issue with contact resistance that was not negligible, prior to sending a stack to HNEI.

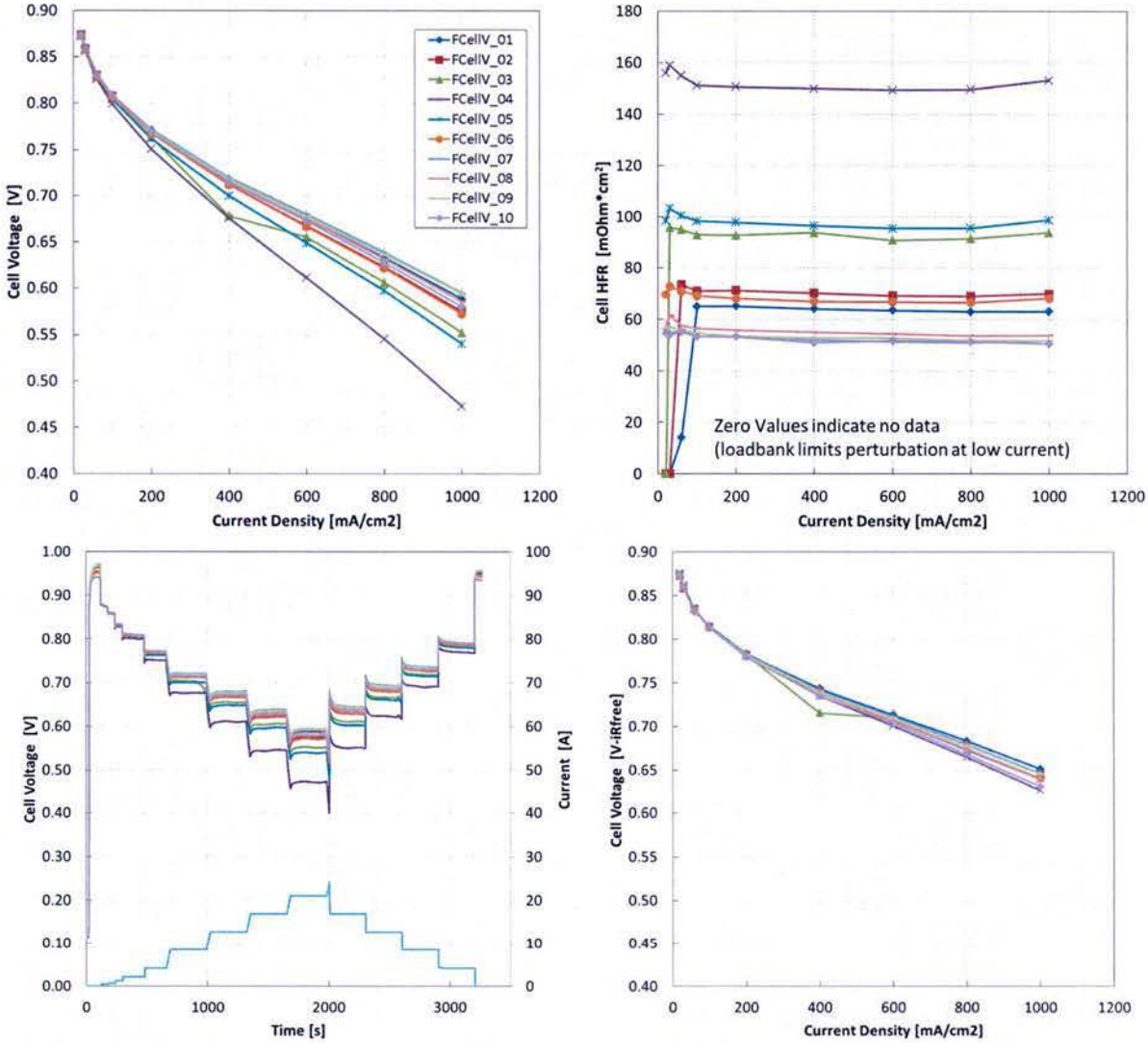

Figure 2.1.5. Initial 10 cell stack evaluation polarization curve data. Average cell voltage vs current density data (top, left), high frequency resistance vs. current density (top, right), individual cell voltages and current vs. time (bottom, left), and ohmic-corrected average cell voltage vs. current density (bottom, right).

Following the short testing evaluation performed at HNEI, the stack was returned to NRL for disassembly and evaluation of the plate flatness which confirmed cell 4 was shaped like a 'potato chip'. In summary:

- The initial polarization curve showed highly variable high frequency resistances with some cells displaying values 3x greater than expected
- Further parametric testing was halted due to the large variability observed
- A surface area estimation methodology (flows, connections, scan metrics) was developed and demonstrated to correct data for electrical shorts prior to estimating the cell real active area
- The most significant issue was contact resistance, but electrical shorting was also evident
- An Agilent 4338B milliohm meter was recommended for fast QA/QC of builds at NRL
- NRL indicated that the observed issues were not unexpected as the stack was made up of "B-grade" plates.

After the return of the 10 cell stack to NRL, NRL implemented the HFR QA/QC procedure into their build process. As a result, they re-built and disassembled the 10 cell stack multiple times using the same internal components, while checking the HFR QA/QC results after each re-compression sequence. These activities resulted in the elimination of cells with high HFR values. NRL returned to HNEI a shorter 8 cell stack for re-evaluation. Experiments performed on this stack were a repeat of the HFR QA/QC procedure, air polarization curve, multi-cell electrochemical impedance spectroscopy, ECSA measurements, and the newly optimized ramp and hold method to determine the H2X and SHORT magnitudes. Figure 2.1.6 displays the polarization curve data recorded on the 8 cell stack (10 cell stack rebuild).

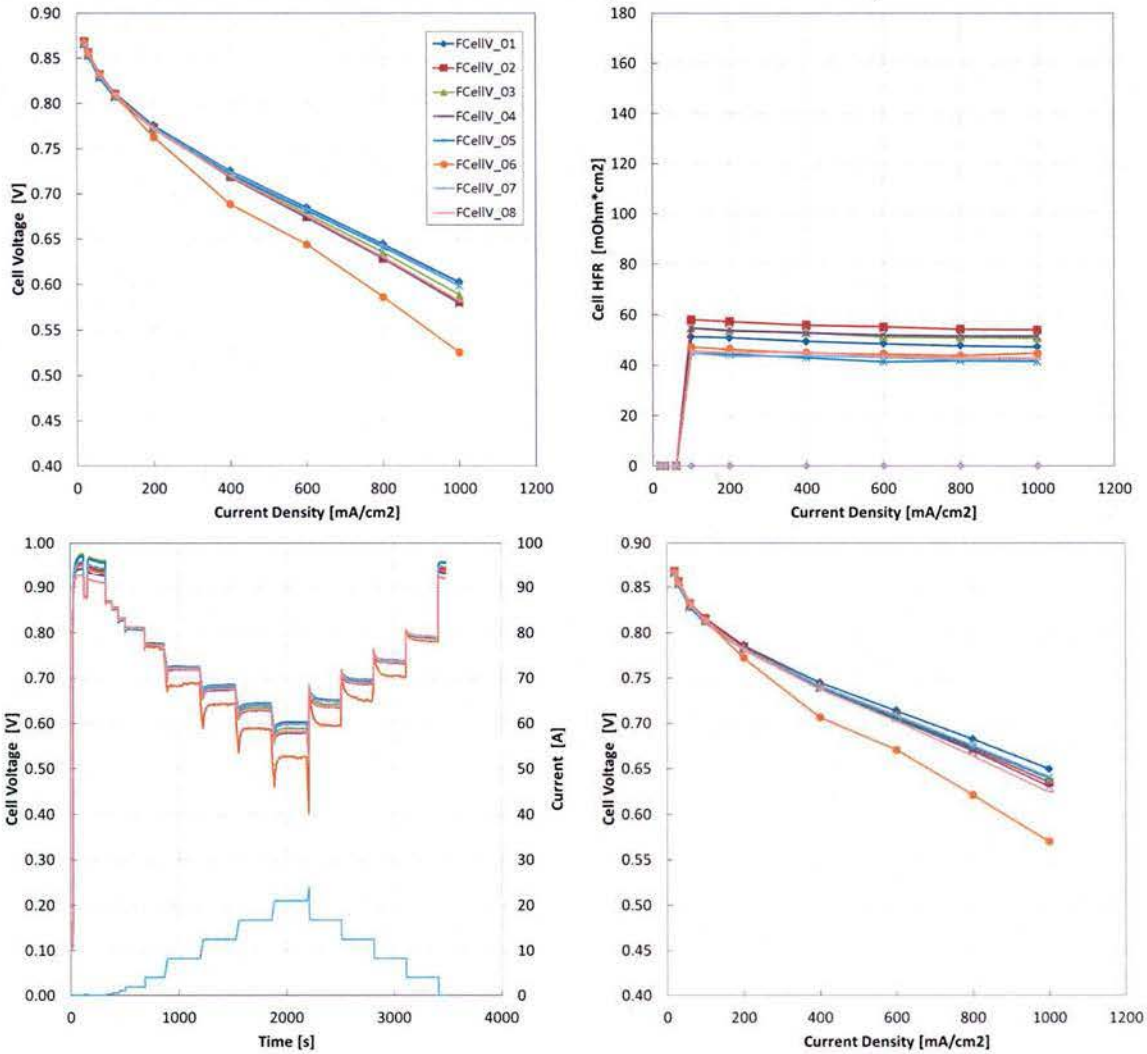

Figure 2.1.6. Evaluation polarization curve data of 8 cell stack (re-built 10 cell stack). Average cell voltage vs. current density data (top, left), high frequency resistance vs. current density (top, right), individual cell voltages and current vs. time (bottom, left), and ohmic-corrected average cell voltage vs. current density (bottom, right).

The initial ambient temperature HFR QA/QC evaluations as well as the HFR data recorded during the polarization curve demonstrated that the contact resistance issue observed in the previous 10 cell stack build was mitigated. However, as shown in Figure 2.1.6, cell 6 was still low performing even after the ohmic correction. A significant drop in cell 6 voltage was also

observed in the time series after each current step. This observation indicated a significant mass transport issue, which may have been caused by repeatedly re-building the stack leading to a collapse in the GDL properties or a possible physical blockage in the flow channels from a misaligned gasket or some other similar cause. HNEI's in-house developed multi-cell electrochemical impedance spectroscopy (EIS) system was used to deconvolute the stack performance losses at 800 mA cm^{-2} to confirm the mass transport issue with cell 6. Figure 2.1.7 displays the EIS data as recorded, as well as the reduced data in bar plots showing the ohmic/HFR impedance and the activation plus mass transport resistance magnitudes. Figure 2.1.8 presents data from the MEA diagnostics. As shown in Figure 2.1.7, right, cell 6 was found to exhibit a significantly higher activation plus mass transport losses. Although more advanced analyses were available to differentiate the activation and mass transport losses, the basic analysis displayed was sufficient to deduce and confirm the low performance observed in cell 6 was due to a mass transport issue, particularly as the ECSA tests results displayed in Figure 2.1.8 showed the absence of a decrease in cathode catalyst surface area which would indicate a higher activation impedance. The source of the mass transport loss, however, could not be identified. This could have been a blockage in the flow field from a misaligned gasket or over-compression of the gas diffusion layers from the repeated stack re-builds. A high variability in the electrical shorting behavior was also noted, as shown in Figure 2.1.8, which also correlated with the variability in the Open Circuit Voltage (OCV) during the polarization curve. Several cells showed a shorting resistance at or below the Department of Energy's limit of 1000 ohm cm^2, which is used for accelerated durability testing of MEAs. The hydrogen crossover results, although showing a skew from inlet to outlet (possibly due to an uneven gas flow distribution) were within acceptable ranges for new MEAs (less than 1.5 mA cm^{-2}). Thus, based on the 10 cell and 8 cell test results, the primary impact of the inadequate plate flatness caused issues with high contact resistance from areas of the plates not being close enough, and electrical shorting issues where plates may be pinching the MEAs. In summary:

- NRL rebuilt the 10 cell stack using the same components, by removing 1 cell at a time, and recompressing and checking the HFR before returning an 8 cell stack to HNEI.
- HNEI repeated the ambient temperature HFR QA/QC procedure NRL performed prior to the return shipment which demonstrated the contact resistance issue observed in the 10 cell stack was mitigated.
- The polarization curve data showed a significant mass transport issue in the stack which may have been due to the multiple recompression cycles during the rebuild. A multi-cell EIS scan was performed which confirmed a mass transport loss was predominantly causing the loss of performance.
- The open circuit voltage showed a high variability which was caused predominantly by electrical shorting and not a high hydrogen crossover.
- For future cell builds, it was recommended to focus on ensuring selected plates are sufficiently flat. The number of diagnostics tests can then be reduced by primarily looking at electrical shorting and contact resistance behaviors to validate the stack build.

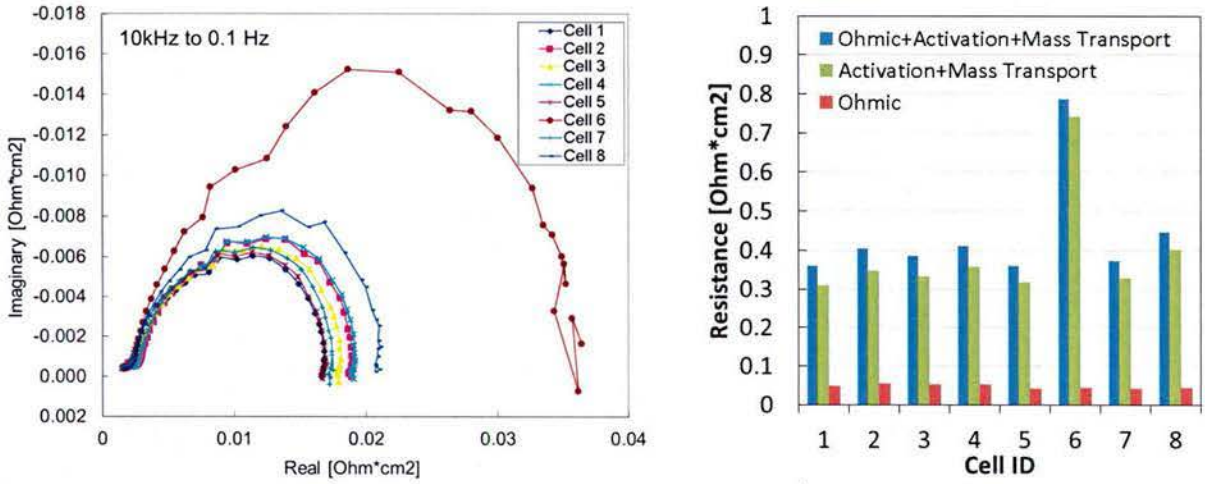

Figure 2.1.7. Simultaneous multi-cell impedance data recorded at 0.8 A cm^{-2} and displayed in a Nyquist plot (left). Calculated impedance/resistance losses per cell from EIS data (right).

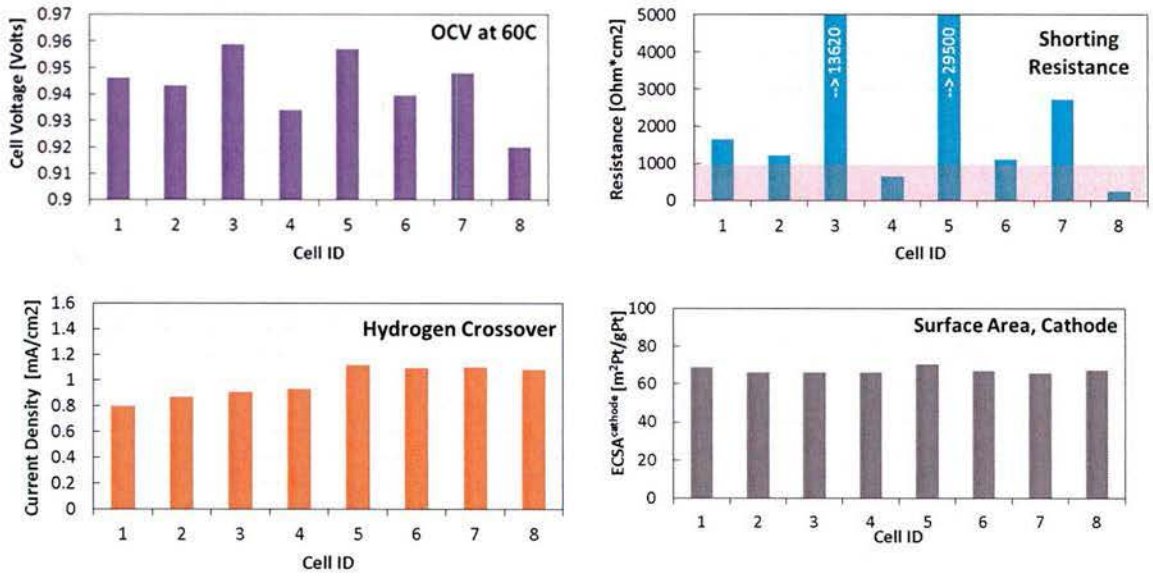

Figure 2.1.8. Membrane/electrode assembly diagnostic test results for the 8 cell stack.

NRL proceeded to identify a series of plates, using the evaluation data and lessons learned from the 10 cell and 8 cell stacks, with similar physical shape in an attempt to group cells into those that will align the best and not cause any significant shorting or contact resistance issues. From the selected plates, a 40 cell stack was built by NRL to complete a short 15 minutes test flight in the Ion Tiger NRL UAV.[8] A pre-test evaluation was not performed at HNEI due to project time restraints. After the flight, the 40 cell stack was sent to HNEI for evaluation. For this round of testing, the full suite of performance diagnostics from Table 2.1.1 was performed on the stack as well as MEA diagnostics on every cell. Figure 2.1.9 displays the results from polarization curves (only selected currents shown) along with HFR measurements to evaluate the contact resistance. Regions highlighted in blue represent the expected levels of cell voltage, ohmic-free cell voltage, and HFR magnitudes at 1 A cm^{-2}. There was still a significant number of cells with poor contact resistance as observed in the 10 and 8 cell stacks. The ohmic-free cell voltage data, after HFR correction, indicate as well that there were several poor performing cells where the performance loss could not solely be attributed to a poor contact resistance. As seen previously in the 8 cell stack test (Figure 2.1.7), these additional losses may be due to mass transport issues, possibly

from misaligned gaskets blocking flow fields, poorly compressed gas diffusion layers, or inadequate water clearing.

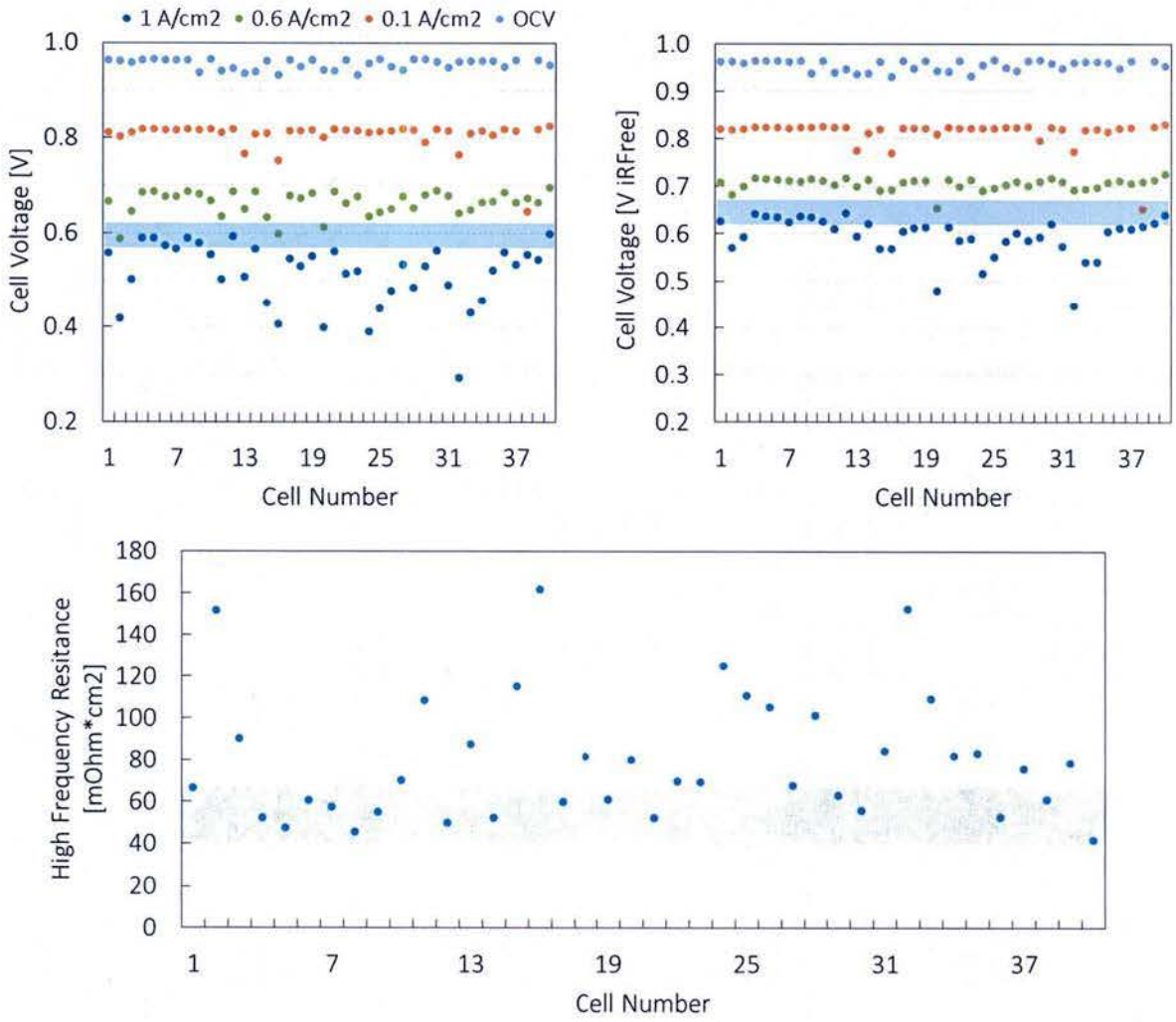

Figure 2.1.9. 40 cell stack post-flight evaluation polarization curve data. Average cell voltage vs. current density data (top, left). Ohmic-corrected average cell voltage vs. current density (top, right), and high frequency resistance vs. current density (bottom). The blue highlighted areas indicate expected range of values at 1 A cm^{-2}.

Mass transport losses were further examined in the cathode stoichiometry sweep, as shown in Figure 2.1.10. The power output of the stack, shown on the left, ranged from 385 W at the lowest flows tested (1.5 stoichiometry) to 415 W at the highest flows tested (3 stoichiometry). The right graph shows the difference in the cell voltages measured at 3 stoichiometry minus the cell voltages measured at all other stoichiometries. Linearly correlated cell voltages vs. cell number show a slight mal-distribution developing as the stoichiometry is decreased, where the cells near the positive end plate (higher cell numbers) are lower than the cells at the negative end plate, thus indicating increasing gas flow per cell with decreasing cell numbers. Overall, however, this maldistribution was not significant indicating the cell to cell flow distribution was not an issue with the 40 cell design.

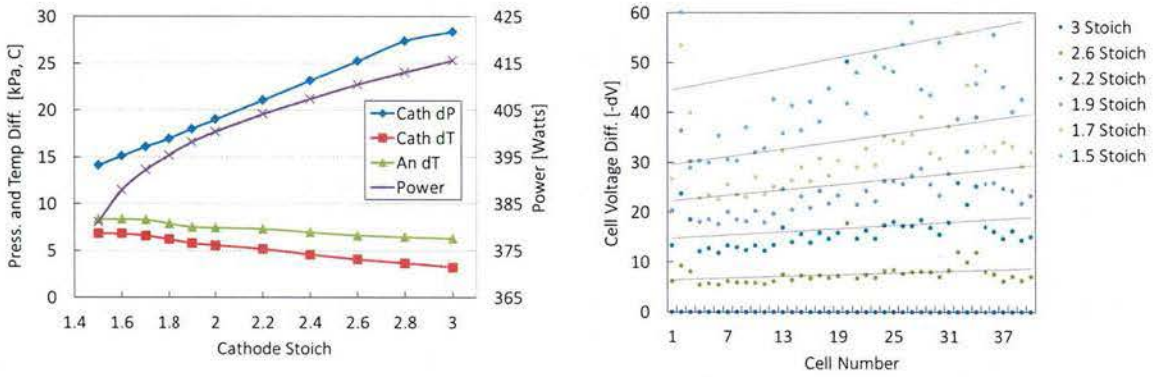

Figure 2.1.10. **C**athode stoichiometry sweep data for 40 cell design. Inlet to outlet cathode pressure and temperature differential, anode temperature differential and stack power vs. cathode stoichiometry (left). Cell voltage differential (difference vs. cell voltage at 3 stoichiometry) for each cell for selected cathode stoichiometries (right).

Figure 2.1.11 presents the results from the MEA diagnostics. In Figure 2.1.11, top the shorting resistance and hydrogen crossover are presented vs. cell number. As observed with the smaller stacks, several cells, i.e. 16 out of 40, showed low shorting resistance indicating an induced electrical short. However the equivalent hydrogen crossover current was within the expected range of approximately 1.0-1.2 mA cm^{-2} for all cells. Figure 2.1.11, bottom, right shows the strong correlation observed between the shorting resistance vs. open circuit voltage. Thus, for this particular stack build, the decrease in open circuit voltage could be used in future stack builds as a qualitative indicator of the presence of an electrical short, without having to perform any advanced diagnostics. Also of interest for this stack was the overall decrease of ~25 % for the cathode surface area measurements in comparison to the NRL pre-flight tests (Figure 2.1.11, bottom, left). This may have been due to airborne contaminants in the atmosphere during the outdoor flight test. The anode surface areas for all cells were within the expected range for new cells, even after the short flight test. Electrical shorting and poor contact resistance were the two major flaws found with the 40 cell 3D printed stack design as found with the small stacks. Four major groups of cells with these two flaws were identified, as shown in Figure 2.1.12. After the return of the stack to NRL, white light prolifometry was performed on 4 cells, one from each of the groups identified in Figure 2.1.12. NRL and HNEI were able to directly correlate the plate flatness and adjacent cell mismatch from line scan profiles of the plates with the diagnostics data. This work was documented in more detail in references [3,4]. After this study, NRL began pursuing stamped metal plate designs, as the 3D printed bipolar plate based stack still did not achieve the desired power to weight ratio for UAVs and manufacturing tolerances were not sufficient for stacks of more than 10 cells. In summary:

- HNEI completed an evaluation of a 40 cell NRL built 3-D printed stack following a successful flight in Ion Tiger UAV chassis.
- Similar issues with the 10 cell and 8 cell stacks were identified, i.e. inadequate plate flatness leading to electrical shorting and poor contact resistance as well as mass transport limitations.
- NRL and HNEI were able to correlate in situ diagnostic measurements with surface height profiles of the plates resulting in 2 publications discussing the limitations of 3D printing using direct metal laser sintering for the production of fuel cell bipolar plates.
- Following the 40 cell post-flight evaluation, HNEI intended to use the 3D printed stack parts and plates to serve as a 'research' stack with replaceable MEAs and a modifiable

design to expand fundamental studies at HNEI. However, the inadequate plate flatness halted this effort and other stack designs were explored.

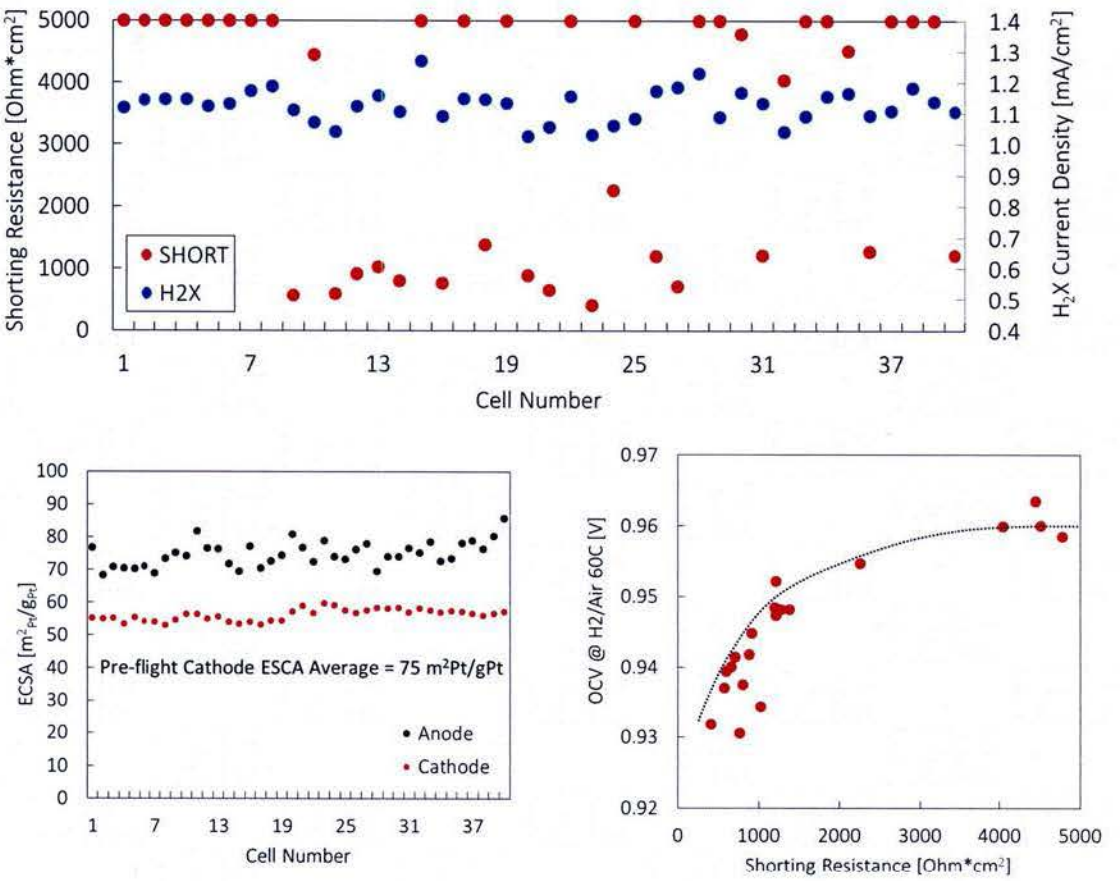

Figure 2.1.11. MEA diagnostic results for 40 cell post flight evaluation. H2X and SHORT results vs. cell number (top), anode and cathode ECSA vs. cell number (bottom, left), and open circuit voltage vs. SHORT results (bottom, right).

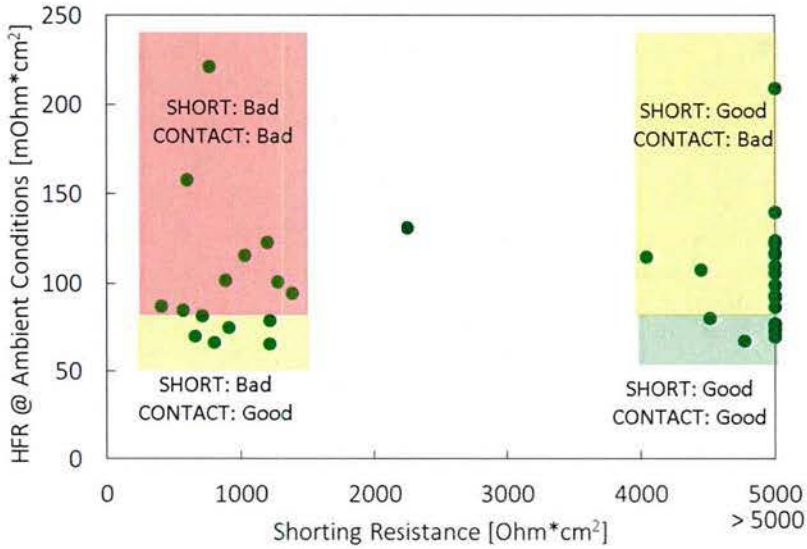

Figure 2.1.12. High frequency resistance vs. shorting resistance for all 40 cells with overlays indicating four major groups of cells identified having none, both, or one of the two major faults (electrical shorting and poor contact resistance).

As the 3D printed bipolar plate design did not meet the weight requirements for lightweight UAVs, NRL continued to explore methods to reduce the weight of the fuel cell stack. These efforts led NRL to look into the use of compression bands as opposed to the classic approach of heavy end plates with Belleville washer/bolt compression. The use of compression bands is not new. Ballard Power Systems, for example, has been using compression bands in combination with spring plates for many years with several pre-2000 patents issued, such as reference [9]. NRL reduced their novel designs to a titanium strap that encompasses the entire fuel cell stack width, with the exception of the end ports, as shown in Figure 2.1.13. This allowed NRL to use a much thinner end plates as well as replacing the metal end plates with plastic. In this case, Ultem plastic was used with the reactant ports machined directly into the end plate. The stack and strap system are compressed in a press, and then the upper and lower strap are spot welded in place, relying on the elasticity of the stack seals to maintain the desired total force and keep all surfaces sealed and leak free. For the initial build test at NRL, this resulted in a reduction of ~300 g, with the new titanium strap band stack mass without coolant of 193 g vs. the equivalent bolted stack weighing 509 g.

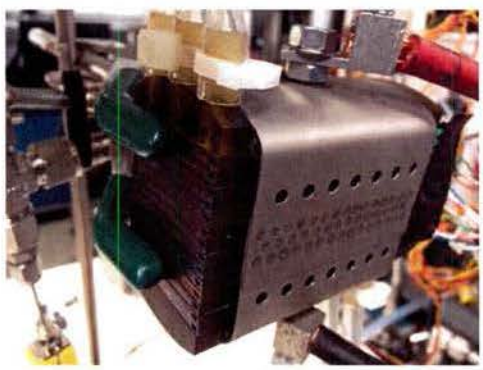

Figure 2.1.13. Test configuration of 13 cell 3D printed bipolar plates (BPP) stack with titanium strap compression system under test at HNEI

A 13 cell stack made with the titanium strap compression system and the 3D printed bi-polar plates was sent to HNEI for a short evaluation to determine whether or not the stack provided similar results to the bolt compression system. Figures 2.1.14 and 2.1.15 provide results from the initial polarization curve performed and the analysis of the cell to cell electrical shorting and contact resistance. Overall, the stack produced a similar power output and exhibited the same issues as the previous builds. The use of the titanium strap compression system was deemed a success even with these issues. The strap approach could be used to replace the heavier metal end-plate and bolt compression system for future stacks under development at NRL, such as the recently initiated stamped metallic bipolar plate 3 kW stack project.

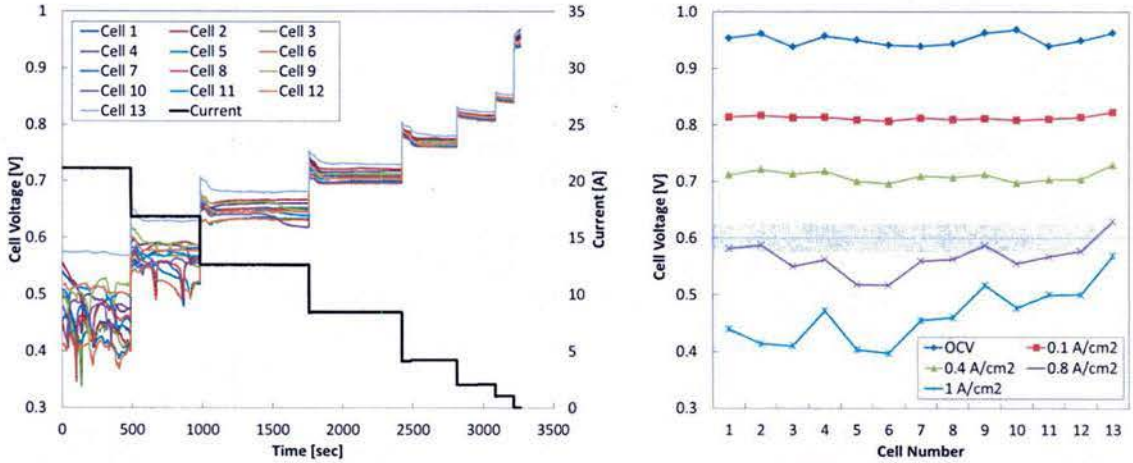

Figure 2.1.14. Polarization curve test results for 13 cell 3D printed BPP stack with titanium strap compression system. Time series data of cell voltage and current vs. time using descending current steps (left). Cell voltage vs. cell number for selected current densities with expected range of cell voltages at 1 A cm^{-2} highlighted in blue (right).

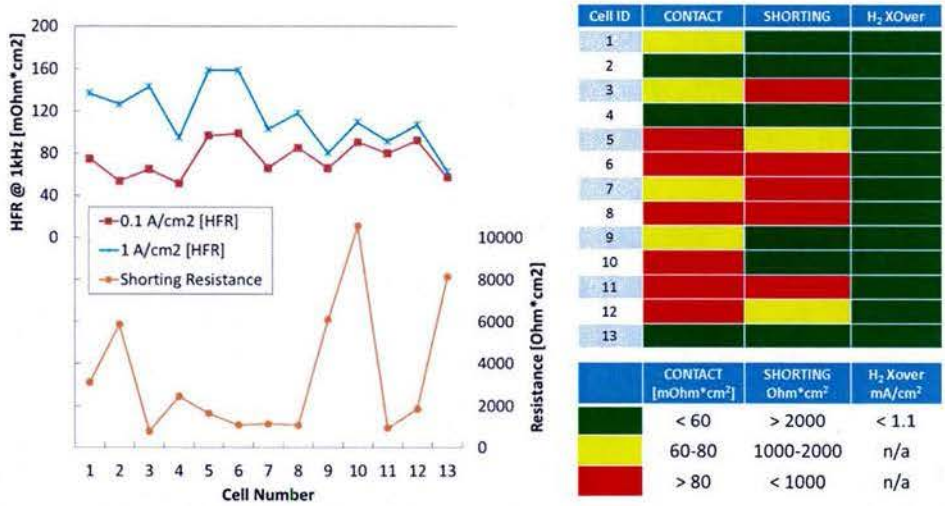

Figure 2.1.15. High frequency resistance, shorting resistance, and hydrogen crossover test results for 13 cell 3D printed BPP stack with titanium strap compression system. Values vs. cell number (left). Results separation into good (green), acceptable (yellow), and unacceptable (red) ranges (right).

HNEI also assisted NRL with several smaller test programs for fuel cell system development. During their brassboard fuel cell system layout activities, NRL was using an older Protonex 60 cell stack as a test article to develop the control system software. NRL was unable to achieve the rated capacity, i.e. 1.5 kW using their brassboard system and requested HNEI for an evaluation of the stack, to validate if it was possible to achieve the rated power and, if applicable, identify corresponding operating conditions. NRL was only able to achieve approximately 1.3 kW. Figure 2.1.16 shows the Protonex 60 cell stack, which has a built in Nafion membrane humidifier from Perma-Pure LLC[10] and custom lightweight manifolds. Two peak power experiments were performed at HNEI, essentially ramping up to 49.6 A or 1.6 A cm^{-2} (31 cm^2 active area for each cell) and varying the air flow to evaluate the effect on peak power. These runs are displayed in Figure 2.1.17. The reactants were connected in co-flow with the coolant and the inlet temperature was set at 50 °C. The anode stream humidification was supplied by the test station at 50 °C (saturated conditions) and the cathode humidification was provided by the integral Nafion humidifier. During the second day of testing, HNEI was able to demonstrate the stack could produce the rated power with a 150 SLPM air flow. The stack was returned to NRL and their compressor controller was adjusted to allow for higher air flows. NRL was subsequently able to achieve peak power on their brassboard.

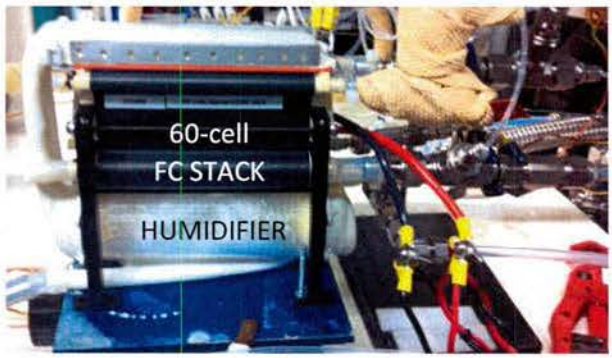

Figure 2.1.16. Protonex 1.5 kW fuel cell stack/humidifier system under test at HNEI.

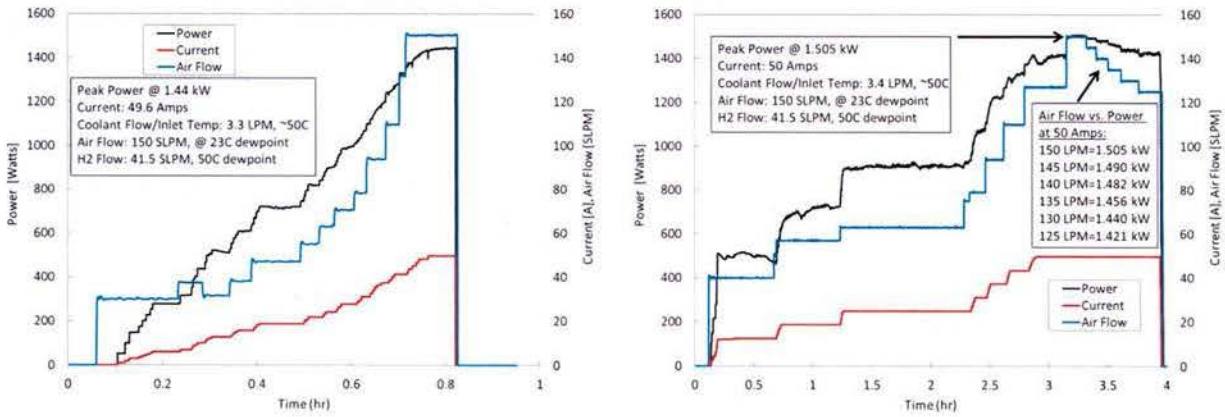

Figure 2.1.117. Protonex peak power assessment: output power, current, and air flow vs. time. Day 1 testing results with 1.44 kW achieved (left). Day 2 testing results with 1.505 kW achieved.

Fuel cell inlet oxidant and hydrogen fuel reactant streams typically require added heat and humidity which are critical to the overall system performance and reliability. For ultra-

lightweight fuel cells for UAVs, the hydrogen gas stream is typically not humidified. However, the oxidant stream is heated and humidified. Very few companies actually manufacture commercially available products. The two most frequently selected are Perma Pure LLC,[10] which produces tubular Nafion humidifiers such as the unit integrated with the Protonex 60 cell stack discussed earlier (Figure 2.1.16), and dPoint Technologies,[11] which produces planar type membrane humidifiers. dPoint Technologies originally licensed Ballard Power Systems' humidifier design back in 2006. NRL requested a basic evaluation of dPoint's Px1-32 (250 W) humidifier, shown in Figure 2.1.18 with the sensor layout and port assignments, to determine its applicability in their fuel cell system balance of plant. The original request from NRL focused on testing the humidifier beyond the manufacturer specified flow rates, temperatures, and pressures. Examples of the data produced and delivered to NRL are shown in Figure 2.1.19. On the left side is the dew-point difference between the supplied wet stream inlet and the humidified dry stream outlet for various temperatures and flow rates. Additional evaluations, such as the influence of CO_2 in the gas stream, as shown on the right, were also performed.

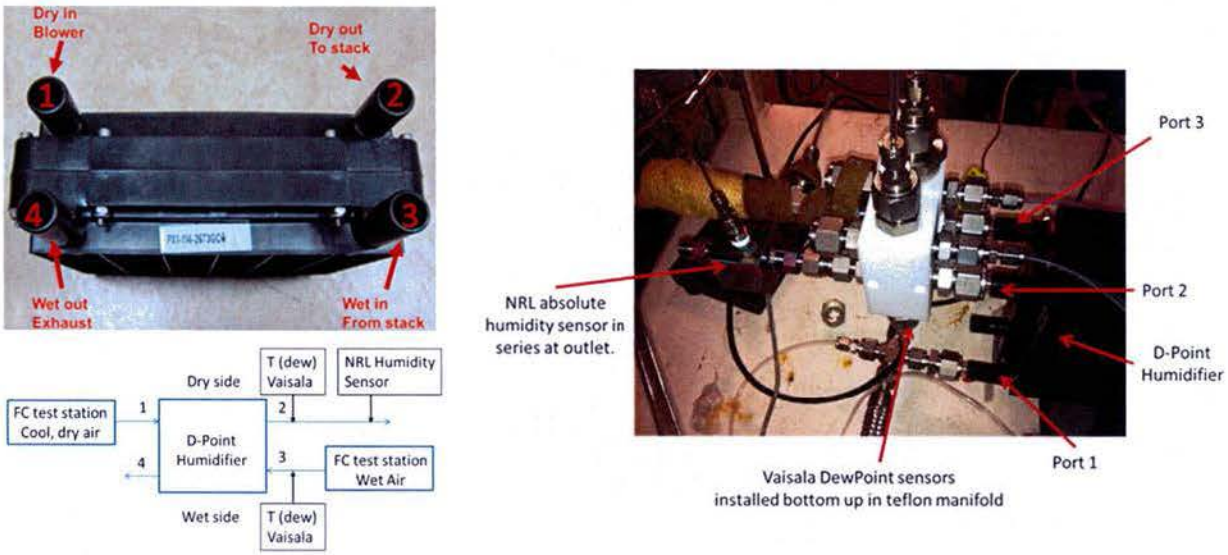

Figure 2.1.18. dPoint humidifier port assignment (top, left), sensor layout (bottom, left), and sensor installation (right).

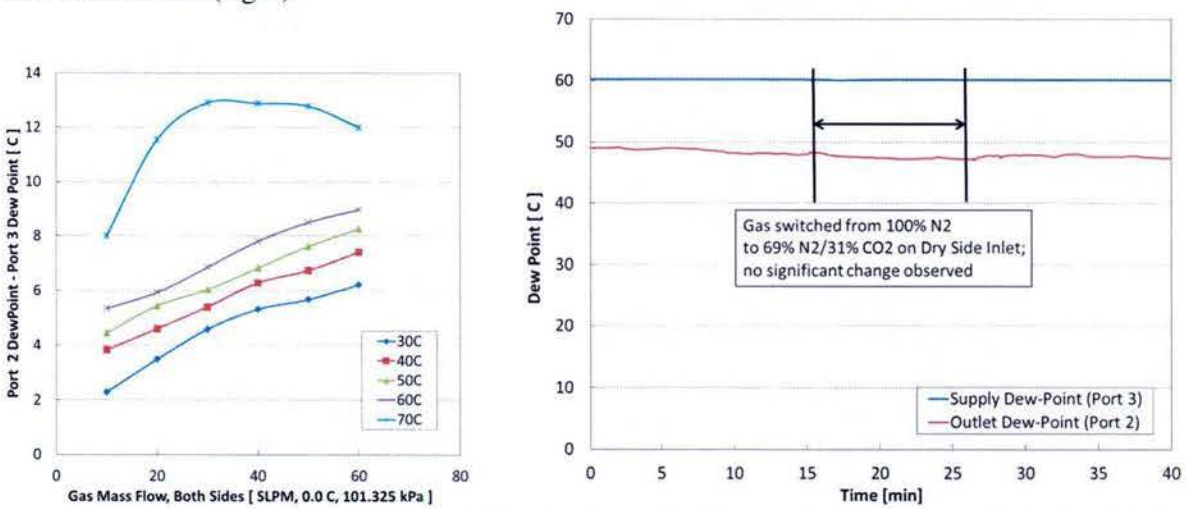

Figure 2.1.19. Example of dPoint humidifier test results. Dew-point difference (wet side inlet – dry side outlet) vs. flow rate (left). Influence of CO_2 on the performance of the humidifier (right).

Data was disseminated to NRL through monthly reports, update meeting presentations, and compressed data files. For more information and specific details of the projects, contact Karen Swider-Lyons (karen.lyons@nrl.navy.mil). More details are also provided in the Publications and Presentations Resulting from these Efforts, (items 8 and 11) listed at the end of this subtask.

Effect of contamination on a PEMFC stack

Interpretation of fuel cell field data that will be obtained from the Hawaii Volcanoes National Park demonstration buses, which will be subjected to elevated concentrations of sulfur dioxide and other volcanic contaminants (section 2.2), implies a good understanding of stack behavior. Few reports detail the effects of contaminants on operating fuel cell stacks.[12,13] However, contaminants that were used are not relevant to an atmosphere with high levels of sulfur dioxide such as a volcanic environment, and observed trends were left unexplained and without an explanatory contamination mechanism.

Laboratory tests were conceived to gain a better understanding of stack contamination. A sub-scale Protonex 36 cell stack (500 W) was chosen as a surrogate because bus stacks (33 kW) exceeded test station limitations (5 kW). Also, propene, which was previously down selected from a list of approximately 200 airborne contaminants,[14] rather than sulfur dioxide was chosen because the performance loss due to propene is in contrast to sulfur dioxide readily recoverable simplifying test procedures. Although a single cell performance is recoverable in a laboratory environment by applying a voltage that exceeds the open circuit potential of ~1 V, such a procedure is not currently applicable to a stack, as each cell potential needs to be independently controlled and electrical connections to each cell are necessary.

Figure 2.1.20 a illustrates the average cell voltage evolution during a test. During the first phase, the stack has a steady state output V_b. In the subsequent phase, the propene is injected and the average cell performance immediately decreases. The average cell performance loss rate decreases until a steady state V_c is reached. In the last phase, only air circulates and the average cell performance recovers at a rate which is greater than the decay rate observed during the second phase. The average cell performance recovery rate also decreases until a steady state V_r is reached. The average cell performance after recovery is larger than the initial value by approximately 6 mV. This transient behavior and larger average cell performance after recovery are consistent with prior single cell experiments.[14]

Figure 2.1.20 b depicts the cell voltage V_b distribution during the first phase (baseline) at 2 h (specific times are indicated in Figure 20 a by red dashed lines). The cell voltage distribution is relatively uniform with a linear regression indicating a 10.4 mV change between cells 1 and 36. The cell voltage V_c distribution (contamination) shows that propene contamination steepens and renders the distribution less uniform at the end cells, whereas the cell voltage V_r distribution (recovery) indicates that propene contamination has a positive effect and uniformly increases cell performance. These trends are better emphasized by displaying cell voltage differences $V_b - V_c$ and $V_r - V_b$ to isolate these contaminant effects and remove other causes of cell variability (Figure 20 c). Figure 20 c shows these steady-state cell voltage change distributions obtained, respectively, at 3 h and 20 min and 7 h and 30 min by subtracting first phase data at 2 h. The cell voltage change $V_b - V_c$ distribution during contamination is characterized by two main features. End cells have lower performance than their contiguous cells. The cell performance change for the other cells depicts an increasing value from cell 2 to cell 35 (0.57 mV cell^{-1}). The cell

voltage change $V_r - V_b$ distribution during recovery is almost uniform and identical to the distribution observed before the contamination phase with the exception that cell voltages are higher by ~6 mV on average. It is remarkable that such a small stack (easier to control operating conditions in a small volume) reveals clear effects during contamination (24 and 15 mV for respectively end cells 36 and 1, 19 mV along the stack core from cells 2 to 35). Contamination effects are expected to be even more significant in larger automotive or stationary stacks because it is relatively more difficult to control operating conditions over much larger volumes. Two parameters derived from Figure 2.1.20 c data are used to discuss the effect of propene on stack performance. As end cells do not behave as inner cells, they are not taken into account to linearly correlate $V_b - V_c$ data. The resulting slope $-b$ is used as an indicator of the cell voltage distribution unevenness. The inner cells linear correlation is also used to calculate hypothetical voltage values for end cells 1 and 36 which are subsequently subtracted from corresponding measured values to define the voltage difference between end cells and inner cells ΔV_{end}.

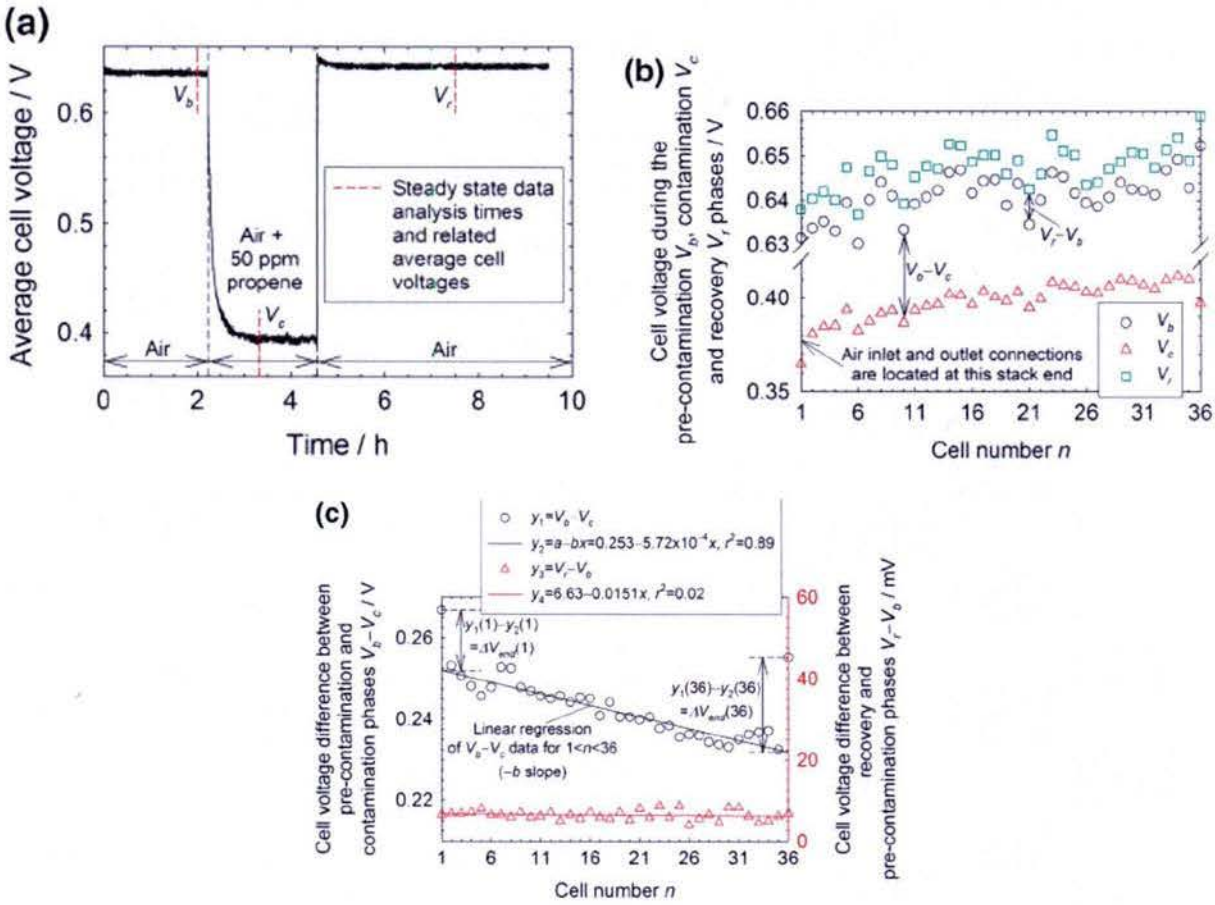

Figure 2.1.20. PEMFC stack average cell voltage before, during, and after a 50 ppm propene in air exposure (a). Individual cell voltages during the pre-contamination V_b, contamination V_c, and recovery phases V_r (b). Cell voltage differences between pre-contamination and contamination phases $V_b - V_c$, and recovery and pre-contamination phases $V_r - V_b$ (c). Baseline operating conditions: air/H_2, 2.5 stoichiometry/dead end with intermittent purges, 75/0 % relative humidity, and ambient/ambient pressure outlets, 55 °C, 1 A cm^{-2}.

Figure 2.1.21 a schematically shows natural convection heat losses. For inner stack cells 2 to n-1, the steady-state heat balance includes forced convection (all cells are equal and bounded by coolant flow fields on either side) and natural convection terms. The natural convection term

Q_{sides} corresponds to the heat loss from the cell sides. For end cells 1 and n, the steady-state heat balance includes an additional term Q_{end} for the natural convection heat loss from the end plate adjacent to the end cell. Therefore, end cells are cooler than inner cells because end cells have a greater heat loss (Figure 2.1.20 b). The anomalous end cell behavior is consistent with a mathematical model that showed that a local heat anomaly such as an end cell only affects approximately 2 adjacent cells with an impact progressively lessened with the distance from the anomaly.[15]

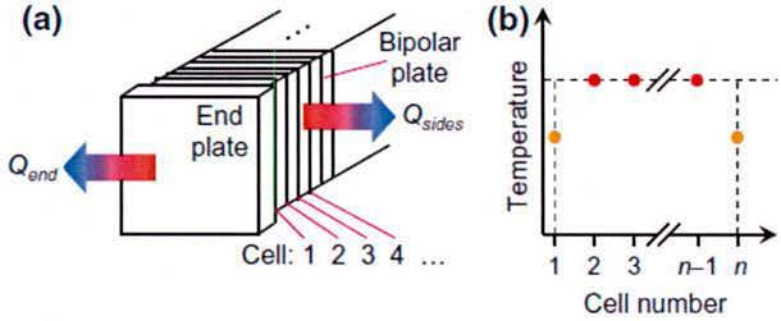

Figure 2.1.21. PEMFC stack heat losses (a) and schematic temperature distribution (b).

In the presence of propene contamination, the end cell effect is exacerbated as shown in Figure 20 c with the cell voltage difference between the pre-contamination and contamination phases ΔV_{end}. After the contamination phase, the exacerbated end cell effect disappears as the cell voltage difference between pre-contamination and recovery phases is approximately constant for all cells (Figure 2.1.20 c). The exacerbated effect is ascribed to the lower local temperature and its significant effect on propene contamination.[16] The loss in cell performance for propene is approximately 0.0086 % $°C^{-1}$ ppm^{-1}.[16] Therefore, the decrease in temperature is equal to 8.7 and 5.4 °C for an initial performance of 0.641 V (Figure 20 a), end cell losses of, respectively, 24 and 15 mV (Figure 2.1.20 c), and a 50 ppm concentration (0.024 or 0.015 V x 100/(0.641 V x 50 ppm x 0.0086 % $°C^{-1}$ ppm^{-1})). The larger loss in cell performance at a lower temperature is mostly related to kinetic effects. Kinetic effects are represented by the oxygen reduction reaction[17,18] and the contaminant oxidation reaction, which are both hampered by lower temperatures. Additionally, contaminant adsorption on the catalyst surface is favored at lower temperatures. Therefore, the oxygen reduction reaction proceeds more slowly at low temperature and is more impacted by the presence of the contaminant which is strongly adsorbed and is less easily removed by oxidation. Mass transfer effects are not expected to play a significant role because propene is diluted at a 50 ppm concentration.

The end cell temperature can be changed by either varying the coolant flow rate (forced convection) or the ambient atmosphere air flow (natural convection). The heat transfer surfaces as well as the heat transfer coefficient within the stack itself (conduction) are assumed to be constant because all experiments were carried out with the same stack. As a result, the natural convection heat loss is directly proportional to the temperature gradient $T_{cell} - T_{ambient}$. However, the individual cell temperatures are not accessible without stack design modifications. As a substitute, an approximate and more convenient temperature gradient is used and is formed by the difference between the average coolant temperature and the end plate surface temperature $[(T_{c,in} + T_{c,out})/2] - T_s$.

Figure 2.1.22 a depicts the transient cell voltages for the last 3 cells of the stack (cells 34, 35 and 36). These cell voltage time series share the same features with the one illustrated in Figure 2.1.20 a. In addition, the calculated cell 36 approximate temperature gradient perpendicular to the cell plane is also included in Figure 2.1.22 a. The temperature gradient is intentionally modified by intermittently turning on and off a fan blowing air on the end plate adjacent to cell 36. The fan induces changes in the temperature gradient of approximately 7 °C. The first change in temperature gradient takes place before the cell is contaminated by propene (period t2). This change negligibly affects all 3 cell voltages. By contrast, two additional temperature gradient changes during the contamination period (t5 and t7 periods) significantly affect end cell 36. The impact on cell 35 is relatively smaller, whereas cell 34 is hardly affected. Figure 2.1.22 a data reveal that a link exists between the end cell performance during a contamination event and the end cell temperature.

The differences between end and inner cells ΔV_{end} are plotted in Figure 2.1.22 c against the temperature gradient. Other test data obtained under different coolant flow rates are also added to Figure 2.1.22 c, which show a strong correlation between end and inner cells voltage differences ΔV_{end} and the temperature gradient confirming the hypothesis that the end cell performance is tied to its temperature during a contamination event. Data obtained by varying the air relative humidity, the coolant flow rate and the cathode potential on the stack inner cells voltage loss distribution slope $-b$ (not shown) indicate that the reactant flow distribution is also linked to the presence of propene.

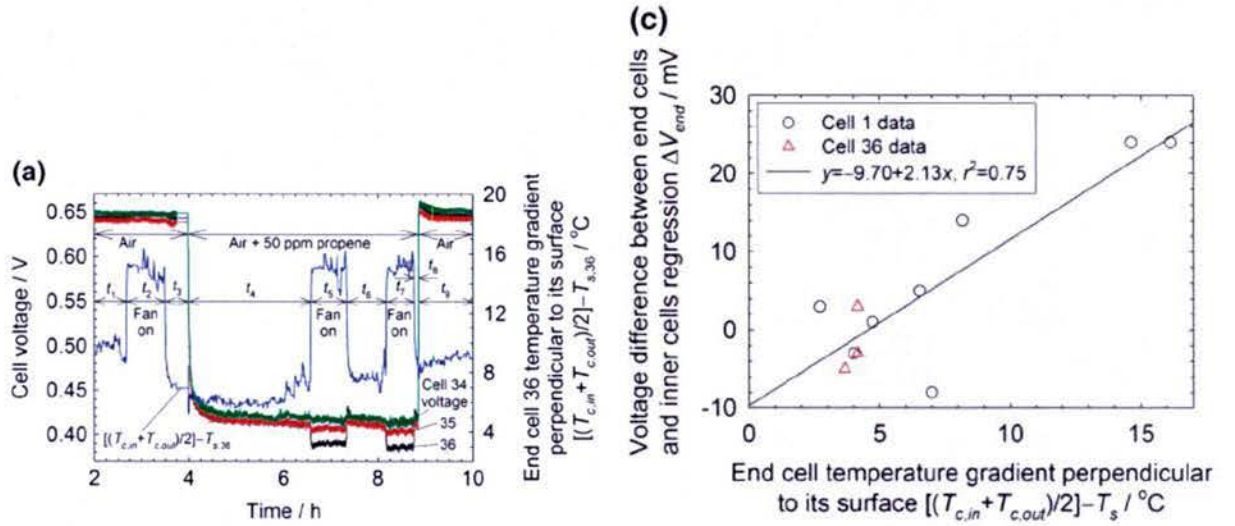

Figure 2.1.22. PEMFC stack cells 34 to 36 voltage and end cell temperature gradient $[(T_{c,in} + T_{c,out})/2] - T_s$ transients (a). Voltage difference between end cells and inner cells regression ΔV_{end} as a function of the end cell temperature gradient $[(T_{c,in} + T_{c,out})/2] - T_s$ during contamination (c). Intermittent operation of a fan directed toward cell 36. Otherwise baseline operating conditions for figure a: air/H_2, 2.5 stoichiometry/dead end with intermittent purges, 75/0 % relative humidity, and ambient/ambient pressure outlets, 55 °C, 1 A cm^{-2}.

Single cells that are subjected to different operating conditions will not age at the same rate. This statement means that the stack cell voltage distribution will become more uneven over time and will more easily trigger a fuel cell system shutdown. Such a conclusion is supported, for example, by long duration fuel cell experiments with different reactant humidification levels that led to dissimilar times to failure by membrane gas crossover.[19] Therefore, efforts should be

devoted to the development of early detection and preventive measures to reduce contamination risks in a stack.

The stack contamination mechanisms developed for propene are readily applicable to other organic and more prevalent inorganic contaminants. From that standpoint, the selection of propene was, in retrospect, not critical and other contaminants could have equally been chosen to complete the present study. A larger contaminant effect on stack end cells is possible considering that for naphthalene, the loss in cell performance is 0.51 % $°C^{-1}$ ppm^{-1},[16] which is much larger than for propene (0.0086 % $°C^{-1}$ ppm^{-1}). The end cell effect is expected to be small for sulfur dioxide because temperature has a small impact on cell performance loss between 45 and 80 °C.[20] For sub-saturated reactant streams, a more moderate contaminant effect on stack inner cells is anticipated for species that do not involve water in oxidation or reduction reactions. Similar to propene, SO_2, NO_2, and CO oxidation reactions include a water molecule,[21-23] and therefore, a more uneven contaminant effect on stack inner cells is expected for a sub-saturated reactant stream. However, this statement is based on overall reactions. For instance, the elementary rate determining step for CO oxidation involves an adsorbed hydroxyl species,[24] and therefore, the inner cells voltage distribution may not be impacted. A larger contaminant effect is also expected for electrode potentials located in a region where only species adsorption takes place due to the absence of active mechanisms cleansing the catalyst surface. This is the case for both SO_2 and NO_2 which lead to adsorbates on the Pt surface in the PEMFC operating range of 0.6–1 V vs. the standard hydrogen electrode.[22,25] More details are provided in the Publications and Presentations Resulting from these Efforts section (items 5 and 12).

Future tests are planned to confirm the link between the stack inner cell voltage loss distribution slope *-b* and the presence of a contaminant. Operating conditions more directly impacting reactant flow distribution will be used for these tests (change in O_2 diluent from N_2 to He and C_3F_8, U and Z type manifold configurations).

Non-precious metal catalyst tolerance to airborne contaminants

The viability of proton exchange membrane fuel cells still requires substantial decreases in cost. Pre-commercial membrane/electrode assemblies utilize platinum or platinum group metal catalysts on the anode and cathode. The high price of platinum group metals currently accounts for 50 % of the total stack cost (cost analysis for a volume of 500,000 units/year).[26] The substitution of platinum by inexpensive catalysts has been explored since the mid-1960s. Significant progress has only occurred within the last few years with the development of active Fe/N/C catalysts.[27,28] Substitute catalysts are subject to the same requirements including activity and durability. For simplicity, fuel cells utilize ambient air as an oxidant. Therefore, the operation of fuel cells is dependent on air quality. Thus, substitute catalysts should be tolerant to prevalent airborne contaminants, especially those emitted by internal combustion engine cars (CO, NO_x) and coal fed power plants (SO_2). However, few reports discuss the behavior of substitute iron based catalysts exposed to air contaminants.

Fe/N/C catalysts were obtained from the University of New Mexico and integrated into membrane/electrode assemblies by air brushing a catalyst ink onto gas diffusion layers (2.0 to 3.9 mg cm^{-2}) followed by an ionomer coating and heat pressing to a membrane and a commercial gas diffusion electrode for the anode. Membrane/electrode assemblies were exposed to SO_2 (10 ppm), NO_2 (2 and 10 ppm) and CO (5 and 20 ppm) in a segmented cell at a low current density of 0.2 A cm^{-2} because their performance was substantially lower than for Pt

based membrane/electrode assemblies (hence the much higher loading). Under these conditions, the average cell voltage was approximately 0.43 to 0.52 V (~0.75 V for Pt at a 0.1 mg cm^{-2} loading) and limited by high kinetic overpotentials for oxygen reduction, ohmic overpotentials and mass transfer overpotentials (much thicker electrode than for Pt). Several diagnostics were used to clarify observations including polarization curves, impedance spectroscopy, x-ray photoelectron spectroscopy and ab initio density functional theory calculations.

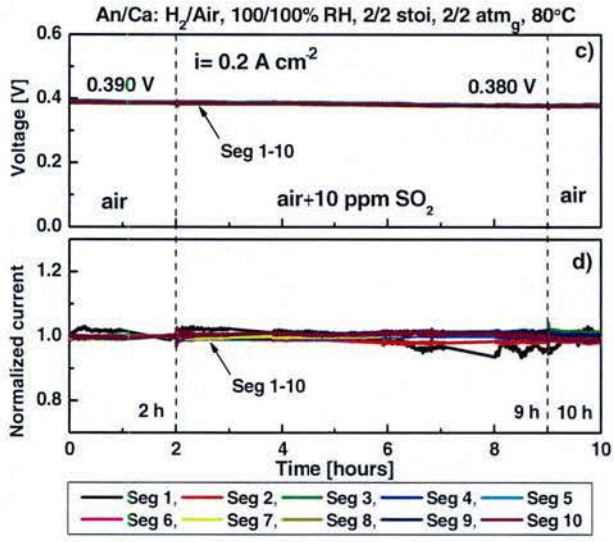

Figure 2.1.23. Voltage and normalized current densities for individual cell segments versus time for a Fe/N/C cathode catalyst based membrane/electrode assembly exposed to SO_2.

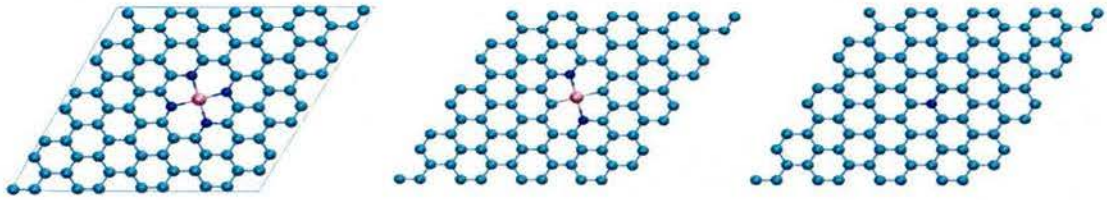

Figure 2.1.24. Density functional theory optimized Fe/N/C catalyst site structures. Fe (dark blue), N (yellow), C (light blue).

Table 2. Adsorption energies for O_2, NO, NO_2 and SO_2 on Fe-N_4, Fe-N_2C_2 and N-doped graphene sites as calculated by density functional theory.

	Adsorption energy [eV]		
Adsorbate	Fe-N_4	Fe-N_2C_2	N-doped graphene
O_2	-1.01	-2.34	-0.15
SO_2	-0.81	-1.63	-0.17
NO	-1.97	-3.37	-0.09
NO_2	-1.45	-2.63	-0.43
CO	-1.61	-2.09	-0.01

The cell voltage and current distribution for the Fe/N/C catalyst was not affected by the presence of SO_2 in air even for a high concentration of 10 ppm SO_2 (Figure 2.1.23). The observed Fe/N/C tolerance to SO_2 is explained by the absence of SO_2 adsorbates on Fe-N_2C_2 and Fe-N_4 sites that

are more stable than O_2 adsorbates (Figure 2.1.24), as confirmed by density functional theory calculations (Table 2.1.2). In comparison, the exposure of Pt catalysts to SO_2 results in a significant decrease in performance (hundreds of mV at ppm levels) which is only partially recoverable after exposure unless the cathode potential is above 1 V vs. a hydrogen electrode.[29]

Exposure of the Fe/N/C cathode to 2 and 10 ppm NO_2 resulted in a performance loss of 30 and 70-75 mV, respectively (Figure 2.1.25). In comparison, a Pt cathode loses 50-100 mV when exposed to 2 ppm NO_2,[30] which indicates that the non-precious catalyst was more tolerant to NO_2 poisoning. The impact of NO_2 on the Fe/N/C electrocatalyst is attributed to NO_2 adsorption and subsequent decomposition into NO and O species.[31] Table 2.1.2 shows that NO_2 and NO molecules are more strongly bound to Fe-N_2C_2 and Fe-N_4 sites than O_2, which block the surface and prevent the occurrence of O_2 reduction. The NO species has an affinity for Fe^{n+} centers (Fe^{2+} and Fe^{3+})[32] and slowly desorb from F-N_x into the gas phase or is released as HNO_3.[33] This information supports the observation of a recovery after NO_2 exposure (Figure 2.1.25).

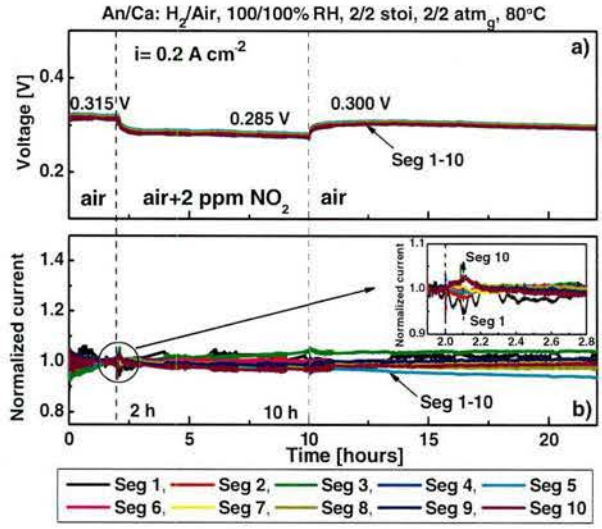

Figure 2.1.25. Voltage and normalized current densities for individual cell segments versus time for a Fe/N/C cathode catalyst based membrane/electrode assembly exposed to NO_2.

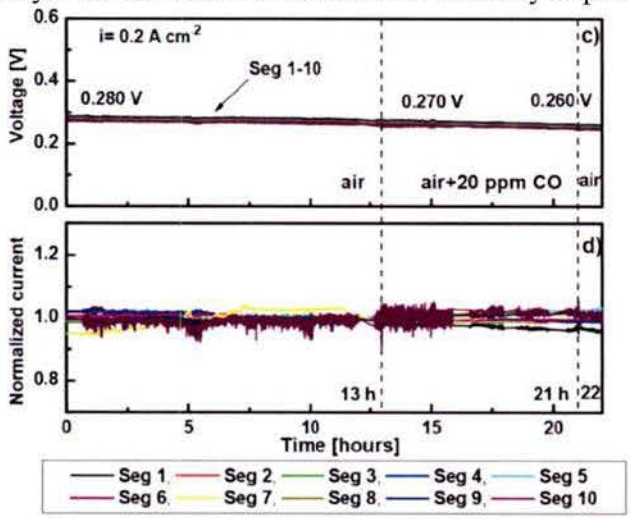

Figure 2.1.26. Voltage and normalized current densities for individual cell segments versus time for a Fe/N/C cathode catalyst based membrane/electrode assembly exposed to CO.

The introduction of 5 or 20 ppm of CO into the air stream did not affect Fe/N/C performance (Figure 2.1.26). This observation is consistent with smaller adsorption energy for CO on Fe-N_2C_2 and N-doped graphene than for O_2 (Table 2.1.2). However, CO adsorbs more strongly than O_2 on Fe-N_4 sites (Table 2.1.2). Therefore, on that basis, CO is expected to have an effect on cell performance. The apparent discrepancy between adsorption energies and cell performance during CO exposure is tentatively explained by factors such as a relatively low CO concentration (the tolerance limit has not been reached) and the relatively smaller number of Fe-N_4 sites.

More details are provided in the Publications and Presentations Resulting from these Efforts section (item 6). For instance, membrane/electrode assembly degradation was accelerated with exposure to contaminants. X-ray photoelectron spectroscopy results highlighted increased ionomer oxidation, which is partly ascribed to the generally enhanced peroxide formation in the presence of contaminants.[34]

Platinum metal catalyst contamination by carbon monoxide in hydrogen

The use of H_2 as a fuel for proton exchange membrane fuel cells is facing several hurdles. For instance, current H_2 production methods include the incumbent natural gas stream reforming technology and water electrolysis. Carbon monoxide is a by-product of the reforming process. Recent standards specify the hydrogen gas purity for fuel cell applications, which include a maximum CO concentration of 0.2 ppm to alleviate contamination issues (ISO 14687-2, SAE J2719). A predictive, one-dimensional along the channel length mathematical model describing the temporal performance evolution of a cell exposed to CO was adapted and extended from prior studies. In contrast with prior studies that reported CO concentrations greater than approximately 50 ppm, segmented cell data obtained with a 2 ppm CO concentration, a value closer to the standards' specification of 0.2 ppm, were used for model validation.

Transient and steady state data before, during and after CO exposure were obtained in different modes corresponding to varied oxygen concentrations at the cathode from 0 to pure oxygen and including air. This was necessary to better evaluate the role of crossover oxygen on CO oxidation. Several diagnostic techniques were used including impedance spectroscopy. Steady state impedance data were fitted to adapted equivalent circuit models.

The mathematical model was centered on a mechanism that accounts for the following elementary electrochemical (Equations 2, 4 and 5) and chemical (equations 1, 3, 6 and 7) reactions:[35-37]

$$H_2 + 2[\,] \leftrightarrow 2[H] \text{ (Equation 1)}$$
$$[H] \leftrightarrow [\,] + H^+ + e^- \text{ (Equation 2)}$$
$$CO + [\,] \leftrightarrow [CO] \text{ (Equation 3)}$$
$$H_2O + [\,] \leftrightarrow [OH] + H^+ + e^- \text{ (Equation 4)}$$
$$[OH] + [CO] \rightarrow 2[\,] + CO_2 + H^+ + e^- \text{ (Equation 5)}$$
$$O_2 + [\,] \leftrightarrow 2[O] \text{ (Equation 6)}$$
$$[O] + [CO] \rightarrow 2[\,] + CO_2 \text{ (Equation 7)}$$

Essentially, CO adsorbs on the Pt catalyst surface and blocks free sites (denoted [ ] in equations 1-7). In addition, the presence of CO on the surface affects the hydrogen oxidation kinetics. CO is also actively removed by electrochemical and chemical oxidation (respectively equation 5 and 7). The anode channel was also modeled as a series of well mixed volumes to account for the

progressive decrease in CO concentration due to adsorption and reaction. Only the H_2+CO/O_2 case was modeled to reduce model complexity, which primarily focuses on anode poisoning processes. Therefore, diffusion and flooding in the cathode were not implemented, and current densities for all segments are equal in the pre-poisoning and recovery stages.

Figure 2.1.27 a and b present transients of segment voltages and current densities normalized to initial values. After the injection of 2 ppm CO into the hydrogen stream, a fast decrease of the segments' voltages occurred and a current density redistribution was observed. The transition period to reach steady state lasted approximately 10 hours. At steady state, the segments' voltages settled at 0.586 V, which yielded a performance loss of 0.089 V. Under CO exposure, the inlet segments 1-4 exhibited the lowest current density (60 % loss), whereas outlet segments 8-10 showed an increase in current density (total current is controlled). After switching back the fuel to H_2, the cell and segments recovered with a performance that is very close to the initial voltage value of 0.662 V within 1 h.

Figure 2.1.27, top, right shows current density simulation results that are in good agreement with experimental data at the beginning of CO injection including the appearance of an undershoot feature. However, the main difference was noted during the recovery stage. Experiments showed a first order decay whereas simulations revealed the appearance of overshoots attributed to higher order dynamics. The time required to reach a steady state during the recovery stage is of the same order (~4 h) as the experimental value. The simulated local CO concentration distribution at steady state (Figure 2.1.27, bottom) is consistent with adsorption and reaction processes and the current distribution. Simulated and experimental results reveal that the proposed model represents reasonably well the behavior of a fuel cell exposed to CO.

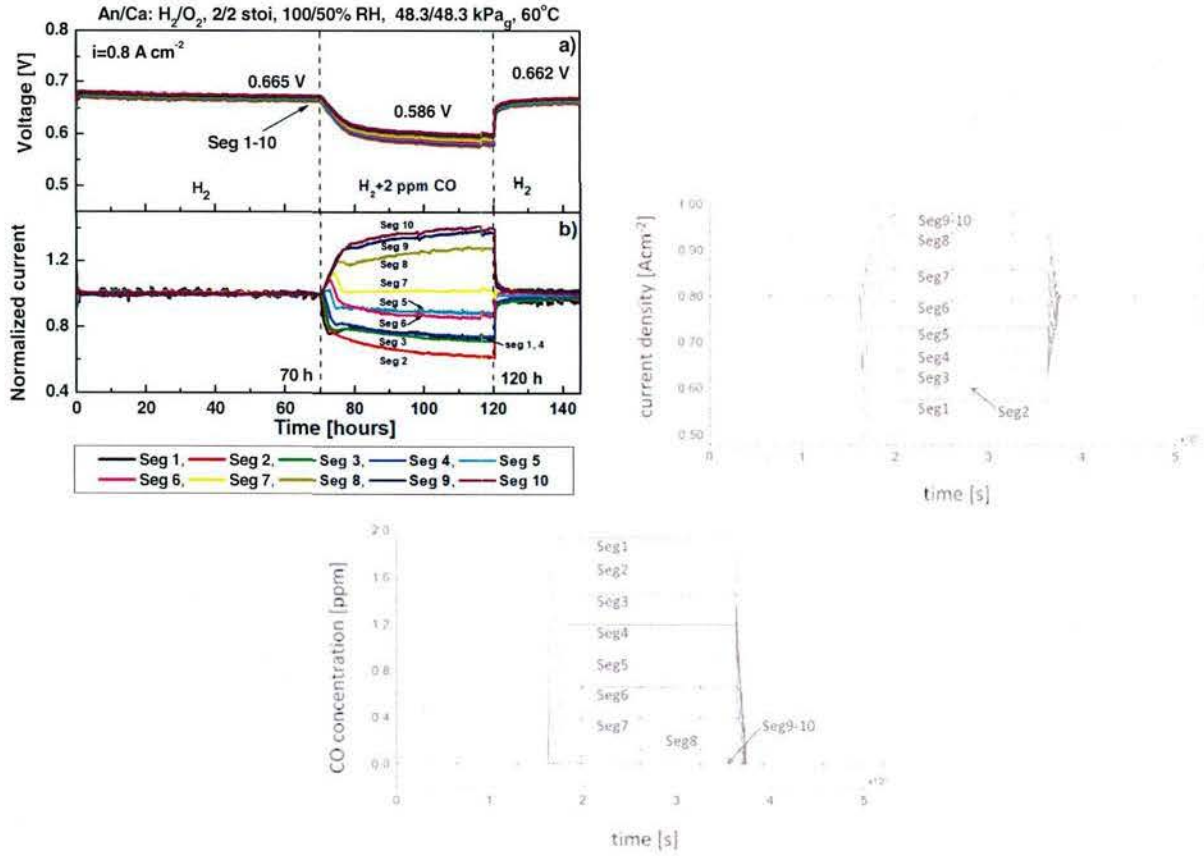

Figure 2.1.27. Transient voltage (a) and normalized current densities (b) for individual segments, an overall current density of 0.8 A cm^{-2} and 2 ppm CO. Simulation of current density (top right) and CO concentration (bottom) distributions. H_2/O_2 case.

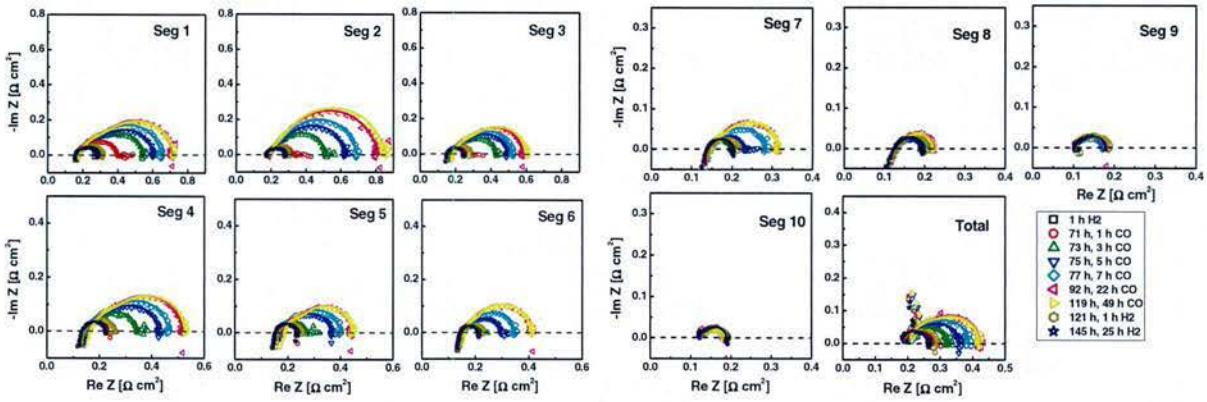

Figure 2.1.28. Impedance spectra for segments 1-10 and the overall cell during a 2 ppm CO exposure at 0.8 A cm^{-2}. Experimental data are represented by symbols and the modeling results are depicted as solid lines. Spectra at 92 h were recorded down to 0.01 Hz whereas all others were recorded down to 0.05 Hz. H_2/O_2 case.

Figure 2.1.28 summarizes impedance data (Nyquist representation with imaginary Im Z versus real impedance Re Z values) for all ten segments and the overall cell. Spectra before and after CO contamination overlap whereas during the contamination phase, spectra were modified with a progressively larger loop. In addition, modified spectra are confined to cell segments located near the hydrogen inlet port. These features are consistent with normalized current (Figure 2.1.27 b) and CO concentration (Figure 2.1.27, bottom) transients. It is emphasized that a typical pseudo-inductive loop (positive imaginary impedances) representative of slow CO electrooxidation and removal of CO_2 from the Pt surface was not obtained in the low frequency region, which suggests that the chemical mechanism is predominant (Equations 6 and 7) and similar to air bleeding[38] with O_2 diffusing from the cathode through the membrane. This hypothesis is also justified by the low anode potential (~0.089 V versus the hydrogen electrode) which is insufficient to oxidize CO at a high rate unless it is above 0.4-0.5 V vs. the hydrogen electrode.

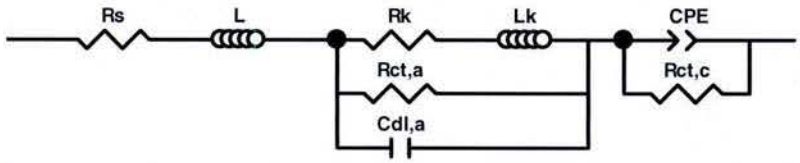

Figure 2.1.29. Equivalent electrical circuit used to fit impedance spectra for the H_2 + CO/O_2 case.

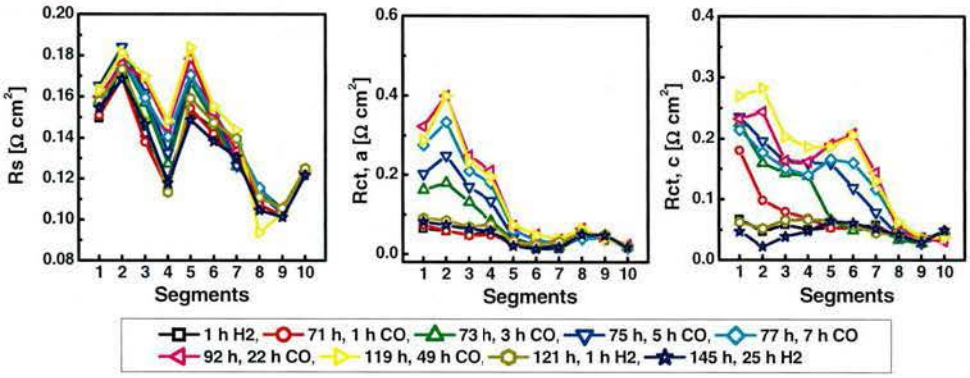

Figure 2.1.30. Distributions of serial resistance R_s, anode $R_{ct,a}$ and cathode $R_{ct,c}$ charge transfer resistances at various CO exposure times. Equivalent electrical circuit fitting was completed in the 10 000-0.05 Hz frequency range. H_2/O_2 case.

The equivalent electrical circuit depicted in Figure 2.1.29 was used for fitting impedance data and separate the anode contributions. However, R_K and L_K elements were eliminated because the anticipated pseudo-inductive loop was not observed with the O_2 oxidant. Figure 2.1.30 illustrates distributions for the three equivalent electrical circuit resistances. Most significantly, the anode kinetic resistance $R_{ct,a}$ increases during exposure to CO near the cell hydrogen inlet. Again, this result is consistent with the current density and CO concentration distributions (Figure 2.1.27 b and 2.1.27, bottom). The serial resistance R_s distribution reflects the sub-saturated inlet O_2 stream and the incompletely moistened membrane near the inlet. The cathode kinetic resistance $R_{ct,c}$ is indirectly increased due to the concurrent decrease in inlet current density induced by CO (the cathode kinetic resistance for a Tafel process is inversely proportional to the current density).

For the other two cases studied, air or hydrogen fed to the cathode rather than O_2, the contribution of the electrochemical CO oxidation path (Equations 3 and 5) to the total CO oxidation rate increased, as demonstrated by an increase in the size of the pseudo-inductance feature at low frequencies (not shown), owing to the decrease in O_2 diffusing to the anode compartment through the membrane and the consequent increase in the anode potential (larger anode overpotential promoted by a more difficult CO oxidation).

These studies have demonstrated that the prior knowledge about fuel cells operated with hydrogen contaminated by CO was applicable to a lower than previously studied CO concentration that is much closer to the hydrogen fuel standard requirement. More details are provided in the Publications and Presentations Resulting from these Efforts section (item 10).

Impact of contaminant hydrophobicity on fuel cell water management

A multitude of fuel cell contaminants exist and the majority of those that have been tested have shown several detrimental effects including kinetic, ohmic and mass transfer overpotential increases. Contamination mechanisms are still not fully understood especially in relation to water management. Impedance spectra have often shown an increase in the low frequency loop diameter (Nyquist representation) and associated resistance generally ascribed to mass transfer.[39] This may be explained by contaminant adsorption on the carbon (gas diffusion layer, catalyst support) affecting hydrophobicity and liquid water content in gas diffusion electrodes.[39]

Confirmation of the existence of this effect would focus activities to minimize mass transport losses induced by contamination. Additionally, if there is an impact of contaminants on gas diffusion electrode water content, it would reveal the existence of synergy between contaminants adsorbing on carbon and cationic contaminants (salts in sea water) which require a liquid water path to reach the ionomer or membrane for ion exchange with protons and affect all overpotential types.[40,41] This contaminant synergy is directly relevant to applications because reactant streams contain more than one contaminant (contaminant mixtures).

The correlation between gas diffusion electrode water content and contamination will be assessed by measuring the amount of liquid water by neutron imaging using the National Institute of Standards and Technology facilities. Through- and in-plane neutron images will be acquired considering the liquid water distribution is 3 dimensional. Propene and methyl methacrylate were selected as contaminants because they both lead to increases in mass transfer resistance and adsorb on carbon (Table 2.1.3). Both contaminant have a relatively different hydrophobicity as revealed by a surrogate measure (solubility in water, Table 2.1.3).

Table 2.1.3. Solubility in water and adsorption on carbon capability of organic contaminants.

Species	Acetonitrile	Acetylene	Bromomethane	Iso-propanol	Methyl methacrylate	Naphthalene	Propene
Solubility in H_2O (mg L^{-1})	Miscible[a]	1170	17,500	Miscible[a]	15,000	31.6	0.61
C adsorption	Yes[42]	Yes[43]	Yes[b,44]	Yes[45]	Yes[c,46]	Yes[47]	Yes[d,48]

[a] 786 g L^{-1} for pure acetonitrile and iso-propanol. [b] Dichloromethane. [c] Methyl acrylate. [d] 4-methyl-1-pentene.

Propene and methyl methacrylate were also selected for other reasons to ensure that the gas diffusion electrode water content is not affected by current re-distribution and only the contaminant adsorbs on carbon. Propene and methyl methacrylate minimally affect current distribution (not shown), are less extensively converted to products at the steady state cathode potentials considered for cell operation (not shown) and are only slightly soluble in water.[14]

Two different types of experiment were planned. The first experiment minimizes the impact of contaminants on current distribution and reactions with a non-operating fuel cell modified by eliminating the anode gas diffusion layer and circulating water in the anode compartment. Water is transferred to the cathode compartment, mimicking water production, by applying a slightly higher temperature to the anode end plate than the cathode end plate (thermo-osmosis).[49] Contaminants in N_2 will be temporarily introduced in the cathode compartment which will allow the acquisition of imaging data after reaching a steady state and, before, during and after contamination. The difference between neutron images acquired during pre-contamination and contamination phases will reveal the impact of contaminant adsorption on carbon on the gas diffusion electrode liquid water content.

The second experiment uses a cell operated at a constant current density with a temporary injection of contaminants in air. Otherwise, this experiment is similar to the first one. Variations in contaminant concentration, which would affect carbon surface hydrophobicity because the amount of contaminant adsorbed on carbon is dependent on gas phase concentration, were also planned. Table 2.1.4 summarizes initially planned tests.

Table 2.1.4. Planned tests summary.

Test number	**Cell type[a]**	**Test type[b]**	**Contaminant[c]**	**Operating conditions**

1	IP	O	MMA	Baseline + variations in contaminant concentration
2	IP	NO	MMA	Baseline + variations in contaminant concentration
3	TP	O	MMA	Baseline + variations in contaminant concentration
4	TP	NO	MMA	Baseline + variations in contaminant concentration
5	IP	O	PP	Baseline + variations in contaminant concentration
6	IP	NO	PP	Baseline + variations in contaminant concentration
7	TP	O	PP	Baseline + variations in contaminant concentration
8	TP	NO	PP	Baseline + variations in contaminant concentration

[a] IP: in-plane water distribution (50 cm^2 active area); TP: through-plane water distribution (3.08 cm^2 active area).
[b] O: operating cell; NO: non-operating cell.
[c] MMA: methyl methacrylate; PP: propene.

Preparations for the tests and the test campaign at the National Institute of Standards and Technology were completed. Detailed analyses of the results will be summarize in a subsequent report. A 50 cm^2 active area cell for in-plane water distribution measurements was borrowed from Los Alamos National Laboratory and modified by replacing bipolar plates with zinc and gold coated aluminum substitutes with flow field designs in use at HNEI (Figures 31 and 32). These plate materials maximize water absorption sensitivity by minimizing neutron absorption for all other materials in the neutron beam path. A 3.08 cm^2 active area cell was also built for through-plane water distribution measurements (Figure 31).

Membrane/electrode assemblies were conditioned to verify in advance the proper operation of both cells. Additionally, a calibration curve was obtained to determine the temperature difference between cathode and anode end plates that led to the same cathode outlet water content as for cell operation at 1 A cm^{-2} (Figure 33).

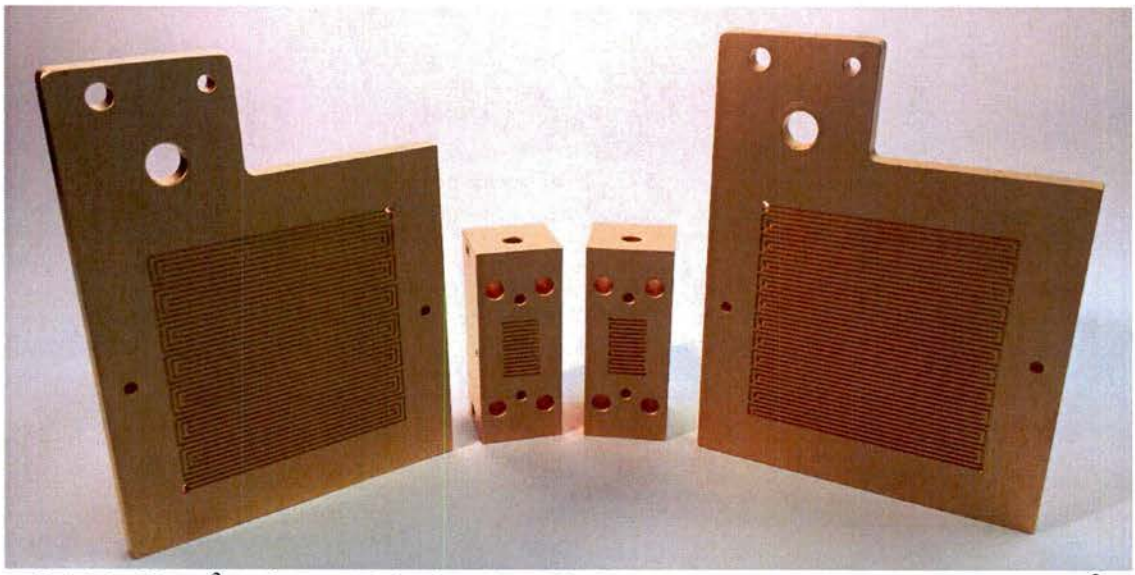

Figure 2.1.31. 50 cm^2 active area bipolar plates for in-plane neutron imaging and 3.08 cm^2 active area bipolar/end plates for through-plane neutron imaging.

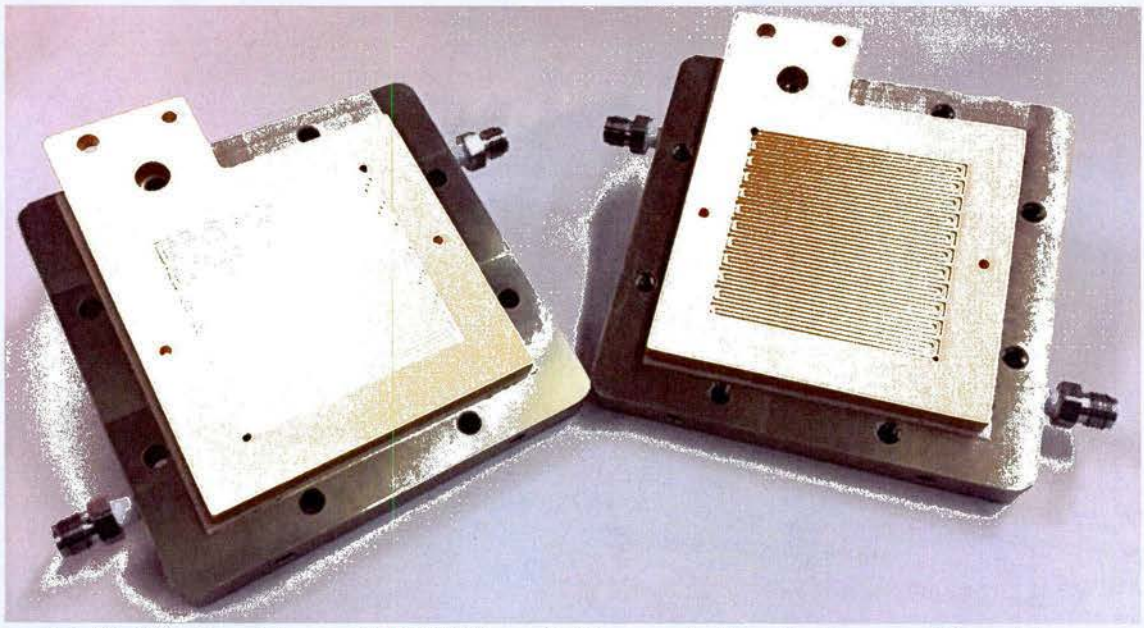

Figure 2.1.32. Bipolar plates with HNEI flow fields mounted on the borrowed Los Alamos National Laboratory end plates.

Both cells mounted at the National Institute of Standards and Technology facilities are shown in Figure2.1. 34. The test plan (Table 2.1.4) was not only completed but extended to take advantage of leftover time (5 days were allocated). For these few additional tests, the effect of relative humidity and contaminant mixing (synergy between species) were explored. Additional fuel cell tests will be completed at HNEI which include verification of the water transfer calibration curve (Figure 2.1.33) for the 3.08 cm^2 active area cell, multi-component gas analyses (O_2, O_2+He, O_2+N_2) to isolate O_2 mass transfer contributions in the ionomer and gas phases and correlate liquid water content data, and cyclic voltammograms to verify the presence of contaminant reactions at the cell operating potentials.

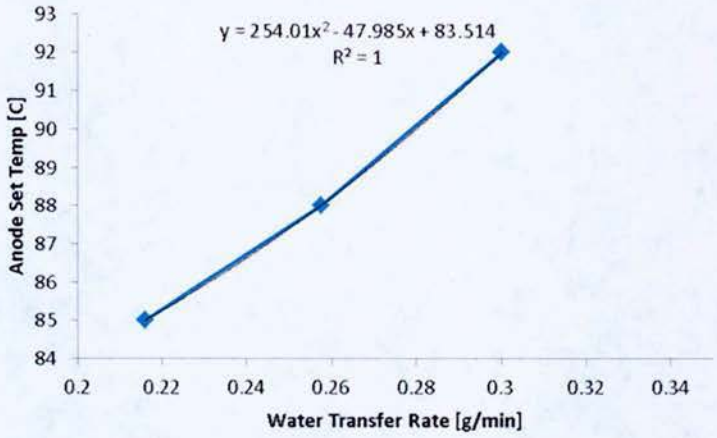

Figure 2.1.33. Thermo-osmosis calibration curve obtained by cathode outlet water collection. Cathode end plate maintained at 80 °C.

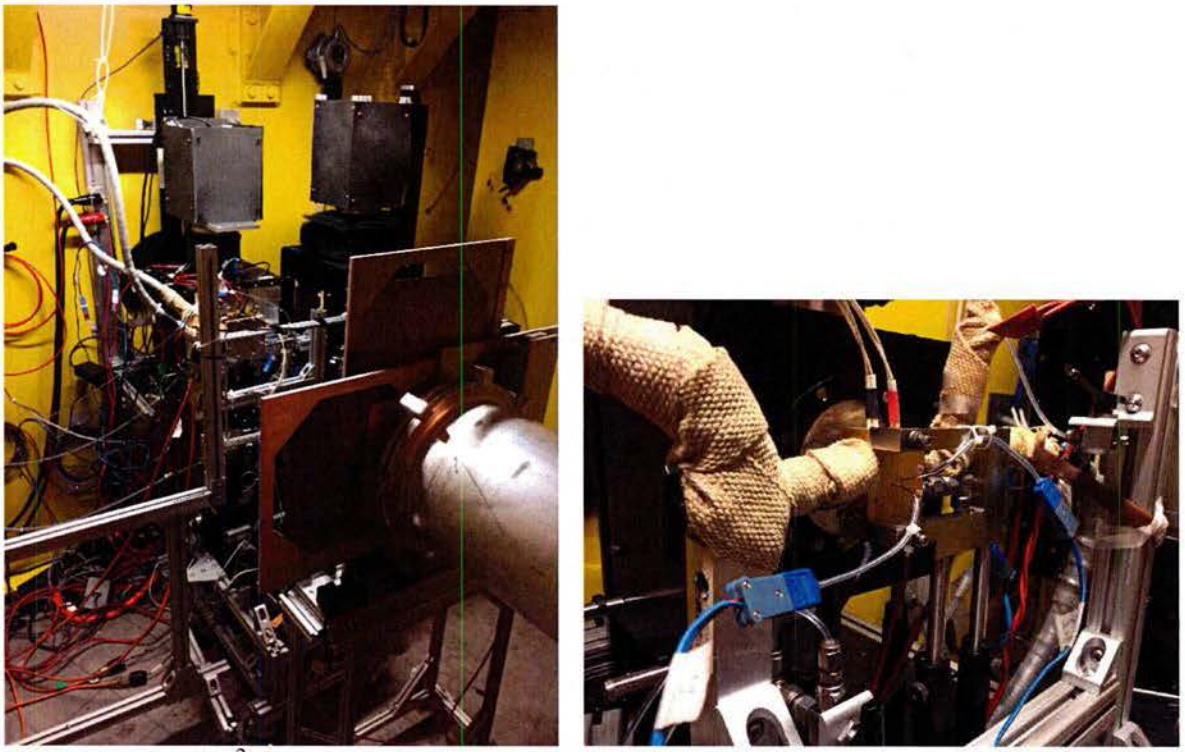

Figure 2.1.34. 50 cm^2 active area cell mounted in the path of the collimated neutron beam (tube on the right of the left image) and in front of the neutron detector. 3.08 cm^2 active area cell mounted in front of the neutron detector (right image).

Recovery of fuel cell performance losses caused by contamination

Contamination mechanisms were established for several species that affect fuel cell performance. Data gathered at the Hawaii Sustainable Energy Research Facility (HiSERF) using ex situ (rotating ring/disc electrode) and in situ methods (gas chromatography/mass spectrometry, segmented cell) have highlighted the complexity of these mechanisms and their dependence on multiple factors including contaminant, electrode potential and the variability in intermediates and products, and localization either along the flow field length or along the cell stacking direction (cell number). Although not every contaminant leads to irreversible fuel cell performance losses (cell voltage does not fully recover after contaminant exposure), recovery procedures should be effective irrespective of these factors.

Contaminants may cover the catalyst surface by adsorption of neutral or charged intermediates, or penetrate the ionomer or membrane by ion or solvent exchange. In the former case, the adsorbate reduces the catalyst surface area and interacts with oxygen reduction by charge density redistribution. In the latter case, the presence of the contaminant in the ionomer or membrane disrupts proton conduction. Sulfur dioxide is an important contaminant originating from natural and anthropogenic sources, which has a severe and partly irreversible impact on fuel cells. Its contamination mechanism involves both molecular (SO_2, S) and anion (SO_4^{2-}, HSO_4^-) adsorption.

During self-recovery periods, contaminant intermediates are reduced, oxidized and/or desorbed from the catalyst surface, ionomer and membrane. However, for several cases, a cathode potential exceeding 1 V vs. a hydrogen electrode (at open circuit, a fuel cell has a voltage

approximately equal to 1 V corresponding to a cathode of approximately 1 V vs. a hydrogen electrode) is necessary to oxidize adsorbed sulfur and halogen anions (Cl^-, Br^-).[50] This procedure is impractical requiring electrical connections to and voltage control for every cell in a fuel cell stack.

Recently, ozone with a reduction potential of 1.6 V vs. a hydrogen electrode was added to the cathode reactant stream to locally create a corrosion cell and oxidize adsorbed sulfur on the catalyst.[51] This approach circumvents the need for connecting and controlling the cathode potential of individual cells in a stack. Ozone itself is an airborne contaminant which can cause permanent damage.[14] Recovery attempts were nevertheless successful because ozone exposures were short. In a similar fashion, the effectiveness of nitrous oxide (N_2O, reduction potential of 1.77 V vs. a hydrogen electrode)[52] was investigated. For this specific situation, the local corrosion cell electrode reactions are:

$$N_2O + 2H^+ + 2e^- \rightarrow N_2 + H_2O \text{ (Equation 8)}$$

$$SO_{x,ads} + (4-x)H_2O \rightarrow HSO_4^- + (7-2x)H^+ + (6-2x)e^- \text{ (Equation 9)}$$

Figure 2.1.35 shows N_2O recovery experiments. N_2O was introduced at different contamination phases (2 ppm SO_2). The baseline cell voltage is characterized by typical features: a steady state with a significant cell performance loss and a partial cell performance recovery at steady state.[53] N_2O injection does not modify any of these features which implies its ineffectiveness and the absence of a N_2O contamination effect.

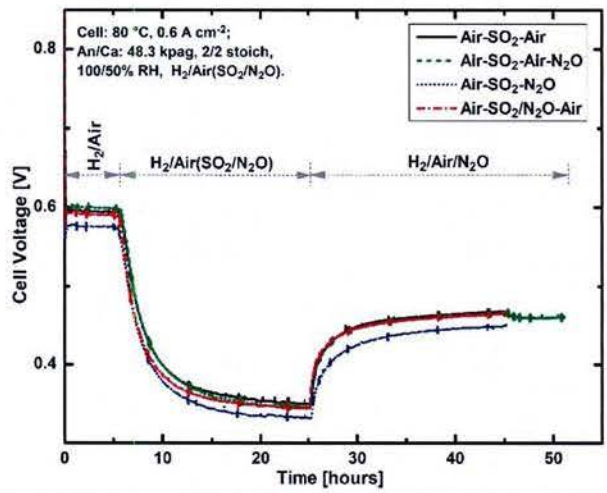

Figure 2.1.35. Cell voltage responses to 2 ppm sulfur dioxide in neat air. For the baseline case, nitrous oxide was not introduced. For the other cases, 50 ppm nitrous oxide was injected after recovery with neat air, after sulfur dioxide contamination and during sulfur dioxide contamination.

Impedance spectra support Figure 2.1.36 findings. Figure 2.1.36 depicts impedance data (Nyquist representation with the imaginary impedance Im(Z) plotted as a function of the real impedance Re(Z)) during the different SO_2 contamination phases. All spectra show similar features with 2 semi-circles. The higher frequencies semi-circle is attributed to oxygen reduction (~10 Hz to >1 kHz) whereas the low frequencies semi-circle (<1 Hz to ~10 Hz) is ascribed to oxygen transport (baseline) and an SO_2 process (SO_2 cases). Spectra changes associated with SO_2 (decrease in real impedance Re(Z) at frequencies >1 kHz, appearance of an inductive

behavior at low frequencies below 1 Hz with positive Im(Z) impedance values, etc) are consistent with prior results.[54] Most importantly, the injection of N_2O does not affect impedance spectra (only the air-air+2 ppm SO_2-air-air+50 ppm N_2O sequence case from figure 36 is shown).

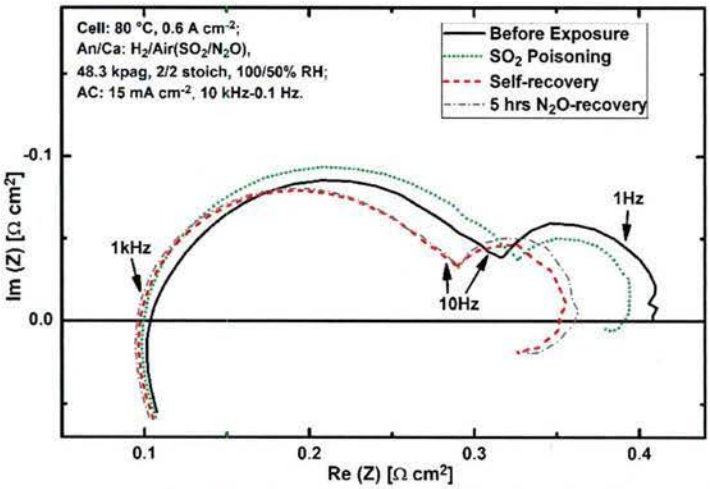

Figure 2.1.36. Impedance spectra for the air-air+2 ppm SO_2-air-air+50 ppm N_2O sequence case.

Cyclic voltammetry and polarization curves diagnostics were also completed to confirm N_2O recovery results. Figure 2.1.37 results are representative of all N_2O injection cases. Figure 2.1.37, left illustrates the baseline cyclic voltammogram in black. In comparison, the cyclic voltammograms completed after SO_2 contamination and N_2O recovery are characteristic of an SO_2 poisoned electrode with, for example, a smaller hydrogen oxidation peak (positive current values in the ~0.1 to 0.3 V vs. the hydrogen electrode) and an additional sulfur adsorbate oxidation peak (positive current values) at 1.04 V vs. the hydrogen electrode. Polarization curves (Figure 37, right) obtained after cyclic voltammetry scans show an increase in Tafel slope from 78 to 103 mV decade^{-1}, a lower cell performance and a reduced internal cell resistance. Polarization curve changes are similar to those previously noted after SO_2 contamination and without N_2O treatment, which were attributed to the impacts of sulfate anions left in the catalyst layer.

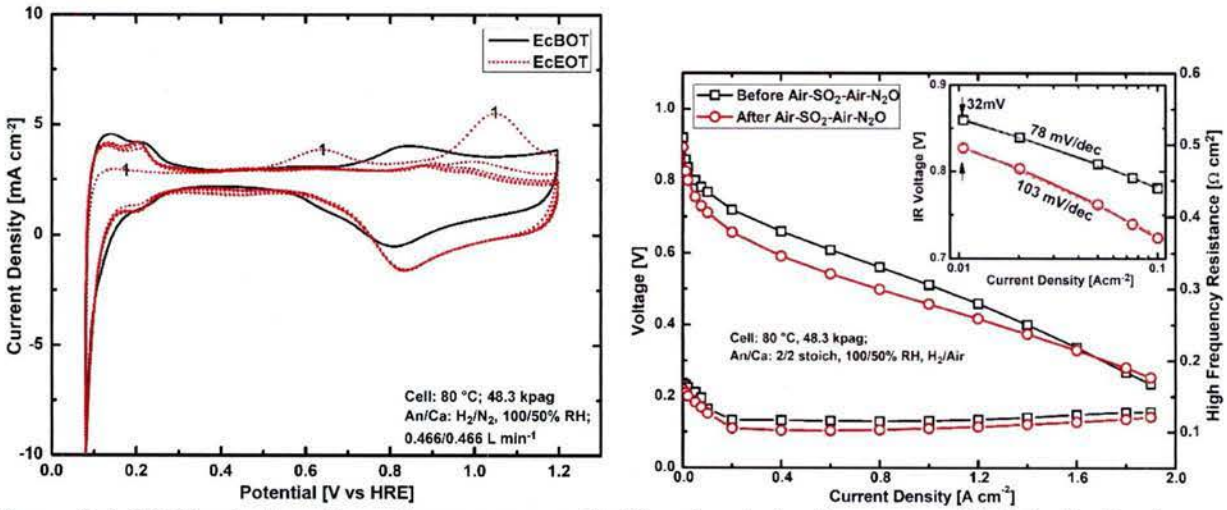

Figure 2.1.37. Typical cyclic voltammograms (left) and polarization curves (right) obtained before and after SO_2 contamination and N_2O treatment.

In retrospect, N_2O was not able to oxidize adsorbed SO_2 despite a significantly higher reduction potential than ozone but testing results enhanced HiSERF's knowledge in this important research area. A fuel cell was operated with hydrogen fuel and nitrous oxide rather than air as the oxidant for confirmation. The polarization curve displayed in Figure 2.1.38 indicates that the cell has a relatively low open circuit voltage (<0.7 V with a cathode potential <0.7 V vs. a hydrogen reference). The cathode potential is insufficient to oxidize absorbed SO_2 on the catalyst. The lower cathode potential is partly explained by a large Tafel slope of 370 mV decade^{-1}, which implies that N_2O reduction is irreversible. The rich nitrogen compounds chemistry and multiple reactions that may create unwanted mixed potentials (corrosion cells) is also partly responsible for the low cathode potential. Interestingly, the cell was able to operate with an oxidant that is easily liquefied. However, the cell performance would need to be improved with a more effective and selective catalyst for N_2O reduction.

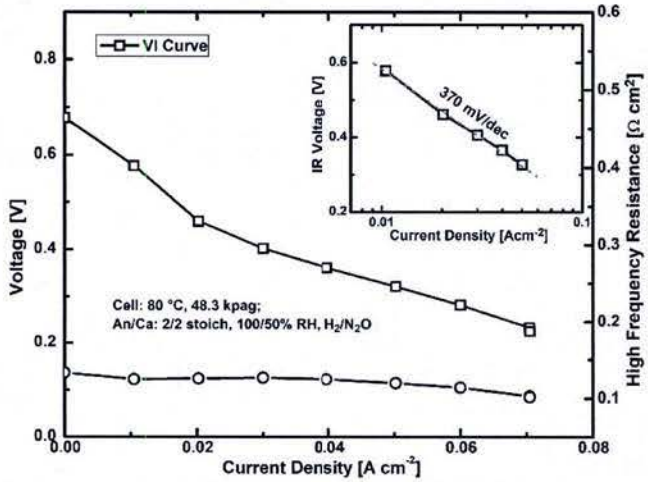

Figure 2.1.38. Polarization curve for a single cell operated with hydrogen fuel and nitrous oxide oxidant.

The fuel cell performance recovery concept based on ozone was only tested with inorganic sulfur gases (H_2S, SO_2).[51,55] Tests are planned for the important halogen anion class of contaminants, which include chloride (salt water) and bromide (a decomposition product of bromomethane, an atmospheric contaminant). This contaminant class has been neglected and positive results are anticipated because chloride and bromide are easily oxidized at a cathode potential above, respectively, 1.36 and 1.07 V vs. a hydrogen electrode, values that are smaller than the ozone reduction potential of 1.6 V.

Measurement and separation of reactant mass transfer coefficients in fuel cells

Reactant transport in fuel cells involve many different processes including molecular and Knudsen diffusion in the gas phase, diffusion in solid (ionomer) and liquid (water) phases and interfacial transport between all these phases. The optimization of gas diffusion electrodes partly relies on an understanding of the relative contribution of all transport processes and is particularly relevant to fuel cell commercialization efforts because mass transfer limitations are exacerbated by lower platinum catalyst loadings.[56] As a result, there is a need to develop or improve in situ methods to measure and separate mass transfer coefficients into fundamental contributions. Such a method is currently being developed at HiSERF with Army Research Office funds.

In support of these Army Research Office efforts, HiSERF has collaborated with the Institute of Energy and Climate Research, Jülich, Germany to validate, as a first step, an existing impedance model containing mass transfer parameters. Ultimately, model parameters obtained by fitting the impedance model will be compared to those derived from the HiSERF measurement and separation method for parameter cross-validation. The transient, one dimensional, through the membrane/electrode assembly plane model was fitted to impedance spectroscopy data obtained with a segmented cell operated with oxygen at a high stoichiometry and a low 0.1 A cm^{-2} current density to minimize gradients along the flow field length and match the model dimensionality, and ensure model applicability (the low current density minimizes but does not eliminate the mass transport losses). Use of a segmented cell provides a larger dataset that improve data analysis statistics.

The impedance model[57] was developed with the objective to obtain an analytic solution that accelerate data processing. This was achieved by only including key processes including oxygen mass transport at the expense of other considerations that would have significantly increased model complexity (liquid water management, temperature, pressure and concentration gradients along the flow field length, etc). The model includes a proton current conservation equation, Ohm's law for the proton current density and an oxygen mass balance equation. The gas diffusion layer is represented by a linear oxygen mass balance equation. These four equations were linearized assuming a small amplitude for the applied current perturbation and subsequently modified by the Fourier transform. The resulting system of linear equations for the perturbation amplitudes was analytically solved assuming that the steady state shapes of the oxygen reduction overpotential and concentration are constant along the through membrane/electrode assembly plane coordinate. This last assumption limits the model applicability to low cell current densities (a criterion was also derived). As a final step, the analytical perturbation amplitudes were used to calculate the cell impedance.

Experimental impedance spectra contain two arcs: a large low frequency arc and a small arc in the high frequency region. The high frequency arc of unknown origin was taken into account by adding a simple parallel resistance/capacitor circuit to the model (same parameters for all cell segments). Raw impedance spectra were pre-processed before model fitting. High frequency data points with a positive imaginary part were ignored (cable inductance). Experimental spectra were also shifted to the left to ensure that the lowest real impedance data point has a real impedance equal to zero.

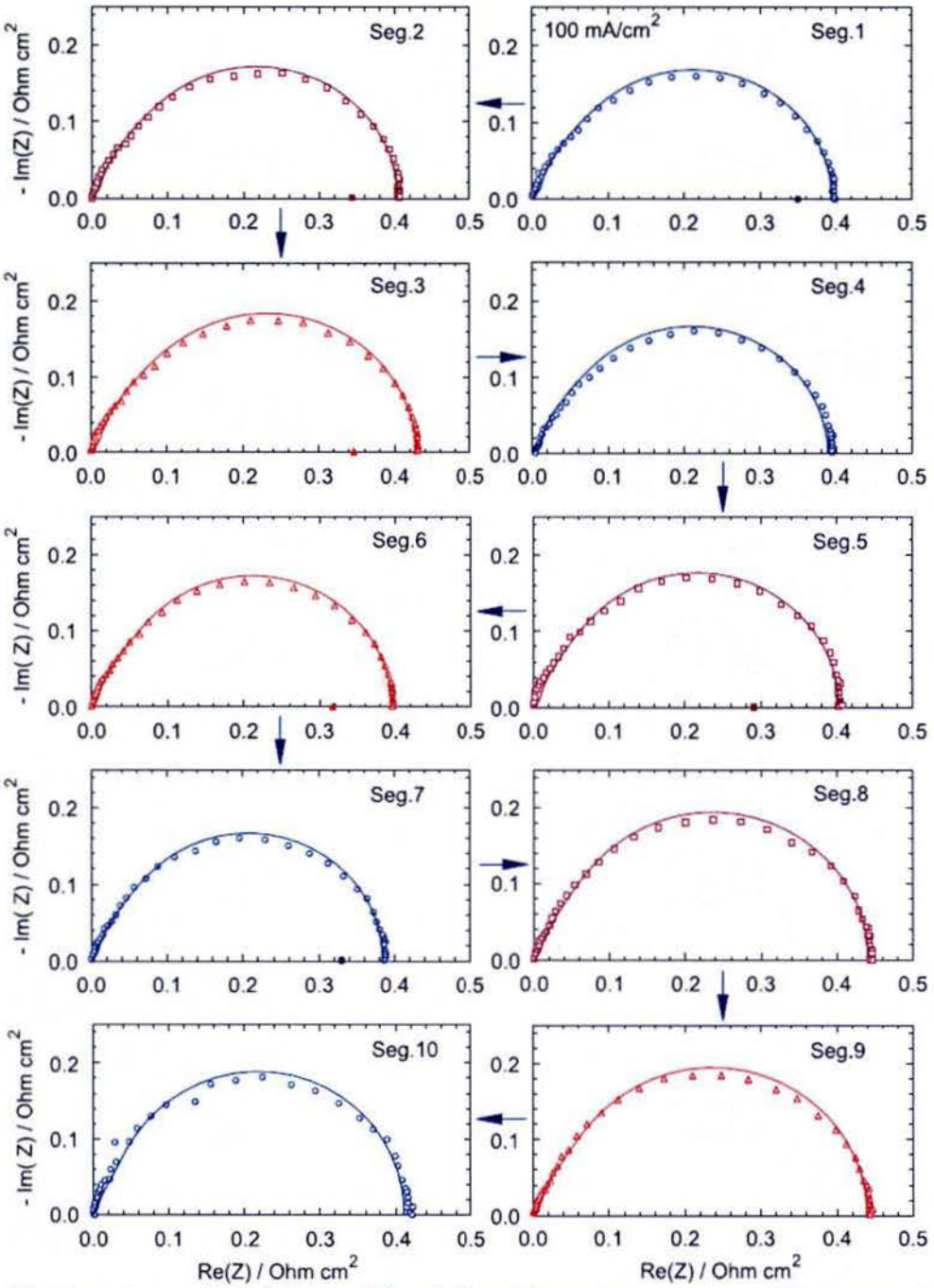

Figure 2.1.39. Experimental (points) and fitted (lines) impedance spectra. The oxygen inlet is located at segment 1. Arrows indicate the direction of the oxygen flow. The ohmic corrected direct current resistivities for segments 1-3 and 5-7 as determined by fitting corresponding polarization curves are indicated by filled symbols on the real impedance axis.

Figure 2.1.39 shows the experimental impedance spectra and fitted model curves for all segments. The model adequately reproduce experimental data with the exception of small differences near the top of the low frequency semi-circle, which are attributed to the small spatial variation in static oxygen concentration and overpotential profile in the through plane direction that are ignored in the model. The fitting accuracy for the high frequency part of the spectra is less accurate due to the neglected cable inductance effect. The fitted model parameters are shown in Figure 2.1.40.

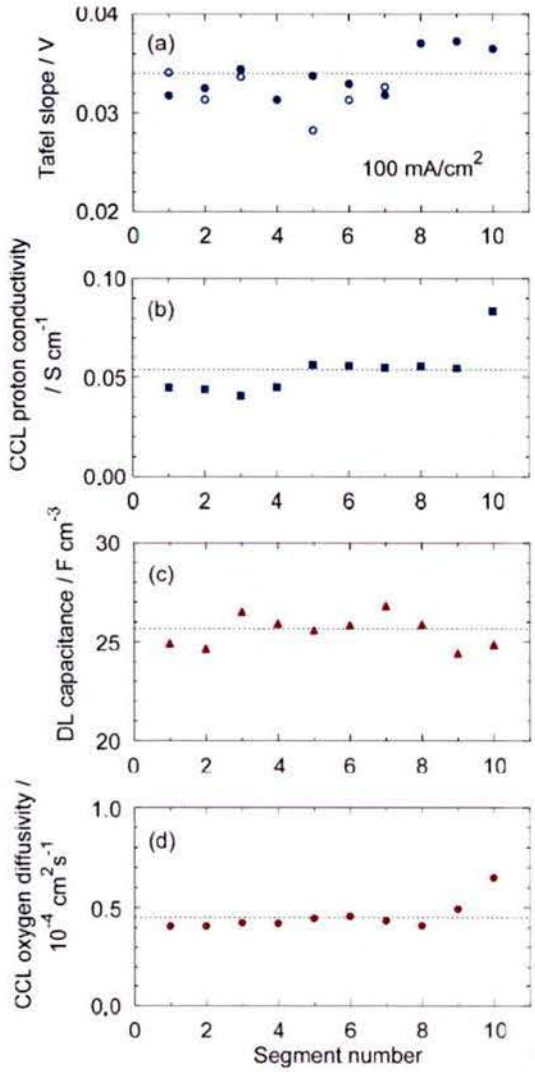

Figure 2.1.40. Fitting parameters for segments 1 to 10. Open circles in (a) correspond to Tafel slopes as determined by fitting polarization curves. All other points are obtained by fitting impedance spectra. Average values are indicated by dotted lines.

The oxygen reduction Tafel slope varies between 71 to 85 mV decade^{-1} owing to small variations in local currents (Figure 40 a). The average value of 78 mV decade^{-1} agrees with the theoretical value of 69 mV decade^{-1}. The catalyst layer proton conductivity is nearly the same for all segments with the exception of segment 10 (Figure 40 b). Impedance data for segment 10 are less accurate and scattering is more prevalent (Figure 39). The high proton conductivity value of 0.054 ohm^{-1} cm^{-1} is located at the high end of the other measurements' range (10^{-4} to 0.03 ohm^{-1} cm^{-1}). The double layer capacitance varies between 24 and 27 F cm^{-3} with an average of 25.5 F cm^{-3} (Figure 40 c). This value is close to the reported values of approximately 15 F cm^{-3} reported for similar systems. The oxygen diffusion coefficient in the catalyst layer is nearly constant along the cell active surface with an average of approximately 0.454 x 10^{-4} cm^2 s^{-1} (Figure 40 d). This parameter has apparently not been measured in situ and therefore cannot be compared to other values. However, the fitted oxygen diffusivity is approximately 30 times lower than reported values derived from ex situ measurements with a dry cathode catalyst layer. This observation suggests a strong effect of liquid water produced at the cathode, which fills the catalyst layer and explains the low oxygen diffusivity fitted value. The measured oxygen diffusivity is nearly equal to the value for liquid water (0.53 x 10^{-4} cm^2 s^{-1}). However, this

suggestion does not take into account the catalyst layer porosity which would lower the theoretical oxygen diffusivity in water. Hence, the discussion supports the original objective of this work to compare parameters obtained by different methods. Finally, the model was unable to capture the oxygen diffusion coefficient in the gas diffusion layer. The oxygen transport loss in the gas diffusion layer is very small with an oxygen feed, and the respective contribution to the cell impedance seemingly is below the measurement accuracy.

More details are provided in the Publications and Presentations Resulting from these Efforts section (item 7). Future efforts will focus on upgrading the model from oxygen to air operation for improved application relevance.

State of health monitoring of Li-ion battery packs

Individual cell voltages can deviate and become unequal in high energy density Li-ion battery packs because during charge and discharge only the current is controlled which leads to an imbalance in state of charge. The cell pack voltage may indicate a normal state but individual cells may have different state of charge subsequently leading to overdischarge or overcharge and failure by thermal runaway.[58] Battery management systems are therefore essential for preventive purposes to detect the state of health of single cells in a stack. However, to minimize circuitry, complexity and cost, there is a desire to limit measurements to the stack level.

Impedance based diagnostics were considered because measurements are influenced by battery health indicators. However, signal generation, data acquisition and processing hardware need simplification to reduce cost and analysis time for onboard real time use. NRL has identified a single frequency leading to an invariant cell impedance under normal operating conditions (in absence of overcharge, overdischarge and thermal abuse) which was linked to the solid electrolyte interface, the passivation layer that protects electrodes.[59] A single overcharge was sufficient to significantly alter the cell impedance. In collaboration with NRL, the validity of the single frequency diagnostic was extended to a battery pack to assess the measurement sensitivity at that frequency to the state of health of single cells.

The test program had 3 steps: i) identification of the single cell frequency leading to minimal variations in impedance over the full state of charge range (0 to 100 %) and validation of the impedance change following an overcharge, ii) duplication of the frequency identification step for 4 cells serial packs, iii) detection assessment for a pack with a cell replaced with an overcharged cell.

Cylindrical 18650 lithium-ion rechargeable cells were used (Tenergy Battery Corp., Fremont, CA, $LiCoO_2$/C chemistry). Galvanostatic cycling was performed within the manufacturer specified voltage range of 3.0-4.2 V unless otherwise noted. The upper voltage boundary was increased to 4.6 V for the overcharge (OC) condition. The electrochemical impedance of single cells and packs was measured at various states of charge between 50 kHz to 10 mHz by applying a voltage perturbation of 40 mV.

Lithium-ion cells produce different impedance responses with changes in cell voltage and state of charge. The Nyquist plot in Figure 2.1.41 shows changes in both the shape and magnitude for the real versus imaginary impedance curves of a single cell during a typical discharge/charge cycle between 3.0 and 4.2 V, or 0-100 % state of charge. At 100 % state of charge, the impedance response forms a small single arc. The single arc contains impedance contributions

from both the negative and positive electrodes although it is dominated by the cathode effects. As the state of charge decreases to 3.8 V (57 % state of charge) a second arc emerges in the mid- to low frequency region and grows until the cut-off voltage is reached at 3.0 V (0 % state of charge). The second arc decreases upon charging and returns to the fully charged state. The low frequency arc is assigned to a charge transfer resistance and impedance due to ionic diffusion within the porous electrodes.

Figure 2.1.41 demonstrates that there is little deviation in the impedance response of a representative cell from 0 to 100 % state of charge in the high frequency inductance region ($Z''>0$, not shown) and in the initial portion of the high frequency arc. Three frequencies exhibit the smallest deviation in impedance with state of charge: 500, 316 and 100 Hz. The observed deviations are almost entirely due to changes in Z' (Figure 2.1.42 a). The single point state of health frequency for the Tenergy 18650 cells is determined to be approximately 316 Hz where the standard deviation of the real impedance with SOC, $\sigma_{Z'}$, reaches a minimum while the standard deviation of the imaginary impedance, $\sigma_{Z''}$, is nearly constant (Figure 2.1.42 c).

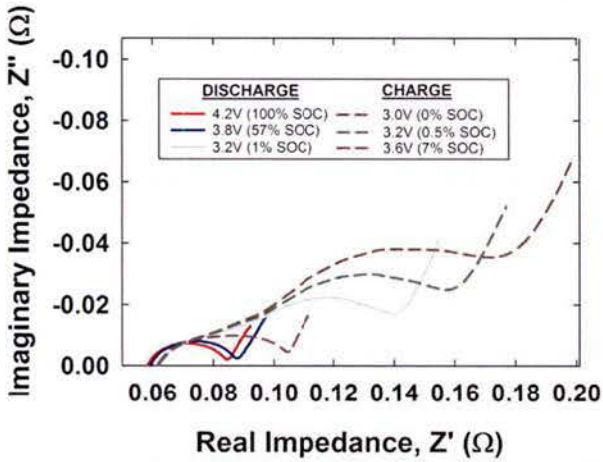

Figure 2.1.41. Impedance spectra collected at various state of charge SOC of a 18650 cell during a typical discharge or charge between 3.0 and 4.2 V (0-100 % SOC).

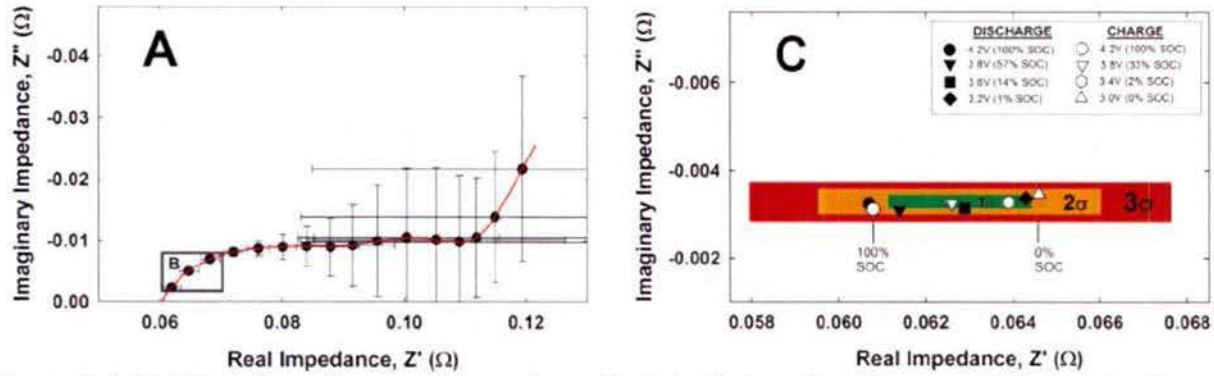

Figure 2.1.42. Mean impedance values and standard deviations for all states of charge (a). For clarity, the black circles represent every 3rd data point. State of health chart illustrating the change in impedance response collected at 316 Hz perturbation frequency with state of charge SOC (c). Deviation from the average impedance is shown by the increasing factors of deviation: 1, 2 and 3 times the standard deviation (1σ, 2σ, 3σ) with state of charge.

Single Tenergy 18650 cells were mildly overcharged to 4.56 V (125 % state of charge) for 5 consecutive cycles. The impedance responses to overcharge at the state of health frequency is

shown in Figure 2.1.43 and compared to the average impedance and variance of a cell operated under normal conditions. The initial impedance at the full state of charge lies within the 3σ boundary. As expected, the real impedance value is nearly identical to that shown in Figure 2.1.42 c (4.2 V, 100 % state of charge). The impedance collected at the first overcharge condition (4.56 V) is designated by *OC*1. At the overcharge condition of *OC*1 (125 % state of charge) both *Z*' and *Z*'' increase. After *OC*1, the cell was returned to 4.2 V to compare the initial impedance. There is a small shift in the real and imaginary impedance towards more positive values when the cell is returned to 4.2 V (point "1"). The impedance collected at repeated overcharge conditions shifts towards lower *Z*' and change to positive *Z*'' during *OC*2 through *OC*5 further demonstrating the identification of a cell malfunction (data located outside the 3σ bound area for a healthy cell). Each subsequent overcharge cycle increases the real impedance when the cell is returned to 4.2 V showing a trend towards higher real impedance that still lies within the 3σ boundary.

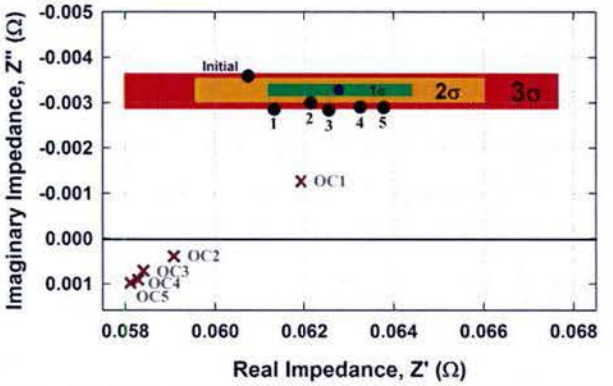

Figure 2.1.43. State of health chart illustrating the average impedance value at the 316 Hz state of health frequency (blue circle) encircled by the ±1, 2 and 3 times standard deviation (1σ, 2σ, 3σ) as determined in Figure 42 c. The repeated sequence of the impedance response of the cell at 4.56 V (125 % state of charge) overcharge and subsequent discharge to 4.2 V (100 % state of charge) are respectively represented by red "X OC" marks and black circles labeled 1 through 5.

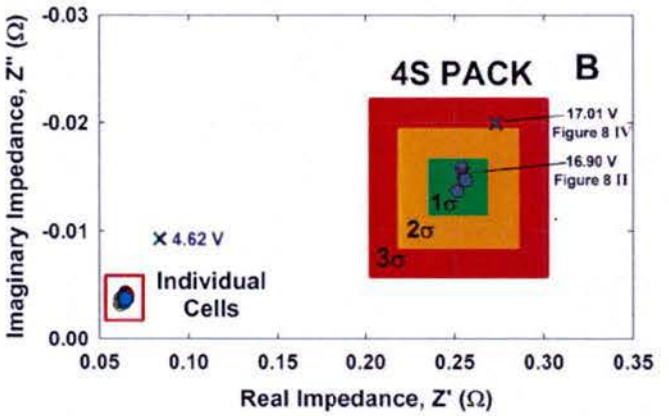

Figure 2.1.44. State of health chart illustrating the impedance at the 316 Hz state of health frequency for cells 1 through 4. The "X" mark labeled 4.62 V denotes the overcharge condition experienced by cell 2 within the 4 cells pack. The 4 cells pack impedance data are encircled by the $\pm 1\sigma$, 2σ and 3σ boundaries with σ the standard deviation. The "X" mark labeled 17.01 V denotes the overall pack voltage associated with the pack with an overcharged cell 2.

The single point impedance diagnostic was employed to monitor the impedance response of the individual cells and the 4 cells in series pack before and after an overcharge of cell 2. Figure 44

shows the tight grouping of impedance values for individual cells. The impedance response collected at 4.62 V for cell 2 deviates outside of the 3σ state of health range, clearly indicating abuse to the pack. After the subsequent discharge to the normal voltage of ~4.2 V, the cell 2 impedance is recovered within the 2σ region. The large variation in cell 2 impedance at 4.6 V is also clearly seen in the 4 cells pack impedance. The pack impedance at 17.01 V enters into the 3σ state of health region. Since the state of health region of the pack includes the summation of deviations from the individual cells, it provides a more conservative estimate of error. Therefore, the pack impedance state of health region could be taken as 1σ clearly identifying a problem encountered within the pack after the 4.62 V overcharge of cell 2. More details are provided in the Publications and Presentations Resulting from these Efforts section (item 9). Future tests are planned and will extend the data base beyond the room temperature.

Other activities

The analysis and publication of additional fuel cell contamination data were also completed during this period for the following air contaminants: Ca^{2+}, propylene, methyl methacrylate, isopropanol and acetylene (data was obtained as part of another federally funded program). Support was also provided to Kathryn Hu, a mechanical engineering department master student who graduated in spring 2017. In this effort, fuel cell characterization data was acquired for different gas diffusion layer materials. Carbon nanotube nanoforests were used as prepared or in combination with carbon paper or ceramic substrates. More details are provided in the Publications and Presentations Resulting from these Efforts section (items 1 to 4).

This APRISES11 task continues and extends to field studies, work in previous ONR awards focused on the understanding, performance, and durability of fuel cell systems subject to harsh environments.

A purposely designed air filter test station was constructed to select the best air filter option to retrofit buses with fuel cell systems (contaminant slippage and anticipated life). Under future funding, the air filter test station will also be used to characterize new adsorbent materials synthesized at HNEI and to obtain data under a wide variety of controlled conditions to facilitate the interpretation of field bus data.

Under future APRISES funding, fuel cell buses will be operated at the Hawaii Volcanoes National Park to serve as a field test region to study fuel cell operation in harsh environments. The fuel cell buses will be exposed to elevated levels of sulfur dioxide in combination with hydrocarbons such as benzene as well as other acidic gases including nitrogen dioxide. Data will be used to understand the lifetime and steady state contaminant removal rates of the air filtration media being installed on the buses and establish correlations between the buses performance in the field and controlled laboratory experiments. Under APRISES11, laboratory scale testing of commercially available and novel air filtration media was enabled by designing, building and installing the air filter test bed at HiSERF. The design focused on tests that measure the effectiveness of passive and active filter systems that prolong fuel cell operation in harsh environments. Furthermore, the design focused on gas phase contaminant removal/adsorption capacities as opposed to particulate or coalescing type filtration. The test bed will initially be used to identify the best performing filtration technology from commercial suppliers. The design of the test bed was based on the general guidelines given in Table 2.1.5.

Table 2.1.5. Air filtration test bed initial specifications.

Parameters	Parameter values
Test condition 1	100 standard L min^{-1} air at 80 % relative humidity and 25 °C (~ambient pressure)
Test condition 2	100 standard L min^{-1} air at 0 % relative humidity and 25 °C (~ambient pressure)
Additional parameters	Post-humidifier impurity injection of up to 3 gas phase contaminants with maximum impurity flow rates of 0.25 standard L min^{-1}

Test condition 1 is based on the average temperature and relative humidity observed at Hawaii Volcanoes National Park whereas test condition 2 was established to include analyses in the absence of water vapor, because water competes with contaminants for adsorption sites. Therefore, test condition 2 provides a baseline. Figure 2.1.45 shows a general overview of the experimental test bed design. Figure 2.1.46 provides the process and instrumentation diagram (P&ID) of the first iteration test bed. The test bed was developed in a cost effective manner using available parts from the facility. This reduced overall cost by approximately 50 %, saving over $15,000 in new materials, parts and instrumentation.

The system is composed of 3 major sections (Figure 2.1.45): i) a pre-filter gas supply and conditioning rack, ii) a heat exchange coolant and humidifier deionized water supply rack, and iii) the filter housing, sensor array, and temperature control chamber.

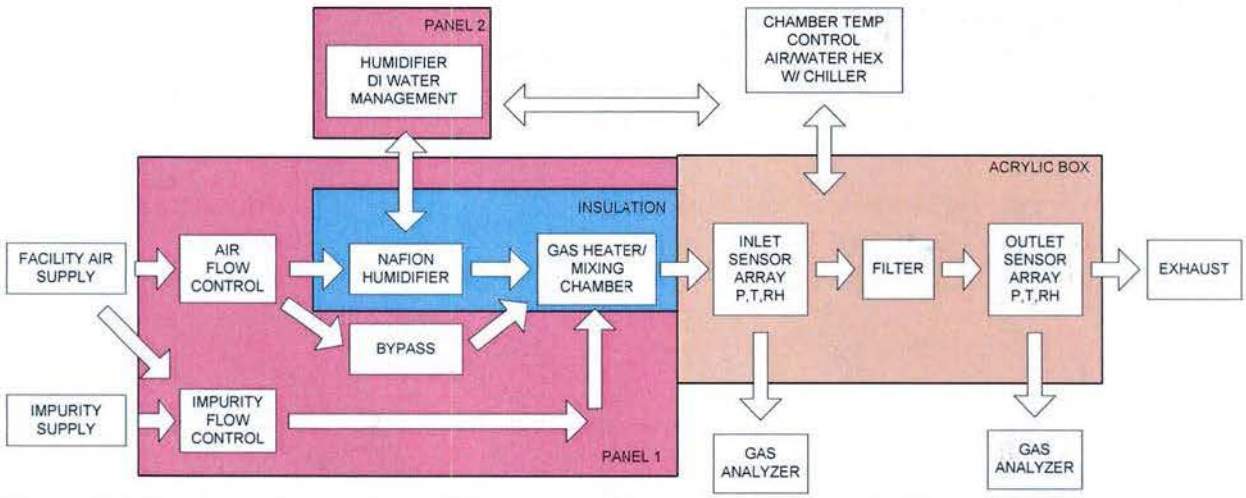

Figure 2.1.45. General overview of the design of the experimental air filter test bed.

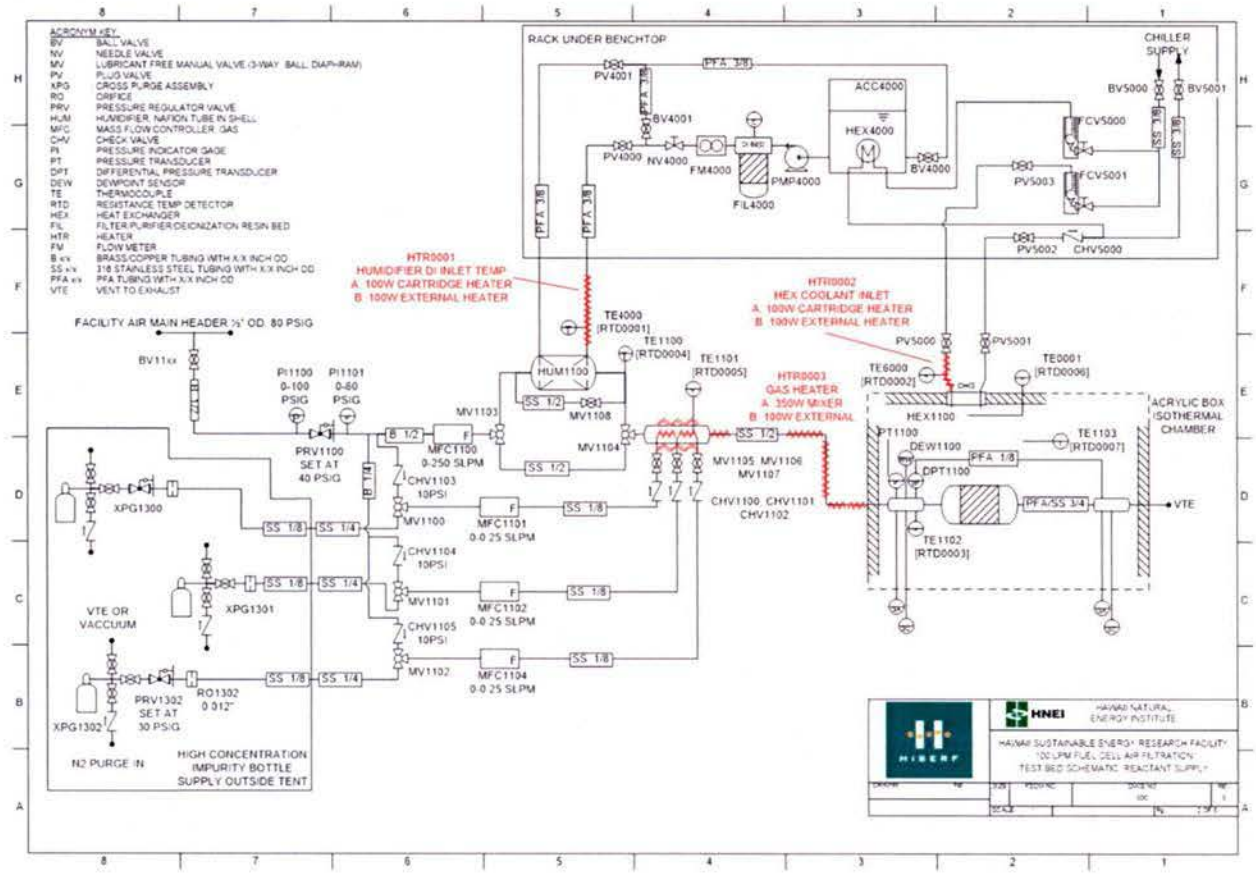

Figure 2.1.46. Process and instrumentation diagram of the air filtration test bed.

The pre-filter gas supply and conditioning rack is composed of the air supply interconnect with HiSERF's supply header, the impurity gas cylinders, the gas flow controllers, humidifier, gas mixing chamber, and gas temperature control heater.

The facility air is supplied by two oil-free scroll compressors with filtering and purification media including refrigerated dryers, a Molecular Sieve 13X pressure swing adsorption system, activated carbon filters, and a final filter/purifier (Donaldson Lithoguard Model P512045) designed for removing acid/base/organic vapors along with a 0.3 μm HEPA level particulate filter. The resulting air composition has a dew point of –70 °C with <1 ppm CO, CO_2, and total hydrocarbons while maintaining a 20.7 to 20.9 % oxygen content.

In order to supply impurity concentrations on the order of 0.2 to 20 ppm in air at the 100 standard L min^{-1} flow rate for long duration experiments, impurity source gas cylinders must be purchased with concentrations exceeding OSHA limits, for example, 8000 ppm SO_2 in air. This is necessary to avoid a high turnover in impurity gas cylinders which are purchased from Matheson Tri-Gas, a mainland vendor. Rather than installing a series of gas cabinets within the facility, impurity bottles were placed outside the laboratory but within the outer warehouse structure which is open to ambient air. Thus, in the unlikely event of a gas leak, the impurity gas would not enter the air conditioning system within the laboratory and come in contact with personnel and would be diluted by the air in the open warehouse. In addition, as corrosive gases are being used in addition to source concentrations exceeding OSHA limits, each impurity gas bottle utilizes a cross purge gas assembly for vacuum and nitrogen pre-purging. All materials are constructed of 316L stainless steel with ultra-high purity regulators.

The main air supply is controlled by an Alicat MCR laminar mass flow controller with a maximum flow of 250 standard L min^{-1}. The three impurity mass flow controllers are Brooks Model 5850s thermal mass flow controllers with a maximum flow rate of 0.25 standard L min^{-1}. A non-lubricated 3-way ball valve (Swagelok SS-43GXS4-1466) is installed prior to the impurity mass flow controllers to allow for purging of each impurity flow controller with neat air in between various experiments. The non-lubrication option is important for material compatibility, for example, nitrogen dioxide is not compatible with standard fluorocarbon lubricants used by Swagelok.

The gas humidification selector 3-way valve follows the clean air mass flow controller. This part is also non-lubricated. The 3-way valve allows the operator to either run the gas through a humidifier (PermaPure Model FC125-240-7) or a bypass loop. On the humidifier side of the 3-way valve, an additional ½ inch ball valve was added after a month or two into service to allow for a portion of the neat air flow to bypass the humidifier. As the humidifier requires a deionized water flow with the outlet dew point controlled by the cooling water inlet temperature on the shell side, the lower relative humidity is set by the facility chiller system (17 °C is the lowest chiller temperature). Dew points lower than 17 °C are achieved by mixing the saturated air flowing out of the humidifier with the air from the bypass stream. For example, at 25 °C, a 50 % relative humidity stream corresponds to a dew point of approximately 14.5 °C. After the humidifier section, the clean air enters the mixing chamber. The mixing chamber is a modified in-line gas heater (Watlow CHJTJT0375KXKT, 375 W heater) which has a diameter of 3 inches diameter and a length of 10 inches. The electro-polished interior surface and geometric features provide a high tortuosity for a uniform gas heating which is leveraged to achieve a sufficient gas mixing. Impurities are injected into the gas stream after the humidifier because they are water soluble. Injection points are located at the inlet of the mixing chamber through 3 machined ports. Check valves and all metal diaphragm valves are added at the injection point as close as possible to the mixing chamber to reduce dead spaces in the impurity injection tubing and facilitate purging. The outlet of the mixing chamber is then directed to a bulkhead fitting in the temperature control chamber, which is attached to the inlet sensor array.

A heat exchange coolant and humidifier deionized water supply rack support the gas supply and conditioning equipment. As already mentioned, the humidifier requires deionized water and temperature control. This is achieved by using a 20 L accumulator with a circulation pump, metering valve, ultrasonic flow meter and deionized resin bed to maintain ultra-clean, Type I deionized water with its flow controlled in the range of 1–2 L min^{-1} through the humidifier. A cartridge heater and tape heater were added to the cooled deionized water inlet to interact with a software controller to adjust the inlet dew point. The system design relies on active cooling of the deionized water. This was achieved by adding a heat exchanger, composed of coiled 316L tubing, inside the reservoir with the facility chiller liquid providing heat removal. The deionized water supply is manually refilled with the reservoir volume selected to allow operation for a 3–4 days period of at the test condition 1 (Table 2.1.5). Two rotameters are installed in the rack to control the facility chiller liquid supply to the deionized water reservoir and the air/water heat exchanger used to control the temperature within the filter housing chamber.

The sensor manifolds and filter are housed in a 2 feet by 1 foot by 1 foot acrylic chamber to provide a constant temperature environment for the filter under test. The chamber temperature is controlled using a 4 inch square air/water heat exchanger blowing air into the chamber and a recirculation duct to minimize fluctuations due to changes in the laboratory air temperature. The

facility chiller liquid flow through the heat exchanger is controlled by a rotameter and a heater on the liquid line controls the chiller liquid inlet temperature based on feedback received from a probe measuring the air temperature inside the chamber. The heat exchanger air flow rate is approximately 120 ft^3 min^{-1}. Several bulkhead fittings are present to allow interconnection with the facility gas chromatographs and gas concentration sensor arrays. The air flow to be delivered to the unit under test enters the chamber through a ½ inch outer diameter bulkhead fitting, and exits through a ¾ inch bulkhead fitting which is routed to the facility exhaust duct. At the inlet of the main gas flow, a 2 inches by 1 inch, 316L stainless steel sensor manifold is positioned (B&R Industries D-375-4), which includes a RTD temperature probe (Omega PR-17-2-100-1/8-6-E), a dew point sensor (Vaisala HMT317), an absolute pressure sensor (Meas. Specialties US381-000005-030PA) and a differential pressure sensor (GE Druck PTX2165-8971) with the low pressure side connected to a port in the filter outlet fitting connector. Compression fittings, either 316 stainless Swagelok or Polyvinylidene fluoride (PVDF) JACO style, can be used to attach the filter housing. Other custom adaptors may be necessary for specific filter housings.

The data acquisition hardware and control system was developed at HiSERF using National Instruments hardware (cDAQ-9174 4-module chassis with modules NI9208, NI9217, NI9263, and NI9239) and a custom Labview software program also developed at HiSERF for data acquisition, recording and control. Three Watlow heater controllers (PM3C1CJ-AAAAAAA) were also employed for heater control.

After the construction of the system and facility integration were completed (Figure 2.1.47), a test was initiated to validate the performance of the system, particularly the ability to control a 100 standard L min^{-1} air flow at 25 °C, 80 % relative humidity at ambient pressure representative of test condition 1 (Table 2.1.5). As the system is designed to control the gas inlet temperature and the gas stream dew point to produce the desired relative humidity, the humidifier controller was set to produce a 21.3 °C dew point with a 25 °C gas inlet temperature. Figure 2.1.48, left presents results of a 24 h stability test. An excellent stability was achieved during the entire 24 h period, with the relative humidity stability less than ±1 % (includes other uncertainties such as temperature probe errors). As the dew point is measured by a sensor, there is a possibility of an interaction with impurities. As a secondary measurement, an RTD temperature probe was placed at the exit of the humidifier, which is assumed to produce saturated gas. Figure 2.1.48, right shows the humidifier exit temperature and the measured dew point are offset by a nearly constant 0.2 °C. Thus, the humidifier exit temperature can also be used directly to establish the mixture's relative humidity or as a secondary validation of the dew point sensor feedback signal. Figure 48, right also depicts the humidifier set point and inlet water temperature over the 24 h period, which validates the software based integral type dew point controller.

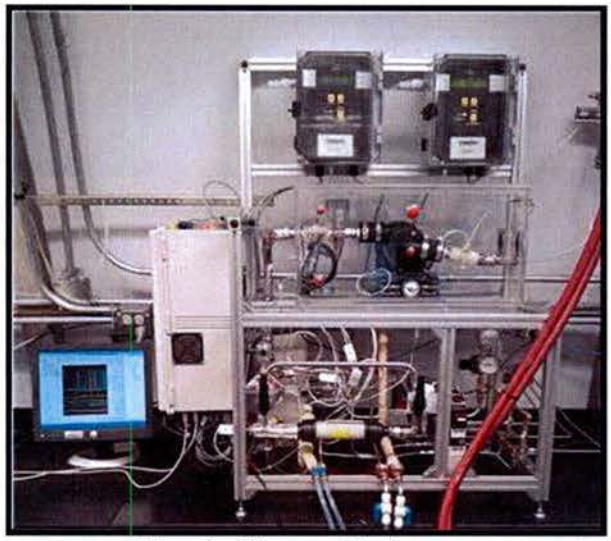

Figure 2.1.47. Main components of the air filter test bed.

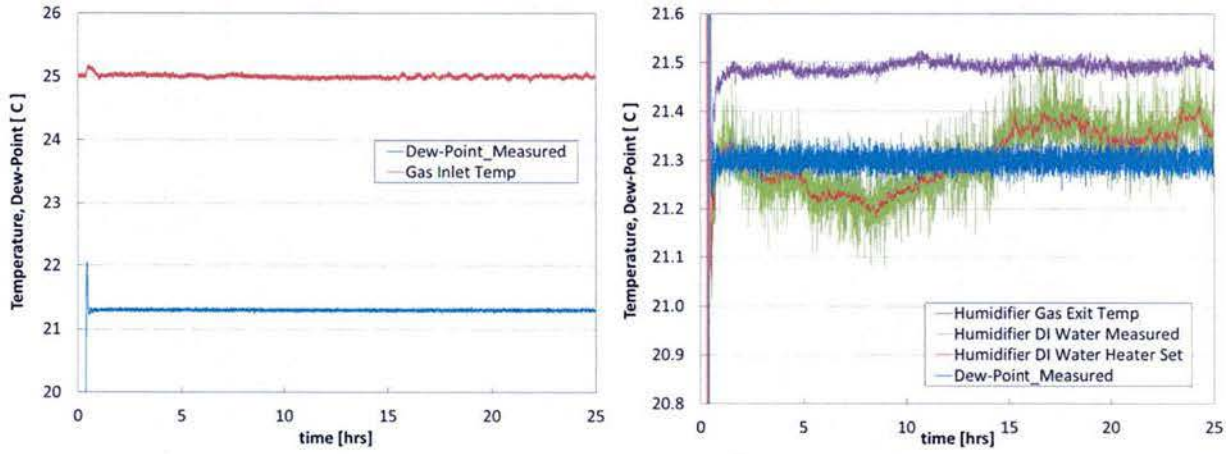

Figure 2.1.48. Stability test (24h) at 100 standard L min^{-1}, 25 °C and 80 % relative humidity. Gas temperature and dew point measured at the inlet sensor array (left). Humidifier exit gas temperature versus measured dew point and humidifier inlet water temperature control (right).

References

1. C. J. Netwall, B. D. Gould, J. A. Rodgers, N. J. Nasello, K. E. Swider-Lyons, *J. Power Sources*, **227** (2013) 137.

2. K. Swider-Lyons, B. D. Gould, *Mater. Sci. Forum*, **879** (2017) 613.

3. B. D. Gould, J. A. Rodgers, M. Schuette, K. Bethune, S. Louis, R. Rocheleau, K. Swider-Lyons, *ECS J. Solid State Sci. Technol.*, **4** (2015) P3063.

4. B. D. Gould, J. A. Rodgers, M. Schuette, K. Bethune, S. Louis, R. Rocheleau, K. Swider-Lyons, *Electrochem. Soc. Trans.*, **64**(3) (2014), 935.

5. B. D. Gould, J. A. Rodgers, M. Schuette, K. Bethune, S. Louis, R. Rocheleau, K. Swider-Lyons, 'Performance of 3D-Printed Fuel Cells and Stacks', in *Meeting Abstracts*, Electrochemical Society volume 2014-2, The Electrochemical Society, Pennington, NJ, 2014, abstract 1103.

6. K. Swider-Lyons, *Naval Research Laboratory Spectra* (winter 2014) P24.

7. http://www.desktopmetal.com.

8. https://www.nrl.navy.mil/lasr/content/ion-tiger-fuel-cell-powered-uav.

9. B. Wozniczka, N. J. Fletcher, P. R. Gibb, United States Patent 5,993,987, November 30, 1999.

10. http://www.permapure.com.

11. https://www.dpoint.ca/fuel-cell-2/.

12. F. N. Büchi, in *Polymer Electrolyte Fuel Cell Durability*, F. N. Büchi, M. Inaba, T. J. Schmidt (Editors), Springer, 2009, p. 431.

13. J. H. Jung, S. H. Kim, S. H. Hur, S. H. Joo, W. M. Choi, J. Kim, *J. Power Sources*, **226** (2013) 320.

14. J. St-Pierre, Y. Zhai, M. S. Angelo, *J. Electrochem. Soc.*, **161** (2014) F280 and *J. Electrochem. Soc.*, **162** (2015) X7.

15. K. Promislow, B. Wetton, *J. Power Sources*, **150** (2005) 129.

16. Y. Zhai, J. St-Pierre, M. Angelo, *Electrochem. Soc. Trans.*, **50** (2) (2012) 635.

17. A. Parthasarathy, S. Srinivasan, A. J. Appleby, C. R. Martin, *J. Electrochem. Soc.*, **139** (1992) 2530.

18. E. L.Thompson, J. Jorne, H. A. Gasteiger, *J. Electrochem. Soc.*, **154** (2007) B783.

19. S. D. Knights, K. M. Colbow, J. St-Pierre, D. P. Wilkinson, *J. Power Sources*, **127** (2004) 127.

20. Y. Zhai, G. Bender, K. Bethune, R. Rocheleau, *J. Power Sources*, **247** (2014) 40.

21. D. E. Ramaker, D. Gatewood, A. Korovina, Y. Garsany, K. E. Swider-Lyons, *J. Phys. Chem. C*, **114** (2010) 11886.

22. J. St-Pierre, N. Jia, R. Rahmani, *J. Electrochem. Soc.*, **155** (2008) B315.

23. S. J. Lee, S. Mukerjee, E. A. Ticianelli, J. McBreen, *Electrochim. Acta*, **44** (1999) 3283.

24. N. M. Marković, P. N. Ross Jr, *Surf. Sci. Rep.*, **45** (2002) 117.

25. J. A. O'Brien, J. T. Hinkley, S. W. Donne, S.-E. Lindquist, *Electrochim. Acta*, **55** (2010) 573.

26. J. Spendelow, J. Marcinkoski, *Fuel Cell System Cost – 2013*, United States Department of Energy Fuel Cell Technology Office, record #14012, June 12, 2014.

27. G. Wu, K. L. More, C. M. Johnston, P. Zelenay, *Science*, **332** (2011) 443.

28. M. Lefèvre, E. Proietti, F. Jaouen, J. P. Dodelet, *Science*, **324** (2009) 71.

29. B. D. Gould, O. A. Baturina, K. E. Swider-Lyons, *J. Power Sources*, **188** (2009) 89.

30. M. Cheng, J. Zhang, P. Wang, T. Zhu, *J. Power Sources*, **196** (2011) 620.

31. M. Busch, A. Kompch, S. Suleiman, C. Notthoff, U. Bergmann, R. Theissmann, B. Atakan, M. Winterer, *Appl. Catal. B*, **166-167** (2015) 211.

32. Q. Wu, G. Mul, R. van de Krol, *Energy Environ. Sci.*, **4** (2011) 2140.

33. A.A. Franco, B. Barthe, L. Rouillon, O. Lemaire, *Electrochem. Soc. Trans.*, **25** (1) (2009) 1595.

34. J. St-Pierre, M. Angelo, K. Bethune, J. Ge, S. Higgins, T. Reshetenko, M. Virji, Y. Zhai, *Electrochem. Soc. Trans.*, **61** (23) (2014) 1-14.

35. T. E. Springer, T. Rockward, T. A. Zawodzinski, S. Gottesfeld, *J. Electrochem. Soc.*, **148** (2001) A11.

36. J. Zhang, R. Datta, *J. Electrochem. Soc.*, **149** (2002) A1423.

37. T. Kadyk, S. Kirsch, R. Hanke-Rauschenbach, K. Sundmacher, *Electrochim. Acta*, **56** (2011) 10593.

38. S. Gottesfeld, J. Pafford, *J. Electrochem. Soc.*, **135** (1988) 2651.

39. J. St-Pierre, J. Ge, Y. Zhai, T. V. Reshetenko, M. Angelo, *Electrochem. Soc. Trans.*, **58** (1) (2013) 519.

40. J. St-Pierre, *J. Power Sources*, **196** (2011) 6274.

41. J. St-Pierre, *Int. J. Hydrogen Energy*, **36** (2011) 5527.

42. J. J. Park, S. Y. Jung, C. G. Park, S. C. Lee, J. N. Kim, J. C. Kim, *Korean J. Chem. Eng.*, **29** (2012) 489.

43. G. Onyestyák, J. Valyon, K. Hernádi, I. Kiricsi, L. V. C. Rees, *Carbon*, **41** (2003) 1241.

44. R. N. Eissmann, M. D. LeVan, *Ind. Eng. Chem. Res.*, **32** (1993) 2752.

45. P. M. K. Reddy, K. Krushnamurty, C. Subrahmanyam, *Microelectron. Eng.*, **126** (2014) 60.

46. F. Wang, J. Li, J. Wang, H. Gao, *Adsorption*, **12** (2006) 205.

47. F. Di Gregorio, F. Parrillo, E. Salzano, F. Cammarota, U. Arena, *Chem. Eng. J.*, **291** (2016) 244.

48. M.-H. Lai, Y.-L. Shih, Y.-H. Chen, S. H. Shu, T. W. Chung, *J. Chem. Eng. Data*, **55** (2010) 723.

49. J. St-Pierre, B. Wetton, Y. Zhai, J. Ge, *J. Electrochem. Soc.*, **161** (2014) E3357.

50. B. D. Gould, G. Bender, K. Bethune, S. Dorn, O. A. Baturina, R. Rocheleau, K. E. Swider-Lyons, *J. Electrochem. Soc.*, **157** (2010) B1569.

51. B. Kakati, A. Unnikrishnan, N. Rajalakshmi, R. Jafri, K. Dhathathreyan, A. Kucernak, *Int. J. Hydrogen Energy*, **41** (2016) 5598.

52. K. Kanazawa, H. Yamamura, M. Nakayama, K. Ogura, *J. Electroanal. Chem.*, **521** (2002) 127.

53. Y. Zhai, G. Bender, S. Dorn, R. Rocheleau, *J. Electrochem. Soc.*, **157** (2010) B20.

54. Y. Zhai, K. Bethune, S. Dorn, G. Bender, R. Rocheleau, *J. Electrochem. Soc.*, **159** (2012) B524.

55. B. K. Kakati, A. R. J. Kucernak, *J. Power Sources*, **252** (2014) 317.

56. A. Kongkanand, M. F. Mathias, *J. Phys. Chem. Lett.*, **7** (2016) 1127.

57. A. A. Kulikovsky, *J. Electrochem. Soc.*, **162** (2015) F217.

58. B. Wu, V. Yufit, M. Marinescu, G. J. Offer, R. F. Martinez-Botas, N. P. Brandon, *J. Power Sources*, **243** (2013) 544.

59. C. T. Love, K. Swider-Lyons, *Electrochem. Solid-State Lett.*, **15** (2012) A53.

Publications and Presentations Resulting from these Efforts

Journal Publications

1. J. Qi, J. Ge, M. A. Uddin, Y. Zhai, U. Pasaogullari, J. St-Pierre, 'Evaluation of Cathode Catalyst Contamination with Ca^{2+} in Proton Exchange Membrane Fuel Cells using a Rotating Ring Disk Electrode', *Electrochim. Acta*, submitted.
2. T. V. Reshetenko, J. St-Pierre, 'Study of Spatial PEMFC Performance under Propylene, Methyl Methacrylate and Isopropanol Exposure', *J. Power Sources*, submitted.
3. Y. Zhai, J. St-Pierre, 'Tolerance and Mitigation Strategies of PEMFCs Subject to Acetylene Contamination', *J. Power Sources.*, submitted.
4. Y. Zhai, J. St-Pierre, 'Impact of Operating Conditions on the Acetylene Contamination in the Cathode of PEM Fuel cells', *J. Power Sources*, submitted.
5. J. St-Pierre, M. B. V. Virji, *J. Appl. Electrochem.*, **46**, 169, (2016)
6. T. Reshetenko, A. Serov, K. Artyushkova, I. Matanovic, S. Stariha, P. Atanassov, *J. Power Sources*, **324,** 556 (2016).
7. T. Reshetenko, A. Kulikovsky, *J. Electrochem. Soc.*, **162,** F627, (2015).
8. B. D. Gould, J. A. Rodgers, M. Schuette, K. Bethune, S. Louis, R. Rocheleau, K. Swider-Lyons, *ECS J. Solid State Sci. Technol.*, **4,** P3063, (2015).
9. C. T. Love, M. B. V. Virji, R. E. Rocheleau, K. E. Swider-Lyons, *J. Power Sources*, **266,** 512-519, (2014).
10. T. V. Reshetenko, K. Bethune, M. A. Rubio, R. Rocheleau, *J. Power Sources*, **269,** 344, (2014).

Conference Proceedings

11. B. D. Gould, J. A. Rodgers, M. Schuette, K. Bethune, S. Louis, R. Rocheleau, K. Swider-Lyons, *Electrochem. Soc. Trans.*, **64** (3), 935-944, (2014).

12. J. St-Pierre, M. B. V. Virji, *Electrochem. Soc. Trans.*, **58** (1), 555-562, (2013).

Conference Presentations

13. T. V. Reshetenko, A. Serov, S. Stariha, I. Matanovic, K. Artyushkova, J. St-Pierre, P. Atanassov, 'Comparative and Comprehensive Studies of Tolerance to Airborne Contaminants of PEMFC with Pt and Non-Pt Cathodes Using Segmented Cell Approach and Spatial EIS', in *Meeting Abstracts*, Electrochemical Society volume 2015-2, The Electrochemical Society, Pennington, NJ, abstract 1527, (2015).
14. B. D. Gould, J. A. Rodgers, M. Schuette, K. Bethune, S. Louis, R. Rocheleau, K. Swider-Lyons, 'Performance of 3D-Printed Fuel Cells and Stacks', in *Meeting Abstracts*, Electrochemical Society volume 2014-2, The Electrochemical Society, Pennington, NJ, abstract 1103, (2014).
15. J. St-Pierre, M. Virji, 'Cell Performance Distribution in a PEMFC Stack during Contamination', in *Meeting Abstracts*, Electrochemical Society volume 2013-2, The Electrochemical Society, Pennington, NJ, abstract 1337, (2013).

2.2 Support for Big Island Fuel Cell Electric Buses

Under this subtask, HNEI supported the conversion of two (2) internal combustion engine powered shuttle buses into Fuel Cell Electric Buses (FCEB) (Figure 2.2.1). A services agreement with the Hawaii Center for Advanced Transportation Technology (HCATT) was arranged to perform Non-Recurring Engineering (NRE) design services and maintenance support services. Hawaii Volcanoes National Park (HAVO) will evaluate the performance of the buses as a component of the HAVO Hydrogen Bus Demonstration Project. Due to high levels of air contamination caused by volcanic gas emissions, the buses were fitted with air filtration systems designed to protect the Proton Exchange Membrane (PEM) fuel cells from severe and irreversible degradation. This report provides detail on the bus conversion and broader evaluation efforts.

The buses will be operated on routes that include potential exposure to elevated levels of Sulfur Dioxide (SO_2) and other contaminants to provide valuable data on the performance of PEM fuel cells in environments that may be similar to those found on the battlefield. The NRE effort addressed mitigation techniques such as commercially available passive and active protective filter systems, and control systems that will shut off the fuel cell power system when an Environmental Sensor System, (developed under subtask 2.1) identifies a contaminant threshold has been reached, thus allowing the bus to "ride-through' the area under battery power. The buses have a battery-only range of approximately 20 miles – sufficient to allow them to "evade" the immediate high contaminant concentration area and either continue the route or return to base.

Figure 2.2.1: Converted Fuel Cell Electric Bus for demonstration at Hawaii Volcanoes National Park.

In addition to the systems development work, the HCATT services contract also provided maintenance support including the supply of vehicle lifts and technical support.

System Description

The HAVO FCEB is based on a Ford F550 Cabin and manufactured by Eldorado National Co. The top level specifications of this bus are provided in Table 2.2.1. HCATT contracted with US Hybrid to convert the F550 shuttle bus into a FCEB incorporating an electric drive system with plug-in battery charging customized to this vehicle configuration. A fuel cell system supplied by two 5075 psi (350 BAR) type III hydrogen tanks powers the electric drive system to extend the battery-only operating range of the vehicle. The total hydrogen capacity is 10 kg.

Two plug-in 14 kWh Lithium-ion (Li-ion) battery packs provide power to a 200 kW electric drive system during acceleration and cruising. The electric motor generates power and charges the battery during deceleration (regeneration). US Hybrid incorporated an electric A/C compressor for the passengers as well as the driver comfort. The bus operating controls are unchanged. With conservative driving practices, the vehicle is projected to have a range in excess of 100 miles.

Table 2.2.1: Specifications

Hybrid Fuel Cell Shuttle Bus Specifications	
Bus Chassis	El Dorado National Co.
Passenger Capacity	19 seated
Hybrid System	US Hybrid Corp.
Fuel Cell	Hydrogenics: HyPM HD30
Energy Storage	Johnson Controls PHEV 14 kWh x 2
Traction Motor	US Hybrid Corp: ED04-200 KW, Induction Motor
Accessories	Electrically Driven
Fuel/Storage	2 DyneTek Compressed Hydrogen @ 350 bar, 5 KgType III tanks

The hydrogen fuel cell system is located in the engine compartment. The hydrogen tanks are under the bus on each side of the shuttle bus chassis frame. The conversion to electric drive required changes to the basic vehicle chassis components. The ICE engine and transmission were removed, along with the fuel tank. Engine-driven accessories have been relocated and modified for electric drive and accessory loads were converted to electric drive. Major components of the electric drive system include the battery pack, motor control unit (MCU), A/C induction

propulsion motor, battery charger, and Fuel Cell.

Three coolant loops were added replacing the original engine coolant loop. One coolant loop circulates water to the fuel cell using two radiators located behind the engine compartment front grill. The second loop circulates water to the MCU and other electronic equipment and converters. A third coolant loop circulates water to the battery packs through a small lateral radiator.

Once the vehicle has been driven and the battery requires recharging, the vehicle is connected to a J1772 charging station supplying 6.6 kW of AC power. An on-board charger manages the battery charging profile as defined by the Johnson Controls battery monitoring system.

All components of the electric drive system are located below the vehicle cabin floor resulting in no change to the cargo space within the vehicle. Road clearance remains unchanged from the original vehicle. The only driver interface changes to the vehicle include the addition of an electronic shift knob and an additional instrument cluster.

At a steady cruising speed, the motor's power is provided by the fuel cell. When more power is needed, for example during sudden acceleration, the battery supplements the fuel cell's output. During deceleration, the motor functions as an electric generator to capture kinetic energy, which is stored in the battery.

The following tasks were completed by US Hybrid under contract to HCATT:

Non-Recurring Engineering:

- Developed the conversion system specification, electrical schematic, and system block diagram;
- Developed a 3-dimensional Computer Aided Design (CAD) integration package to include the layout of the OEM chassis components, fuel cell, hydrogen storage, battery system, and traction drive system;
- Developed the design and integration package for the hydrogen storage, fuel cell, traction power and auxiliary systems:
- Developed a design for the power steering and braking system components to adapt to the OEM power steering system.
- Developed the complete software package for the powertrain, fuel cell interface including motoring, charge control, fault reaction and driver interface.
- Designed the hydrogen safety monitoring system.
- Coordinated the installation of the air conditioning compressor and the commissioning of the air conditioning system with the system installer.

Environmental Sensor Array (ESA) Integration:

- Coordinated with HNEI and the ESA system manufacturer for the development and integration of the Environmental Sensor Array (ESA) system specification and block diagram.
- Developed and delivered the ESA mechanical and electrical system integration packages.
- Coordinated with HNEI and the ESA system manufacturer on the Controller Area Network (CAN) system integration specification.
- Modified vehicle system software to include control, data acquisition, storage, transmission and operator display functions of the ESA system.

- Procured and delivered the data acquisition system capable of wireless data transmission and local storage of 16 GB minimum for HAVO Bus #1 and Bus #2.
- Procured and delivered the ESA system electromechanical mounting and electrical interconnect provisions for HAVO Bus #1 and Bus #2.
- Installed the ESA systems into HAVO Bus #1 and Bus #2.
- Coordinated comprehensive ESA testing with HNEI to include all sensor data storage and transmission functions into HAVO Bus #1 and Bus #2.

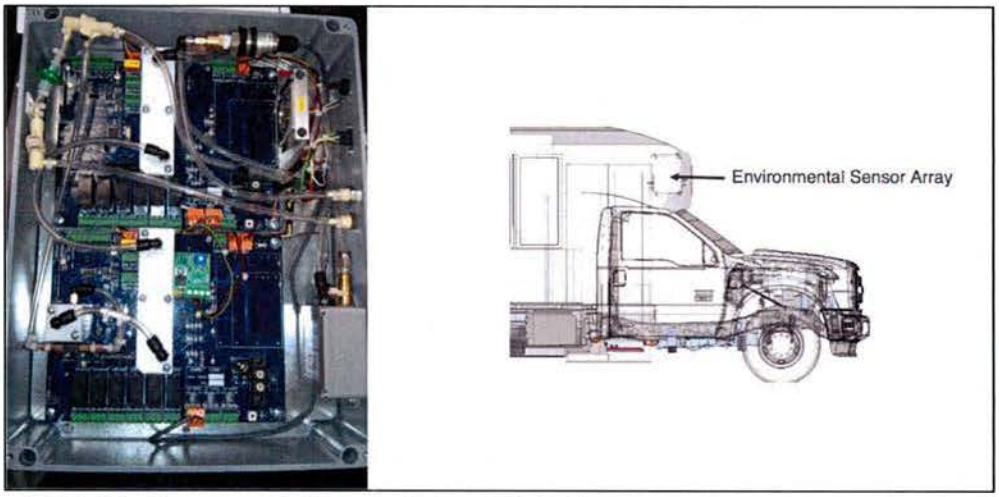

Figure 2.2.2: Environmental Sensor Array (ESA) System and location on the shuttle bus.

Maintenance Services

- Provided maintenance services including the shipment and repair of defective fuel cells, towing of vehicles, post warranty component logistical support, replacement parts and all associated labor and travel costs for personnel.
- Procured a vehicle lift system rated at 72,000 pounds and shipped it to the Hawaii Mass Transit Agency (MTA) maintenance depot with the concurrence of HAVO where heavy maintenance of the HAVO buses will be performed by MTA technicians.

Figure 2.2.3: Vehicle Lifts

Task 3. ALTERNATE FUELS

Alternative fuels, technologies and processes investigated in this effort include Methane Hydrates, Technology for Synthetic Fuels Production, Sustainable Biomass, Low-cost Material for Solar Fuels Production, and Hydrogen Fuel Production.

3.1 Methane Hydrates

This effort focused on methane hydrate stability and related environmental issues; hydrogen fuel storage in binary hydrates; and promoting international research collaborations. Fundamental laboratory studies were performed on hydrate formation and dissociation in porous media and determining the effects of transition metal salts on hydrate behavior. Hydrates that form in relatively fine sands were found to melt at lower temperatures than hydrates that occur in larger void spaces. Most of the transition metal salts tested in the present study inhibited methane hydrate formation at high concentrations, but none to the extent of sodium chloride except for ferric chloride. As a continuation of our investigation of the microbiology of methane and other hydrocarbons in seafloor sediments and the oceanic water column, we conducted an exploratory study to evaluate the potential of employing fluorescence microscopy to identify methanogenic and methanotrophic microorganisms, and also investigated single cell techniques for determination of gene expression in microorganisms that are difficult or impossible to culture in the laboratory, such as the benthic microbes collected from deep ocean hydrate sediments. As part of APRISES11, we completed an experimental study to explore the use of binary gas hydrates as a storage medium for hydrogen fuel for propulsion applications. Results suggested that hydrate H_2 storage capacity was too low to be viable. Finally, to foster international collaborative R&D on methane hydrates, HNEI supported and helped to organize the 8th International Workshop on Methane Hydrate R&D that was held in Sapporo, Japan on 28 May – 1 June 2012.

Methane hydrates are crystalline compounds consisting of polyhedral cavities formed from networks of hydrogen-bonded water molecules, in which methane molecules reside. Methane hydrates in ocean sediments constitute an enormous energy reservoir that is estimated to exceed the energy content of all known coal, oil, and conventional natural gas resources. Located on continental margins throughout the world, methane hydrates offer unique opportunities as an onsite source of fuel for various marine applications and are believed to play a major role in seafloor stability and global climate.

Over the years of APRISES awards, the Methane Hydrates activities comprised four subtasks: Hydrate Energy, Environmental Impacts of Methane Release from Hydrates, Hydrate Engineering Applications, and International Collaborative R&D. The objectives arose from the Methane Hydrate Research and Development Act of 2000 (Public Law 106-193), which included seven technical areas of focus: (1) identification, exploration, assessment, and development of methane hydrate as a source of energy; (2) technology development for efficient and environmentally sound recovery of methane from hydrates; (3) transport and storage of methane produced from methane hydrates; (4) education and training related to methane hydrate resource R&D; (5) assessment and mitigation of environmental impacts of natural and purposeful hydrate degassing; (6) development of technologies to reduce the risks of drilling through methane hydrates; and (7) support of exploratory drilling projects. The objectives of the Methane Hydrates Task of the overarching APRISES initiative reflect most of the priorities of P.L. 106-193, but emphasize those areas of particular relevance to the Office of Naval Research and which are consistent with the overall goals of APRISES over the years. Specifically, the development of hydrates and related sources of seafloor methane as logistical fuels for Naval applications, and

related marine environmental issues, have been the principal areas of interest; exploratory drilling projects and seafloor stability/safety have received limited attention. Work also was performed to explore engineering applications of hydrates such as hydrogen fuel storage. Task objectives were devised to leverage fully hydrate R&D expertise and infrastructure that had been developed at HNEI during previous research programs on CO_2 ocean sequestration and deep oil spills.

During the present reporting period, the goals of the APRISES11 Methane Hydrates Task were:

- Pursue development of methods to recover methane gas from hydrates.
- Investigate environmental impacts of methane hydrates on the marine environment.
- Explore engineering applications of hydrates.
- Promote international collaborative research on methane hydrates.

Each of these subject areas are discussed in more detail below

Hydrate Energy:

A major priority of this subtask was to elucidate the fundamental mechanism of methane hydrate destabilization for the purpose of producing fuel gas and, to a lesser extent, to clear hydrate blockages that can form in natural gas conduits or deep ocean oil wells (such as occurred during the 2010 Deepwater Horizon incident in the Gulf of Mexico). Toward that end, we conducted experimental studies on: (1) the effects of transition metal salts found in seawater on the stability of clathrate hydrates; and (2) phase equilibrium of hydrates in porous media such as seafloor sediment and Arctic permafrost.

The primary accomplishments of this subtask were: (1) completed a study of hydrate formation and dissociation in sand matrices; and (2) completed experiments to investigate the effects of transition metal salts on the behavior of clathrate hydrates. The study of hydrate dissociation in sand constituted the basis of the M.S. thesis in Mechanical Engineering at the University of Hawaii, "Effect of the Properties of Porous Media on Hydrate Stability," of a student who graduated in May 2014. The results of the investigation of transition metal salts were published in the journal *Chemical Engineering Science*, "Inhibiting effects of transition metal salts on methane hydrate stability," by T.Y.Sylva, C.K.Kinoshita, S.M. Masutani (July 2016). The following sections provide summaries and conclusions of the two studies. Complete details are provided in the aforementioned M.S. thesis and journal paper that are available on the HNEI website (http://www.hnei.hawaii.edu/publications/project-reports#APRISES11.).

Methane Hydrates in Porous Media

Calorimetric experiments were performed to test the hypothesis that the pressure-temperature phase boundaries of methane hydrate change when formation and dissociation occur in porous media. Two "standard" sands selected by the national methane hydrate R&D programs in Japan and the U.S. were employed in these experiments. The data suggest that a small shift in the phase boundary of hydrates might occur in porous media. The measured change is of the order of scatter in the experimental data but is consistent. For both sands, and over a range of pressures relevant to deep ocean sediments, the phase boundary for a simple water-methane binary system tends to over-predict hydrate melting temperature.

Lower melting temperatures imply that natural hydrate deposits in seafloor sediment are more vulnerable to purposeful or inadvertent increases in temperature. While this can be advantageous for certain methane recovery strategies, it raises concerns about outgassing and seafloor stability in a warming climate. Additional experiments appear to be warranted to confirm this phenomenon for a broader range of porous media properties and to more definitively quantify the shift in the phase boundary and to understand the underlying mechanism.

Reagent Destabilization of Methane Hydrates

Clathrate hydrates can be induced to dissociate (melt) or prevented from forming by application of thermodynamic inhibitors such as alcohols and salts. These inhibitors shift the equilibrium between the three phases, hydrate (H), liquid water (Lw), and guest molecular vapor (V) to lower temperature or higher pressure (Sloan & Koh, 2008). It has been posited that dissolved inhibitors tie up water molecules needed for hydrate formation via hydrogen bonding, as in the case of alcohols and glycols (Nihous *et al.*, 2009), or via Coulombic forces, as in the case of salt ions (Sloan & Koh, 2008).

Alcohols are frequently employed by the oil industry to avoid hydrate blockages in natural gas pipelines since the potential for undesirable side reactions (such as corrosion) is low relative to salts; however, amounts needed may reach 50 wt% (aq), leading to high costs and disposal problems (Kelland, 1994; Dholabhai *et al.*, 1997). In addition to alcohols and salts, other inhibitors include kinetic inhibitors, like polyvinyl caprolactam (PVCap) or polyvinylpyrrolidone (PVP) and ionic liquids, e.g., dialkylimidazolium halide compounds, which have been studied more recently (Sloan *et al.*, 1996; Xiao & Adidharma, 2009). Kinetic inhibitors are quite effective in delaying the crystallization of gas hydrates (Sloan *et al.*, 1996), whereas ionic liquids exhibit both thermodynamic and kinetic inhibition features (Xiao & Adidharma, 2009).

Studies have been conducted to investigate the roles played by cations and anions in the inhibition of hydrate formation (Lu *et al.*, 2001; Sabil *et al.*, 2010). Lu *et al.* (2001) compared the effects of salts with different cations and anions on hydrate phase equilibria of CO_2, CH_4, and C_3H_8 hydrates. In particular, they compared CH_3CO_2Na versus CH_3CO_2H at different concentrations and found that the stability of CO_2 hydrate was affected by the concentration of $CH_3CO_2^-$ and CH_3CO_2H but not Na^+. In addition, it was observed that there was a larger shift in the equilibrium temperature of methane hydrate with $MgSO_4$ versus $MgCl_2$, but not a very large difference between NaCl versus KCl and $CaCl_2$. They concluded that the anion has a greater influence on hydrate stability than the cation, and posited that difference was due to interactions between liquid water molecules and ions.

In electrolyte solutions, hydrate formation may be hindered by disruption of the ambient water network that is driven by hydrogen bonding. Lu *et al.* (2001) argued that, based on studies performed by Mizuno *et al.* (1997) on hydrogen bonds in aqueous solution of halogenated alcohols, anions exert a greater influence on hydrogen bonding of water molecules than cations and are, therefore, more important in inhibiting hydrate crystallization.

Sabil *et al.* (2010) compared the effects of salts with different cations and anions on hydrate phase equilibria of mixed CO_2/THF hydrates using a Cailletet apparatus. Their observations did not support the assertion by Lu *et al* (2001) that anions are more important than cations in suppressing hydrate formation. They found that the inhibiting effect increased in the following order: $NaF < KBr < NaCl < NaBr < CaCl_2 < MgCl_2$, and concluded that the inhibition of the

hydrate increased with the charge of the cation, and the radius of the anion. They proposed that this trend was the result of the strength of the ion-hydrogen bonds which either disrupts or reinforces the ambient water networks. The authors noted that the electrolyte concentrations that were investigated (0.5 and 1 mol%) were relatively low and that higher concentrations might yield different results.

It is important to understand the mechanism underlying the influence of salts on hydrate stability since methane recovery and transport from marine hydrate or conventional reservoirs can take place in an ocean environment that contains these types of salts. According to Barnes (1954), and more recently, Millero *et al.* (2008), the top five ions present in seawater with the highest molality (moles/kg of solvent) are Cl^-, Na^+, Mg^{2+}, SO_4^{2-}, and Ca^{2+}. Transition metals, such as iron, manganese, copper, cobalt and nickel, are also commonly found in seawater at trace concentrations. The source and biogeochemical processes related to these elements are still not well understood (Aparicio-Gonzalez *et al.* 2012).

Other studies of the effects of metals on methane hydrate formation have been conducted, although these studies focused on the elemental forms of the metal. Fan *et al.* (2012) examined the effect of aluminum foam along with sodium dodecyl sulfate on methane hydrate formation. They concluded that aluminum foam accelerated formation of methane hydrate by promoting hydrate nucleation and enhancing heat transfer. Unlike salts, elemental aluminum does not dissolve in the water phase.

In the present investigation, we conducted experiments to determine the effects of some transition metal salts and other salts on the behavior of clathrate hydrates decomposition using a Differential Scanning Calorimeter (DSC). Specifically, a DSC was employed to determine the onset temperature for methane hydrate decomposition in the presence of ferric chloride hexahydrate, $[FeCl_2(H_2O)_4]Cl{\cdot}2H_2O$ (Lind, 1967), anhydrous ferric chloride, $FeCl_3$, $MnSO_4$, $FeSO_4$, $CuSO_4$, and $AgNO_3$ and to compare the inhibiting properties of these transition metal salts with NaCl and $CaCl_2$, two well-known salt inhibitors. These transition metals salts were chosen because they are soluble in water and each transition metal represents metals with varying charges (+1, +2, +3), which are commonly found in the ocean. We attempted to determine whether the inhibiting properties of these salts on methane hydrates follow the trends observed by Sabil *et al.* (2010).

Decomposition temperature was studied rather than formation temperature since the formation of non-stoichiometric gas hydrates may be influenced by a host of factors such as nucleation, diffusion, and history, which can result in various levels of subcooling when using the DSC (Sloan & Koh, 2008). This complicates identifying a formation temperature. If, however, care is taken to form pure phases of hydrates with fixed compositions, then decomposition processes may be investigated using DSC, and the measured dissociation temperature can be correlated to the temperature of hydrate formation of those fixed compositional phases.

Most of the transition metal salts investigated in the present study inhibited methane hydrate formation at high concentrations but none to the extent of sodium chloride except for ferric chloride. $FeSO_4$ and $CuSO_4$ at concentrations up to 2 mol% were observed to have minimal impact on hydrate stability. At lower concentrations (0.5 mol %), some of the salts ($FeCl_3$, $FeSO_4$, and $MnSO_4$), appeared to promote hydrate formation, i.e., dissociation temperature increased slightly. This effect has not been observed with other chloride salts, but has been observed with other water soluble compounds such as alcohols (Abay & Svartaas, 2010).

The present results appear to confirm Sabil *et al.*'s (2010) assertion that the inhibitor effect increases with increasing charge on the cation. The chloride salt of the higher charged Fe^{3+} exhibits greater inhibition of methane hydrate formation in comparison to Na^{+}; but the iron salt of the larger polyatomic anion, sulfate, exhibits less inhibition than the ferric chloride salt. One possible explanation for the behavior observed in this and previous studies is that, when salts dissolve, the ions interact with the dipoles of the water molecules. The stronger interaction between water with salt ions (versus hydrate guest molecules) interferes with the organization of the water lattice around the clathrate hydrate guest molecule, and thus inhibits hydrate formation. The strength of the salt ion-dipole bond between the metal ion and water molecules may correlate with the degree of inhibition of hydrate formation. The strength of the ion-dipole bond in the primary solvation shell is expected to increase with the electrical charge, z, on the metal ion and decrease as its radius, r, increases (Petrucci *et al.*, 2007). Therefore, higher charged metal ions, such as Ca^{2+} and Fe^{3+} would be expected to have a greater attraction to the water molecules and thus more effectively impede hydrate formation. Furthermore, larger polyatomic anions, such as SO_4^{2-} would have a weaker attraction to the water molecules and would be less effective inhibitors.

The degree of methane hydrate inhibition induced by the salts that were studied (as indicated by the reduction in dissociation temperature at a given pressure), when compared between mixtures with the same mole percentages of the salt, increases in the following order: $FeSO_4 \approx CuSO_4 < MnSO_4 \approx AgNO_3 \approx CaCl_2 < NaCl < FeCl_3$. A smaller decrease in the dissociation temperature was observed with salts that contained the larger sulfate anion when compared to salts that contained the smaller chloride anion. A smaller decrease in the dissociation temperature was observed with salts that contained smaller cations like Fe^{2+} when compared to salts that contained larger cations such as Ag^{+} and Mn^{2+}. Therefore, consideration of the charge and size characteristics of the anion and cation components of the tested salts appears to support the mechanism based on the ion-dipole interaction between the ions and water posited above to explain this behavior. Several other water soluble metal salts are available and additional inhibitor activity on methane hydrates provided by these salts should be investigated to confirm this trend.

Environmental Impacts of Methane Release from Hydrates:

Microbes affect free methane gas levels in, and methane leakage from, the seafloor sediment and arctic permafrost; and mediate methane concentrations in the ocean water column. Understanding the mechanisms of microbial consumption and production of methane and other hydrocarbons is necessary to evaluate environmental impacts of methane fuel production from naturally-occurring accumulations of hydrates, as well as deep ocean oil spills--like the 2010 Deepwater Horizon incident--and marine and terrestrial waste disposal (e.g., near-shore organic runoff and deposition; dumping of dredged material; landfills). Previous attempts to isolate, and culture methanogenic and methanotrophic organisms from marine hydrate sediments have been unsuccessful. In response to this problem, benchtop experiments were performed to investigate novel methods to isolate and identify microorganisms that generate or consume hydrocarbons in marine sediments.

Technical accomplishments of this subtask included: (1) an exploratory study employing fluorescence microscopy to identify microorganisms that can produce or consume methane and other hydrocarbons from communities found in sediments rich in organic matter; and (2)

investigation of single cell techniques for determination of gene expression in microorganisms that are difficult or impossible to culture in the laboratory, such as the benthic microbes collected during previous research cruises in the Gulf of Mexico, off the North Slope of Alaska, and New Zealand with the marine biogeochemistry group of the Naval Research Laboratory.

Identification of Methanogen and Methanotrophs Using Fluorescence Microscopy

In order to develop novel, reliable, and sensitive methods to identify methanotrophic and methanogenic organisms, as well as species that can metabolize other hydrocarbons, we elected to employ sediment samples that were readily accessible and which were expected to contain large populations of these types of organisms. Although organic sediment deposition is typically low in coastal zones around the main Hawaiian islands, brackish waterways on the island of Oahu are known to be rich in terrestrial organic matter. These sediments have a high likelihood of containing large communities of methane-producing *Archaea* and methanotrophic bacteria.

Sediment samples were collected from a canal located in the Ala Moana beach park in the city of Honolulu. This location is connected to the ocean and is impacted by tidal flushing. DNA was extracted from the sediment using a Mobio extraction kit. Genetic sequencing of the collected DNA was performed by the University of Hawaii Advanced Studies in Genomics, Proteomics nd Bioinformatics (ASGPB) facility using next-generation Illumina sequencing and analyzed with Genious software. Short sequence generation was performed using primers having broad group coverage (Klindworth *et al.*, 2013). Community profiles for this analysis showed the presence of both methanotrophic bacteria and methanogenic *Archea* , as seen in Figures 3.1, 3.2, and 3.3. Fluorescent *in situ* Hybridization was performed using a Marker Gene Technologies OliGlo kit and a modified procedure. Oligonucleotide probes specific for *Archaea* (Jupraputtasri *et al.*, 2005) and methanotrophic bacteria (Dedysh *et al.*, 2001) were used for visualization of heat-fxed cells on a glass slides. An Olympus BX-23 having fluorescence capability was used for visualization. Although many attempts were made, cells were not observed utilizing this method.

The sequencing results indicated the presence of the target organisms within the community; however, their relative proportions may have been undetectably small. If this line of investigation is continued, then concentration of the cells or selective enrichment should be pursued to enhance the probability of detection by increasing the target organisms' relative community abundance.

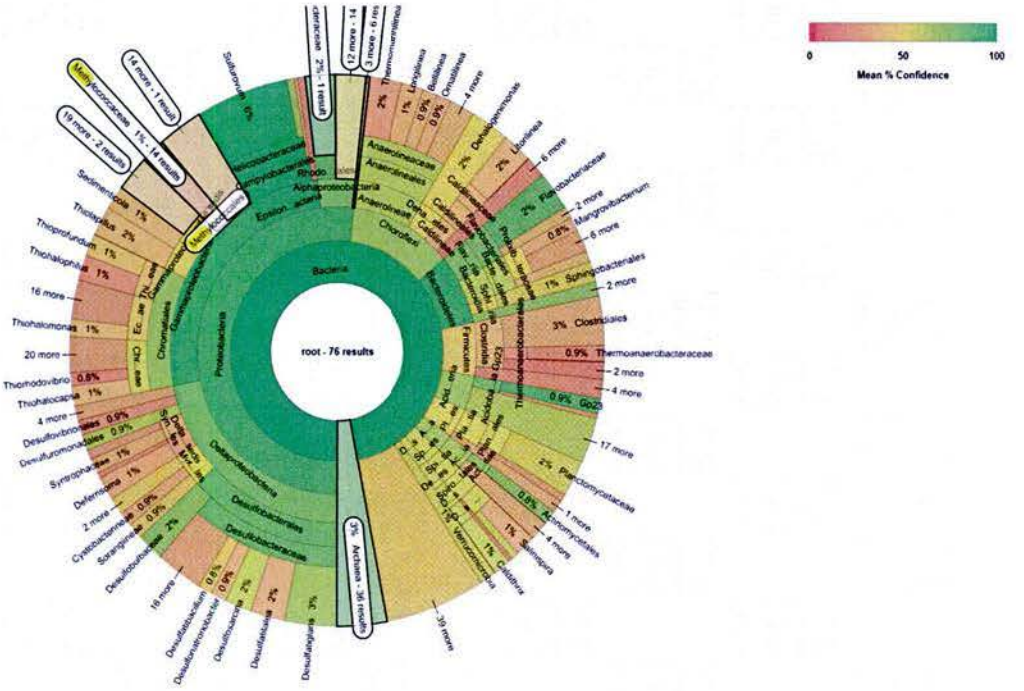

Figure 3.1 Illumina sequence distribution using 16s rDNA primers and analyzed using Geneious software. From 558k paired end reads, 3% of the sequences are representative of *Archaea* and 1% from the order Methylococcales which contain methanotrophic bacteria.

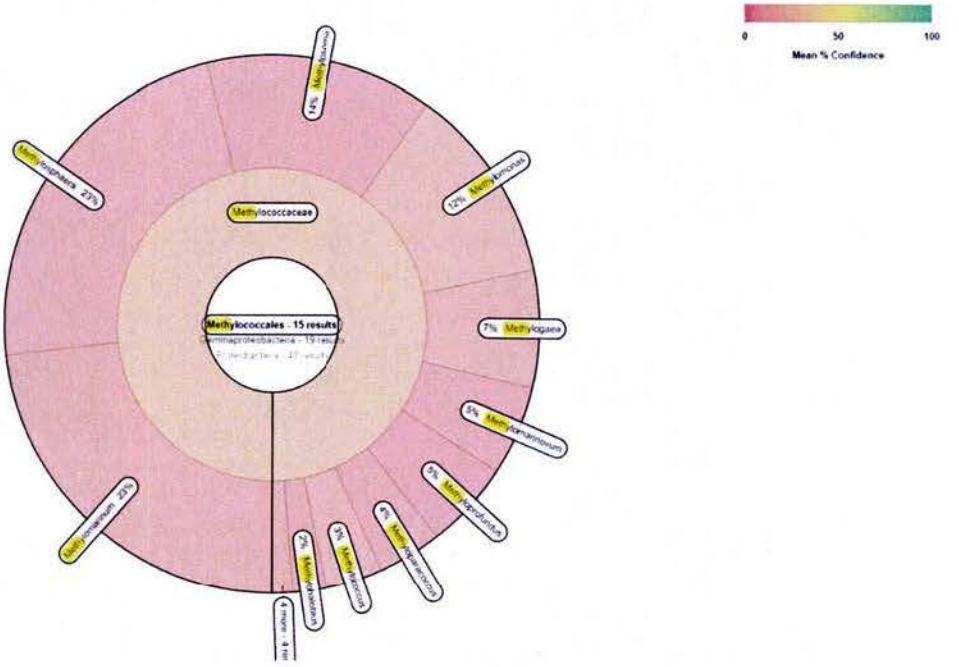

Figure 3.2 Distribution of methanotrophic bacteria from the order Methlylococcales.

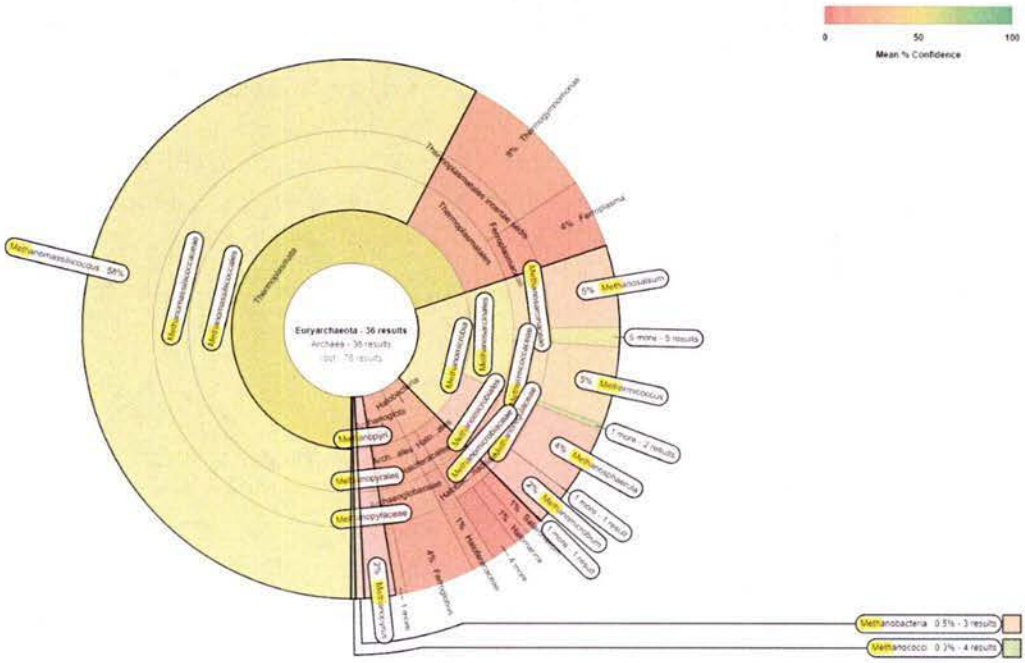

Figure 3.3 Sediment distribution of the Euryarchaeota phylum that includes the genus containing methanogens.

Single Cell Techniques

A Zeiss PALM laser microdissection tweezer/microscope was utilized for the isolation and genome amplification of single cells using a Qiagen Repli-Q kit. Single cell techniques are especially useful for the determination of gene expression in microorganisms that are difficult or impossible to culture in the laboratory. From this analysis, certain metabolic mechanisms can be inferred based upon genome sequences. Multiple cells were successfully isolated with the laser tweezer from porewater samples collected from offshore hydrate sediments during previous oceanographic research cruises. Unfortunately, since we did not have a means to identify specific cell types while we performed the isolation process, the target methanogenic/methanotrophic microorganisms were not obtained according to the results of the 16S PCR and Sanger sequence analysis. This result was not entirely unexpected, given the failure to identify these target microorganisms with fluorescence microscopy from the Ala Moana sediment samples that had significantly higher total abundance of microorganisms than the hydrate sediment porewater.

Hydrate Engineering Applications:

The goal of this subtask was to conduct exploratory studies of the use of gas hydrates for various engineering applications relevant to DOD interests. During the present phase of the APRISES initiative, we completed an investigation to assess the feasibility of employing hydrates as a storage medium for hydrogen fuel for propulsion applications.

The primary accomplishment was the completion of an investigation to assess the feasibility of employing hydrates as a storage medium for hydrogen fuel for propulsion applications. This investigation constituted the basis of the M.S. thesis in Science in Ocean & Resources

Engineering at the University of Hawaii, "Hydrogen Storage Capacity of Tetrahydrofuran and Tetra-N-Butylammonium Bromide Hydrates at Favorable Thermodynamic Conditions" of a student who graduated in May 2014. The results of the investigation were recently published in the open-access journal *Energies,* "Hydrogen storage capacity of Tetrahydrofuran and Tetra-N-Butylammonium Bromide hydrates at favorable thermodynamic conditions", by J.T. Weissman, S.M. Masutani, (August 2017). The following section provides a summary and conclusions of the study. Complete details are provided in the aforementioned M.S. thesis and journal paper that are available on the HNEI website) and online at http://www.mdpi.com/1996-1073/10/8/1225/pdf.

Hydrates for Hydrogen Storage

There is interest in employing hydrates to store H_2 fuel for transportation applications (Schüth, 2005; Shariati *et al.*, 2010). Pure H_2 hydrate requires very high pressures, which makes them impractical under most storage scenarios (Schüth, 2005; Shariati *et al.*, 2010; Hu & Ruckenstein, 2006). In order to reduce the prohibitively high pressure requirement, H_2 mixed gas hydrates have been investigated (Schüth, 2005; Shariati *et al.*, 2010; Hu & Ruckenstein, 2006; Veluswamy *et al.*, 2014; Florusse *et al.*, 2004). Hashimoto *et al.* (2008) demonstrated that adding small amounts of tetra-*n*-butylammonium bromide (TBAB; $C_{16}H_{36}NBr$) to water reduced the hydrogen hydrate formation pressure from 350 MPa to ~1 MPa at 280 K. TBAB is a salt that forms a semi-clathrate hydrate crystal ($C_{16}H_{36}N^{+}\cdot Br^{-}\cdot 38H_2O$) at atmospheric pressure and near room temperature with a unit-cell composed of 16 small (S)-cages and eight large (L)-cages. The bromide anion forms cage structures with water molecules while the cation occupies empty L-cages (Shimada *et al.*, 2005). At moderate pressures and temperatures (e.g., 1 MPa and 280 K), hydrogen molecules can be stabilized and trapped within available empty S-cages (Lee *et al.*, 2005).

Tetrahydrofuran (THF; C_4H_8O) has also been reported to reduce hydrogen hydrate formation pressures (Lee *et al.* 2005; Strobel *et al.*, 2006; Hester *et al.*, 2006). THF is a water miscible organic liquid compound that generates structure II hydrates at 278 K at 0.1 MPa (Hawkins & Davidson, 1966). The ideal composition of a THF hydrate is 17 mol H_2O per mol THF (Gough & Davidson, 1971) or about 5.56 mol % THF. According to Lee *et al.* (2005), THF hydrate can store about 4 wt % H_2 at 12 MPa and 270 K; however, experiments by Ogata *et al.* (2008) suggest that, under similar conditions, stoichiometric THF hydrate can store only 0.26 wt % H_2.

Hydrogen is the most abundant element in the universe and can be produced from natural gas and other hydrocarbons, or by electrolysis of water. H_2 is the fuel of choice for many types of fuel cells under development for propulsion and power generation applications (Dyer, 2002; Cheng *et al.*, 2007). Employing hydrogen hydrate as an energy carrier has attracted interest (Hu & Ruckenstein, 2006; Veluswamy *et al.*, 2014; Florusse *et al.*, 2004), primarily since oxidation of H_2 produces no greenhouse gas carbon emissions (although H_2 produced by reforming or pyrolysis of hydrocarbon fuels does have an associated carbon footprint).

One of the primary advantages of H_2 hydrate storage for propulsion applications is that, unlike metal hydrides, which must undergo a chemical reaction (often having slow kinetics and requiring heating up to 473 K) to release hydrogen fuel (Schlapbach & Züttel, 2001), hydrates undergo a rapid, on-demand, phase transformation (i.e., melting), making them ideal for onboard use in fuel cell vehicles and other specialized applications.

The greatest uncertainty related to onboard hydrogen hydrate storage for propulsion is energy density. The U.S. Department of Energy previously set a 2015 target of 5.5 wt % hydrogen storage in hydrates (U.S. Department of Energy, 2009; Willow & Xanheas, 2012). Theoretical studies performed to date by Willow and Xantheas (2012) suggest that hydrates may be able to store up to 5.3 wt % hydrogen; however, limited experimental data exist to validate these results.

Since binary hydrates, such as those employing THF and TBAB, can store H_2 at considerably lower pressure than pure H_2 hydrate, the overall goal of this study was to explore whether THF or TBAB hydrates represent a viable medium for H_2 storage. Candidate protocols to form binary hydrogen hydrates at relatively low formation pressure and high formations temperatures were identified via a series of exploratory experiments that employed a Differential Scanning Calorimeter (DSC) and Raman spectroscopy system. Since earlier studies of the hydrogen storage capacity of binary H_2 hydrates have produced conflicting results, it was important to quantify this parameter. H_2 wt % could not be accurately determined in the small-scale DSC tests, so these formation protocols were scaled up to produce samples large enough to measure the hydrogen content (gm H_2/gm hydrate) of the selected binary hydrates.

Aqueous solutions of THF and TBAB at concentrations extending from under-saturated to super-saturated with respect to proportions needed to form hydrate were tested at pressures up to 13.8 MPa. Results from a series of calorimetry experiments suggested that THF forms a binary hydrate with H_2; results for TBAB were not definitive. The measured THF+H_2 hydrate stability data agreed well with the results of Hashimoto (2006) and Anderson (2007). To confirm that binary THF + H_2 hydrates had formed in the calorimetry experiments, Raman spectra were taken at different points of the hydrate synthesis process using a separate facility. The spectra exhibited the signature characteristic of H_2 entrapment in the small cages of binary hydrate.

Based on the calorimetry and Raman results, it was decided to focus on solutions of THF and to conduct scale-up experiments to determine H_2 storage capacity. Three solutions of THF (2.78, 5.56, and 8.34 mol %) were tested at pressures up to about 11 MPa over a > 40 h hydrate synthesis process. GC and pressure drop analyses confirmed that H_2 was stored in the solid phase. The measured hydrogen storage capacities, unfortunately, were very low. Weight percentages of H_2 in hydrate were less than 0.1%. Interestingly, the unsaturated solution of THF appeared to store the most hydrogen. The reason for this is not clear, although it might be posited that this is related to the lower occupancy of the hydrate cages.

Although the present results are not encouraging from the perspective of employing THF binary hydrate for H_2 transportation applications, it is clear that promoters are successful in significantly shifting the operational pressures and temperature of hydrogen hydrates to values that are feasible for a host of other H_2 storage applications. In consideration of this, additional work appears to be warranted on other binary hydrate storage options for H_2. Possible topics include:

- Add surfactants to the solutions, since recent studies have shown that surfactants can promote the formation kinetics of binary hydrates.
- Conduct extended scale-up experiments that include multiple formation and dissociation cycles and longer hold times to overcome kinetic limitations.
- Conduct scale-up tests with TBAB solutions.

International Collaborative Research and Development:

To promote international R&D cooperation on methane hydrates in order to accelerate development of this energy resource, HNEI has sponsored and helped to organize a series of workshops on methane hydrates that began in 2001. During the current phase, the objective of this subtask was to provide final logistical and organizational support for the 8th Workshop in Sapporo, Japan.

The 1st International Workshop on Methane Hydrate R&D was organized by HNEI and held in Honolulu, HI in 2001 as part of the previous ONR HEET program. HNEI has served on the organizing committee and as a sponsor for all subsequent workshops. Under APRISES 11, the 8th International Workshop on Methane Hydrate R&D was held in Sapporo, Japan on 28 May-1 June 2012. Planning for this workshop began earlier as a HEET activity. The 8th Workshop was attended by 101 scientists, engineers, and other stakeholder from 16 countries. The workshop comprised three overview lectures (two keynote speeches and the banquet talk), 13 national reports, six breakout sessions and 50 individual research presentations consisting of 15 oral and 35 poster presentations. The Final Workshop Report, which includes abstracts of the presentations and summaries of the national reports and breakout sessions, is available on the HNEI website.

Publications Resulting from these Efforts

Peer Reviewed Journal Papers

Sylva, T.Y., Kinoshita, C.K., and Masutani. S.M. 2016. Inhibiting effects of transition metal salts on methane hydrate stability. *Chem. Eng. Sci.* **155** doi: 10.1016/j.ces.2016.06.028.

Weissman, J.T. and Masutani, S.M. 2017. Hydrogen storage capacity of Tetrahydrofuran and Tetra-N-Butylammonium Bromide hydrates at favorable thermodynamic conditions. *Energies,* **10**(8), 1225, doi: 10.3390/en10081225.

Masters Theses

Weissman, J.T., May 2014. Effect of the Properties of Porous Media on Hydrate Stability," M.S. thesis in Mechanical Engineering at the University of Hawaii.

Miyakita, S., May 2014. Hydrogen Storage Capacity of Tetrahydrofuran and Tetra-N-Butylammonium Bromide Hydrates at Favorable Thermodynamic Condition, M.S. thesis in Master of Science in Ocean & Resources Engineering, at the University of Hawaii.

References

Abay, H.K. and Svartaas, T.M. 2010. Effect of ultralow concentration of methanol on methane hydrate formation. *Energy & Fuels*, 24, 752-757.

Anderson, R., Chapoy, A., and Tohidi, B. 2007. Phase relations and binary clathrate hydrate formation in the system H_2–THF–H_2O. *Langmuir*, 23(6), 3440-3444, doi: 10.1021/la063189m

Aparicio-Gonzalez, A., Duarte, C.M., and Tovar-Sanchez, A. 2012. Trace metals in deep ocean waters: a review. *Journal of Marine Systems*, 100-101, 26-33.

Barnes, H. 1954. Some tables for the ionic composition of sea water. *The Journal of Experimental Biology*, 31, 582-588.

Cheng, X., Shi, Z., Glass, N., Zhang, L., Zhang, J., Song, D., Liu, Z.-S., Wang, H., and Shen, J. 2007. A review of PEM hydrogen fuel cell contamination: Impacts, mechanisms, and mitigation. *J. Power Sources*, 165, 739–756, doi: 10.1016/j.jpowsour.2006.12.012.

Dedysh S.N., Derakshani M., Liesack W., 2001. Detection an enumeration of methanotrophs in acidic sphagnum peat by 16S rRNA fluorescence in situ hybirdication including the use of newly developed oligonucleotide probes with *Methylocella palustris. Appl. Environ. Microbiol.* 67(10), 4850-4857.

Dyer, C.K. 2002. Fuel cells for portable applications. *Fuel Cells Bull.*, 2002, 8–9, doi: 10.1016/S1464-2859(02)80334-0.

Fan, S., L. Yang, X. Lang, Y. Wang, and D. Xie. 2012. Kinetics and thermal analysis of methane hydrate formation in aluminum foam. *Chem. Eng. Sci.* 82. 185-193.

Florusse, L.J., Peters, C.J., Schoonman, J., Hester, K.C., Koh, C.A., Dec, S.F., Marsh, K.N., and Sloan, E.D. 2004. Stable low-pressure hydrogen clusters stored in a binary clathrate. *Science*, 306, 469–471, doi: 10.1126/science.1102076.

Gough, S.R. and Davidson, D.W. 1971. Composition of tetrahydrofuran hydrate and the effect of pressure on the decomposition. *Can. J. Chem.*, 49, 2691–2699, doi: 10.1139/v71-447.

Hashimoto, S., Sugahara, T, Sato, H., and Ohgaki, K. 2007. Thermodynamic stability of H_2+Tetrahydrofuran mixed gas hydrate in nonstoichiometric aqueous solutions. *J. Chem. Eng. Data*, 52(2), 517-520, doi: 10.1021/je060436f.

Hashimoto, S., Sugahara, T., Moritoki, M., Sato, H., and Ohgaki, K. 2008. Thermodynamic stability of H_2+tetra-n-butyl ammonium bromide mixed gas hydrate in nonstoichiometric aqueous solutions. *Chem. Eng. Sci.*, 63, 1092–1097, doi: 10.1016/j.ces.2007.11.001.

Hawkins, R.E. and Davidson, D.W. 1966. Dielectric relaxation in the clathrate hydrate of some cyclic ethers. *J. Phys. Chem.*, 70, 1889–1894, doi: 10.1021/j100878a033.

Hester, K.C., Strobel, T.A., Sloan, E.D., Koh, C.A., Huq, A., and Schultz, A.J. 2006. Molecular hydrogen occupancy in binary THF-H_2 clathrate hydrates by high resolution neutron diffraction. *J. Phys. Chem. B*, 110, 14024–14027, doi: 10.1021/jp063164w.

Hu, Y.H.; and Ruckenstein, E. 2005. Clathrate hydrogen hydrate-a promising material for hydrogen storage. *Angew. Chem. Int. Ed.*, 45, 2011–2013, doi: 10.1002/anie.200504149.

Jupraputtasri W., Boonapatcharoen N., Cheevadhanarak S., Chaiprasert P., Tanicharoen M., Techkarnjanaruk S. 2005. Use of alternative *Archaea* specific probe for methanogen detection. *J. Micobiol. Methods* 61; 95-104.

Kelland, K., 1994. Natural gas hydrates: Energy for the future. *Marine Pollut. Bull.* 29: 307–311.

Klindworth A., Pruesse E., Schweer T., Peplies J., Quast C., Hom M., Glockner O. 2013. Evaluation of general 16s ribosomal RNA gene PCR primers for classical and next generation sequencing based diversity studies. *Nucleic Acids Res.* 41(1), doi:10.1093/nar/gks808.

Lee, H.; Lee, J.W., Kim, D.Y., Park, J., Seo, Y.T., Zeng, H., Moudrakovski, I.L., Ratcliffe, C.I., and Ripmeester, J.A. 2005. Tuning clathrate hydrates for hydrogen storage. *Nature*, 434, 743–746, doi: 10.1038/nature03457.

Lind, M.D., 1967. Crystal structure of ferric chloride hexahydrate. *Journal of Chemical Physics* 47, 990-993.

Lu, H., Matsumoto, R., Tsuji, Y., and Oda, H., 2001. Anion plays a more important role than cation in affecting gas hydrate stability in electrolyte solution? – a recognition from experimental results, *Fluid Phase, Equilibria*, 178, 228-232.

Millero, F.J., Feistel, R., Wright, D.G., and McDougall, T.J. 2008. The Composition of Standard Seawater and the Definition of the Reference-Composition Salinity Scale, *Deep-Sea Research* I, 55, 50-72.

Mizuno, K., Mabuchi, K., Miyagawa, T., Matsuda, Kita, S., Kaida, M., and Shindo, Y., 1997. IR study of hydrogen bonds in halogen-alcohol-water mixtures, *J. Phys. Chem. A*, 101(7), 1366-1369.

Nihous, G.C., C.K. Kinoshita, and S.M. Masutani. 2009. A determination of the activity of water-alcohol mixtures using mobile order thermodynamics. *Chem. Eng. Sci.* 64(11), 2767-2771.

Ogata, K., Hashimoto, S., Sugahara, T., Moritoki, M., Sato, H., and Ohgaki, K. 2008. Storage capacity of hydrogen in tetrahydrofuran hydrate. *Chem. Eng. Sci.*, 63, 5714–5718, doi: 10.1016/j.ces.2008.08.018.

Petrucci, R. H., F.G. Herring, J.D. Madura, and C. Bissonnette. 2007. General Chemistry: Principles and Modern Applications. Upper Saddle River, NJ: Prentice Hall.

Sabil, K.M., Roman, V.R., Witkamp, G-J., Peters, C.J., 2010. Experimental observations on the competing effect of tetrahydrofuran and an electrolyte and the strength of hydrate inhibition among metal halides in mixed CO_2 hydrate equilibria, *J. Chem. Thermodynamics.*, 42, 400-408.

Schlapbach, L. and Züttel, A. 2001. Hydrogen-storage materials for mobile applications. *Nature*, 414, 353–358, doi: 10.1038/35104634.

Schüth, F. 2005. Technology: Hydrogen and hydrates. *Nature*, 434, 712–713, doi: 10.1038/434712a.

Shariati, A., Raeissi, S., and Peters, C.J. Clathrate Hydrates, Chapter 3. In *Handbook of Hydrogen Storage: New Materials for Future Energy Storage*, 1st ed.; Hirscher, M., Ed.; Wiley VCH: Weinheim, Germany, 2010; pp. 63–79, ISBN: 978-3-527-32273-2.

Shimada, W., Shiro, M., Kondo, H., Takeya, S., Oyama, H., Ebinuma, T., and Narita, H. 2005. Tetra-n-butylammonium bromide-water. *ACTA Crystollogr. C*, 61 (Pt 2), o65–o66, doi: 10.1107/S0108270104032743.

Sloan, E.D., Koh, C.A., 2008. Clathrate hydrates of natural gases, 3rd edition, Taylor & Francis, CRC Press, Boca Raton, Fl.

Sloan, E.D., Lederhos, J.P., Long, J.P., Sum, A., Christiansen, R.L., 1996. Effective Kinetic Inhibitors for Natural Gas Hydrate, *Chem. Eng. Sci*, 51, 1221-1229.

Strobel, T.A., Taylor, C.J., Hester, K.C., Dec, S.F., Koh, C.A., Miller, K.T., and Sloan, E.D. 2006. Molecular hydrogen storage in binary THF-H_2 clathrate hydrates. *J. Phys. Chem. B,* 110, 17121–17125, doi: 10.1021/jp062139n.

Sylva, T.Y., Kinoshita, C.K., and Masutani. S.M. 2016. Inhibiting effects of transition metal salts on methane hydrate stability. *Chem. Eng. Sci.* 155 doi: 10.1016/j.ces.2016.06.028.

U.S. Department of Energy, Office of Energy Efficiency and Renewable Energy. 2009. Available online: http://www1.eere.energy.gov/hydrogenandfuelcells/storage/pdfs/targets_onboard_hydro_storage_explanation.pdf.

Veluswamy, H.P., Kumar, R., and Linga, P. 2014. Hydrogen storage in clathrate hydrates: Current state of the art and future directions. *Appl. Energy*, 122, 112–132, doi: 10.1016/j.apenergy.2014.01.063.

Willow, S.Y. and Xanheas, S.S. 2012. Enhancement of hydrogen storage capacity in hydrate lattices. *Chem. Phys. Lett.*, 525–526, 13–18, doi: 10.1016/j.cplett.2011.12.036.

Xiao, C., Adidharma, H., 2009. Dual function inhibitors for methane hydrate. *Chem. Eng. Sci.*, 64, 1522–1527.

3.2 Technology for Synthetic Fuels Production

This subtask comprises fundamental research, testing, development and evaluation for a range of fuels and production techniques. Efforts are detailed below and include: Hydrogen Production for Fuel Cell Applications, Evaluation of Second Generation Biofuels, Novel Solvent Based Extraction of Bio-oils and Protein from Oil-Bearing Biomass, Biochemical Conversion of Synthesis Gas into Liquid Fuels, Bio-contamination of Fuels, Biofuel Corrosion Control, and Waste Management Using the Flash-Carbonization™ Process.

3.2a Hydrogen Production for Fuel Cell Applications

The zero footprint camp (ZFC) concept considers the use of waste materials at force provider or contingency bases as resources to meet the base's energy needs [1]. Efforts to identify the components and their relative contributions in waste streams from different bases have provided the basis for design of waste handling systems that include energy conversion as the central component. Test and evaluation of waste to energy (WTE) systems with potential application at contingency bases has been conducted [2]. Test methods developed for contingency base WTE systems include recipes for synthetic waste streams that can be used to evaluate system performance and enable direct comparison between candidate WTE systems. Characterization of the material components of the synthetic waste stream is a first step in informing design of WTE systems for contingency base applications. Toward that end, this task focused on acquiring samples of components of the synthetic waste streams and analyzing their fundamental properties. In addition to informing design of WTE systems, these analyses can also play a role in the redesign of goods and packaging knowing that they will be used as fuel at the end of their useful life.

APRISES11 is the initial phase of this task, focused on acquiring sample materials and designing a thermogravimetric analysis apparatus capable of accommodating sample masses of ~100 mg. The larger sample mass allows inhomogeneous materials with greater variability in composition (often present in waste streams) to be analyzed. (Further work on hydrogen production for fuel cell applications is planned under APRISES12 and 13.)

Methods

Margolis et al. selected materials that could be used to simulate contingency base waste stream components and formulated recipes for synthetic contingency base waste streams (SCBWS) to allow for standardized testing of WTE systems and comparison of candidate systems operated under similar conditions [2]. Table 3.2.a.1 summarizes the contents of five SCBWS recipes including a standard recipe (R1) and four challenge recipes. The materials in the SCBWS include cardboard, mixed paper (white paper and food trays), food waste (dog food, canola oil, and water), plastics, wood, rubber, textiles, metal, glass, and miscellaneous/other. The challenge recipes include elevated quantities of a single component, either mixed paper (R2), food waste (R3), plastic (R4-R7), or wood (R8).

Table 3.2.a.1. Recommended "standard" and "challenge" recipes by weight percent, wt/% [3]

Recipe	Standard Recipe	Challenge Recipes with primary category			
		Mixed Paper	Food waste	Plastic	Wood
Waste Category	R1	R2	R3	R4, R5, R6, R7	R8
#1 Cardboard	15	19	11	10	10
#2 Mixed paper	10	**38**	7	6	6
#2-1White paper	1	3.8	0.7	0.6	0.6
#2-2Food tray	9	34.2	6.3	5.4	5.4
#3 Food waste	32	18	**51**	21	21
#3-1 Dogfood	6.7	3.8	10.7	4.4	4.4
# 3-2 Canola oil	1.9	1.1	3.1	1.2	1.2
# 3-3 Water	23.4	13.1	37.2	15.4	15.4
#4 Plastic (total)[1]	15	8	11	**44**	10
#5 Wood	14	8	10	9	**43**
#6 Rubber	1	1	1	1	1
#7 Textile	3	2	2	2	2
#8 Metals	6	3	4	4	4
#9 Glass	1	1	1	1	1
#10 Miscellaneous Waste/Other	3	2	2	2	2
Total	100	100	100	100	100
Non-combustible portion[2]	10	6	7	7	7

1. Including 7 types of plastic materials. See details in Table 3.2.a.2.
2. Including Metals, Glass, and Miscellaneous waste/other.

Four plastic challenge recipes are included based on elevated contents of total plastics (44%) and in particular plastic components as well. Details of the types of plastics included in each recipe are provided in Table 3.2.a.2. Recipe R4 has an elevated (44%) content of mixed plastics; R5 has elevated content of polyethylene terephthalate (PET) typically present as water bottles; R6 has a high content of polyvinyl chloride (C_2H_3Cl) and the therefore chlorine; and R7 has a high content of polystyrene and therefore elevated concentrations of aromatic ring molecules.

Table 3.2.a.3 details the materials chosen to standardize the recipes used for SCBWS [2]. Each was procured in sufficient quantities to allow all tests to be conducted on a single, consistent, lot of material.

Samples listed in Table 3.2.a.3 were subjected to ultimate analysis using a LECO CHN628 analyzer for element C, H, and N, and high heating value (HHV) using a Parr 6200 Calorimeter, with the exception of samples #3-2 canola oil and #4-3 PVC, where literature data were cited [3,4].

Table 3.2.a.2. Contents (wt%) of plastic materials in the recipes, wt/% (Ref. 3)

Plastic Type [1]	Standard recipe	Challenge Recipes						
		Cardboard /Paper	Food	Total plastic	#1 PET[2]	#3 PVC [2]	#6 PS [2]	Wood
Recipe #	R1	R2	R3	R4	R5	R6	R7	R8
#4 Plastic (total)	15	8	11	44	44	44	44	10
#4-1 PET	6	3.2	4.4	17.7	27.8	12.9	11.1	4
#4-2 HDPE	2.7	1.4	2.0	7.8	4.8	5.7	4.9	1.8
#4-3 PVC	0.9	0.5	0.7	2.6	1.6	13.7	1.6	0.6
#4-4 LDPE	2.7	1.4	2.0	7.8	4.8	5.7	4.9	1.8
#4-5 PP	0.3	0.2	0.2	0.8	0.5	0.6	0.5	0.2
#4-6 PS	1.8	1.0	1.3	5.4	3.3	4	19.6	1.2
#4-7 Other	0.6	0.3	0.4	1.6	1	1.2	1	0.4

1. PET = polyethylene terephthalate, HDPE = high density polyethylene, PVC = polyvinyl chloride, LDPE = low density polyethylene, PP = polypropylene, PS = polystyrene, Other = Other plastics that may include polycarbonate, acrylic, nylon, bioplastics, composites, etc.
2. Table entries in bold represent the plastic type that presents a challenge: PET because of its relatively high amount due to surges in water bottle usage; PVC because of the presence of chlorine, and PS because of the aromatic rings in its molecular structure.

Table 3.2.a.3. Simulated synthetic contingency base waste streams (SCBWS) components used in experiments

Waste category	Id #	Represented Material
Cardboard	#1	300Uline 11x17", 1/8" inch thick, corrugated pads model no. S3585
	#2-1	Costco Copy Paper, Letter, 20lb, 92-Bright
	#2-2	Chinet® Beige 5-Compartment Molded Fiber Cafeteria Tray - 8.5" x 10.5"
	#3-1	Gravy Train® Beef Dry Dog Food
	#3-2	Crisco Pure Canola Oil, 128 Ounce
	#3-3	Water
	#4-1 PET	12 oz. Vinegar bottle by Aloha Bottling Co. (no lids)
	#4-2 HDPE	128 oz. 1- Gallon Bottle Clear by Aloha Bottling Co. (no lids)
	#4-3 PVC	1-1/2 in. x 10 ft. PVC Sch. 40 DWV Plain End Pipe
	#4-4 LDPE	Fortune Plastics DuraRoll LDPE 30 Gallon Waste Can Liner, Star Seal, Clear, 0.19 Mil, 36" x 30"
	#4-5 PP	Choice-Pac 3D-1429T Polypropylene Bowl, White, Medium, 24-Ounce
	#4-6-2 PS	Verbatim 700 MB 52x 80 Minute Branded Recordable Disc CD-R - 100-Disc Spindle, FFP 97458
	#4-6-2 PS	White Heavy Weight PolySty Plastic Fork
	#4-7 other	Dart Container 95HT3 Carryout Food Container, Foam Hinged 3-Compartment, 9-1/2 x 9-1/4 x 3
Wood	#5	2 in. x 4 in. x 96 in. Prime Kiln Dried Heat-Treated Untreated SPF Stud
Rubber	#6	International Mulch #rm16bk-mw 16lb Black Rubberific Mulch
Textile	#7	#7: All Rags Cotton blend t-shirt material, light to medium weight, no color

A thermogravimetric analyzer (TGA) was designed and assembled to characterize the reactivity of the components in the SCBWS and mixtures prescribed in Tables 3.2.a.1 and 3.2.a.2. Commercially available TGAs accommodate sample masses on the order of 1 to 10 mg and this was deemed to be too small to evaluate the multi-component, inhomogeneous waste streams. A schematic of the TGA system capable of accommodating sample masses of 200 mg is shown in Figure 3.2.a.1. The system employs a platinum, 80 mesh, sample basket with a capacity of ~0.5 ml, suspended from a precision balance (Mettler Toledo, Model AG 204) in a vertically-oriented, one inch diameter, quartz tube. A tube furnace (Barnstead Thermolyne) is used to control the heating rate and temperature of the sample and the reactive environment in the tube can be selected from metered flows of air, nitrogen, and/or steam. The latter is fed to the process using a peristaltic pump (Masterflex L/S). The sample mass is monitored by the balance and the temperature near the sample is determined by thermocouples. Signals from both are output through data acquisition systems and recorded. Products of the sample decomposition are swept from the quartz tube volume by the reactant gas streams and pass through a condenser and a sample pump before exhausting. The sampling pump is used to adjust the outlet flow and balance it with the incoming reactant flows.

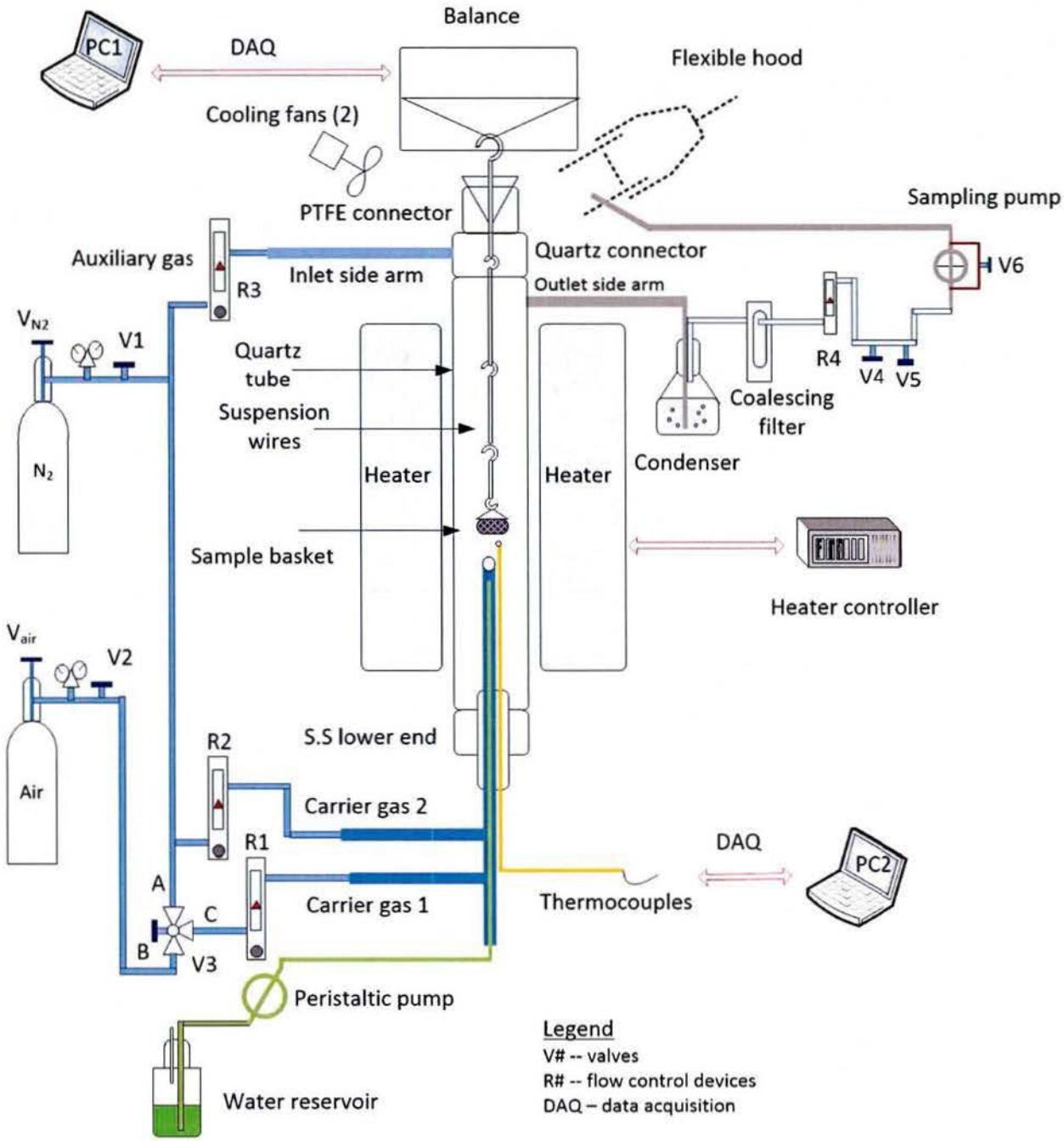

Figure 3.2.a.1. Thermogravimetric analyzer system used to conduct proximate analysis and reactivity measurements on SCBWS components.

Results

Following design and fabrication of the TGA system, initial tests were conducted to evaluate system performance. Figure 3.2.a.2 presents results from proximate analysis under a nitrogen environment of #5 wood material included in Table 3.2.a.3. After an initial lag period the temperature of the sample is increased at a rate of ~20°C/min until it reaches a final temperature of ~600°C. An initial sample mass loss of 11.9% corresponds to sample drying, observed at temperatures approaching 120°C. Sample mass stabilizes until temperatures approach ~200°C beyond which devolatilization is initiated. With nitrogen continuing to flow to the TGA, rapid mass loss is observed as temperature increases to ~350°C. A period of slower mass loss continues as temperature achieves its final set point of 600°C. Total volatile matter measured under the two mass loss rates totals 77.2%, dry basis. The gas flowing to the sample is then changed from nitrogen to air while the temperature is maintained at 600°C. Mass loss observed during the ensuing period is attributed to fixed carbon oxidation and accounts for 22.5%. The residual material, ash, accounts for 0.3% of the dry initial sample mass.

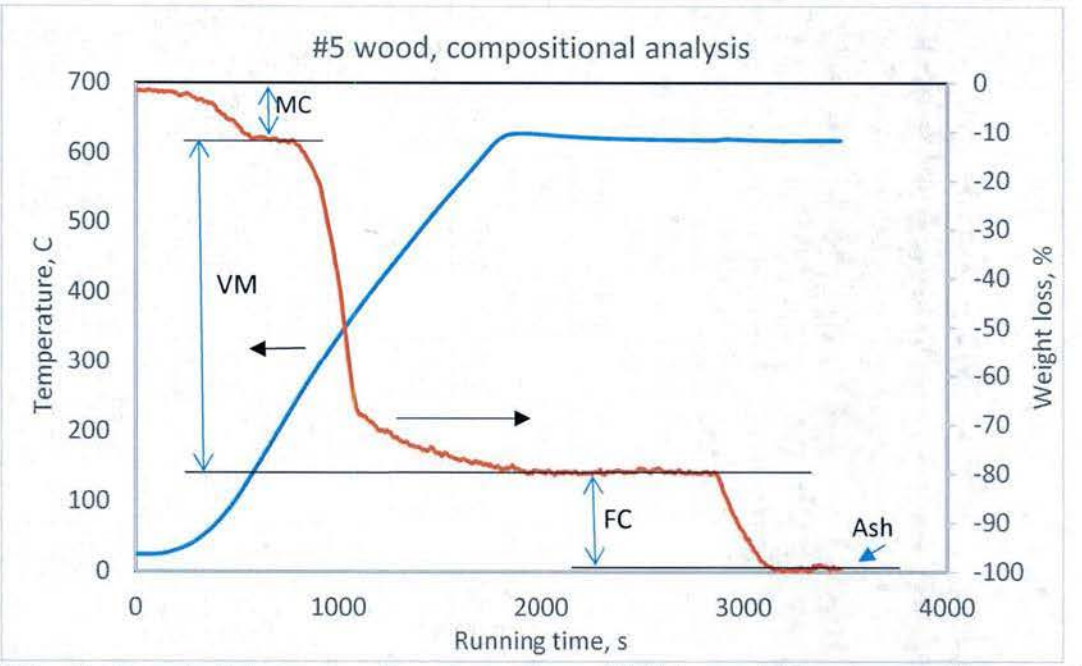

Figure 3.2.a.2. A typical thermogravimetric analyzer (TGA) graph showing proximate analysis for a wood sample: MC (moisture content), VM (volatile matter), FC (fixed carbon), and ash. Temperature (blue), weight loss (orange).

Figure 3.2.a.3 provides initial steam reactivity results from tests of #5 wood material (Table 3) at three reaction temperatures. The figure also includes a fourth thermogram of #5 wood under a nitrogen environment at 825°C. Little difference (~2% absolute) is evident between the steam and nitrogen curves at 825°C due to the relatively low kinetics of the reaction between steam and carbon at that temperature. Both attain ~80% volatile loss. Both sample mass curves under nitrogen and steam at 825°C include final periods (after 3600 sec) under an air environment characterized by steep mass reduction due to carbon oxidation. Steam reactions with the solid material at 875°C and 925°C occur at higher rates compared to the 825°C curve as evidenced by the steeper slopes of mass loss after the initial devolatilization period is concluded at ~500 sec.

The 925°C curve exhibits the higher steam-carbon reaction rate although both curves approach a common final residual mass value after 3500 sec.

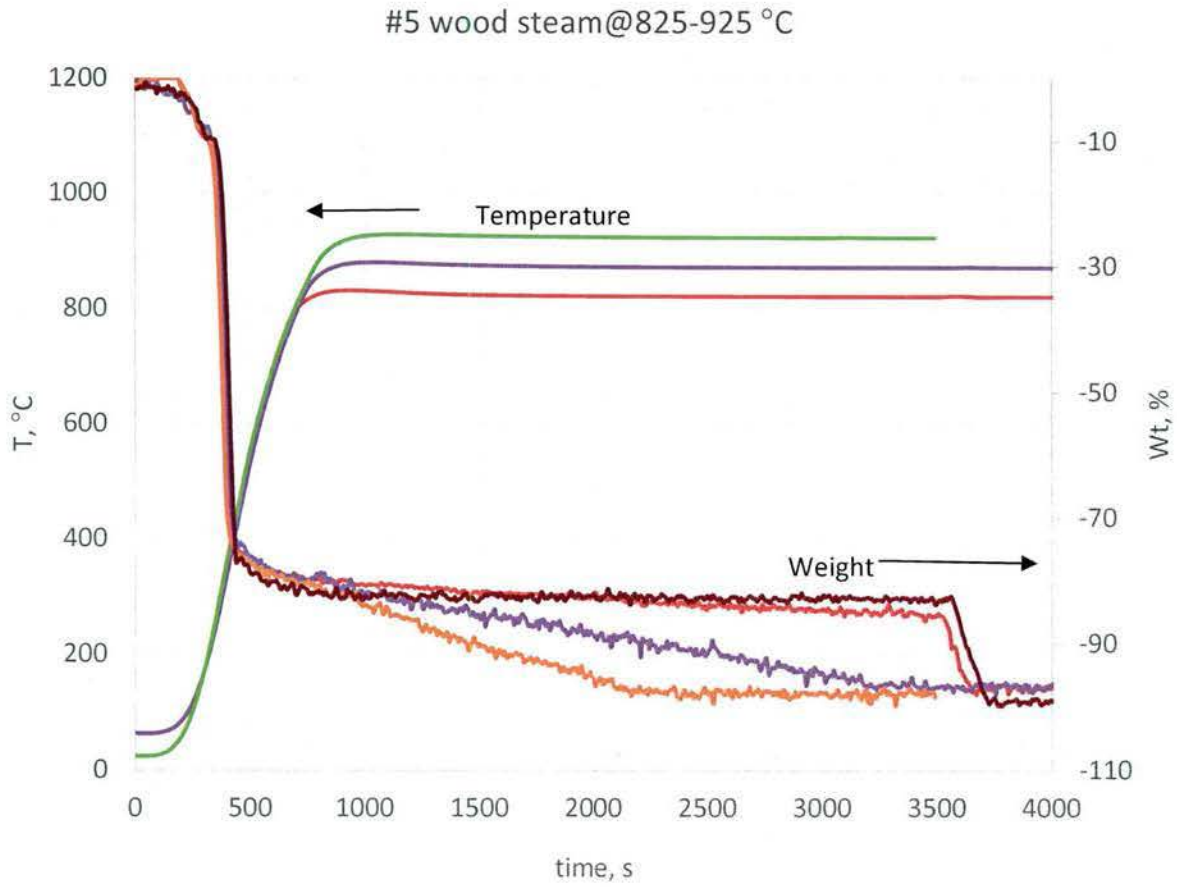

Figure 3.2.a.3. Typical TGA results showing reactivity of #5 wood sample in steam at temperatures of 825°C (orange), 875°C (yellow), and 925°C (green). Mass loss of the same sample under nitrogen (brown) at 825°C is included for reference.

Results of the ultimate analysis and calorimeter measurements of the SCBWS component materials are presented in Table 3.2.a.4. The ultimate analysis indicates that cardboard, paper, dogfood, wood, and textiles exhibit C (carbon), H (hydrogen), and N (nitrogen) values typical of biomass materials. C contents range from 38 to 52% (dry basis), H contents range from 5 to 7% (dry basis), and N contents range from 0.1 to 3.5%. Due to its high protein content, the dog food sample contains 3.5% N (dry basis), higher than any other material tested. The undetermined fraction from the ultimate analysis (i.e. 100%-Σ(%C+%H+%N+%ash)) is often assumed to be oxygen. Although the ash content is not presented, the data indicate that low carbon content will likely be associated with high oxygen content and, as a result, low energy content. Energy content of the materials range from 12.5 to 18.3 MJ/kg. White paper (C content 38.9%) is at the low end and excluding it narrows the range to 16.1 to 18.3 MJ/kg. Canola oil, a biomass component not included in the discussion thus far, has a carbon content of 80.2% and an energy content of 40.2 MJ/kg and these data supports the carbon/heating value correlation.

Ultimate analysis of the plastic components of the SCBWS determined carbon contents ranging from 37.8 to 91% C, 4.2 to 14% H, and 0.2 to 0.5% N. Polyvinyl chloride (C_2H_3Cl) represents

the lower end of this range and different forms of polystyrene had the highest carbon content. Polypropylene (C_3H_6), low density polyethylene (LDPE), and high density polyethylene (HDPE) exhibited high hydrogen content in keeping with their chemical structure, $(C_2H_2)_n$. Energy content of plastics in the SCBWS ranged from 21.2 to 45.8 MJ/kg with PVC and polypropylene representing the lower and upper ends of the range, respectively.

Rubber was the single SCBWS component that was not categorized as biomass or plastics. Rubber has carbon, hydrogen, and nitrogen contents of 79.3, 7.4, and 0.4%, respectively, and a higher heating value of 38.4 MJ/kg.

Table 3.2.a.4. Results of ultimate analysis and energy content of individual SCBWS components

	Ultimate analysis, %			**High heating value, MJ/kg**
	C d	**H d**	**N d**	**HHV d**
#1 Cardboard	46.3	6.4	0.2	16.8
#2 Mixed paper				
# 2-1 White paper	38.9	5.7	0.1	12.5
# 2-2 Food tray	44.0	6.6	0.2	16.3
#3 Food waste				
# 3-1 Dog food	47.6	7.0	3.5	17.6
# 3-2 Canola oil*	80.2	10.9	0.1	40.2
#4 Plastics				
#4-1 PET	61.3	4.2	0.1	23.1
#4-2 HDPE	84.7	13.8	0.1	46.4
#4-3 PVC	37.8	4.9	0.1	21.2**
#4-4 LDPE	73.5	12.2	0.2	37.6
#4-5 PP	83.7	13.9	0.1	45.8
#4-6-1 PS	74.0	5.5	0.1	30.8
#4-6-2 PS	90.0	7.7	0.1	41.2
#4-7 Other	91.0	7.4	0.5	40.1
#5 Wood	51.1	6.9	0.4	18.3
#6 Rubber	79.3	7.4	0.4	38.4
#7 Textile	43.9	6.8	0.2	16.1

Abbreviations: C: carbon, H, hydrogen, N, nitrogen, d: dry basis.
*: Data from [3]
**: Data from [4]

Conclusions

1. Components of contingency base waste streams were reviewed.
2. A recipe for a synthetic contingency base waste stream was identified and recipe components were acquired.
3. Components of the SCBWS were analyzed for carbon, hydrogen, and nitrogen content and energy content/higher heating value.
4. A thermogravimetric analyzer with a sample capacity of 200 mg and the capability to explore sample reactivity under inert, air, and steam environment was designed and fabricated and preliminary tests were conducted on wood.

References

[1] Ruppert, W.H., T.A. Bush, D.P. Verdonik, J.A. Geiman, and M.A. Harrison. 2004. Force provider solid waste characterization study. Prepared for the Development, and Engineering Command. Natick Soldier Center. Technical Report NATICK/TR-04/017.

[2] Margolin, J.A., P.A. Marrone, M.A. Randel, W.R. Allmon, R.B. McLean, and P.M. Bozoian. Test standards for contingency base waste-to-energy technologies. 2015. Prepared for the U.S. Army Research Lab. ARL-TR-7394

[3] Bhimani, S. M. Experimental characterization of canola oil emulsion combustion in a modified furnace. Master of Science, Texas A&M University, 2011, May.

[4] Zevenhoven, R.; Karlsson, M.; Hupa, M.; Frankenhaeuser, M., Combustion and gasification properties of plastics particles. *Journal of the Air & Waste Management Association* 1997, *47* (8), 861-870.

3.2b Evaluation of Second Generation Biofuels

In this study, the physical properties and chemical composition of hydroprocessed renewable diesel derived from algae (HRD-76) were measured. Analysis of HRD-76 showed that the main components are C_{15}–C_{18} n-alkanes and branched monomethyl hexadecanes and heptadecanes. Approximately 50% of HRD-76 is n- and iso-C_{17}. Long-term (ASTM D4625) and accelerated (ASTM D5304) tests were conducted to investigate the storage stability of HRD-76, F-76, and their blends and the effects of long-term storage on the fuel properties. In addition, the ASTM D2274 method was used to test the oxidation stabilities of the neat and blended fuels. HRD-76 has better storage and oxidation stabilities than F-76, and the post-test changes in the fuel properties are influenced by the F-76 fraction in the fuel blend. Extended ASTM D2274 tests were also conducted to investigate the influence of long-term oxidation on the physicochemical properties of the fuel.

Complete details of this study were presented in the publication:

> Fu, J. and S.Q. Turn. 2014. Characteristics and stability of neat and blended hydroprocessed renewable diesel. *Energy & Fuels*. 28. pp 3899-3907.

Complete details can be found at:
dx.doi.org/10.1021/ef500544p

3.2c Novel Solvent Based Extraction of Bio-oils and Protein from Oil-Bearing Biomass

The goal of was to characterize the capacity of the co-solvent to both extract bio-oil and simultaneously "pretreat" the biomass such that it can be readily hydrolyzed (to simple sugars) using appropriate mixtures of hydrolytic enzymes. Successful outcomes will help to develop a process methodology by which a variety of product streams can be recovered from oil-bearing biomass.

Research was conducted on the applicability of ionic liquid-methanol co-solvent system to both extract bio-oil and simultaneously pretreat the carbohydrate fraction of *jatropha* and *safflower* biomass for enzymatic hydrolysis to fermentable sugars. In this study, an ionic liquid – methanol co-solvent was shown for the first time to effectively extract bio-oil and recover

fermentable sugars from oil-seed biomass. Specifically, a combined carbohydrate and bio-oil co-recovery of 61.2 and 38.4 wt % of the *safflower* and *jatropha* whole seeds, demonstrating a new pathway for processing increased products from oil-seed biomass.
For more detail, see the publications available on the HNEI website and listed below.

Publications Resulting from these Efforts

Cooney, M. J., and K. Benjamin. *Ionic Liquids in Lipid Extraction and Recovery.* In (Zu, X., Guo, Z., and L.-Z. Cheon, Editors) *Ionic Liquids in Lipid Processing and Analysis: Opportunities and Challenges.* Elsevier AOCS Press, New York. ISBN: 978-1-63067-047-4, (2016).

Severa, G., G. Kumar, and M. J. Cooney. Co-Recovery of lipids and fermentable sugars from *Rhodosporidium toruloides* using ionic liquid co-solvents: Application of recycle in batch fermentation. Journal of Biotechnology Progress. 30(5):1239-1242, (2014).

Severa, G., Kumar G., and Michael J. Cooney. *Co-recovery of bio-oil and fermentable sugars from oil-bearing biomass.* International Journal of Chemical Engineering. Article ID 617274 http://dx.doi.org/10.1155/2013/617274, (2013).

Cooney, M. J. Co-Recovery of Lipids, Fermentable Sugars, and Protein from Bio-Oil Bearing Biomass Using Ionic Liquid co-Solvents. 2015 meeting of the AICHE, Salt Lake City Utah, November 8-13th, (2015).

3.2d Biochemical Conversion of Synthesis Gas into Liquid Fuels

The objective of this task is to make drop-in transportation liquid fuel from synthesis gas. The new technology consists of two steps: microbial synthesis of polyester from the gas, and polyester reforming into liquid fuels. In this work, the research was focused on increasing: (1) the conversion efficiency of gas to polyester, and (2) the energy content of liquid fuel. Two corresponding activities were performed and the results are reported as follows.
Bioreactor Innovation

In a conventional bioreactor, gas is introduced into an aqueous solution at a high gassing rate and dispersed as small bubbles. Because of very short retention time of the gas bubbles in the solution, most gas leaves the bioreactor without use, resulting in a low gas conversion efficiency. This problem was solved in this work by developing a novel bioreactor in which liquid was dispersed in gas phase as shown in Figure 3.2.d.1. The aqueous solution containing microbial cells were sprayed though nozzle(s) as tiny liquid droplets into the overhead gas phase and recycled via an external loop. The gas retention time in the bioreactor could be controlled by adjusting the gas feeding rate. More importantly, a high gas mass transfer rate could be achieved even at a very low gassing rate (10-20% of the normal gassing rate in a conventional bioreactor).

Oxygen is a typical gas of low solubility in water and was used to measure the mass transfer rate in a process of physical absorption. The superficial air velocity was set at 0.00028 m s^{-1}, or 0.2 vvm (gas volume per liquid volume per min) in terms of liquid gassing rate. Table 3.2.d.1 gives the value of oxygen mass transfer coefficient (k_La) under different operation conditions. When one nozzle was used, the k_La value (0.03-0.04 s^{-1}) was in the range of conventional aerated bioreactors (see the result in A1.3). It was almost doubled (0.064 s^{-1}), however, when multiple nozzles were used for a larger open area. Interestingly, this increase in k_La was observed with decrease of the pressure drop across the nozzle(s) and decrease of the velocity of liquid droplets, a phenomenon in contrast to our expectations. According to the mechanical energy balance around the nozzle(s), a high pressure drop would generate a high velocity and flow turbulence of liquid in the gas phase. The high turbulence would also generate smaller droplets to give a high gas-liquid contact area. All these factors could intensify the gas mass transfer, but in experiment, a low value of k_La was observed. Our explanation is that the conventional analysis may be true for individual liquid droplets, but not applicable to the liquid pool or whole bioreactor. It was observed that the liquid circulation rate through the pump declined with a smaller nozzle open area, which reduced the frequency of liquid exposure to the gas phase. At a high circulation rate (4.7 L min^{-1}), the pressure drop and liquid velocity were the lowest, but the retention time in the liquid pool (1.5L) was the shortest (0.32 min), i.e. the frequency of liquid-gas contact was the highest. Therefore, to intensify the gas mass transfer in spray bioreactors, a high liquid circulation rate associated with a low pressure drop is preferred rather than a low circulation rate with a high pressure drop. This may also save a significant amount of energy because of a low power dissipation rate as shown in Table 3.2.d.1. The energy saving will be further analyzed in A1.3.

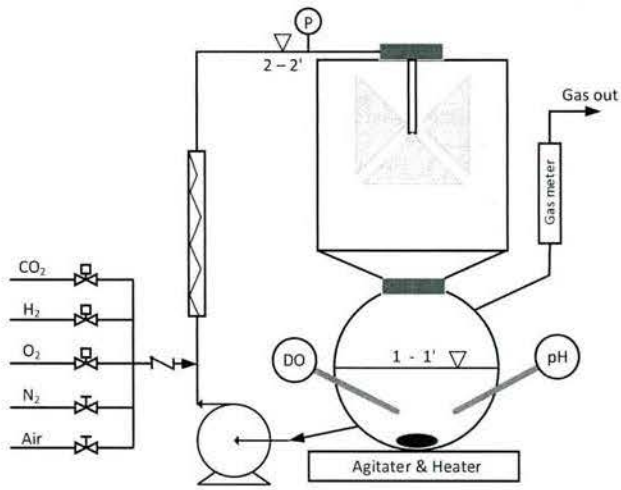

Figure 3.2.d.1. Schematic structure of a spray bioreactor. Gas composition and flow rate can be controlled by adjusting the individual gases. The number of nozzles and locations could be adjusted according to the open area and the spray plume (see Table 3.2.d.1).

The effect of liquid plume size on gas mass transfer was also investigated. When multiple nozzles were used for liquid spray, the liquid plume was larger and contained more liquid droplets than created by a single nozzle. This raised a question: whether or not a large spray plume should be provided to intensify the gas mass transfer. This was examined when the top cylinder was removed and the nozzles were installed directly on the top of the glass vessel (Figure 3.2.d.1). The spray plume was reduced dramatically from 7.5L to 1.5 L. Under the same operation conditions, however, the k_La reached 0.075 s^{-1} or increased by 17% as shown in Table 3.2.d.1. Obviously, the small plume did not reduce, but intensified the gas mass transfer. This is attributed to a fact that gas-liquid mass transfer occurs primarily under the tip of nozzles. A long retention time of small liquid droplets in the gas phase did not make a substantial contribution to mass transfer. Instead, the impact of the liquid droplets at free liquid surface could to some extent intensify the gas mass transfer.

Table 3.2.d.1. Physical absorption and mass transfer of oxygen in water [a]

Nozzles [b]	Orifice diameter (mm)	Open area (mm^2)	Circulation rate (L min^{-1})	Pressure drop [c] (x10^5 Pa)	Droplets velocity [d] ($m.s^{-1}$)	k_La (s^{-1})	Power dissipation (kw. m^{-3})
1	1.44	1.63	2.4	2.57	22.7	0.031	6.9
1	1.65	2.14	2.8	2.38	21.9	0.033	7.3
1[e]	2.06	3.33	3.5	1.92	19.6	0.044	7.5
2	2.06	6.66	4.6	0.61	11.0	0.062	3.3
3	2.06	9.99	4.7	0.48	9.8	0.064	2.7
3[f]	2.06	9.99	4.7	0.48	9.8	0.075	2.7

a. Gassing rate at 0.2 vvm (gas volume per liquid volume per min): 1.5 L water with 0.3 L min^{-1} air
b. 90° full cone nozzles
c. Pressure drop (ΔP) across the nozzle(s)
d. Initial velocity of droplets from the nozzles ($U_0 = Cp\sqrt{\frac{2\Delta P}{\rho_L}}$, Cp = 0.95)
e. The same liquid retention time (0.4 min) as in the experiment of biological enhancement
f. The same nozzles and operations with reduced spray plume.

Autotrophic microbes can consume CO_2 as the carbon source by extracting energy from the reaction of H_2 and O_2. Carbohydrate (CH_2O) and water (H_2O) are the two products from CO_2 fixation: CO_2 (gas) + $4H_2$ (gas) + O_2 (gas) → CH_2O (liquid) + $3H_2O$ (liquid). The carbohydrate is further used for cell growth and/or polyester synthesis. Biological gas consumption by microbial cells in a mineral solution may enhance the gas mass transfer rate. An enhancement factor (E) is defined with Eq. 1,

$$E = \frac{(k_La)_{Bio}}{(k_La)_{Phy}} \qquad \text{(Eq.1)}$$

Where the subscripts *Bio* and *Phy* indicates the conditions of biological gas consumption and physical absorption in water, respectively. Table 3.2.d.2 gives the measurements of oxygen utilization rate (OUR) and k_La at different time points in a gas fermentation (70% H_2, 20% O_2 and 10% CO_2). To maintain good mixing and frequent exposure of liquid to the gas phase, the medium solution (0.5L) was stirred at 100 rpm and circulated at 1.2 L min^{-1} to give a liquid retention time of 0.4 min in the liquid pool as discussed above. The pressure drop across a nozzle (φ1.65 mm) was 90 kPa and did not change with increase of cell density. Under the operation conditions, the energy dissipation in the liquid solution from the pump was about 3.6 kw m^{-3} (see the result in A1.3). The optical density (OD) of mineral solution increased from 1 to 25, i.e. the dry cell mass concentration increased from 0.4 g L^{-1} to 10 g L^{-1}. Because of biological gas consumption, the outlet gas flow rate dropped from 104 mL min^{-1} at the beginning to 50-60 mL min^{-1}, i.e. about 40-50 vol% of gas was absorbed and consumed by the microbes. Each gas flowrate and composition were the averages of three measurements taken within 30 min. Because of the relatively slow biological activity, quasi steady state of gas composition was assumed during the sampling time.

The value of k_La (0.042 s^{-1}) was low at the low optical densities (ODs) because of a low oxygen utilization rate, and increased to the highest level (0.083 s^{-1}) along with cell growth. At the peak level, the dissolved O_2 concentration dropped to zero, indicating that the microbial growth was

limited by oxygen mass transfer. The highest value of k_La (0.083 s^{-1}) therefore reflected the maximum oxygen mass transfer rate of the spray bioreactor under the operation conditions. The k_La then declined with further increase in cell density. This was attributed to a low OUR because of the reduced microbial activity after the obligate aerobic strain had been exposed to oxygen depletion for a long time. Compared with the k_La (0.044 s^{-1}) of physical absorption in water at the same liquid retention time (0.4 min) (Table 3.2.d.1), the enhancement factor of oxygen mass transfer by biological activity was calculated (Eq. 1) and presented in Table 3.2.d.2. The oxygen mass transfer was intensified to a great extent because of the biological gas consumption. It should be pointed out that the mass transfer rates of hydrogen and carbon dioxide were also intensified according to the stoichiometric coefficients of CO_2 fixation as shown above.

Table 3.2.d.2. Intensified oxygen mass transfer in spray bioreactor with one nozzle [a]

Time (hour)	OD [b]	Dissolved O_2 (mg L^{-1})	Outlet gas [c] (mL min^{-1})	Outlet O_2 (mole%)	OUR (mmole L^{-1} min^{-1})	k_La (s^{-1})	E [d] (-)
0	1	6.43	104	20.64	0	0	-
16	2.1	2.25	75	21.34	0.45	0.042	0.95
24	6	0.25	64	21.58	0.64	0.055	1.25
32	15.1	0	51	17.83	0.96	0.083	1.89
40	25.1	0	60	16.62	0.86	0.074	1.68
48	23.6	0	62	19.84	0.75	0.073	1.66

a. Nozzle orifice diameter φ1.65 mm, open area 2.14 mm^2, 90° full cone
b. Optical density of culture medium at 600 nm (1 OD = 0.4 g dry cell mass/L)
c. The outlet volumetric gas flow rate (25 °C, 1 atm)
d. Comparison with physical absorption of oxygen in water (k_La = 0.044 s^{-1}) in Table 3.2.d.1.

The spray bioreactor has a simple structure. The pump in liquid circulation line provides the mechanical energy for liquid spray and mixing. A mechanical energy balance between two points (1-1'and 2-2') in Figure 3.2.d.1 shows that the energy input (W_s) from the pump minus friction loss is equal to the increase of kinetic energy, potential energy and pressure energy of the fluid (Eq. 2a).

$$W_s - \sum F = \frac{(U_2^2 - U_1^2)}{2} + g(Z_2 - Z_1) + \frac{(P_2 - P_1)}{\rho_L} \text{ (J/kg) (Eq. 2a)}$$

Because of negligible friction loss ($\Sigma f \approx 0$), the small height difference between the two points (Z_2-Z_1), and stable liquid surface in the bioreactor ($U_1 = 0$), Eq. 2a is simplified as Eq. 2b,

$$W_s = \frac{U_2^2}{2} + \frac{\Delta P}{\rho_L} \qquad \text{(Eq. 2b)}$$

Where U_2 is the liquid velocity in the tubing (inner diameter 6mm) and ΔP the pressure drop across the nozzle. Under the experimental conditions (Table 3.2.d.1), the dynamic energy ($U^2/2$) accounted only for a small portion (<8%) of the pump work (W_s). The energy was primarily used to raise the pressure of liquid (ΔP) for spray. The power consumption per liquid volume (kW m^{-3}) or the power dissipation rate in Table 1 was calculated from the liquid circulation rate and the pressure drop with Eq. 2b. As shown in Table 3.2.d.1, a high liquid circulation rate under low pressure drop has a much lower energy dissipation (2.7 kw m^{-3}) than a low circulation rate under a high pressure drop (7.3 kw m^{-3}). In the latter case, the energy was dissipated as surface energy and heat in formation of tiny liquid droplets.

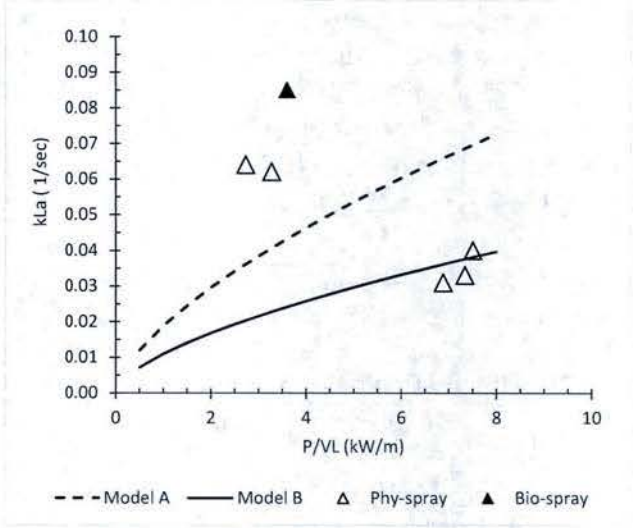

Figure 3.2.d.2. Volumetric mass transfer coefficient and power dissipation at a superficial gas velocity of 0.00028 m s^{-1} in the spray bioreactor (Phy-spray for physical water absorption, Bio-spray for biological gas utilization) and conventional stirred bioreactors: Model A (α=0.0126, β=0.65 and γ=0.5) [2], and Model B (α=0.0083, β=0.62 and γ=0.49) [3].

In conventional agitated bioreactors, the oxygen mass transfer coefficient (k_La) is dependent on the superficial gas velocity as well as the power dissipation in liquid solution. A widely used correlation for stirred vessels has a general form (Eq. 3) [1].

$$k_L a = \alpha(\frac{P}{V_L})^{\beta} U_s^{\gamma} \qquad \text{(Eq. 3)}$$

Where k_La is the oxygen mass-transfer coefficient in units of s^{-1}. P is the power dissipated by the stirrer in W, and V_L is the liquid volume in m^3. U_s is the superficial gas velocity in m s^{-1} and is defined as the volumetric gas flow rate divided by the cross-sectional area of the bioreactor. Numerous correlations have been obtained from experimental data and/or derived from theory. Two of them are plotted in Figure 3.2.d.2 for analysis and comparison: Model A is derived from Kolmogorov's theory and not restricted to experimental conditions and special configuration of the bioreactor [2], and Model B from experimental correlation [3]. Most experimental correlations gave quite consistent predictions on k_La while the theory-based correlation gives a higher prediction [4]. They are compared with the k_La of the spray bioreactor at the same energy dissipation rate in Figure 3.2.d.2. It should be pointed out that the empirical correlations are obtained from special experiments in which the minimum superficial gas velocity is 0.001 m s^{-1} or above [1]. When the correlations are used at a very low gas velocity in this work (0.00028 m s^{-1} in Tables 3.2.d.1 and 3.2.d.2), they are only for reference purposes. Figure 3.2.d.2 revealed some interesting information. First, a spray bioreactor should not be operated at a high nozzle pressure drop because the high energy dissipation cannot secure a high mass transfer coefficient. With high energy dissipation, the spray bioreactor exhibits a similar k_La to a conventional bioreactor at very low gassing rates. Second, with low energy dissipation, spray bioreactors can

provide higher mass transfer rates than conventional bioreactors do. The gas mass transfer rate is enhanced by 100% or above. At a very low gassing rate, mechanical energy is more efficiently used to break down liquid into droplets than to break down gas into bubbles. A spray bioreactor can therefore use the same amount of energy to provide a much higher k_La. Finally, biological gas consumption can enhance the gas mass transfer in the medium solution.

Polyester Deoxygenation

Under controlled conditions, 50-60% of dry cell mass from a gas fermentation is polyhydroxybutyrate (PHB), a form of carbon and energy storage in bacterium. The oxygen content of biopolyester ($C_4H_6O_2$) is 37.2 wt%, resulting in a relatively low energy content (21.4-24.6 MJ/kg) of a liquefied oil derived from the polyester. Oxygen removal from polyester or deoxygenation is therefore necessary to make a drop-in transportation fuel. Initial work in Activity 2 investigated thermal degradation of PHB under hydrogen to see if the oxygen could be removed as water via hydrogenation. This early effort, however, was not successful. Other deoxygenation methods were researched, and some very interesting results were obtained. Specifically, a solid phosphoric acid (SPA) was prepared in the laboratory and used as a catalyst in PHB reforming. Under inert nitrogen gas, a mixture of PHB and SPA was heated gradually in a differential scanning colorimeter (DSC). As shown in Figure 3a, a large endothermic peak was observed at 212-213 °C, followed by a few smaller peaks at higher temperatures up to 226 °C,

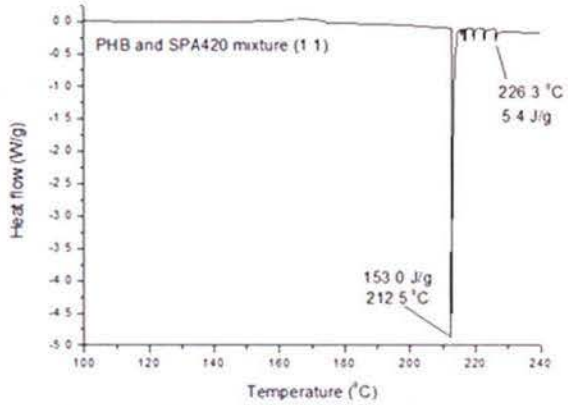

Figure 3.2.d.3a. Differential scanning colorimeter thermograms of a mixture of PHB and solid phosphoric acid (SPA420).

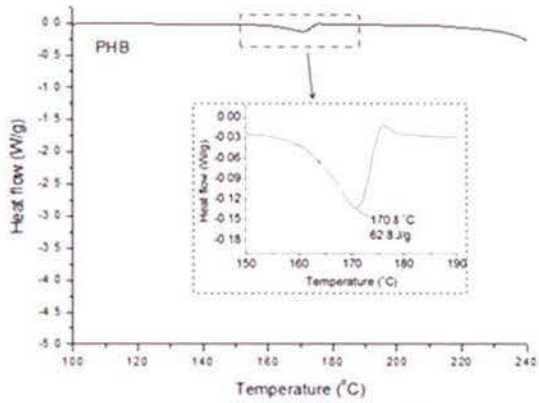

Figure 3.2.d.3b. Differential scanning colorimeter thermograms of PHB only.

indicating a chemical reaction or reactions at the temperatures. In contrast, in the absence of SPA, PHB was melted around 171 °C with a small endothermic peak as shown in Figure 3b, and no reaction was observed up to 240 °C. Obviously, the SPA played a role in the reaction as a catalyst.

More interestingly, the PHB reforming under catalysis of SPA generated a liquid oil and an elemental analysis confirms that the oil is a hydrocarbon oil containing: 81.4% C, 11.3% H, and 0.4% N. The residual oxygen is less than 6.9%, calculated from the elemental weight balance. The high heating value (HHV) of the hydrocarbon oil is 41.4 MJ/kg, the same as a commercial gasoline from a local gas station. Further investigation will be conducted for the reaction conditions, reaction mechanisms and hydrocarbon oil composition and so on under funding from ONR (APRISE 12).

Conclusions

A novel bioreactor with liquid-in-gas dispersion can be operated at very low gassing rate to reduce the gas wastage. The gas feeding rate could be reduced to as low as 10-20% of a conventional bioreactor, which reduced gas wastage by 80-90%. A fundamental study on gas mass transfer and energy consumption indicates that the bioreactor can provide a higher gas mass transfer rate (about 100%) by using less energy (37%) in comparison with conventional bioreactors. A patent has been filed by University of Hawaii and licensed to a company [5]. In addition, a simple reforming method was discovered to make a hydrocarbon oil from polyester (PHB). The liquid oil has a low oxygen content (<7 wt%) and a high energy content (41 MJ/kg).

References

[1] Garcia-Ochoa F, Gomez E. Bioreactor scale-up and oxygen transfer rate in microbial processes: An overview, Biotechnol. Adv. 27 (2009) 153–176.

[2] Kawse Y, Moo-Yong M. Volumetric mass transfer coefficients in aerated stirred tank reactors with Newtonian and non-Newtonian media. Chem. Eng. Res. Des. 66 (1988) 284–288.

[3] Nocentini M, Fajner D, Pasquali G, Magelli F. Gas-liquid mass transfer and holdup in vessels stirred with multiple Rushton turbines: water and water-glycerol solutions, Ind. Eng. Chem. Res. 32 (1993) 19–26.

[4] M. Xie, J. Xia, Z. Zhou, J. Chu, Y. Zhuang, S. Zhang, Flow pattern, mixing, gas hold-up and mass transfer coefficient of triple-impeller configurations in stirred tank bioreactors, Ind. Eng. Chem. Res. 53 (2014) 5941–5953.

[5] Pradeep Munasinghe and Jian Yu. A novel bioreactor for high efficiency gas utilization by microbes. Provisional patent 62433748. December 13, 2016

3.2e Biocontamination of Fuels

From a petroleum-contaminated sample, two isolates have been used to study the biodegradation of sulfur containing compounds. *Arthrobacter* sp. P1-1 and *Burkholderia* sp. C3 have been utilized to investigate the biodegradation of dibenzothiophene (DBT), a thermodynamically stable, sulfur containing poly aromatic hydrocarbon (PAH) compound that is inherently present in all diesel fuels (Li *et al.* 2012).

Glycerol is the main byproduct that is formed during the fatty acid transesterification process for the production of biodiesel. In use, biodiesel is often blended with petroleum diesel fuels. During the blending process, a glycerol carbon source and dibenzothiophene (DBT) becomes bioavailable. Metabolic enhancement using different nutrient sources such as glycerol can increase linked biochemical pathways. Co-metabolic studies for the simultaneous utilization of both compounds are expected to offer knowledge and information about sulfur metabolism and for this study also a fuel pre-treatment protocol. For FY 2011 continuation of work initiated during FY 2010 that utilized *Burkholderia* sp. C3 was performed.

Glycerol was previously found to stimulate both rhamnolipid production and DBT degradation. Increased rhamnolipid biosynthesis and secretion facilitated the degradation of DBT.

Rhamnolipid could be involved in cell transport and may increase the biodegradation of hydrophobic chemicals (Bai *et al.* 1997) such as petroleum or biodiesels. The determination of the biological impact that the secretion of rhamnolipids has on the rate of DBT degradation provides addition insight into how we might better understand sulfate uptake metabolisms.

Further investigation suggests that proteins having catalytic activity that are involved with Rhamnolipid degradation was also found in related species of *Burkholderia* (Table 1). To test the hypothesis that RL was the biosurfactant being secreted, we designed primers to target conserved regions of 13 *rhlB* sequences from *Burkholderia* species. Degenerative primers were designed based on conserved regions of 13 rhlB and 55 rhlC gene sequences from Burkholderia species collected from the NCBI database and using Geneious Pro 5.6.7 (Biomatters limited, Auckland, New Zealand) multiple sequence alignment default options. Inverse PCR was done using a high fidelity polymerase (Finnzymes), degenerate primers for rhlB and self-ligated genomic DNA as template. PCR products were sequenced in duplicate and primers were designed based on the newly sequenced PCR product until a complete self-ligated plasmid was assembled. Sequences were assembled using Geneious Pro 5.6.7. Open reading frames (ORFs) were identified using the fgenesB bacterial operon and gene prediction program on 11 March 2016 (http://www.softberry.com/). Sequence homology was determined using UniProt database (http://www.uniprot.org/) and gene cluster homology was determined using Burkholderia Genome database (http://burkholderia.com/) and blastX algorithm. A DNA sequence (280 bp) matching Rhamnosyltransferase I subunit B from *Burkholderia glumae* (78.5% identity) was obtained. This sequence was used to design inverse PCR primers. The full self-ligated plasmid was 3284 bp. A search for bacterial operons identified 3 ORFs located on the positive strand of this plasmid. These ORFs were determined to be the *rhlA, rhlB* and isoprenylcysteine carboxyl methyltransferase genes. Further analysis showed a 4th gene to be the *MFS transporter*, which was partially sequenced. Gene *rhlC* (298 bp) was not found in the self-ligated plasmid and was obtained using degenerate primers instead. Comparisons of the gene cluster to those of *Burkholderia* species in the *Burkholderia* database suggested the *rhlABC* gene cluster.

The determination of the biological impact that the secretion of rhamnolipids has on the rate of DBT degradation provides addition insight into how we might better understand sulfate uptake metabolisms. Due to its amphipathic chemistry, biosurfactants interact with PAHs in solution and at water-particle and water-oil interfaces. Those interactions alter the physicochemical properties of PAHs, making them more soluble and bioavailable (Makkar and Rockne 2003). The presence of RL significantly decreased DBT half-life when inoculated with C3 (Table 2). The production of both biosurfactants and hydrocarbon degradative enzymes have been previously observed in bacteria (Xia *et al.* 2014). The dual functions of RL production and PAH degradation may confer to the microorganism an evolutional adaptation to survive in environmental conditions where hydrophobic chemicals are scarce.

A publication for work supported by this and previous awards has been published in the journal, International Biodeterioration and Biodegradation (Ching *et al.* 2016). Briefly, a putatively novel basidiomycetous fungus termed *Moniliella wahieum* Y12T was isolated and found to degraded biodiesel at a rate of 3.56 x 10^2 mg/h during log phase growth. Furthermore, induction of metal corrosion by the strain was observer due to medium acidification.

Investigation of napieer grass as a biomass resource was also performed and supported in part through this award that resulted in a publication in the journal, Bioresource Technology (Wen *et al.* 2015). The grass was pretreated with a microbiological consortia and subject to enzymatic

saccarification. The lignocellulose loss rates of Napier grass varied largely. The biomass pretreated by the consortium WSD-5 gave 43.4% and 66.2% total sugar yield under low and moderate loadings of commercial enzyme mixtures, while the highest yield was 83.2% pretreated by the consortium MC1 under a high enzyme loading. The maximum methane yield of pretreated samples by the consortia MC1, WSD-5 and XDC-2 were 259, 279, 247 ml/g VS, respectively, which were 1.39, 1.49 and 1.32 times greater than the values of the untreated controls.

Additionally, experiments have been performed using F-76 fuel as a standard source of carbon for the production of experimental data that would be comparable with other ONR related projects. Successful transition was made from using commercially available diesel to the standardized F-76. This work is being completed under later APRISES funding, and will be reported in detail in that final report.

Protein name	Organism	Identity (%)	Query length (bp)
Rhamnosyltransferase 1, subunit A	*Burkholderia pseudomallei*	79.6	1011
Isoprenylcysteine carboxyl methyltransferase	*Burkholderia fungorum*	99.3	450
Rhamnosyltransferase I, subunit B	*Burkholderia glumae* PG1	72.7	1131
MFS transporter	*Burkholderia* sp. MSMB617WGS	64.5	107
Rhamnosyltransferase I subunit C	*Burkholderia glumae* PG1	73.7	298

Table 3.2e.1. C3 *rhlABC* genes homology to other *Burkholderia* species. BLASTP algorithm and UniProt database were used to find sequence homology.

Treatment	Rate constant (Day^{-1})	R^2	Half-life (Day)	N	Fold change
0.5 mM DBT (0.05 OD_{600} C3 inoculum)	0.025±0.01	0.63	27.5	30	0.0
0.5 mM DBT with RL (0.05 OD_{600} C3 inoculum)	0.053±0.01	0.91	14.0	30	1.1*
0.5 mM DBT (0.2 OD_{600} C3 inoculum)	0.047±0.00	0.98	15.8	15	0.7*
0.5 mM DBT with RL (0.2 OD_{600} C3 inoculum)	0.133±0.01	0.95	5.2	30	1.8**

Table 3.2e.2. Influence of RL fortification and C3 density in DBT biodegradation rate constant and DBT half-life. The final RL concentration was 20 μg/mL. Exponential decay equation, $C = C_0 \times e^{-kt}$, was used for fitting "N" data points where k is rate constant and t is time in day. Relative to rate constant of 0.5 mM DBT with * 0.05 OD_{600} C3 inoculum and ** 0.2 OD_{600} C3 inoculum.

References

Bai G, Brusseau ML, Miller RM. 1997. Influence of a rhamnolipid biosurfactant on the transport of bacteria through a sandy soil. Appl Environ Microbiol 63:1866–1873.

Ching T.H., Yoza B.A., Wang R., Masutani S., Donachie S., Hihara L., Li Q.X. 2016. Biodegradation of biodiesel and microbiologically induced corrosion by *Moniliella sp.* Y12. *International Biodet. Biodeg.* 108; 122-126

Li M, Wang TG, Simoneit BRT, Shi S, Zhang L, Yang F. 2012. Qualitative and quantitative analysis of dibenzothiophene, its methylated homologues, and benzonaphthothiophenes in crude oils, coal, and sediment extracts. J Chromatogr A 1233:126–136.

Makkar RS, Rockne KJ. 2003. Comparison of synthetic surfactants and biosurfactants in enhancing biodegradation of polycyclic aromatic hydrocarbons. Environ Toxicol Chem 22:2280–2292.

Wen B., Xufeng Y., Li Q.X., Liu J., Ren J., Wang X., Cui Z. 2015. Comparison and evaluation of concurrent saccharification and anaerobic digestion of Napieer grass after pretreatment by three microbial consortia. *Bioresource Techn.* 175; 102-111

Xia W, Du Z, Cui Q, Dong H, Wang F, He P, Tang Y. 2014. Biosurfactant produced by novel Pseudomonas sp. WJ6 with biodegradation of n-alkanes and polycyclic aromatic hydrocarbons. J Hazard Mater 276:489–498.

3.2f Biofuel Corrosion Control

Corrosion can be a major concern in the storage, transportation, and use of biofuels. The substitution of conventional fuels with biofuels could result in unexpected corrosion failures. Studies were conducted in biofuels and its blends in simulated marine environments with plain-carbon 1018 steel (UNS G10180), which is within specifications for steels typically used for pipelines and storage vessels and tanks. The goals were to study the corrosion mechanisms and the effect of biological activity on 1018 steel exposed to seawater-fuel mixtures to determine if corrosion was governed primarily by electrochemical effects or from biological activity originating from the fuel, seawater, or both. The seawater was either natural, off-shore, surface water or synthetic according to ASTM International (ASTM) specifications. The fuel was either traditional, petroleum-based F-76; hydro-treated renewable diesel (HRD) derived from algae (HRD-76); or a 50%:50% by volume (50:50 v/v) blend of F-76 and HRD-76. To differentiate between abiotic electrochemical corrosion and microbiologically influenced corrosion (MIC), various permutations of filtered and unfiltered fuel and seawater combinations were used as exposure medium. A 0.22 micron filter was used to filter the seawater and fuel. Both aerobic and anaerobic conditions were examined. There were two aerobic conditions: Filtered aerobic where a 0.22 micron filter prevented larger air-borne contaminates into the test bottles, and an open aerobic where airborne contaminants were allowed to enter the test bottles. Hence, the test conditions were filtered-aerobic, aerobic, or anaerobic of the following seawater-fuel mixtures: 1) filtered seawater/filtered fuel, 2) filtered seawater/non-filtered fuel, 3) non-filtered seawater/filtered fuel, and 4) non-filtered seawater/non-filtered fuel conditions.

Corrosion behavior was evaluated at various intervals for one year: i) with and without naturally-occurring microbes; ii) under aerobic and anaerobic conditions; and iii) in natural and synthetic seawaters. Immersion tests were conducted and corrosion products were visually assessed for extent of steel coupon surface coverage. Corrosion rates were calculated based on mass-loss data for each coupon. Molecular biological techniques were the primary method employed to identify bacterial species. As a supplement, biochemical techniques were also used in characterizing bacteria species. Common techniques employed in biochemical characterization include Gram staining, enzyme production, and carbohydrate fermentation tests. Molecular identification of bacteria and fungi was performed via 16S rRNA and 18S rRNA sequencing. The corrosion of the steel samples was characterized visually, and by measuring weight loss. (Characterization of the corrosion products was performed in detail under APRISES12, and will be included in that technical report).

Corrosion rates of 1018 carbon steel were driven by oxygen reduction and were highest in HRD-76, followed by the F-76:HRD-76 blend, and then F-76. This ordering was similar to that of the dissolved oxygen diffusion coefficients (from highest to lowest) for the HRD-76, blend,

and F-76 fuels. White precipitate (e.g., likely carbonate and hydroxide) formation in the fuel layer was shown to be a consistent visual indicator for a high corrosion rate of steel. Precipitation was likely induced by a high amount of oxygen reduction (in the fuel layer) that generated OH^-, which precipitated the carbonates and hydroxides. Corrosion rates in synthetic ASTM seawater was statistically lower that corrosion rates in the natural Pacific Ocean seawater, but the difference was less than ≈10%. Throughout the one-year exposure period, however, there was significant complexity in the microbial community from the diesel/seawater interface layers (primarily from the unfiltered seawater combinations). After one year of incubation, 299 *Bacteria/Archaea* genera were still detected. It is likely that the very high corrosion rates of plain carbon steel in aerated seawater overshadowed microbial effects.

For more information, see the Master's Thesis listed below

Publications resulting from these efforts

J. Kealoha, *Microbiologically Influenced Corrosion of 1018 Carbon Steel in Static Seawater/Fuel (Petroleum-Based and Renewable) Mixtures*, Microbiology Thesis Submitted to the Graduate Division of the University at Manoa, (August 2017).

References

Altschul, S. F., Madden, T. L., Schäffer, A. A., Zhang, J., Zhang, Z., Miller, W., & Lipman, D. J. (1997). Gapped BLAST and PSI-BLAST: A new generation of protein database search programs. *Nucleic Acids Research*, *25*(17), 3389–3402. http://doi.org/10.1093/nar/25.17.3389

ASTM International. (1999). Standard Practice for Preparing, Cleaning, and Evaluating Corrosion Test Specimens. *Annual Book of ASTM Standards*, 15–21. http://doi.org/10.1520/G0001-03

Baird, C., Ogles, D., & Baldwin, B. R. (2016). Molecular microbiological methods to investigate microbial influenced corrosion in fully integrated kraft pulp and paper mills. In *Corrosion* (pp. 1–11). NACE International.

Bento, F. M., Beech, I. B., Gaylarde, C. C., Englert, G. E., & Muller, I. L. (2005). Degradation and corrosive activities of fungi in a diesel-mild steel-aqueous system. *World Journal of Microbiology and Biotechnology*, *21*(2), 135–142. http://doi.org/10.1007/s11274-004-3042-2

Bingham, F. M., & Lukas, R. (1996). Seasonal cycles of temperature, salinity and dissolved oxygen observed in the Hawaii Ocean Time-series. *Deep-Sea Research II*, *43*(3), 19–213. Retrieved from http://cmore.soest.hawaii.edu/members/HOTEL/1996/BinghamandLukas1996.pdf

Brislawn, C. (2014). JC_qiime_pipline. Retrieved January 1, 2014, from https://bitbucket.org/colin_brislawn/jc_qiime_pipeline/src/372d92398ff0?at=master

Brown, M. V, Philip, G. K., Bunge, J. A., Smith, M. C., Bissett, A., Lauro, F. M., … Donachie, S. P. (2009). Microbial community structure in the North Pacific ocean. *The ISME Journal*, *3*(12), 1374–86. http://doi.org/10.1038/ismej.2009.86

Caporaso, J. G., Kuczynski, J., Stombaugh, J., Bittinger, K., Bushman, F. D., Costello, E. K., … Knight, R. (2010). QIIME allows analysis of high-throughput community sequencing data. *Nature Methods*, *7*(5), 335–336. http://doi.org/10.1038/nmeth.f.303

Chavez, F. P., Messié, M., & Pennington, J. T. (2011). Marine primary production in relation to climate variability and change. *Annual Review of Marine Science*, *3*(1), 227–260. http://doi.org/10.1146/annurev.marine.010908.163917

DeSantis, T. Z., Hugenholtz, P., Larsen, N., Rojas, M., Brodie, E. L., Keller, K., … Andersen, G. L. (2006). Greengenes, a chimera-checked 16S rRNA gene database and workbench compatible with ARB. *Applied and Environmental Microbiology*, *72*(50), 69–72.

Elshafie, A., AlKindi, A. Y., Al-Busaidi, S., Bakheit, C., & Albahry, S. N. (2007). Biodegradation of crude oil and n-alkanes by fungi isolated from Oman. *Marine Pollution Bulletin*, *54*(11), 1692–6. http://doi.org/10.1016/j.marpolbul.2007.06.006

Francis, R. (2012). Iron and carbon steel. In *The corrosion performance of metals for the marine environment: a basic guide* (pp. 3–13). Maney Publishing.

Fu, J., & Turn, S. Q. (2015). Effects of biodiesel contamination on oxidation and storage stability of neat and blended hydroprocessed renewable diesel. *Energy and Fuels*, *29*(8), 5176–5186. http://doi.org/10.1021/acs.energyfuels.5b01260

Gaylarde, C. C., & Beech, I. B. (1988). Molecular basis of bacterial adhesion to metals. In C. A. C. Sequeira & A. K. Tiller (Eds.), *Microbial Corrosion* (pp. 20–28). Elsevier Applied Science.

Geissler, B., Keller-schultz, C., & Keasler, V. (2015). Don't just blame the SRBs and APBs for MIC. In *CORROSION2015* (pp. 1–12). Dallas.

Harayama, S., Kasai, Y., & Hara, A. (2004). Microbial communities in oil-contaminated seawater. *Current Opinion in Biotechnology*, *15*(3), 205–214. http://doi.org/10.1016/j.copbio.2004.04.002

Hassanshahian, M., Emtiazi, G., & Cappello, S. (2012). Isolation and characterization of crude-oil-degrading bacteria from the Persian Gulf and the Caspian Sea. *Marine Pollution Bulletin*, *64*(1), 7–12. http://doi.org/10.1016/j.marpolbul.2011.11.006

Hawaii Ocean Time-series (HOT). (2015). Retrieved October 8, 2012, from http://hahana.soest.hawaii.edu/hot

Little, B. J., Staehle, R., & Davis, R. (2001). Fungal influenced corrosion of post-tensioned cables. *International Biodeterioration and Biodegradation*, *47*(2), 71–77. http://doi.org/10.1016/S0964-8305(01)00039-7

Magot, M. (2005). Indigenous microbial communities in oil fields. In B. Ollivier & M. Magot (Eds.), *Petroleum Microbiology* (pp. 21–34). Washington D.C.: ASM Press.

Mahdi, L. E., Statzell-Tallman, A., Fell, J. W., Brown, M. V, & Donachie, S. P. (2008). *Sympodiomycopsis lanaiensis sp. nov.*, a basidiomycetous yeast (Ustilaginomycotina: Microstromatales) from marine driftwood in Hawai'i. *FEMS Yeast Research*, *8*(8), 1357–

1363. http://doi.org/10.1111/j.1567-1364.2008.00448.x

Marty, F., Ghiglione, J.-F., Païssé, S., & Gueuné, H. (2012). Evaluation and optimization of nucleic acid extraction methods for the molecular analysis of bacterial communities associated with corroded carbon steel. *Biofouling*, *28*(April), 37–41. Retrieved from http://www.tandfonline.com/doi/abs/10.1080/08927014.2012.672644

McDonald, D., Price, M., Goodrich, J., Nawrocki, E., DeSantis, T., Probst, A., … Hugenholtz, P. (2012). An improved Greengenes taxonomy with explicit ranks for ecological and evolutionary analyses of bacteria and archaea. *International Society for Microbial Ecology*, *6*(3), 610–618.

NACE. (2013). *Standard Practice: Preparation, installation, analysis, and interpretation of corrosion coupons in oilfield operations* (Vol. SP0775-201).

O'Rorke, R., Cobian, G. M., Holland, B. S., Price, M. R., Costello, V., & Amend, A. S. (2015). Dining local: The microbial diet of a snail that grazes microbial communities is geographically structured. *Environmental Microbiology*, *17*(5), 1753–1764. http://doi.org/10.1111/1462-2920.12630

Olsen, E., & Szybalski, W. (1949). Aerobic microbiological corrosion of water pipes. In *Microbioloical Corrosion 1* (pp. 1019–1110).

Pacific Islands Ocean Observing System. (2012). Retrieved October 8, 2012, from http://www.pacioos.hawaii.edu

Petersen, R. B., & Melchers, R. E. (2012). Long-term corrosion of cast iron cement lined pipes. In *Corrosion & Prevention* (Vol. 23, pp. 1–12).

Prince, R. C. (2005). The microbiology of marine oil spill bioremediation. In B. Ollivier & M. Magot (Eds.), *Petroleum Microbiology* (pp. 317–336). Washington D.C.: ASM Press.

Rabus, R. (2005). Biodegradation of hydrocarbons under anoxic conditions. In B. Ollivier & M. Magot (Eds.), *Petroleum Microbiology* (pp. 277–300). Washington D.C.: ASM Press.

Revie, R. W., & Uhlig, H. H. (2008). *Corrosion and corrosion control: An introduction to corrosion science and engineering*. *British Corrosion Journal* (4th ed., Vol. 7). Hoboken: John Wiley & Sons, Inc. http://doi.org/10.1179/000705972798323134

Riser, S. C., & Johnson, K. S. (2008). Net production of oxygen in the subtropical ocean. *Nature*, *451*(7176), 323–5. http://doi.org/10.1038/nature06441

Rueckert, A., & Morgan, H. W. (2007). Removal of contaminating DNA from polymerase chain reaction using ethidium monoazide. *Journal of Microbiological Methods*, *68*(3), 596–600. http://doi.org/10.1016/j.mimet.2006.11.006

Smith, D. P., & Peay, K. G. (2014). Sequence depth, not PCR replication, improves ecological inference from next generation DNA sequencing. *PLoS ONE*, *9*(2). http://doi.org/10.1371/journal.pone.0090234

van Beilen, J. B., & Witholt, B. (2005). Diversity, function, and biocatalytic applications of

alkane oxygenases. In B. Ollivier & M. Magot (Eds.), *Petroleum Microbiology* (pp. 259–276). Washington D.C.: ASM Press.

Wang, L., Wang, W., Lai, Q., & Shao, Z. (2010). Gene diversity of CYP153A and AlkB alkane hydroxylases in oil-degrading bacteria isolated from the Atlantic Ocean. *Environmental Microbiology*, *12*(5), 1230–1242. http://doi.org/10.1111/j.1462-2920.2010.02165.x

Witherby & Co. Ltd. (2002). *Guidelines for Ballast Tank Coating Systems and Surface Preparation*. London.

Yakimov, M. M., Giuliano, L., Gentile, G., Crisafi, E., Chernikova, T. N., Abraham, W. R., … Golyshin, P. N. (2003). *Oleispira antarctica* gen. nov., sp. nov., a novel hydrocarbonoclastic marine bacterium isolated from Antarctic coastal sea water. *International Journal of Systematic and Evolutionary Microbiology*, *53*(3), 779–785. http://doi.org/10.1099/ijs.0.02366-0

Zhu, X., Lubeck, J., & Kilbane, J. (2003). Characterization of microbial communities in gas industry pipelines. *Applied and Environmental …*, *69*(9). http://doi.org/10.1128/AEM.69.9.5354

3.2g Waste management using the Flash-Carbonization™ Process

The goal of this task was to identify process conditions that improve the yield of charcoal from wood. To realize this goal, we first calculated the theoretical fixed-carbon yield of charcoal by use of the elemental composition of the wood feedstock. Next, we examined the influence of particle size, sample size, and pressure on experimental values of the fixed-carbon yields of the charcoal products and compared these values with the calculated theoretical limiting values. The carbonization by thermogravimetric analysis of small samples of small particles of wood in open crucibles delivers the lowest fixed-carbon yields, closely followed by standard proximate analysis procedures that employ a closed crucible and realize somewhat improved yields. The fixed-carbon yields (as determined by thermogravimetry) improve as the sample size increases and as the particle size increases. Further gains are realized when pyrolysis occurs in a closed crucible that hinders the egress of volatiles. At atmospheric pressure, high fixed-carbon yields are obtained from 30 mm wood cubes heated in a closed retort under nitrogen within a muffle furnace. The highest fixed-carbon yields are realized at elevated pressure by the flash carbonization process. Even at elevated pressure, gains are realized when large particles are carbonized. These findings reveal the key role that secondary reactions, involving the interaction of vapor-phase pyrolysis species with the solid substrate, play in the formation of charcoal. Models of biomass pyrolysis, which do not account for the impacts of sample size, particle size, and pressure on the interactions of volatiles with the solid substrate, cannot predict the yield of charcoal from biomass. These findings also offer important practical guidance to industry. Size reduction of wood feedstocks is not only energy and capital intensive; size reduction also reduces the yield of charcoal and exacerbates demands made on the forest resource.

Complete details of this study were presented in the publication:

Wang, L., Ø. Skreiberg, M. Gronli, G.P. Specht, and M.J. Antal. 2013. Is elevated pressure required to achieve a high fixed-carbon yield of charcoal from biomass? Part 2: The importance of particle size. *Energy & Fuels*. 27. pp 2146-2156.

Complete details can be found at:
dx.doi.org/10.1021/ef400041h

3.3 Sustainable Biomass

The long-term goal of this subtask is to increase Hawaii's energy security by developing high-yielding tropical feedstocks that are economically viable and sustainable. This subtask focused on assessing the use of C4 tropical grasses as a lignocellulosic feedstock for biofuel production and developing methodologies for assessing the sustainability of biofuel production in Hawaii. This work is a result of interagency collaboration between the Navy, U.S. Department of Energy (DE-FG36-08GO88037, Development of High Yield, Tropical Feedstocks for Bioenergy), and U.S. Department of Agriculture (NIFA/BRDI GRANT11010878, Conversion of High-Yield Tropical Biomass into Sustainable Biofuels).

Tropical C4 grasses are arguably the best biofuel crop for Hawaii and the tropics due to their high biomass yields, low input requirements, and suitability to modern commercial harvesting technology. Project objectives were to: develop high yield, tropical feedstocks; optimize biomass conversion processes, and; develop sustainable, high-yield biomass production systems. Significant genotype-environment interactions were observed during the five-year crop trials. There was a correlation of higher dry matter yields with higher elevations, being more pronounced for energycane than the banagrass. There also was a strong correlation of higher dry matter yields with increased irrigation levels, being most pronounced with sugarcane and least so with banagrass. Energycane produced greater aboveground biomass than sugarcane and banagrass under all irrigation regimes. Results from a study of the root systems of energycane and sugarcane showed greater biomass production and higher levels of soil carbon under energycane than sugarcane. Compositional analyses of the energy crops were measured to evaluate how feedstock characteristics affect biochemical and thermochemical conversion processes to produce biofuels and/or co-products. Data from these trials were used to calibrate the ALMANAC and DSAT models to simulate energy crop yields under various growing conditions in the tropics and subtropics.

In summary, this project resulted in improved understanding of the differences in the chemical composition of C4 grasses relative to its growth and development at benchmark locations, an established baseline carbon stock present at benchmark locations on Maui, and improved knowledge of methods to assess soil organic carbon and understanding of role of C4 grasses on carbon sequestration.

For more information and detail, see the publications resulting from this work (below).

Publications Resulting from these Efforts

Refereed Journal Articles

Illukpitiya, P., J. F. Yanagida, R. Ogoshi and G. Uehara. 2013. Sugar-ethanol-electricity co-generation in Hawaii: An application of Linear Programming (L.P.) for optimizing strategies. Journal of Biomass and Bioenergy 48: 203-212.

Mochizuki, J., J.F. Yanagida, D. Kumar, D. Takara, and G.S. Murthy. 2014. Life Cycle Assessment of Ethanol Production from Tropical Banagrass (Pennisetum purpureum) Using Green and Dry Processing Technologies in Hawaii. Journal of Renewable Sustainable Energy. 6, 043128-1 – 043128-18.

Mochizuki, J., M. Coffman, and J.F. Yanagida. 2015. Market, Welfare, and Land-Use Implications of Lignocellulosic Bioethanol in Hawai`i. Renewable Energy, 76:102-114.

Mochizuki, J., J.F. Yanagida, R. Ogoshi, T. Miura, and PS Leung. GIS Analysis of an Optimal Plant Location – the Case of Banagrass-based Bioethanol Production in Hawai`i. Biomass and Bioenergy (under review).

Ma, S., M. Karkee, P. Scharf, and Q. Zhang. 2014. Sugarcane harvester technology: a critical overview. Applied Engineering in Agriculture 30(5): 727-739.

Ma, S., P. A. Scharf, M. Karkee, and Q. Zhang. 2015. Performance Evaluation of a chopper harvester in Hawaii sugarcane fields. Transactions of the ASABE. Accepted.

Takara, D., and Khanal, S.K. 2015. Characterizing compositional changes of Napier grass at different stages of growth for biofuel and biobased products potential. Bioresource Technology (in-press).

Wells, J., S. Crow, R Ogoshi, B. Torino, A. Hashimoto. 2015. Optimizing Feedstock Selection for Biofuel Production in Hawaii: CuO Oxidative Lignin Products in C4 Grasses. Biomass and Bioenergy.

Technical Reports

Takara, D., Green Processing of Napier Grass for Generation of Biofuel and Biobased Products. PhD dissertation, University of Hawaii at Manoa. Ann Arbor: ProQuest/UMI. 2012.

Sumiyoshi, Yudai. M.S. Plan A, Thesis option, "Belowground carbon cycle of Napier and Guinea grasses grown for sustainable biofuel feedstock production", degree awarded December 2012.

Yamazaki, Hironao. M.S. Plan B, Capstone Project Title "Alteration in soil carbon pools following land use and management change for bioenergy feedstock production," degree awarded December 2013.

Pawlowski, Meghan. M.S. Plan A, Thesis option, "Greenhouse gas flux and fine root dynamics of sugarcane and Napier grass under deficit irrigation," degree awarded May 2013.

Mochizuki, Junko, John Yanagida, and Makena Coffman. 2013. Market, Welfare and Land-use Implications of Lignocellulosic Bioethanol in Hawaii, UHERO Working Paper No. 2013-10, November, 2013.

Norris Energy Crop Technology. Evaluation of Alternative Sugarcane Production Systems – Strategies for Trash Recovery in Both One Year and Two Year Cane in Hawaii. Final Report, January, 2013.

Ma, Shaochun, Manoj Karkee, and Qin Zhang. 2013. Sugarcane harvesting system: a critical review, ASABE Paper No. 131574361. ASABE St. Joseph, Mich.

Sierra Research. Evaluation of Alternative Renewable Biomass Fuels for HC&S Boilers. Final Report, April 2013.

Drielak, E., and S.K. Khanal, Investigation of acid concentration, retention time and temperature on dilute acid pretreatment of banagrass. ASABE Paper No. 141912249. St. Joseph, Mich.: ASABE.

Ma, S., P. A. Scharf, Q. Zhang, M. Karkee, J. Tong, and L. Yu. Effect of off-track errors of a sugarcane harvester on stubble height and weight. In proc. of 6th Automation Technology for Off-road Equipment Conference (ATOE). September 16-19, 2014, Beijing, China.

Ma, S., P. A. Scharf, M. Karkee, and Q. Zhang, 2014. Performance evaluation of a chopper harvester in Hawaii sugarcane fields. ASABE Paper No. 1898120. St. Joseph, Mich.: ASABE.

McDaniel, A., G.S. Murthy, and A. Hashimoto, 2014. Development of An Life Cycle Impact Assessment Method Based on GBEP indicators. ASABE Abstract No. 1909170. ASABE St. Joseph, Mich.

McDaniel, A., G.S. Murthy, and A. Hashimoto, 2014. Evaluation of Environmental Impacts of Biofuels from Sugarcane and Napier Grass Produced in Hawaii. ASABE Abstract No. 1909313. ASABE St. Joseph, Mich.

Mochizuki, J., D. Kumar, J.Y. Yanagida, A. Hashimoto, and G.S. Murthy, 2014. A. Life cycle assessment of tropical banagrass (Pennisetum purpureum) derived ethanol as transportation fuel in Hawaii. ASABE Abstract No. 1909948. ASABE St. Joseph, Mich.

Ray, Whitney. Greenhouse Gas Emission Balance of Biofuel Feedstock for Potential Carbon Trading, M.S. Thesis, Department of Natural Resources and Environmental Management, University of Hawaii at Manoa, December 2014.

Stern, I.R., and B. DeBaryshe. On-farm Renewable Energy and Sustainable Local Food Production: A Case Study. University of Hawaii, Center on the Family, Honolulu, HI. 2014. (http://uhfamily.hawaii.edu/publications/brochures/bb683_14101001_COF_ResearchReport-FINAL%20(Jan%2021%202014).pdf)

Takara, D., and S.K. Khanal, Biorefining potential of a high-yielding tropical feedstock for biofuel and biobased products. ASABE Paper No. 141909876. St. Joseph, Mich.: ASABE.

Contributed Presentations

Hashimoto, A., J. Arnold, J. Ayars, S. Crow, T. Eggeman, L. Jakeway, M. Karkee, S. Khanal, J. Kiniry, J. Matsunaga, N. Meki, G. Murthy, M. Nakahata, R. Ogoshi, B. Turano, S. Turn, J. Yanagida, Q. Zhang. High-Yield Tropical Biomass for Advanced Biofuels. Sun Grant National Conference, New Orleans, LA, October 3-5, 2012. (http://sungrant.tennessee.edu/NR/rdonlyres/3880A277-C502-4EC9-9DEB-C385186A5C85/3706/214Hashimoto_Andy.pdf).

Takara, D., A.G. Hashimoto, S.K. Khanal. Green processing: a biorefinery perspective. In conference proceedings of Sun Grant National Conference: Science for Biomass Feedstock Production and Utilization, New Orleans, LA, Oct. 2-5, 2012. (http://sungrant.tennessee.edu/NR/rdonlyres/DDF120E1-C312-4065-B095-6EC87BD11DA8/3650/317Khanal_Samir.pdf).

Hashimoto, A. G. Farming and Energy: Sustainability in America. National Association of State Energy Officials, Minneapolis, MN, September 10-12, 2012.

Meki, M., J. Kiniry, A. Youkhana, M. Nakahata, S. Crow, R. Ogoshi, and J. Steiner. ALMANAC model parameterization for high biomass bioenergy crops. American Society of Agronomy Annual Meeting, Cincinnati, OH, October 21-24, 2012.

Pawlowski, M., S. E. Crow, J. L. Deenik, C. Evensen. Linking soil and water conservation practices to greenhouse gas flux and fine root dynamics: A comparison of sugarcane and Napier grass grown for bioenergy production. ASA, CSSA, and SSSA International Annual Meetings, Cincinnati, OH, October 2012.

Sumiyoshi, Y., S. E. Crow, C. M. Litton, J. L. Deenik, B. Turano, and A. Taylor. Belowground carbon cycle of Napier and Guinea grasses grown for biofuel feedstock production. ASA, CSSA, and SSSA International Annual Meetings, Cincinnati, OH, October 2012.

Takara, D., A. G. Hashimoto, and S.K. Khanal. Green processing of dedicated energy crops for biofuel and biobased products. International Conference on Challenges in Environmental Science and Engineering (CESE) 2012, Melbourne, Australia, September 9-13, 2012.

Takara, D., A.G. Hashimoto, and S. K. Khanal. Green processing of high yield tropical grass for biofuel and biobased products. S-1041-The Science and Engineering for a Biobased Industry and Economy Annual Meeting and Symposium, Waterfront Center (USDA), Washington, DC, August 6-7, 2012.

Hashimoto, A. Conversion of High-Yield Tropical Biomass into Sustainable Biofuels. Green Initiative for Fuels Transition Pacific (GIFTPAC, working group of the U.S. Department of Defense Joint Forces Pacific Command) working group meeting. Honolulu, HI. June 21, 2013.

Jakeway, Lee. 2013. "Biofuel Outlook at HC&S Co." Presented at the Asia Pacific Clean Energy Summit and Expo, September 9-11, 2013. Honolulu, Hawaii.

Meki, M. N., J. R. Kiniry, A. Youkhana, M. Nakahata, R. Ogoshi, and S. E. Crow. Key crop parameters for ALMANAC modeling of high biomass energy sorghum growth and productivity. ASA, CSSA, and SSSA International Annual Meetings, Tampa, FL, November 2013. (Contributed poster)

Mochizuki, Junko, John F. Yanagida, Richard Ogoshi, Tomoaki Miura, and PingSun Leung. "GIS analysis of an optimal plant location—the case of Banagrass-based bioethanol production in Hawaii." Paper presentation, College of Tropical Agriculture and Human Resources, Student Research Symposium, University of Hawaii, April 12-13, 2013.

Mochizuki, Junko, John F. Yanagida, Devin Takara, Deepak Kumar, and Ganti S. Murthy. "Life cycle assessment of ethanol production from tropical Banagrass (Pennisetum purpureum) using green and non-green processing technology in Hawaii." Poster presentation, College of Tropical Agriculture and Human Resources, Student Research Symposium, University of Hawaii, April 12-13, 2013.

Ogoshi, R., A. Youkhana, L. Jakeway, M. Nakahta, and P. Shingaki. Feedstock Crop Trials for Hawaii and the Tropics. S-1041-The Science and Engineering for a Biobased Industry and Economy Annual Meeting, Kahului, Maui, HI, June 17-18, 2013.

Youkhana, A., S. E. Crow, M. N. Meki, J. R. Kiniry, R. Ogoshi, and M. Nakahata. Belowground biomass and C dynamics in sugarcane and ratooning energycane cultivated as

biofuel production in Hawaii. ASA, CSSA, and SSSA International Annual Meetings, Tampa, FL, November 2013. (Contributed poster)

Hashimoto, Andrew, Richard Ogoshi, Devin Takara, Samir Khanal, Susan Crow. High-Yield Tropical Feedstocks for Bioenergy Production. European Biomass Energy Conference, Hamburg, Germany, June 23-26, 2014.

Kablan, R.A., R.M. Ogoshi, A. Youkhana, and M. Nakahata. 2014. Spatial and temporal distribution of soil moisture In drip irrigated tropical grasses grown in Hawaii. ASA, CSSA, SSSA International Annual Meeting, November 2-5, 2014, Long Beach, California.

Ma, S., P. A. Scharf, Q. Zhang, M. Karkee, J. Tong, and L. Yu. "Effects of Growth Characteristics of Sugarcane Clusters and Cutting Height on Harvester Performance: Cutting Quality." Presented at 18th World Congress of CIGR, Beijing, China, September 16-19, 2014.

Ogoshi, R., R. Kablan, A. Youkhana, and M. Nakahata. 2014. Biomass yield response to temperature for three tropical grass species. ASA, CSSA, SSSA International Annual Meeting, November 2-5, 2014, Long Beach, California.

Meulemans, Jabez, Susan E. Crow, John Yanagida, and Jonathan Deenik. "Linking global warming potential and economics to the sustainability of biochar use in Hawaii agriculture", Poster presentation, CTAHR Student Research Symposium, University of Hawaii at Manoa, April 9, 2015.

3.4. Low Cost Materials for Solar Fuels Production

In order to obtain substantial reductions in installed photovoltaic (PV) costs, significant achievements are required in discovering new absorber materials that are low-cost, can be processed easily using high-throughput techniques, and still provide high solar conversion efficiencies. One candidate that can meet these requirements is a multi-compound alloy containing five Earth-abundant chemical elements: copper, zinc, tin, sulfur and selenium (CZTSSe). Leading institutions have reported efficiencies over 10% with CZTS thin film materials. However, CZTSSe has the potential to achieve the 20% efficiencies already demonstrated by analogous multi-elemental thin film materials such as copper-indium-gallium-selenide alloys. During this reporting period, our team at HNEI focused on the development of a low-cost high throughput process to create functional CZTSSe cells. Our process includes three key steps: 1) synthesis of liquid inks containing CZTS nanocrystals, 2) ink printing onto conductive substrates and 3) thermal annealing of printed inks to form dense CZTSSe polycrystalline solar absorbers.

In step 1, printable CZTS nano-crystalline inks were synthesized using the so-called "hot injection technique". First, precise amounts of metal chlorides ($CuCl_2$, $ZnCl_2$ and SnCl) were dissolved in ethylene glycol (EG). The solution was then transferred into a 3-neck flask, purged with nitrogen and heated at 250°C. After this step, a second EG solution containing sulfur was rapidly injected in the hot CZT/EG mixture, leading to the spontaneous formation of CZTS nanoparticles. The CZTS/EG solution was kept at 250°C for 30 minutes. Then, the reaction was quenched by placing the flask in a water bath. Finally, the CZTS nanoparticles were collected by centrifugation and washed 3 times with hexane to remove impurities (mainly chlorides). With this technique, we have achieved mono-dispersed CZTS nanocrystals approximately 10 nm in

diameter (Figure 3.4.1. a). In step 2, ink containing the CZTS nanocrystal "building blocks" were deposited onto conductive substrates (molybdenum coated glass) using spray pyrolysis techniques. In this process, the substrates were placed onto a hot plate (200°C) approximately 10 inches below the spray nozzle. Ink flow and volume were adjusted to achieve compact layers of CZTS nanocrystals. In step 3, CZTS-coated substrates were placed into a furnace with few milligrams of elemental selenium and heated at 500°C for 30 minutes. During this step, the selenium reacted with the CZTS nanoparticles to form large CZTSSe crystals. Eventually, the entire spray-deposited CZTS film was converted into a dense polycrystalline thin film material (Figure 3.4.1. b), comparable to what one would achieve with conventional vacuum-based processes. Finally, newly formed CZTSSe materials were integrated as solar cells using a standard architecture for thin film-based absorbers (Mo/CZTSSe/CdS/ZnO/ITO). The photocurrent vs. voltage characteristic of a typical CZTSSe-based solar cell is presented in Figure 3.4.1.c. The cell's short-circuit photocurrent density, open circuit voltage and efficiency were 19 mA/cm^2, 375 mV and 2.3%, respectively.

This study demonstrates that liquid processing can be used to create functional CZTSSe solar cells, a necessary step towards low-cost solar cell technologies. Future efforts will be focused on tuning CZTSSe absorber chemical composition to improve solar cell efficiency. We will also explore post-synthesis treatments, such as alkali doping, to heal electrical defects.

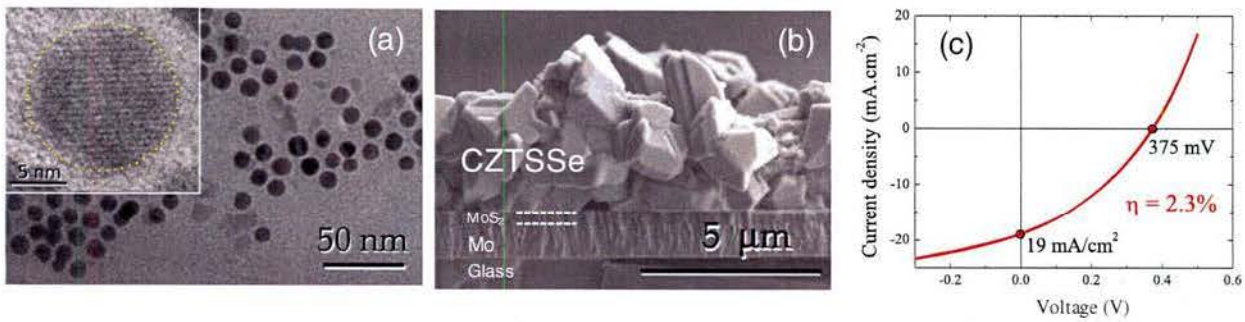

Figure 3.4.1. (a) transmission electron micrograph of CZTS nanoparticles, (b) scanning electron micrograph of an annealed CZTSSe solar absorber and (c) current vs. voltage characteristic of a CZTSSe-based solar cell.

3.5 Hydrogen Fuel Production

With collaborative funding from ONR, the US Department of Energy (US DOE), and the State of Hawaii, HNEI is developing and implementing hydrogen projects in Hawaii on Oahu and the Island of Hawaii. These projects support the objectives of developing/evaluating: 1) hydrogen technologies for operational missions for Navy, 2) hydrogen infrastructure to displace fossil fuels in transportation applications, and 3) validating hydrogen as a contributing technology for increasing the amount of renewable energy on the electrical grid, to displace fossil fuel power generation. APRISES 11 funding was used to maintain the Marine Corps Base Hawaii (MCBH) hydrogen fueling station, and to study the impact of the environment on the equipment.

To support ONR's deployment of 5 General Motors (GM) Equinox Fuel Cell Vehicles at MCBH, HNEI provided hydrogen fueling technology to enable the US Navy/Marine Corps to conduct technical evaluations and gain experience in the operation of Fuel Cell Electric Vehicles

(FCEV). Hydrogen fueling was examined for potential use in operational systems as well as non-tactical commercial fleet vehicle operations.

In related research efforts on the Island of Hawaii, HNEI is evaluating the ability to use a dynamically operated electrolyzer as a grid management tool to allow greater penetration of intermittent renewable energy sources on the grid, and to produce hydrogen fuel. Under future funding, the hydrogen will be used to fuel hydrogen fuel cell electric buses (FCEBs) operated by the County of Hawaii Mass Transit Agency (MTA), and the Hawaii Volcanoes National Park (HAVO) bus demonstration project. The HAVO buses will be operated in an intermittent high SO_2 environment and will provide ONR valuable data on the performance of Polymer Electrolyte Membrane (PEM) fuel cells in environments that may be similar to those found on the battlefield.

Demonstration of Hydrogen Fueling Technology at Marine Corps Base Hawaii

APRISES 11 funding was used during the 2016 to mid-2017 operational period to support ongoing maintenance of the MCBH hydrogen station. The close proximity to the ocean, trade wind conditions, dust, and high temperatures provide and aggressive environment that is very harsh on the equipment and enclosures. Since operations were suspended, considerable maintenance work was required in order to preserve the equipment. A variety of maintenance challenges were revealed and are documented in order to support future design considerations for operation in such an environment. Periodic operation of major components such as the electrolyzer and compressors is very important for preserving the overall operability of the system. The following findings were developed from our experience in the operation and maintenance of this station:

- Design the system to meet the challenges of the environmental conditions at the site and consider ample ventilation and filtration of salty or dusty air;
- Only use high quality stainless steel components. While it increases the initial procurement cost, the reduced maintenance and replacement costs will more than pay back the additional upfront cost;
- Operate major components weekly. Sitting in a hot, humid, and corrosive environment reduces life span of the system. Operating the machinery (e.g. compressor, pumps etc.) ensures that bearings remain lubricated and metal parts will not seize up;
- Wash exterior surfaces with fresh water, especially air breathing radiators, and change filters frequently;
- Keep a stock of filters and other consumables to avoid prolonged down time during which operation is not possible;
- Use corrosion prevention measures from the outset to prevent problems, and then also inspect frequently for corrosion and initiate maintenance as soon as problems are discovered to keep them from spreading; and
- Ensure proper grounding of all metal objects.

The full maintenance report, "Maintenance Report: MCBH Hydrogen Filling Station", (June, 2017) is available on the HNEI website.

Island of Hawaii Integrated Hydrogen Systems

This project included the following tasks:

- Demonstrate the use of electrolyzers to mitigate the impacts of intermittent renewable energy by regulating grid frequency;
- Characterize the performance & durability of commercially available electrolyzers under dynamic load conditions.

Intermittent Renewable Energy Sources and the Grid

The increase in penetration of intermittent renewable wind and solar energy onto the grid is accelerating rapidly, particularly in island locations such as Hawaii where renewable sources are locally abundant and conventional fossil fuel energy sources only exist by importing and hence are expensive. As the amount of renewable energy has increased, it is apparent that a major limitation of renewables on grids is their intermittent capacity, as they sometimes over-feed the grid with excess capacity or drop off completely, both on a short term (minutes) and long term (days) basis. Most grids must use expensive backup power generators that are at idle power settings ("spinning reserve") ready to ramp up quickly to support the grid when wind is idle or photovoltaic (PV) arrays are shaded by cloud cover. While large grids with only 5-20% of grid capacity coming from renewable sources see little effect, the variability of renewable power significantly affects frequency regulation on smaller grids – that is, it becomes increasingly difficult to keep the grid at its nominal frequency. The goal to have stand-alone grids operating 100% from renewable sources is presently challenging due to the technical and economic challenges of energy buffering.

The line frequency, or to be precise, deviation from it, is a measure of the load balance of the grid as the utilities' synchronous generators respond to a higher load with a slightly slower spin and vice versa. There are multi-stage control systems to stabilize the frequency, such as ramping power generation up/down, but a battery can be very useful as a fast source/sink of power. HNEI hypothesized that an electrolyzer could also be used to help manage these variable loads. While an electrolyzer cannot source power, it can represent a controllable load that can be reduced when other loads increase in order to keep the total balance and the frequency stable. So in general, the faster and bigger the electrolyzer is, the more useful it is for load balancing. A battery will always remain faster than an electrolyzer to respond to frequency deviations, and therefore able to smooth power supply before frequency becomes an issue, as well as being able to smooth out fine ripples. However, slower load change (seconds) can be counteracted by the electrolyzer, reducing the size of the required battery.

The use of an electrolyzer in this way provides an "ancillary service" to the grid that can be assigned a monetary value. This monetary value can be used to offset the cost of hydrogen production. The hydrogen in turn can be used in high value applications such as a transportation fuel. HNEI has been conducting research to assess the technical potential and economic value of using an electrolyzer-based hydrogen production and storage system as a demand response tool for grid management. A 65 kg/day hydrogen energy system (HES) consisting of a PEM electrolyzer, 35 bar buffer tank, 450 bar compressor, and associated chiller systems, has been purchased and will be installed at the Hawaii Natural Energy Laboratory Hawaii Authority

(NELHA) to demonstrate long-term durability of the electrolyzer under cyclic operation required for frequency regulation on an island grid system. The hydrogen produced by the electrolyzer will be used to supply hydrogen for two fuel cell electric buses (FCEB) to be operated at Hawaii Volcanoes National Park (HAVO) and one FCEB by the County of Hawaii Mass Transit Authority. As illustrated in Figure 3.5.1, the hydrogen will be transported in hydrogen tube trailers from the NELHA production site to the HAVO dispensing site. A second dispensing site is located at the NELHA production site.

Figure 3.5.1: Project Concept

A comprehensive test plan was developed to characterize the performance and the durability of the electrolyzer under dynamic load conditions and initial testing was conducted at Powertech Labs in Vancouver Canada. A main objective of the test plan was to determine the operating envelope and dynamic limits of the electrolyzer and the overall HES. A multi year study at NELHA will evaluate the HES performance under a load profile developed from a fast acting Battery Energy Storage System (BESS) that is currently in use as a grid management tool on the Big Island grid. These tests shall demonstrate whether the electrolyzer has the capability to effectively mitigate the impacts of intermittent solar and wind power on the grid, while continuously generating 90-80% of its designed hydrogen production capacity.
HNEI was invited to present a paper to the Electrochemical Society (ECS) that describes the HES configuration, plans for operation in the field, and results of initial tests to determine the dynamic response of the electrolyzer and overall system. A link to the paper is available on the HNEI website, "M. Ewan, R. Rocheleau, K. Swider-Lyons, P. Devlin, M. B.V. Virji, G. Randolf, Development of a Hydrogen Energy System as a Grid Frequency Management Tool, ECS Trans. 2016 75(14): 403-419 (Oct. 2016).

It is planned to continue the test program utilizing APRISES 12 funding.

Hydrogen Energy System Simulation Model for Grid Management Applications

HNEI utilized data collected from its test program conducted at Powertech Labs to develop and validate a dynamic simulation model of the HES.

The main objectives of the Hydrogen Energy System (HES) Simulation Model are to:

- Develop electrolyzer, battery energy storage system (BESS), renewable power sources and utility grid models using measured performance data of a hydrogen energy system deployed on the Island of Hawaii;
- Develop, evaluate and optimize a grid management control algorithm under a wide range of grid operating conditions;
- Characterizes the performance of an HES system under realistic dynamic or cyclic load profiles;
- Study the trade-off between different sizes of electrolyzer systems (kW to MW) and storage systems required for optimal grid management strategies incorporating different renewable power sources; and
- Evaluate the performance of a hybrid electrolyzer system (electrolyzer + BESS) using different grid management control algorithms.

Grid Management HES Simulation

- The HES simulation is being developed in the Matlab and Simulink Environment.
- The HES simulation will have a HES model which will include the following:
    - Electrolyzer system model;
    - Grid power system model;
    - BESS model;
    - Control algorithms model; and
    - Different renewable power source models.
- HES simulation will be used to evaluate the hybrid electrolyzer-BESS system under different grid management control algorithms as functions of frequency deviations.

For more on results of the model development, see the detailed report on the HNEI website, "Hydrogen Energy System Simulation Model for Grid Management Applications", (June 2017). The modeling effort will be continued under APRISES 12 funding.

Hydrogen Gas Sampling System

A hydrogen gas sampling system was developed and procured to support the operation of FCEBs on the Island of Hawaii. There is an ongoing requirement to ensure that the purity of the hydrogen dispensed to the Fuel Cell Electric Buses meets the specifications defined in SAE J2719 (2015). Once the sample is taken it will be sent to a test laboratory for analysis. As recommended in SAE J2719, a system that is capable of sampling particulate concentration per ASTM D7650-13 and capturing hydrogen for gas quality measurements per ASTM D7606-11 was designed and fabricated by Powertech Labs. The completed system is illustrated in Figure 3.5.2 and includes the following:

- 0.22 micron polytetrafluoroethylene (PTFE) filter holder for collecting particulate samples;
- Hydrogen isolation valves, regulator, receptacle, and adapter fittings;

- A hose to connect to the NELHA and HAVO hydrogen dispenser vent stacks for safely venting hydrogen;
- Connections for a 1 liter sampling cylinder; and
- Hard case for shipping and safe storage.

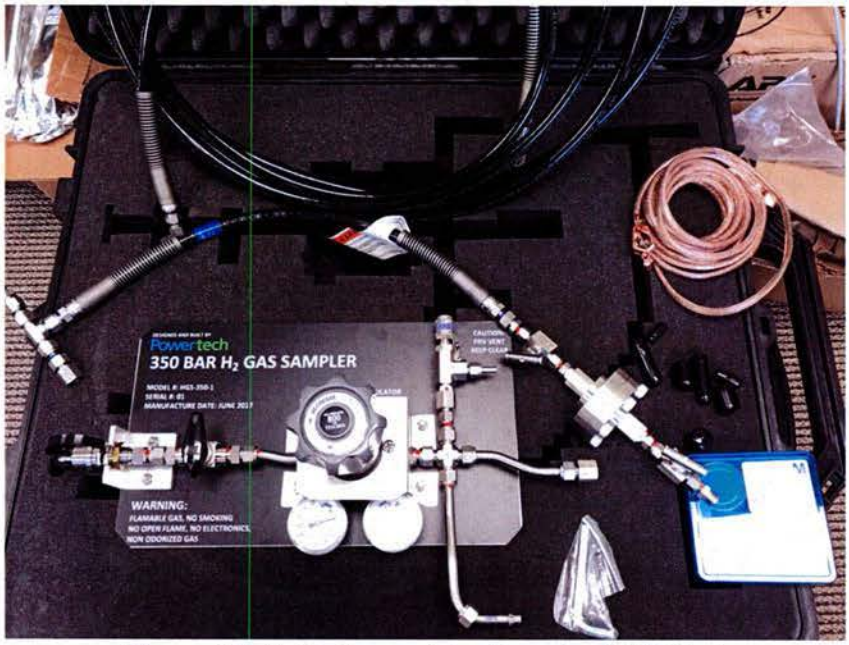

Figure 3.5.2 Hydrogen Gas Sampler (350 Bar)

Publications Resulting from these Efforts

G. Randolf, Grandalytics, *Maintenance Report: MCBH Hydrogen Filling Station*, (June, 2017)

M. Ewan, R. Rocheleau, K. Swider-Lyons, P. Devlin, M. B.V. Virji, G. Randolf, *Development of a Hydrogen Energy System as a Grid Frequency Management Tool*, ECS Trans. 2016 75(14): 403-419, (Oct. 2016).

M.B. V. Virji, Hydrogen Renewable Energy System Analysis, *Hydrogen Energy System Simulation Model for Grid Management Applications*, (June 2017).

Task 4. OCEAN ENERGY

Efforts under Task 4 included continued development and testing of cost effective heat exchangers for Ocean Thermal Energy Conversion by Makai Ocean Engineering; and preliminary efforts in support of wave energy testing at the Navy's Wave Energy Test Site (WETS), off Marine Corps Base Hawaii (MCBH).

4.1 OTEC Heat Exchanger Development and Testing

Building on previous ONR-funded work, APRISES11 continued efforts to test, evaluate and develop an Ocean Thermal Energy Conversion (OTEC) heat exchanger. HNEI subcontracted with Makai Ocean Engineering Inc. to conduct testing at the OTEC test facility at the Hawaii Natural Energy Laboratory of Hawaii Authority (NELHA). The long term goal of effort is to develop an economically viable OTEC power plant. As one of the most expensive components in an OTEC plant, proper heat exchanger selection is crucial to the economic viability of OTEC. Heat exchanger development must balance size, cost, and performance. To meet this goal, the OTEC HX Testing Program is divided into three areas: HX Performance Testing, HX Design Development, and Corrosion Testing. This report summarizes the activities conducted by Makai Ocean Engineering from March 2013 to December 2014, under APRISES11. For detailed information, please refer to the online report "OTEC HX Testing Program; 2014 Annual Report", prepared by Makai Ocean Engineering, December, 2014.

Major accomplishments under APRISES11 include:
HX Performance Testing Facility

- Facility used to complete performance testing of APV Titanium Plate-Frame Heat Exchanger, APV Cross Flow Heat Exchanger, and Lockheed Horizontal Heat Exchanger.
- Modifications completed in preparation for turbine installation and testing.
- Upgraded instrumentation and instrument wiring on the facility.
- New revision to the control software.
- Completion of 100-kW Testing Station.

HX Design Development

- APV Titanium Plate-Frame Heat Exchanger was designed, fabricated, installed, and performance tested.
- APV Cross-Flow Heat Exchanger was designed, fabricated, installed, and performance tested.
- Lockheed Martin Horizontal Evaporator was designed, fabricated, installed, and performance tested.

Corrosion Testing

- Removal and analysis of 4-year hollow extrusion corrosion samples.
- Ongoing testing of pit mitigation treatments.
- Completed testing of alternative treatments to prevent biofouling.
- Completed coatings testing.
- Installed Lockheed Martin representative heat exchanger samples and plate samples for the multi-column imaging rack (MCIR) – included WSW pre-treatment for several samples.

Major findings include:
HX Testing Facility

- No major findings

HX Design

- APV Titanium Plate-Frame Heat Exchanger had high overall heat transfer coefficient and very high seawater side pressure drop.
- APV Cross Flow Evaporator had average overall heat transfer coefficient and very low seawater side pressure drop.

Corrosion Testing

- Hypochlorination is the most effective biofoulant control.
- Siloxel and Alodine coatings provide protection but coating uniformity was unreliable and therefore, corrosion protection was limited.
- Steel is no longer being pursued as a potential material for a condenser.
- Pit mitigation treatments should be performed based on the sample's open circuit potential (OCP), not set intervals.

Technical Reports Resulting from these Efforts

Makai Ocean Engineering, *OTEC HX Testing Program; 2014 Annual Report*, (December 2014).

4.2 Wave Energy Testing

Funds in this area were intended to support Navy and US Department of Energy (DOE) efforts to establish and begin to operate the Navy's Wave Energy Test Site (WETS) offshore of Marine Corps Base Hawaii (MCBH), on the windward side of Oahu. The original intent was to support this effort in two primary ways – 1) wave resource characterization at MCBH and 2) small-scale testing of wave energy converters (WECs) at the Makai Research Pier. WETS wave resource assessment, through wave measurements, numerical wave forecasting, and the development of a robust wave hindcast database to support operational planning and WEC developer engineering designs, has been extensively carried out under DOE funding, and continues under both DOE and Naval Facilities Engineering Command (NAVFAC) funding. To this point, ONR funds have not been required in support of this effort. Further, funds have not been required to support small-scale pre-WETS deployments of WEC prototypes or related equipment since there has not yet been any WEC developer with interest in utilizing the Makai Research Pier facilities. Thus, no funds were expended for these purposes.

Instead, funds related to wave energy development were expended in the form of two subcontracts to the first WEC developer to deploy at WETS – Northwest Energy Innovations (NWEI), with activities expected to be of value to future WEC developers testing at WETS. In the first of these, HNEI funded NWEI to examine all issues relevant to the interconnection of a wave energy conversion device at the Navy's 30m (shallow water) test berth. This was the site of testing done by the Navy of various iterations of the Ocean Power Technologies WEC between 2004 and 2011. In order to utilize this test berth for NWEI's device, a survey was needed of hardware available for re-use, electrical instrumentation required for sending DC to shore for inversion and grid-connection, and other issues. For these reasons, NWEI conducted a full assessment of all systems and interconnection strategies for their Azura wave energy device, which was deployed at WETS in late May 2015 through early December 2016. The final report, entitled "NWEI Wave Energy Grid Interconnection at the Navy's WETS 30m Project Site", was provided to HNEI in June 2014, after successful deployment of the device. The report is

available on HNEI's website. Conclusions and methodologies outlined are expected to be of use to future developers utilizing the 30m test berth.

A second, smaller contract was issued to NWEI to examine issues surrounding the permitting and logistics associated with a later redeployment of a modified version of their WEC. In this NAVFAC-funded project, a heave plate was added to the base of the device and a larger float, with greater moment arm, was installed. However, insufficient funds were available to adequately address all permitting and logistics issues surrounding this second deployment at the WETS 30m test berth. NWEI was thus contracted to pursue these issues to address questions surrounding the categorical exclusion (CATEX) process undertaken by NAVFAC. A final report, entitled "Preliminary Design and Analysis to Support Permitting, NEPA Process, and Device Modification Logistics Planning", was provided to HNEI in June 2016 and is available on HNEI's website. Deployment of the modified device is expected in September 2017.

Technical Reports Resulting from these Efforts

NWEI, *Wave Energy Grid Interconnection at the Navy's WETS 30m Project Site*, (June 2014).

NWEI, *Preliminary Design and Analysis to Support Permitting, NEPA Process, and Device Modification Logistics Planning,* (June 2016).

TASK 5. GEOTHERMAL RESOURCE ASSESSMENT

The overall objective of this subtask was to perform preliminary surveys on DOD lands in Hawaii that may have some potential for hosting a geothermal resource. Prior work on the Island of Hawaii had identified electrical resistivity anomalies beneath Army Garrison Hawaii lands at Pohakuloa located between Mauna Kea and Mauna Loa. The methods used to develop those data were magnetotelluric (MT) and audio-magnetotelluric (AMT) survey methods.

The method utilizes naturally occurring broad-spectrum electromagnetic waves that are generated within the ionosphere and magnetosphere that, depending on their wavelength, can penetrate to depths from a few tens of meters to several tens of kilometers where they interact with conductive/resistive formations at depth. Those interactions then re-emit electrical and magnetic signals that can be detected at the ground surface. Current detection and analysis technology allows us to model the detected signals to provide resistivity distributions below our survey instruments to depths of a kilometer or more. The value of this technology to geothermal exploration derives from the observation that subsurface thermal activity can lower the electrical resistivity of subsurface formations in multiple ways: rocks that are saturated with warm water are more conductive than rocks saturated with cold water; thermal waters typically contain higher concentrations of dissolved solids, and therefore are more conductive, than cold groundwater; and thermal fluids break down primary minerals in buried lavas and deposit secondary minerals and clays that are more conductive. The success of this approach has been demonstrated at the Army Garrison Hawaii Pohakuloa site where MT/AMT surveys identified anomalously low resistivity formations that, when drilled into, showed temperatures in excess of 140 °C and a temperature gradient of ~165 °C/km. MT surveys conducted on the surrounding

DOD lands, under other funding, provided data that suggests that a substantial resource is present in that area.

In practice, application of the MT methods on Oahu proved to be extremely difficult: our primary focus was on the DOD lands within the caldera of Waianae Volcano. This is the older of the two major volcanoes making up the island of Oahu and is where the largest expanse of DOD controlled lands exist on the island. These lands are located within Lualualei Valley and the Schofield plateau. Although the Koolau Volcano is known to be younger than Waianae, there is a relatively small expanse of land, the Kaneohe Marine Corps Air Station, (KMCAS) located within vicinity of the Koolau Caldera and it was recognized that the likelihood of finding a substantial resource within this footprint was considerably lower.

The investigation of the Waianae Volcano proved to be logistically much more difficult than anticipated. Among the most time consuming challenges was approval for access: the DOD lands within Lualualei Valley are used as an ammunition depot with extremely high security, whereas the DOD lands of interest on the Schofield Plateau are, in part, a live-fire range and impact area. Hence, gaining access to the survey area consumed well over a year of interaction with various points of contact within the DOD administrative structure. Secondly, because the Lualualei facility is housing live ammunition, radio transmission of any kind by our field staff was strictly prohibited. Although our method of investigation relies on naturally occurring electromagnetic signals, in some environments, where there is anthropogenic radio-noise, we can enhance our ability to filter out that noise using low-power transmission of a controlled source radio frequency (RF) generator. Due to the absolute prohibition on RF generation, we were precluded from employing this technique within the valley. Finally, the use of significant areas of the Schofield lands for live-fire training severely restricted the locations available to us for placement of our survey stations. Hence, we were limited to a single transect outside the boundary of the Waianae Caldera on the DOD lands at Schofield.

In spite of the access restrictions we were able to conduct AMT measurements at 22 stations surrounding and within the Waianae Caldera (Figure 5.1) below. The stations with LLL prefix are within the Lualualei Valley; those with WK are within the Waianae Caldera in a district referred to as Waianae Kai; and those designated SCH are on the Schofield Plateau immediately outside of the mapped Waianae Caldera boundary. Our selection of these sites was based on an effort to detect flow of thermal fluids within and along the boundary faults that are present in caldera regions of Hawaii's volcanoes. Table 5.1 lists the station numbers and their Universal Transverse Mercator (UTM) coordinates.

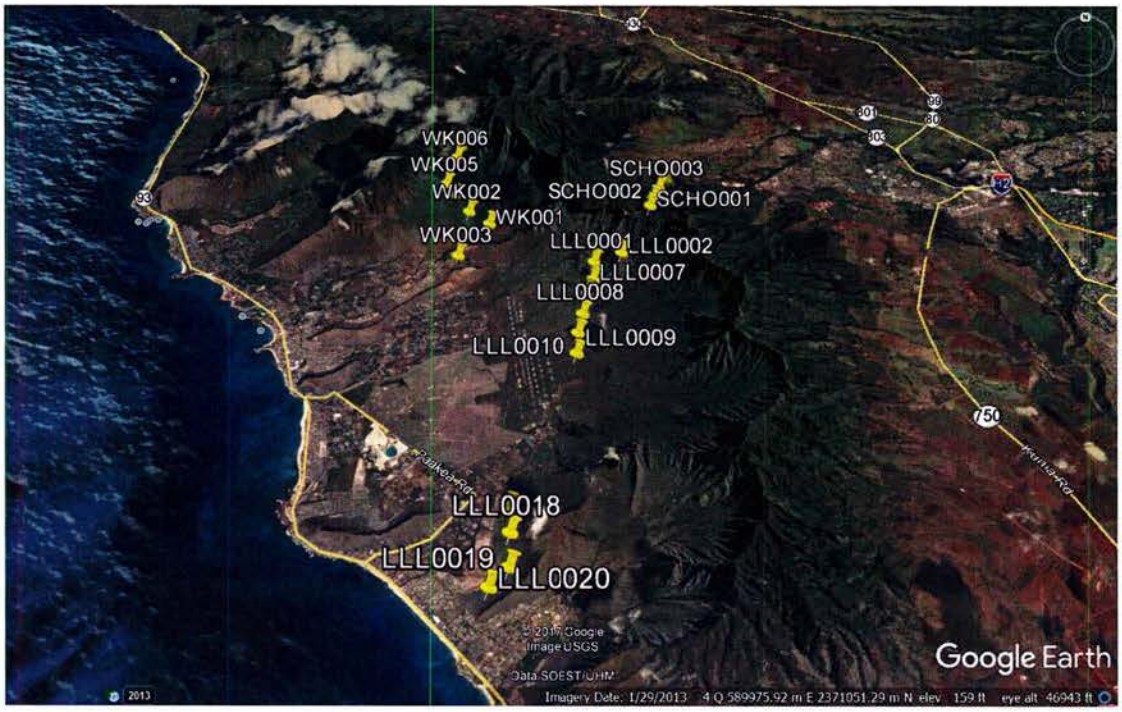

Figure 5.1. Image of the Waianae Caldera and Schofield Plateau area of Oahu. The ridges that define the eastern boundary of the Lualualei Valley define the eastern and southern boundary of the Waianae Caldera.

Site ID	Date of survey	Longitude (UTM)	Latitude (UTM)	Elevation (m)
Lualualei Valley				
LLL006	6/4/2015	590410	2372526	97
LLL010	6/5/2015	590204	2370779	80
LLL009	6/5/2015	590225	2371371	80
LLL008	6/5/2015	590317	2371919	83
LLL007	6/5/2015	590531	2372957	106
LLL001	6/6/2015	590553	2373491	122
LLL002	6/6/2015	591147	2373611	308
LLL017	6/9/2015	589045	2367099	60
LLL018	6/9/2015	589090	2366611	70
LLL019	6/10/2015	589111	2365951	55
LLL020	6/10/2015	588796	2365577	43
Schofield Barracks				
SCH001	5/2/2016	591820	2374994	462
SCH002	5/2/2016	591913	2375311	494
SCH003	5/4/2016	592056	2375740	438
SCH004	5/4/2016	592267	2376101	427
Waianae Kai				
WK001	6/11/2015	588152	2374662	180
WK002	6/11/2015	587659	2375057	211
WK003	6/11/2015	587537	2373621	127
WK004	5/10/2016	587286	2375571	277
WK005	5/12/2016	587064	2375924	333
WK006	5/13/2016	587234	2376821	471
WK007	5/13/2016	587325	2377136	511

Table 5.1. List of Waianae Caldera audio-magnetotelluric (AMT) stations and their Universal Transverse Mercator (UTM) coordinates.

The survey data, once acquired presented additional challenges: as noted above, the presence of anthropogenic noise can seriously impact the AMT results gathered in the field. In Figure 5.2 we present, for comparison, the results of a measurement station on Hawaii Island where there is minimal anthropogenic noise background. The plot of the apparent resistivity given in ohm-meters, (rho) versus the signal period provides relatively smooth curves for the North-South and East-West signal vectors; the divergence in the apparent resistivities at longer periods (and greater depths of penetration) indicates the presence of structural bodies at depth (e.g. dikes) that have differing resistivities across and along the strike of those features. Nonetheless, the relatively smooth apparent resistivity versus frequency relationship indicates a robust set of resistivity data.

Figure 5.3 presents examples of the data recovered from the current surveys. Sounding ZLL0605 was conducted at station LLL0007 near the center of the survey line across

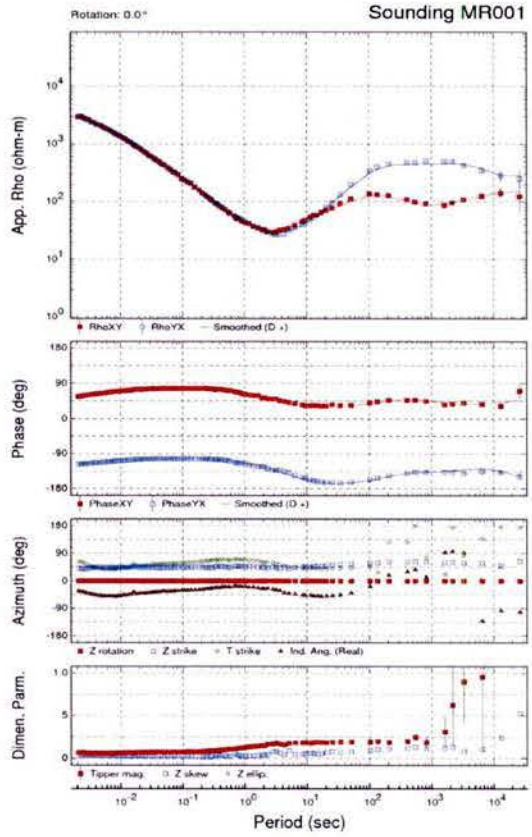

Figure 5.2 (right, set of four graphs). Showing apparent rho values versus signal period over the spectrum recorded at a station on Hawaii Island. The relatively smooth trends in apparent rho versus period are typical of measurements made in a region free of intense radio-noise.

Figure 5.3 (below). Showing apparent rho values versus signal periods, examples of the data recovered from the current surveys. The left-most figure shows data characteristic of a high radio-noise environment that substantially interferes with collection of the natural AMT signals. The right-hand figure, although somewhat better, still is significantly impacted by interfering noise signals.

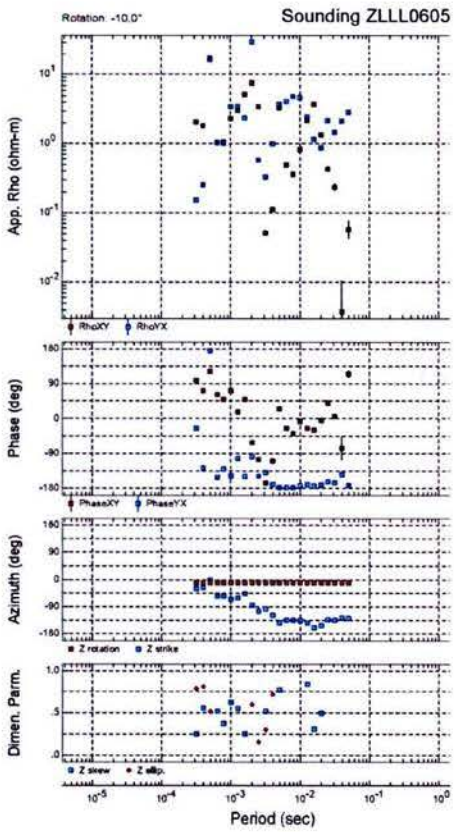

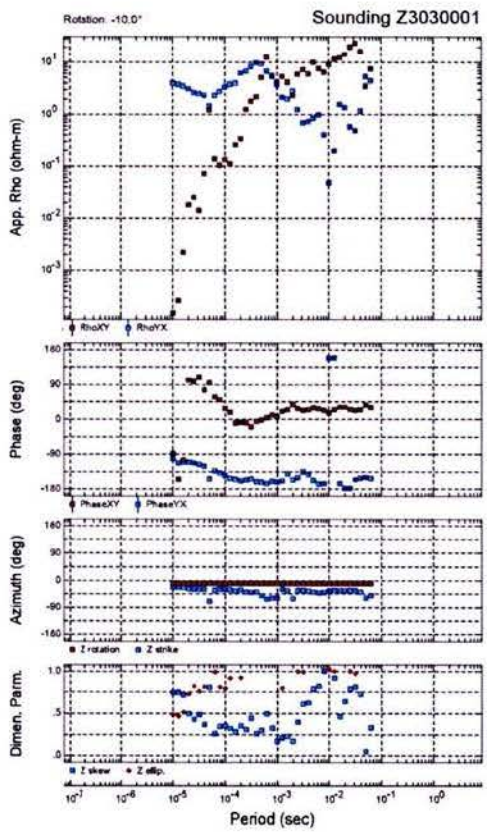

the floor of Lualualei Valley. As is evident, the apparent rho varies wildly over the frequency spectrum recorded for both the N-S and E-W vectors. These highly variable apparent rho values are characteristic of data collected in a high radio-noise environment; in some stations within the caldera, the radio-noise was so intense that the instruments saturated and we were unable to collect useable data at all. At station Z3030001, located at site LLL0020, the apparent rho values are somewhat more consistent, but still show significant random variability through the spectrum as well as significant divergence between the N-S and E-W resistivity vectors. The data recovered from LLL0020 was the best data set that we were able to recover among the stations deployed in this survey; the data do not, however, provide us sufficient reliability or consistency to generate a credible model of subsurface resistivity variations within the caldera and on the caldera boundaries.

It is often possible to conduct extensive post-processing on these data sets to allow us to better define the resistivity structure within the network of stations surveyed, and requires sophisticated mathematical and computational skills. This effort was underway when, unfortunately, our research team member, Dr. Barry Lienert, who had been working with us on developing software to conduct post-processing of these data sets, passed away unexpectedly before he was able to complete that work. We are currently recruiting a geophysicist with the skill set required to resume this effort. We do not, as of yet, have them on staff and hence, further processing of the data to better define the resistivity structures below the Waianae Caldera will need to be deferred until such time as we have those capabilities available to complete this work under other funding. The balance of this APRISES11 funding was used on the APRISES12 geothermal exploration project on DOD lands on Hawaii Island. (Results of that effort will be included in the APRISES12 final technical report.)

Given the challenges that we have encountered with acquiring useable data from the Waianae Caldera area, we don't believe that it will be feasible to collect useable MT data in the vicinity of the KMCAS in the Koolau Caldera region due to the high level of urbanization both on the DOD lands and adjacent to those lands in the Kailua community that abuts the KMCAS. We are, under other funding sources, continuing to pursue investigations of thermal potential in the vicinity of the KMCAS using methods that, although not as informative as MT, are not as sensitive to anthropogenic radio-noise that seems to blanket most of Oahu island.

In summary, we were able to collect a suite of AMT field data across the Waianae Caldera and on its flanks. Unavoidable anthropogenic radio-noise has seriously impacted our ability to process and model the data collected. Further post-processing and a final assessment of the geothermal resource potential in this region will have to be deferred until we can restore data processing and analysis capabilities (to be completed under other funding).

Task 6. MICROGRIDS/GRID INTEGRATION

6.1 Solar Hydrogen at Marine Corps Base Hawaii

Under this task it was planned to deploy a PV test platform at the Marine Corps Base Hawaii (MCBH) to compare side-by-side performance of commercially available PV modules and system architectures. Following concerns about the structural integrity of potential rooftops for PV deployment, the project plan was modified to consider use of carport structures in a lot adjacent to the MCBH hydrogen station. The design of the testing and data acquisition system was completed in 2015. However, due to lack of a gift approval from MCBH, the PV carports were not constructed and the project was canceled in August 2016. The funds were used to support detailed PV performance testing and analysis using existing HNEI PV test beds, primarily one deployed at Maui Economic Development Board (MEDB) under previous funding. This report outlines the work that was accomplished under this subtask to develop the design of the PV test bed and data acquisition system at MCBH, still potentially useful should another research opportunity at an alternate location arise. The report also describes work done at existing PV test beds, including maintenance, as well as analysis of the first year of operation at the new HNEI test platform on Maui.

PV test platform at MCBH

Testing, monitoring, and carport plans were developed during the reporting period, resulting in a final design and cost estimate for the 100 kW PV test platform to be installed at MCBH. Testing at MCBH was to complement experiments done at other HNEI PV test platforms installed under different ONR and Department of Energy (DOE) grants. These include a test bed at UH Manoa campus on Oahu in operation since 2010, PV installed on energy efficiency test platforms (FROG projects) operating since 2013 on Oahu and Kauai (studied under another APRISES task), and the latest platform commissioned in early 2016 at MEDB on Maui. UH Manoa and FROG installations provide side-by-side comparison of 2 to 4 grid-connected PV systems. The MEDB platform consists of 15 PV systems (~2kW each for a total rated power of ~22kW), comparing 10 PV modules and 3 system architectures. MCBH was to include the same set of PV systems for site-by-site comparison between MCBH and MEDB. With the large area available at MCBH, the testing plan included the evaluation of additional PV technologies, i.e. PV modules and auxiliaries (inverter, microinverter, optimizer).

Table 6.1.1 describes the PV modules selected for testing at MCBH. It includes the PV manufacturer, name or acronym, and technology. The next columns detail the rated power and efficiency at standard test conditions (STC), the number of PV modules under test, and the total rated power. The overall installation was to include 412 modules for a total rated power of ~100 kW. The last column indicates the other HNEI test platforms where the modules are already being evaluated.

Selected PV technologies included:

- 12 standard crystalline modules (p-type, poly or monocrystalline) from 9 manufacturers. Multiple module models from the same PV manufacturer were selected for comparison of

different module designs varying by the number of bus bars or the location of the contacts (front versus rear contacts).

- 4 high efficiency modules (n-type) including a mixed technology with intrinsic thin layer (HIT) and a bifacial.
- 4 thin film modules including 3 Copper Indium Gallium Selenide (CIGS) and 1 Cadmium Telluride (CdTe).
- Auxiliaries from 7 manufacturers to evaluate string inverters of different sizes from 2 kW to 7.5 kW, microinverters, and optimizers.

Table 6.1.1: Description of the PV modules selected for MCBH test platform.

#	Manufacturer	PV Name	PV Technology	Rated Power [W]	Efficiency [%]	# of PV	Total Rated Power [kW]	Currently tested at
1	ET Solar	S1	p-type, poly	250	15.4%	14	3.5	MEDB
2	Kyocera	S2	p-type, poly	250	15.2%	14	3.5	MEDB, UH Manoa
3	Solarworld	S3	p-type, mono	250	14.9%	14	3.5	MEDB
4	LG	S4	p-type, mono	250	15.5%	14	3.5	MEDB
5	Canadian Solar	S5	p-type, mono	260	16.2%	14	3.64	
6	Canadian Solar	S6	p-type, mono, 4 bus bars	265	16.5%	14	3.71	
7	Canadian Solar	S7	p-type, mono, rear contacts	265	16.5%	14	3.71	
8	Mitsubishi	S8	p-type, mono, 4 bus bars	260	15.7%	14	3.64	FROG
9	Suntech	S9	p-type, mono	250	15.4%	14	3.5	
10	Suntech	S10	p-type, poly	250	15.4%	14	3.5	
11	Yingli	S11	p-type, poly	250	15.3%	26	6.5	MEDB
12	Trina	S12	p-type, poly, glass/glass	255	15.2%	14	3.57	
13	Panasonic	H1	n-type, mono, HIT	240	19.0%	26	6.24	MEDB, FROG

14	Sunpower	H2	n-type, mono, rear contacts	245	19.3%	18	4.41	MEDB
15	Sunpreme	H3	n-type, mono, bifacial	280	17.1%	14	3.92	
16	Suniva	H4	n-type, mono	265	16.3%	110	29.15	
17	Stion	C1	GIGS	140	12.9%	10	1.68	MEDB
18	Solar Frontier	C2	CIGS	170	13.4%	10	1.7	MEDB, FROG
19	Miasole	C3	CIGS	160	14.9%	14	2.24	
20	First Solar	D1	CdTe	77.5	10.8%	20	1.55	MEDB
					Total	412	98.6	

Figure 6.1.2 shows a schematic of the MCBH PV test platform. The PV modules were to be hosted by 2 carport structures of 160'x21' each, providing shaded parking areas (~34 parking stalls total) in addition to energy generation.

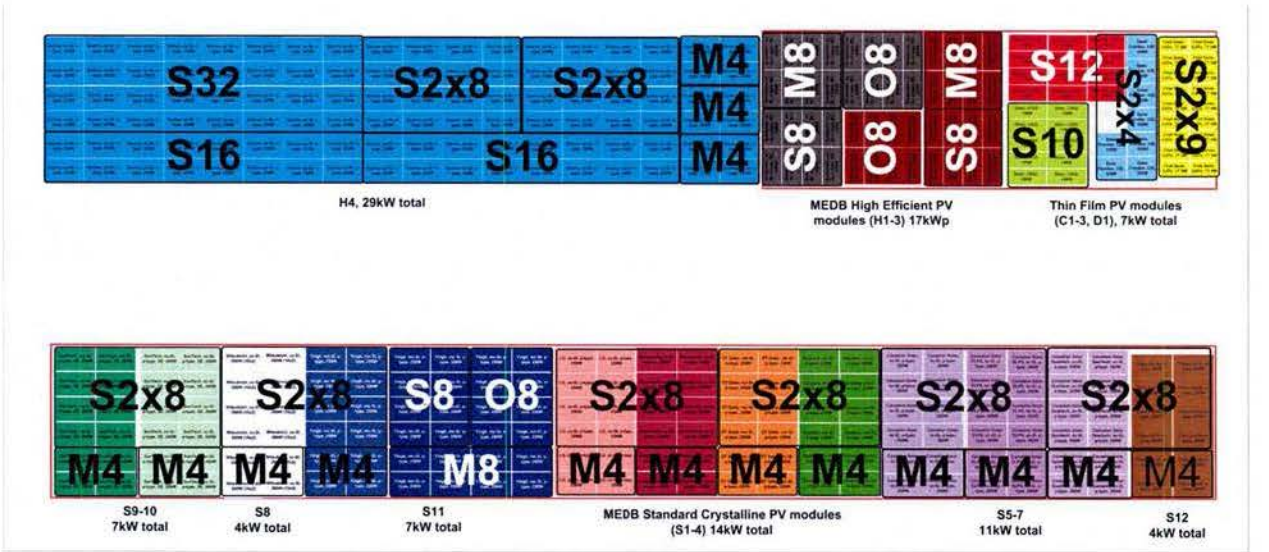

Figure 6.1.2: 100 kW PV test platform planned to be located on 2 carports at MCBH. Top carport includes PV systems made of high efficiency (H) and thin film (C, D) modules; Bottom carport hosts the standard crystalline modules (S). Large symbols indicate the system

architecture and size: first letter for system architecture with S for String, M for Microinverter, and O for Optimizer; the number after the letter is the number of modules and strings (for example, S2x8 for 2 strings of 8 modules).

Under previous ONR funding, HNEI designed and developed a highly accurate, high-resolution data acquisition system (DAS) for long term analytical monitoring of PV systems using any type of PV modules and auxiliaries. The DAS has now been implemented successfully at the MEDB test platform. Similar monitoring was planned for MCBH. The main features of the monitoring system are summarized below.

HNEI developed DC monitoring that is implemented at the module and string level. One DC monitor is required per PV system, meaning that monitoring each individual PV module for microinverter and optimizer systems is not done. For systems with optimizers, at least one optimizer is instrumented. An innovative feature was developed for DC monitoring to collect short-circuit current (I_{SC}) and open-circuit voltage (V_{OC}) on some of the grid-connected PV modules. Long-term accuracy of the DC monitoring is maintained via annual on-site calibration.

Additional off-the-shelf monitoring and testing equipment is needed to fully characterize PV system performance. This equipment is synchronized to a time server and connected to the DAS, which combines all collected data. An AC power meter collects AC voltage, current, frequency, active and reactive power of the PV systems to assess the AC performance of the PV systems, grid availability, and to support grid-connection studies. In terms of environmental measurements, the following sensors are recommended to monitor all parameters potentially affecting the PV systems. The reference solar sensor is a thermopile pyranometer that measures full spectrum global irradiance to analyze any type of PV technology. A spectroradiometer is useful to monitor the light spectrum and its potential impact on performance of the PV modules. An additional solar sensor, a masked thermopile pyranometer device, provides the diffuse/global irradiance to understand the relationship to spectral energy and estimate the impact on I_{SC}. All solar sensors are coplanar with the PV modules to assess the solar resource received by the PV systems. A weather station collects additional parameters such as ambient temperature, rainfall, wind speed and direction. Finally, a current-voltage (IV) tracer is used to collect detailed performance data of each type of PV module. Comparison of the performance of the PV modules, when in operation in a PV system or tested individually, provides information to estimate system losses.

The schematic of the DAS is presented in Figure 6.1.2. The DAS consists of 6 parts: 1) power/communication box, 2) controller box, 3) DC measurement boxes (DC MBs), 4) AC power meter, 5) environmental sensors, and 6) IV tracer. The 3 boxes on the left side of the schematic can be located near the string inverters and the AC breaker panel. The multiple DC MBs are placed underneath the PV modules. One DC MB is required per PV system plus one extra box for each optimizer system. Up to 17 DC MBs were required at MEDB and 42 were planned for MCBH. A router located in the power/communication box interfaces between the internet and the equipment. The router is part of a virtual private network (VPN) for secure communication of the instruments with a server located at UH Manoa on Oahu. The data server connects to the equipment on a daily basis to automatically collect data files created at the test location.

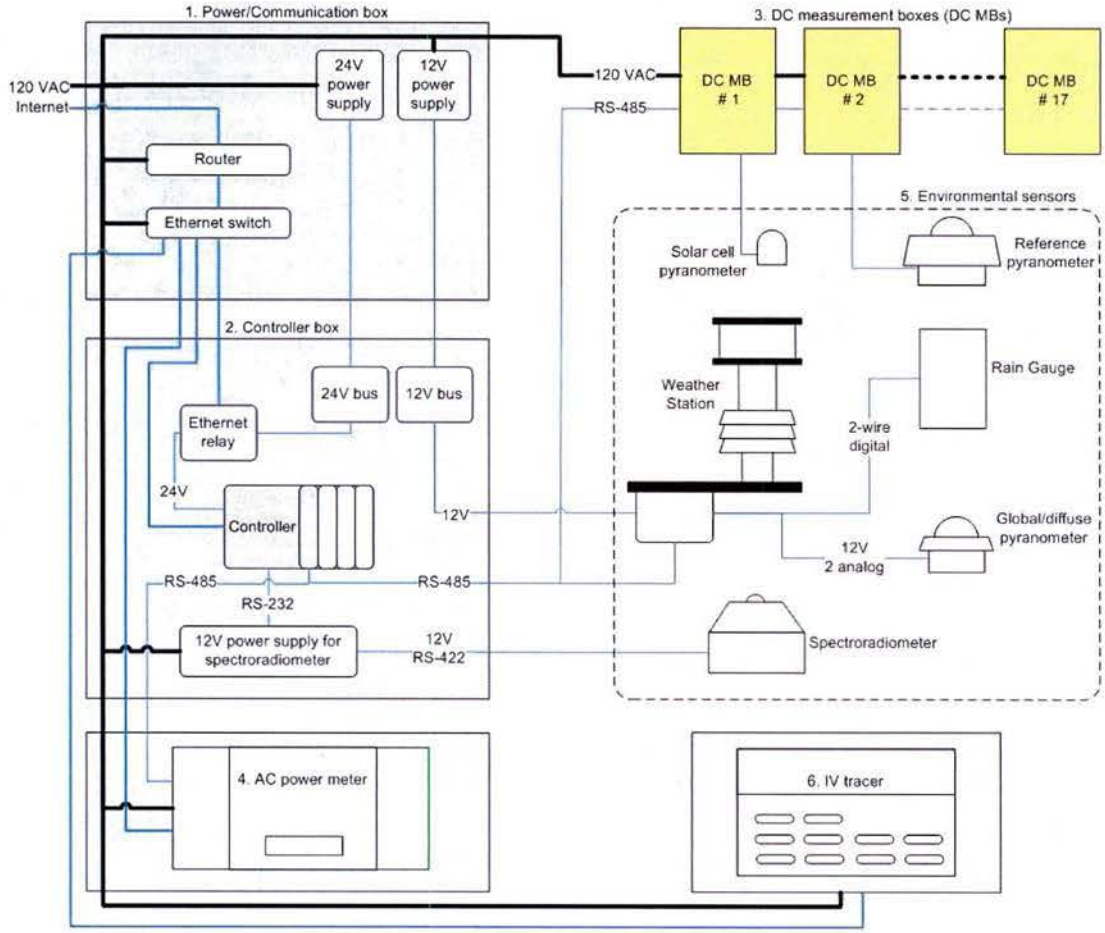

Figure 6.1.3: Data Acquisition System Architecture

Once the final design was completed, requests for proposal and purchase orders for buying PV and monitoring equipment were prepared. At the same time, HNEI prepared documents necessary to request that the base accept the PV carports as a gift. These documents included the final design presented above and the cost estimated by collecting the price of the selected PV technologies through local PV installers and online providers. The total cost for the 100 kW MCBH PV test platform, broken down in Table 6.1. **2**, is close to $1 Million including the PV technologies and carports shipped, installed, and permitted ($810k), the site preparation ($100k), and the HNEI DAS (~$90k).

Table 6.1. 2: Cost breakdown for MCBH test platform.

Description	Estimate Cost
PV modules	$167,699
Auxiliaries (inverters, optimizers, microinverters)	$91,443
Auxiliary DAS	$9,144

Total for PV technologies	$268,287
Two carports	$246,450
Total for PV technologies + carport	$514,737
Installation cost for PV + Auxiliaries + Carport	$295,740
Total for PV carport hardware + labor	$810,477
Electrical Connection	$50,000
Ground preparation	$50,000
HNEI DAS	$89,400
Total Gift Value	$999,877

HNEI worked for many months to provide MBCH with the necessary information for the PV carport test beds described above to be accepted by the Secretary of the Navy as a gift, for the benefit of both MCBH (for electrical generation and shaded parking) and the University (for research, as a direct site comparison opportunity with our test bed in Maui). Given the timeline of the funds and delays in formalizing this gift acceptance, it became apparent that insufficient time remained to undertake the Request for Proposal (RFP) process and build out the carports, and the decision was ultimately made to direct the funds to other APRISES research goals. However, the design developed for this site remains a useful approach to such a site at another location if future research objectives make that an attractive avenue. For the time being, ongoing research into comparative PV module and system performance is focused on existing test sites, with an emphasis on the most recently deployed systems on Maui.

Testing with existing PV test platforms

First-year maintenance was completed at the Maui test platform in January 2017. As mentioned earlier, long-term accuracy of the DC monitoring is maintained via annual on-site calibration using a calibration unit designed and built by HNEI [1]. The unit consists of a connection panel, a high-precision multimeter, and 2 power supplies. The equipment is integrated in a carry-on case for easy transportation between test platforms. Each power supply generates different levels of voltage and current which are applied to the input of the DC MB and the multimeter. The applied signals are measured by the highly accurate reference multimeter, which is the only component subject to annual recalibration to ensure NIST traceability. A computer is connected to the calibrator to collect and store the reference measurements and the signals read by the DC MB. Data is used to calculate the calibration coefficients (scaling factor and offset). Internal relays inside the calibrator connect and disconnect these inputs in sequence to automate the 5-minute long calibration process. First-year calibration of the MBs demonstrated high accuracy of the measurements with an annual drift estimated below 0.05% of full-scale from the original calibration points.

Maintenance at the UH Manoa test site was also conducted. The 2 thermopile pyranometers (for horizontal and plane-of-array irradiance measurements) were alternately recalibrated. The pyranometers were sent to the company ISO_CAL providing accredited calibration according to ASTM G207-11 (indoor calibration at normal incidence against a World Radiometric Reference (WRR) traceable secondary pyranometer).

Support of Existing PV Test Platforms

The first year of operation (April 2016-March 2017) of the Maui PV test platform was analyzed using MATLAB programs. The primary goals of the analysis were to evaluate the daily performance (energy rating) of the 15 grid-connected PV systems and to determine the main parameters of operation. The PV modules (Table 6.1.1) consist of 4 standard p-type mono and polycrystalline, 3 high efficiency n-type monocrystalline (including a heterojunction intrinsic thin layer (HIT) and a bifacial), and 3 thin-film including 2 Copper indium gallium selenide (CIGS) and 1 Cadmium telluride (CdTe). Results were presented at the 44th IEEE Photovoltaic Specialists Conference in June 2017 [2].

Given the cancellation of the MCBH project, additional effort was focused on developing a more detailed understanding of the performance limitations of the PV at the other sites. The energy rating is typically derived by calculating the performance ratio (PR), which is the product of voltage and current performance, as defined by the International Electrotechnical Commission (IEC) 61724 [3]. PR is the operating performance of the PV system and module corresponding to the daily average efficiency relative to the datasheet specifications defined at STC. This single criterion does not allow a full understanding of the performance differences between PV modules. To address this, a novel analysis approach has been developed by HNEI that provides additional performance criteria, including the voltage, current, and optical performance (see performance criteria below). Optical performance is calculated from the short-circuit current (I_{SC}). Simple empirical models are used to characterize performance as a function of irradiation, which is the primary environmental parameter affecting PV module performance (see empirical models below). The model of optical performance is used to identify the period when soiling and shading operating conditions are important. By excluding these periods, operating conditions can be dissociated to better study the impact of irradiation. Current performance can also be used to identify periods with important operating conditions because of the high correlation with optical performance. This was observed for all PV modules, except one which was diagnosed with poor efficiency in low light conditions. From the 330 days available for the first-year analysis, half of the modules were identified as being affected by these important operating conditions.

PR, voltage performance (VN), current performance (IP), and optical performance (IP_{SC}) are determined as follows:

(1) $PR = \frac{\int_{\Delta t} P_{PV} \cdot dt}{P_{MP,STC}} \times \frac{G_{STC}}{\int_{\Delta t} G \cdot dt}$

(2) $PR \approx \mathrm{IP} \times \mathrm{VN}$

(3) $IP = \frac{\int_{\Delta t} I_{PV} \cdot dt}{I_{MP,STC}} \times \frac{G_{STC}}{\int_{\Delta t} G \cdot dt}$

(4) $VN = \frac{\overline{V_{PV}}}{V_{MP,STC}}$

(5) $IP_{SC} = \frac{\int_{\Delta t} I_{SC} \cdot dt}{I_{SC,STC}} \times \frac{G_{STC}}{\int_{\Delta t} G \cdot dt}$

where P_{PV} is the power [W] of either the strings of PV modules, or of a PV module in operation in microinverter and optimizer systems, or in test with the IV tracer [W]; G_{STC} is the irradiance under STC [=1 kWm^{-2}]; Δt is the period of analysis [hour] (using hour to provide energy results directly into Wh); I_{PV} and V_{PV} are the operating current [A] and voltage [V] of the PV system or module; $P_{MP,STC}$, $I_{MP,STC}$ and $V_{MP,STC}$ are the power [W], current [A], and voltage [V] of the maximum power point at STC; I_{SC} and $I_{SC,STC}$ are the operating and STC short-circuit currents [A].

Figure 6.1.4 shows the daily performance (PR, VN, IP, IP_{SC}) of a PV module as a function of irradiation. The standard crystalline S1 was chosen as an example. Differences between modules will be presented in detail in further reports and publications (under preparation at the time of this writing). The data points indicate those days selected for model purposes and those excluded due to important operating condition impacts. The dashed lines are the predictions using the empirical model for each of the performance criteria. Performance is generally linearly correlated with irradiation, showing different sensitivities on overcast and sunny days. The same modelling approach is used for all performance criteria defined above in equations 1, and 3-5. The empirical models use two linear functions (equation 6 below) with a breaking point observed at 3 $kWhm^{-2}$. To characterize sunny days, the linear least squares regression is completed by selecting days with irradiation equal to or above 3 $kWhm^{-2}$. For overcast days, the fitting curve is calculated by including days with irradiation below 3 $kWhm^{-2}$, and constrained to intersect with the other linear fit at the breaking point.

(6) $Perf = O_{IRR} + C_{IRR} \times IRR$ calculated

(6-1) on overcast days (irradiation < 3 $kWhm^{-2}$)

(6-2) on sunny days (irradiation ≥ 3 $kWhm^{-2}$)

where $Perf$ is any one of the PV performance criteria defined in (equations 1, and 3-5); O_{IRR} and C_{IRR} are the offset and coefficient of the linear fit of $Perf$ versus irradiation.

Operating conditions

The first step to dissociate environmental and operating conditions is to determine the fitting curves of IP_{SC} versus irradiation using the least squares method. Second, the days affected by important operating condition impacts are identified as being those on which the difference between IP_{SC} and its prediction is above 1.5%. This was applied to the sunny days only due to the low number of overcast days at this location. In this iterative process, these two steps are repeated, excluding days affected by significant operating condition impacts, to develop fitting curves. The final modelling coefficients are calculated once the number of excluded days is constant.

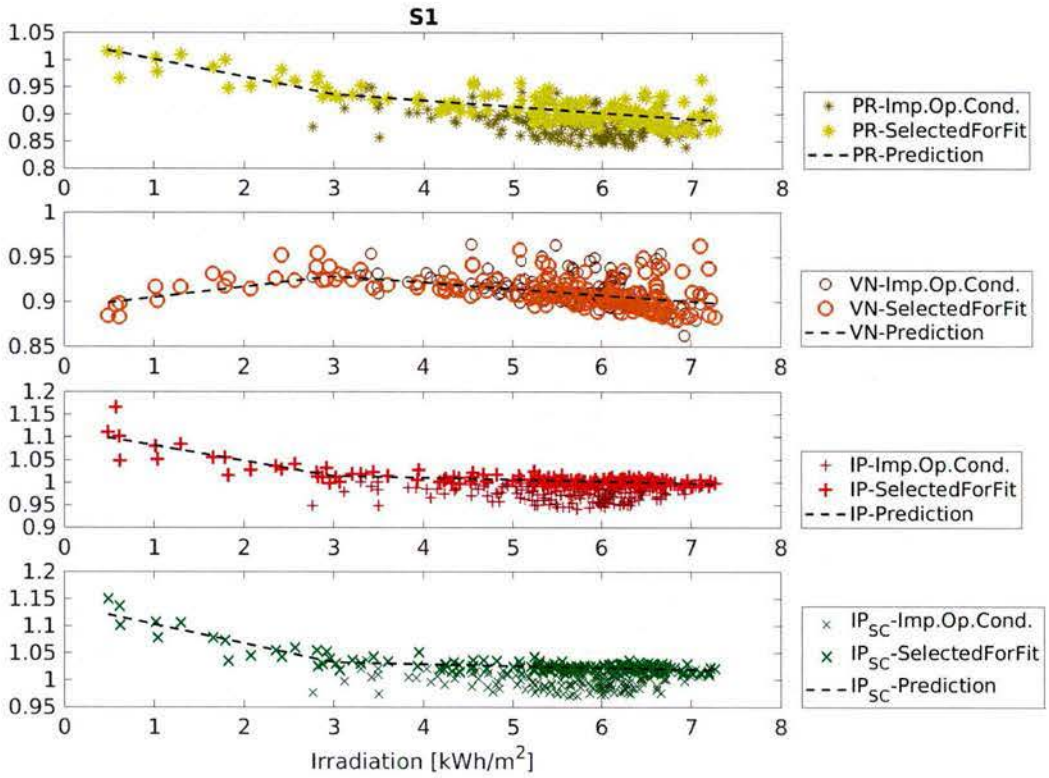

Figure 6.1.4: Impact of irradiation on daily performance criteria (PR, VN, IP, IP_{SC}) of a PV module (Standard crystalline S1); Data selected for fitting the empirical model (SelectedForFit); Data excluded due to important operating issue impacts (Imp.Op.Cond.); Empirical model (Prediction).

The Maui test platform is characterized by a mostly sunny environment with a daily irradiation averaging 5.5±1.3 kWhm^{-2}. The test site has a tropical environment with warm temperatures (28.0±1.8°C) and high spectral energy above the STC spectrum. (See [2] for complete results.)

Yearly average performance varies among PV technologies and manufacturers (See [2] for complete results and analysis.) Crystalline modules have a PR between 87% and 91% with VN between 87% and 93% and IP between 95% and 100%. There is a low difference between the standard and high efficiency crystalline modules. Two thin films outperform the crystalline modules with PR at 95% for the CdTe and 97% for one of the CIGS. This is due to high IP (104%) for the CdTe and high VN (98%) for the CIGS. This confirms that the thin films are suitable in tropical environments [4] and exhibit good energy performance in high irradiation conditions [5]. The second tested CIGS also exhibit high VN (>96%), but its performance is much lower ~10%. This low performing CIGS module was diagnosed with low optical performance (91%) and reduced efficiency in low light conditions. The results for yearly PR are within the range of previous reports [5-6]. Only the CIGS C2 system has very high PR (97%) at our location and will need validation during the second year of operation.

Irradiation is the most important environmental parameter impacting PV module performance (Figure 6.1.4). It is responsible for a range of PR, depending on PV technology, of 8% for the CIGS, 15-18% for the high efficiency modules, 20-22% for the standard crystalline modules, and up to 24% for the CdTe. Additionally, operating conditions have an important impact on daily

performance, with up to 8% reduction due to soiling and up to 20% due to shading. However, soiling effect during the full year of operation is below 2%, due to periodic rainfall. The impact of shading and system losses on PV system performance (PR) is estimated to be below 5% during the first year of operation. Important shading occurred from January to March during the reporting period starting when new structures were constructed in the neighboring property. Second year analysis will provide information on the annual impact of the new constructions on the PV test bed energy generation.

In conclusion, we have compared daily performance of PV modules being tested in Maui during their first year of operation and have identified the main parameters of operation (irradiation, soiling, shading). A novel analysis approach is employed to evaluate of PV performance, in which we expand on the typical performance ratio (PR) and examine optical, current, and voltage performance. These performance criteria are linearly correlated to irradiation, the primary environmental driver of performance. Through this method, we differentiate environmental and operating conditions and supports a better understanding of the performance differences among PV technologies and manufacturers.
Thin film modules outperform crystalline modules at this mostly sunny location. This is due to high current performance for the CdTe and high voltage performance for the CIGS. Performance differences between standard and high efficiency crystalline modules are found to be small. With the CIGS modules, a low CIGS performer exhibits low optical performance and poor efficiency in low light conditions.

In follow-on work under APRISES13, the performance sensitivity to irradiation where we see strong dependence on PV technology and module design will be examined in detail. This will allow the identification of the highest performing technologies in a specified irradiation environment (to be detailed in further publications). Data from all HNEI PV test platforms will be compared to evaluate the impact of location on the PV performance.

References

[1] Final technical report for the Office of Naval Research Hawaii Energy and Environmental Technologies Initiative, N00014-10-1-0310, 2015.

[2] Busquet S., Kobayashi J., Rocheleau R. E., Operation and performance assessment of grid-connected PV systems in operation in Maui, Hawaii, 44th IEEE Photovoltaic Specialists Conference, June 2017.

[3] IEC 61724, Photovoltaic system monitoring - Guidelines for measurement, data exchange and analysis, Edition 1.0, 1998-04.

[4] Akhmad K. et al., Outdoor performance of amorphous silicon and polycrystalline silicon PV modules, Solar Energy Materials & Solar Cells (46), pp. 209-218, 1997.

[5] Canete C., Carretero J., Sidrach-de-Cardone M., Energy performance of different photovoltaic module technologies under outdoor conditions, Energy (65), pp. 295-302, 2014.

[6] Del Cueto J.A., Comparison of energy production and performance from flat-plate photovoltaic module technologies deployed at fixed tilt, 29th IEEE PV Specialists Conference Proceedings, pp. 1523-1526, 2002.

6.2 Secure Microgrids

This subtask focused on integration of emerging renewable energy technologies, and energy control systems and algorithms to support the development and deployment of secure, smart microgrids. HNEI initially identified three potential sites; on Molokai, Maui, and Oahu, each with unique characteristics allowing evaluation of a wide range of technical solutions and comparison of similar technology under different applications. Subsequent to the proposal, HNEI identified opportunities to build upon the proposed scope of the Subtask by adding additional sites. Areas of focus were selected to maximize benefits of the research, test, and evaluation, with the resulting objectives:

A. To understand the issues related to operation of the Molokai island grid with high penetration levels of distributed PV and central renewable resources and to develop new technologies, methodologies and tools to maintain the reliability and operability of the system as it transitions to meet its 100% renewable goal.
B. To develop a reliable, efficient and resilient DC/AC microgrid with high penetration levels of renewable energy resources and battery energy storage, for a research facility with critical energy reliability needs and growing future energy requirements on the UH-owned Coconut Island.
C. Support the collaborative New Energy and Industrial Technology Development Organization (NEDO) smart grid project on Maui ("JUMPSmart Maui") to demonstrate and evaluate electrified vehicle interaction with the power grid.
D. To conduct a feasibility assessment to identify, evaluate and prioritize several candidate energy demonstration opportunities for the US Marine Corp Okinawa.
E. To support the development and implementation of renewable energy technologies with cost reduction analysis on the University's Manoa campus.
F. As part of the Maui Advanced Solar Initiative, to manage voltage and other power issues that occur in neighborhoods with high concentrations of solar PV using smart inverter functions such as Volt-VAR (Volt-Ampere reactive) control.
G. To demonstrate the use of conservation voltage reduction (CVR) to control the voltage on the electrical power grid in real-time and to reduce the voltage drop across each distribution transformer.
H. To test grid-scale energy storage for grid support services by commissioning the third of three battery systems, and develop and test the control system and algorithm.
I. To develop a low-cost real-time power monitor with wireless communications for distribution system operations, controls, and analysis.

A. Molokai Project

Molokai is the fourth smallest of the main Hawaiian Islands in the central pacific. Its power system is small and isolated, making it an inherent microgrid. The island's system peak demand is 5.7 MW with an evening minimum demand as low as 2.2 MW. This island has seen rapid growth of distributed photovoltaics (PV) in the past few years with approximately 2.3 MW of PV systems installed and approved for installation with an additional 665 KW in a queue pending approval from the utility. The load on the island is not large enough to accommodate the PV additions in the queue and the minimum operating points of the must-run generation on the

island. Also, the high penetration of PV on the grid can lead to system stability issues and other challenges in maintaining a healthy operational power grid. A sudden loss of a generating unit or a power line fault on the system can cause the system frequency to drop below 57 Hz in a few cycles. This sudden drop in frequency causes distributed PV to trip offline, which further challenges the system's stability.

Maui Electric, the utility that owns and operates the power system on Molokai, has a goal to make the Molokai power system 100% renewable by 2030 or sooner if possible. The Molokai power system and the utility's aggressive renewable energy goal provide an optimal location to conduct research on renewable and resilient microgrids. There are two main objectives of this project. The first is to understand the issues related to high penetration levels of distributed PV and central renewable resources on the small Molokai island power system. The second is to develop new technologies, methodologies and tools to maintain the reliability and operability of the system as it transitions to meet its 100% renewable goal.

Grid Scale Storage to increase system stability

A 2 MW battery energy storage system (BESS) was installed and commissioned under a previous award to support frequency regulation during contingency events on the island's power system. Through this award new algorithms and control systems were developed for the BESS to meet the minimum required response time of 50 ms (as determined by interconnection requirement studies) for the BESS to be effective. The work to develop the controls systems and algorithms is discussed in greater detail in Section 6.2G titled "Grid Scale Battery Testing". The BESS is shown in Figure 6.2.1.

Figure 6.2.1: 2MW battery energy storage system (BESS) during installation on Molokai

Production Modeling

A production cost model of the island's power system was developed using the HOMER Pro software (HOMER Energy, Boulder, CO). The model was used to determine the amount of excess energy that would be generated with different amounts of PV and wind capacity, given historical load profiles and the operational constraints of the diesel generators on the island. As

shown in Figure 6.2.2, with the current system constraints, the amount of excess energy increases as more PV and wind turbines (WT) are installed. Assuming there is no energy storage, the excess energy must be curtailed and not utilized. Given the current minimum operational levels of the diesel generators, the amount of renewable energy that can be accepted on the grid approaches an asymptotic limit — approximately 50% renewable penetration in this case.

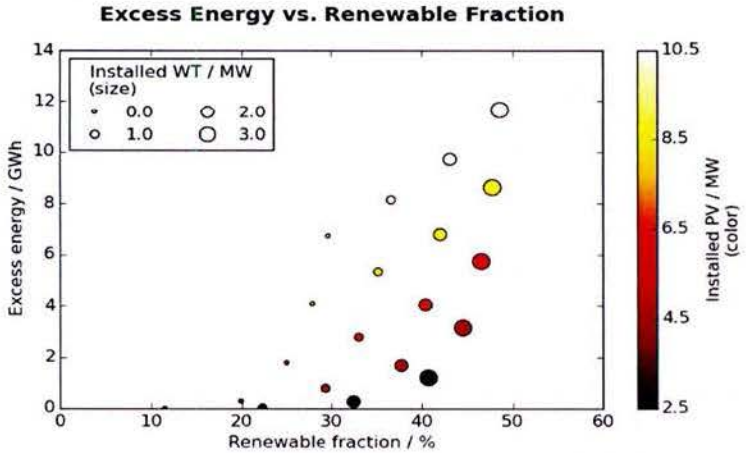

Figure 6.2.2: Results from the HOMER production cost model of Molokai with various levels of PV and wind

As more excess energy is produced, it becomes economic to install BESS capacity to shift this energy to times when it is needed and further increase the renewable penetration. The larger the storage system the more renewable energy can be accommodated, however, a very large BESS will not be fully utilized due to the infrequent occurrence of long periods of excess power during the year. HNEI developed custom software to explore this relationship. As shown in Figure 6.2.3, the daily battery utilization is nearly 100% at a renewable penetration of 50% but drops rapidly as the battery size is increased to achieve higher levels of penetration.

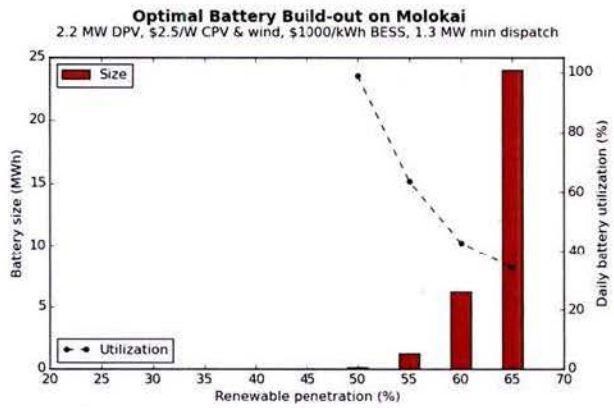

Figure 6.2.3: Results from HNEI's program to consider optimal BESS size on Molokai with various levels of PV and wind

Load Flow and Mid-term Dynamics Modeling

HNEI performed a field survey of the entire island to update the island's electrical geographic information system (GIS) database. This updated GIS database was used to create an electrical distribution model for the distribution circuits that serve the island. A highly detailed electrical model, to include the secondary service lines from the distribution transformer to each customer service point, was developed for circuit 105A due to its high penetration levels of rooftop PV. An overlay of the electrical model on the island of Molokai is shown in Figure 6.2.4.

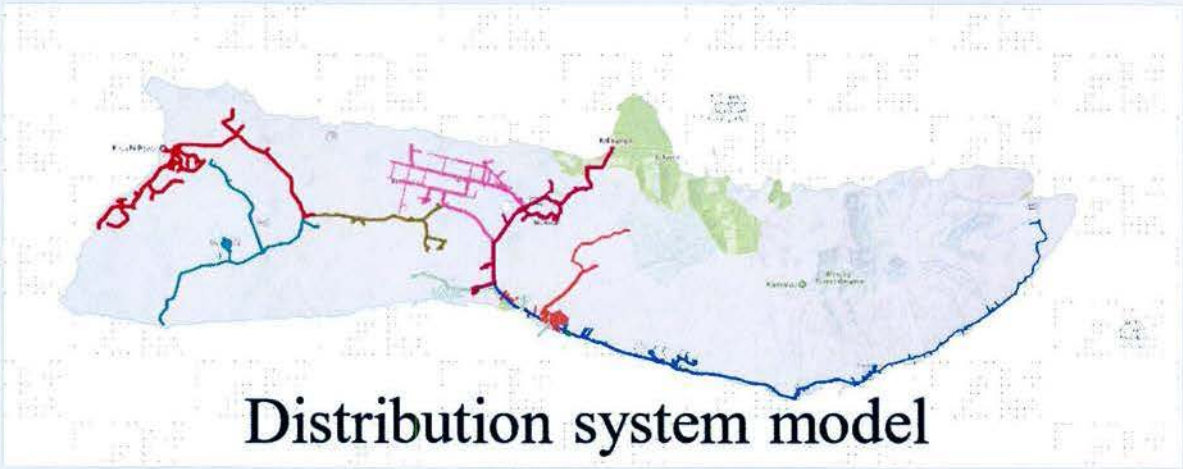

Figure 6.2.4: Distribution System Model

HNEI is conducting a PV Hosting Analysis of the entire island of Molokai using the distribution model in Figure 6.2.4 and Distribution Engineering Workstation (DEW) modeling software to determine the impact on voltage at the circuit level. Under APRISES11, a range of PV penetration levels and locations on the grid (various circuits) were modeled. A preliminary PV Hosting Analysis was run on several circuits using the timeframe of maximum PV generation to day time load ratio. To determine this analysis timeframe, load and PV generation data for each circuit was created from connected kVA, (transformer data provided by MECO) and NREL's clear sky solar profile for Hawaii, then scaled to Supervisory Control and Data Acquisition, (SCADA) data. For each PV penetration level, power flow was run at 10 different random placements of PV sites to check for possible power violations (overvoltage, flicker, overload, etc.). The PV Hosting Analysis for the entire island of Molokai is part of a broader project, currently HNEI has completed the analysis for 2 circuits. The rest of the analysis for the island will be completed under future ONR funding.

The preliminary results for 2 circuits in Molokai are shown in Figures 6.2.5 and 6.2.6.

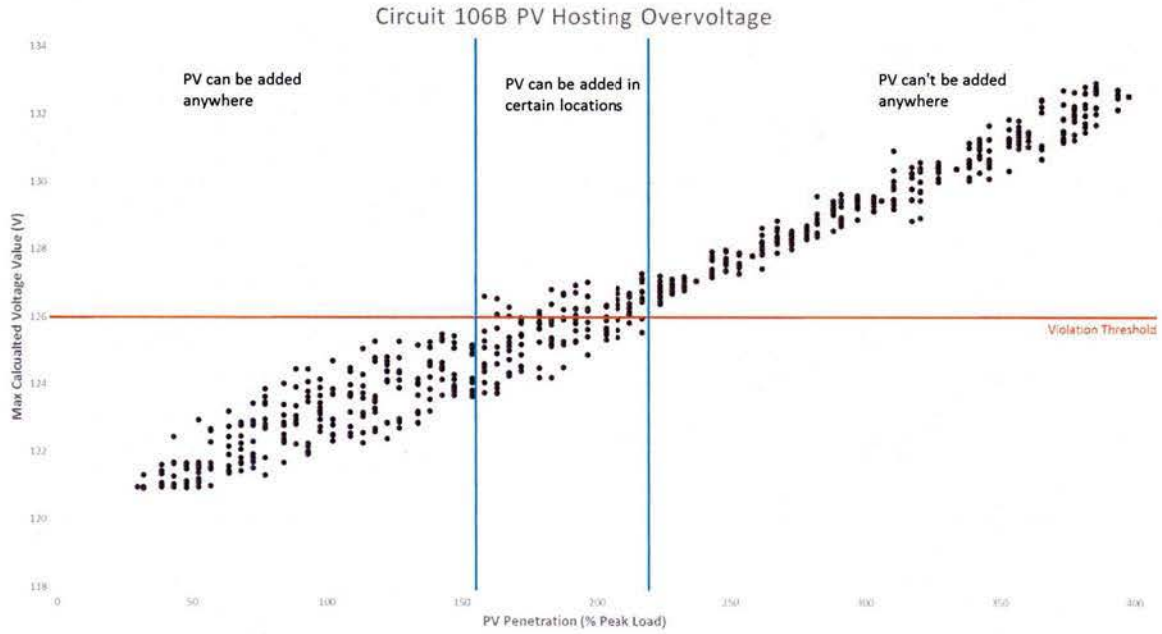

Figure 6.2.5: PV Hosting Analysis Result for Circuit 106B

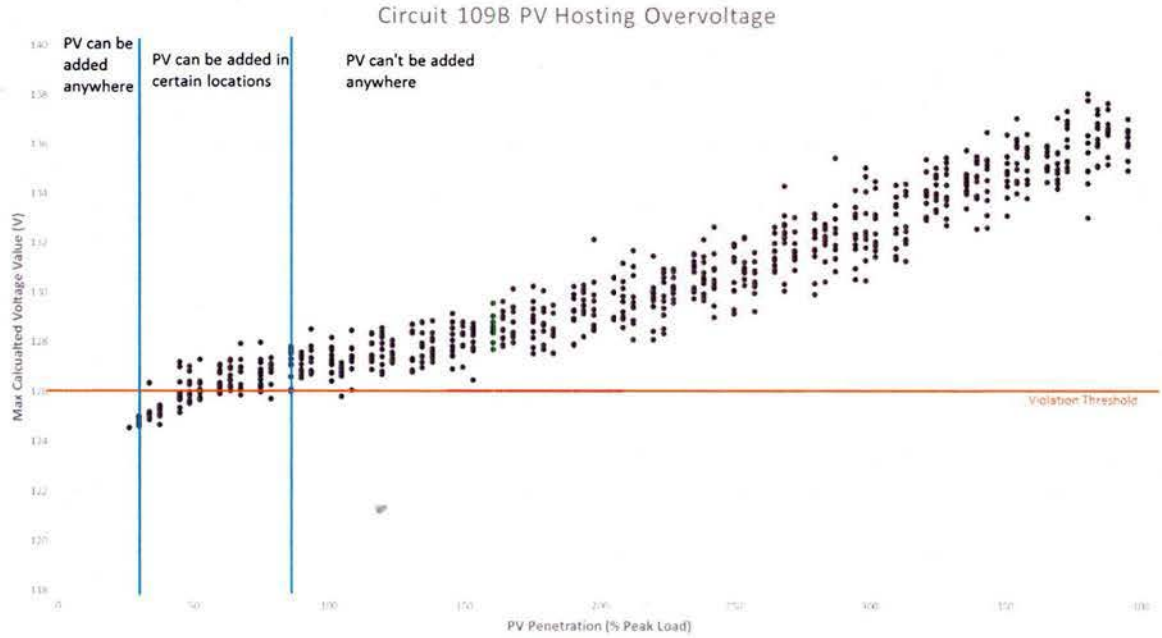

Figure 6.2.6: PV Hosting Analysis Result for Circuit 111A

Circuit 106B serves the Kualapuu and Hoolehua areas of Molokai. It contains 167 distribution transformers with peak load of 0.46MW and minimum daytime load of 0.15MW for the month July 2015. Circuit 106B currently has 33 installed PV sites giving a baseline penetration level of 29.7% peak load (131.4kW). At up to 178.8% penetration, no random PV placements resulted in overvoltage violation. From 178.8% to 220% penetration some of the random placements showed overvoltage violation. This means PV can be added to circuit 106B at any location up to

178.8% penetration level (791.4kW). With the location of PV sites taken into consideration, penetration level can be increased to a maximum of 220% (973.7kW).

Circuit 111A serves South Coast of Molokai; this is the longest circuit on the island with the furthest service point about 27 miles from the substation. It contains 231 distribution transformers with peak load of 0.28MW and minimum daytime load of 0.05MW for the month July 2015. Circuit 111A currently has 11 installed PV sites giving a baseline penetration level of 26.3% peak load (70.43kW). The light loading makes the circuit susceptible to high voltage issues. At up to 33.7% penetration, no random PV placements resulted in overvoltage violation. From 33.7% to 87% penetration some of the random placements showed overvoltage violation. This means PV can be added to circuit 111A at any location up to 33.7% penetration level (90.4kW). With the location of PV sites taken into consideration, penetration level can be increased to a maximum of 87% (233.4kW).

High Resolution Solar Forecasting

HNEI developed a novel solar forecasting system that incorporates a sky imaging camera that is intended to be an inexpensive alternative to Total Sky Imagers typically used for cloud tracking. The hardware design of this imaging device focused on minimizing final production cost by using off-the-shelf instrumentation, open-source single-board computing hardware, and technologies developed by HNEI. The low production cost is meant to facilitate the widespread deployment necessary to forecast distributed solar and allow for the application of stereo photogrammetric techniques for cloud geolocation, which removes the need for ceilometer observations. Each device also contains a solar-cell based pyranometer that provides estimates of irradiance used for real-time calibration and validation. The devices communicate with a centralized server wirelessly via a Long-Term Evolution (LTE) modem, where the imaging information is combined with global weather models and satellite imaging to develop near-real-time irradiance maps (within 6-8 km of the device) and high-resolution forecasts for up to ~30 minutes ahead with 30 second time intervals are computed. The software for this fully automated system has been completed and testing and evaluations were conducted on the University of Hawai'i at Manoā campus using two prototype devices fabricated in the summer of 2016. Since then, the hardware design has been updated to produce a more robust system. With the updated design five camera systems were built and field tested and are ready for deployment on circuit 105A in Molokai. The solar forecasting system is shown in Figure 6.2.7.

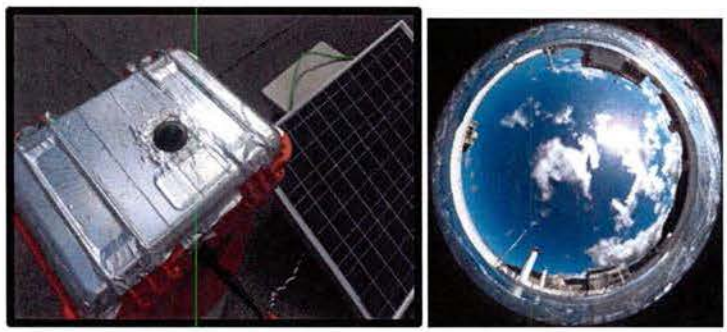

Figure 6.2.7: Solar forecasting system and image

HNEI is currently collaborating with the Korea Electrotechnical Research Institute (KERI) under a separate award from the Korean Government to incorporate the weather model and satellite imaging portion of this solar forecasting system into a microgrid controller that KERI is developing.

The work that has been done on Molokai provided a good framework for further RTD&E work on renewable resilient microgrids. HNEI plans to analyze the system impacts of even higher penetration levels of renewable resources on the island by conducting power flow simulations with the distribution model from this project and considering other technologies needed to reduce or eliminate the must-run thermal generation on the island. HNEI is deploying equipment to collect additional PV and power system data to provide inputs and validation for the distribution model. HNEI will produce forecasts for circuit 105A by deploying five solar forecasting devices on pole tops around the city of Kaunakakai and will work with system operators to determine how to present the forecasts to provide the best value for operations and planning. HNEI is working with the utility to deploy a grid scale resistor that will act as a "safety valve" to help maintain the operability of the system at higher levels of renewable penetration. Finally, HNEI plans to leverage the work done with KERI on the development of a microgrid controller and collaborate with Maui Electric to develop a controller for the Molokai grid that will pull together the system and forecasting information and optimize the operation of the existing and new resources being added to the grid, such as the thermal generation, BESS, resistor, and distributed energy resources on the island.

B. Coconut Island DC Microgrid

Coconut Island is a 28-acre (113,000 m²) island in Kaneohe Bay off the island of Oahu that is home to the Hawaii Institute of Marine Biology (HIMB) of the University of Hawaii. One of the goals for the island is to become a model for sustainable living systems, which makes Coconut Island the ideal place to conduct research on DC microgrid systems and host the Coconut Island DC Microgrid project. The project site is shown in Figure 6.2.8. It is an ideal site for a technology-based test bed since it is representative of a tropical marine environment in an isolated location with critical power needs to be supported. It is directly exposed to persistent trade winds resulting in a highly corrosive environment for material and technology testing in a micro-climate representative of those that are typically encountered by coastal installations.

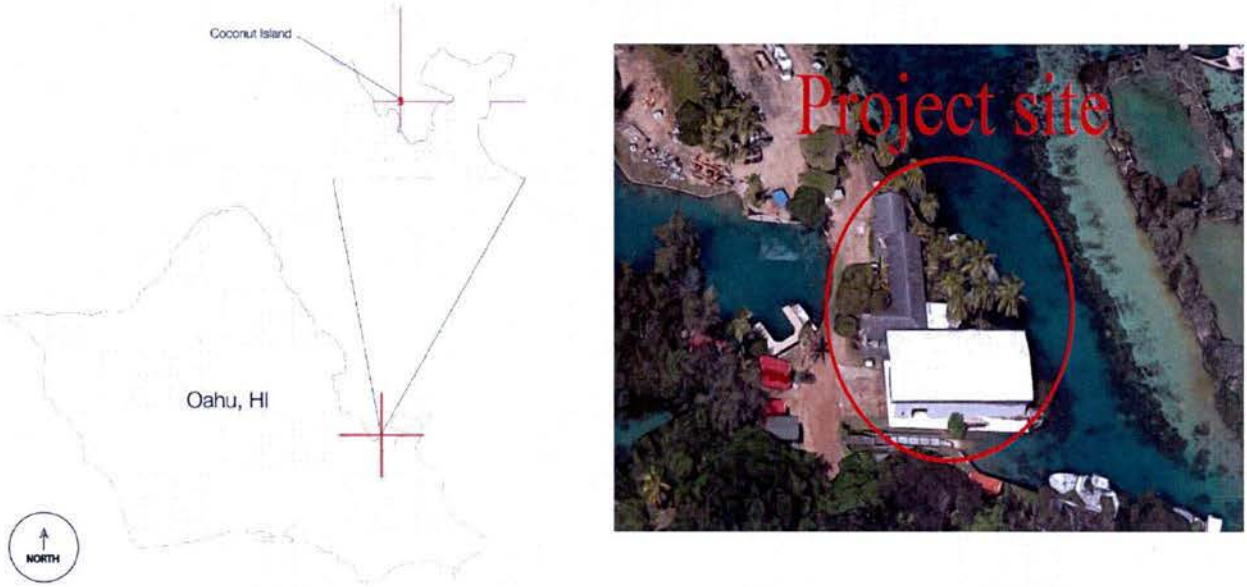

(a) (b)

Figure 6.2.8: a) Coconut Island location b) DC microgrid project buildings

The Coconut Island DC Microgrid Project will integrate a DC distribution system into two existing buildings on the island that are currently served by standard AC power, namely the Marine Mammal Research Project (MMRP) building and the Boat House. The DC microgrid will incorporate PV panels and a stationary battery energy storage system (BESS) as the primary energy sources to a 380V DC bus. A grid connected rectifier will supplement the PV and BESS when energy from the PV system and BESS is insufficient to serve the buildings' loads. Figure 6.2.9 below shows the conceptual schematic for the microgrid.

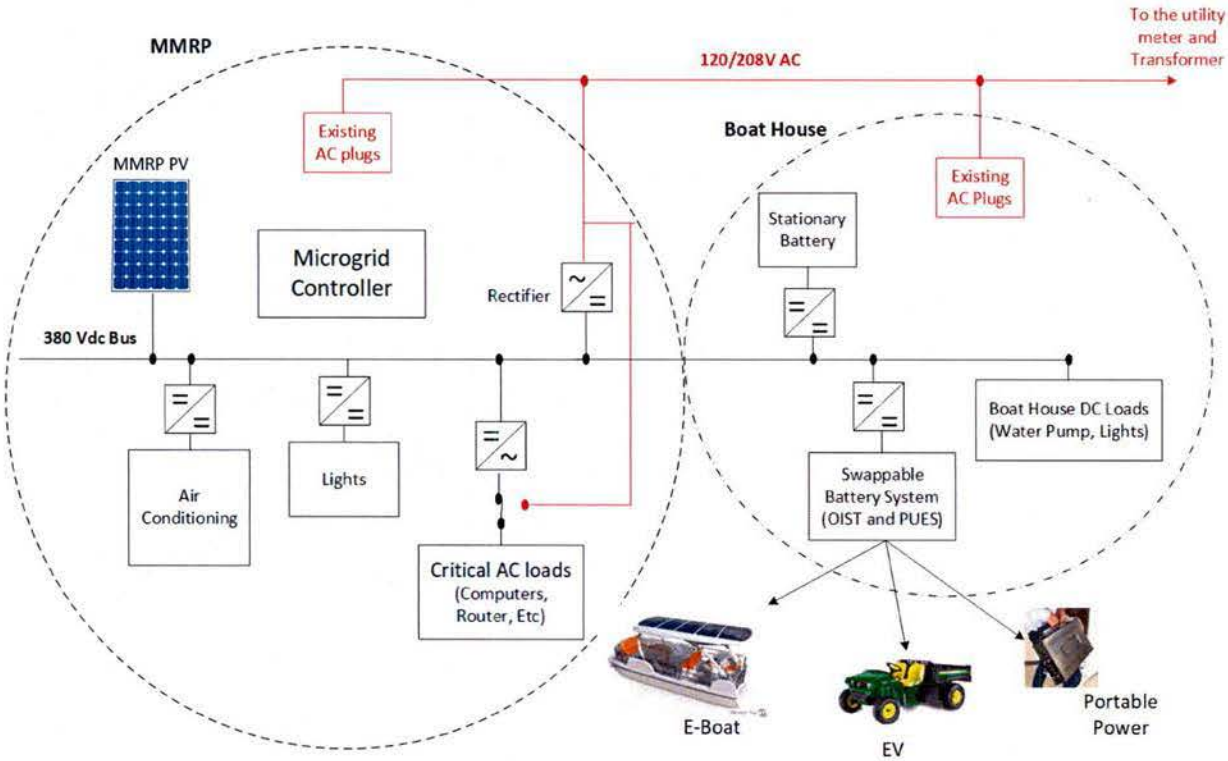

Figure 6.2.9: DC Microgrid Conceptual Single Line

The final implementation of the project will lead to an efficient and resilient DC microgrid with high penetration levels of renewable energy resources and storage (battery). It will seamlessly transition to off-grid operation with the loss of the power from the grid and support electric vehicles (an electric car and an electric boat) where both will be powered by a common swappable battery system charged from solar energy that can also provide energy to critical loads. The first generation of this novel swappable battery all electric transportation system was initially developed and is under demonstration in a car application by the Okinawa Institute of Science and Technology (OIST), a partner on this project and a co-member along with HNEI in the Hawaii-Okinawa Clean Energy Partnership (sponsored by the U.S. Department of Energy and the Ministry of Economy, Trade and Industry of Japan). To demonstrate the benefit of a microgrid on coastal clean energy transportation, HNEI acquired a pontoon boat and started the process to convert it to an all electrical boat that would utilize a swappable battery system common to both the car and boat applications. Further, under this effort, an HNEI faculty member successfully established and conducted a total of four project based engineering courses spread over a period of two semesters for undergraduate electrical engineering students at the University of Hawaii (courses EE296 and EE396), with the objective being to design and build a PV based system to power all on-board auxiliary loads for the electric boat.

To understand the nature of the DC microgrid project's loads and to develop the optimum size for the microgrid's energy resources, seven eGauge power meters were deployed to monitor existing AC loads from the electrical panels at the project site. The meter installations were completed in July 2016 when the meters started recording 1 second resolution data at the project site. All measured eGauge data are uploaded to the eGauge server that is accessible by HNEI

and HIMB personnel. Measured data can be monitored and downloaded from the server for any defined interval for up to 21 days. An installed eGauge meter is shown in Figure 6.2.10.

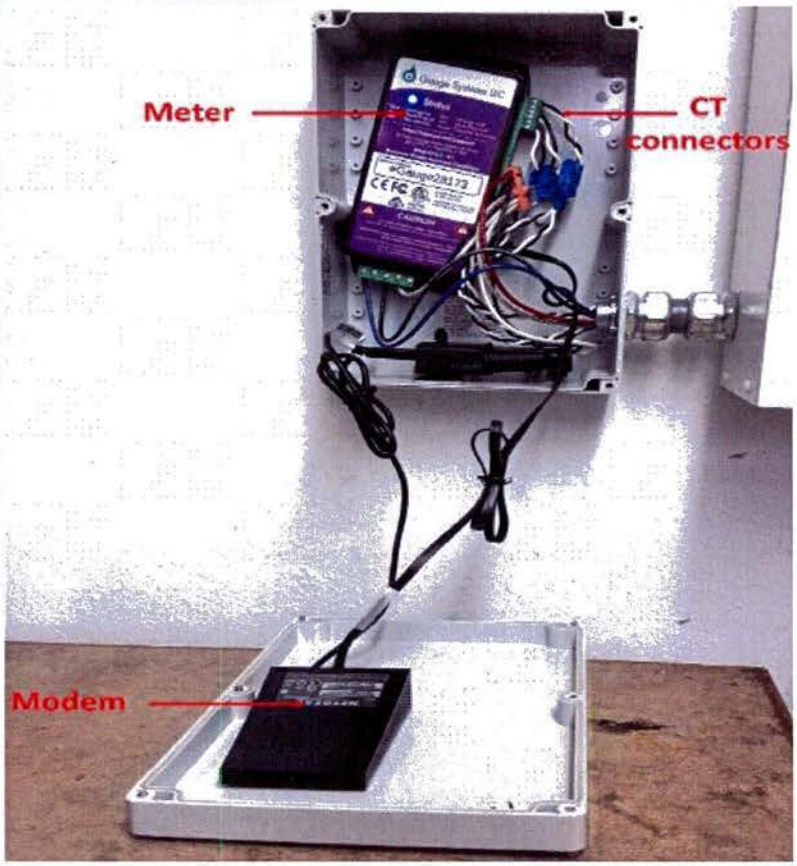

Figure 6.2.10: Meter boxes for monitoring loads

The sizing of the microgrid's energy resources was based on the most current recorded load data and a consideration of the probable new loads to be added to the DC microgrid, such as the swappable battery system for the electric vehicle and boat.

The following parameters are measured and recorded for each circuit in each panel: Power (kW), Energy (kWh), Voltage (V), Real power (W), Apparent power (VA) and Frequency (Hz). In Figure 6.2.11, average values for some of these parameters in measured in June, 2017 have been graphed for the Marine Mammal Lab project building (MMRP) with 15 minute granularity. The power profile for a twelve month period was used to optimize the sizing of the PV and BESS.

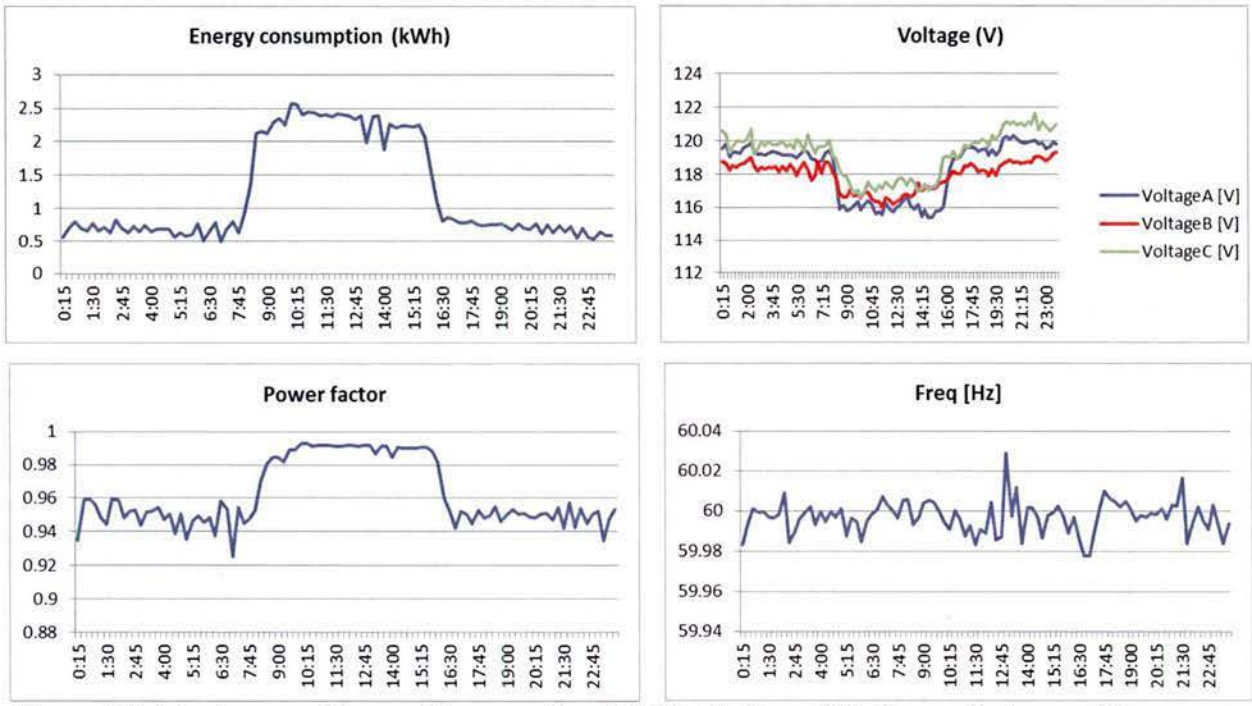

Figure 6.2.11: Average Energy Consumption (kWh), Voltage (V), Power factor, and Frequency (Hz) for MMRP building in June 2017

Based on the recorded data and targeted future loads, the size of the PV system and stationary battery were optimized using the HOMER PRO energy modeling application. HOMER optimization simulations using recent load data helped to provide an economic design that will enable the DC microgrid to be net zero at times and minimize consumption from the utility grid. The HOMER PRO schematic for these simulations is shown in Figure 6.2.12. The DC loads in these simulations have a one hour resolution and were based on the most recent year. The AC loads represented loads we are considering in the boat house to be fed by the DC micro grid through an inverter. To maximize renewable production, the maximum PV system size was chosen for this microgrid. Li-Ion battery storage has been selected with roundtrip efficiency equal to 90% with the full SOC range available for use, representing the usable SOC range of the BESS. The power purchase cost from the grid is assumed to be $0.22 /kWh and no sell back to the grid is allowed.

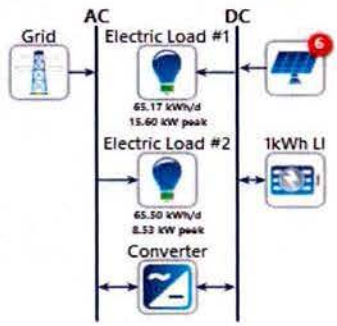

Figure 6.2.12: HOMER schematic

A set of simulations were run with HOMER PRO to determine the yearly power purchase from the grid for different sizes of BESS. Results are presented in Figure 6.2.13. For an 8 kWh BESS, the percentage of the total DC microgrid energy requirement that is purchased from the grid is about 38%, and for a 150 kWh BESS, the utility grid purchase percentage is reduced to about 12%. However, for BESS systems larger than 60-70 kWh, the grid purchase percentage does not change significantly, but the BESS cost increases linearly with increasing size. Considering these results, the preferred BESS size for this microgrid was determined to be at the knee of the curve in Figure 6.2.13, in the range of 60-70 kWh, which cost effectively minimizes the purchase of utility grid energy while avoiding diminishing returns in value of a larger BESS.

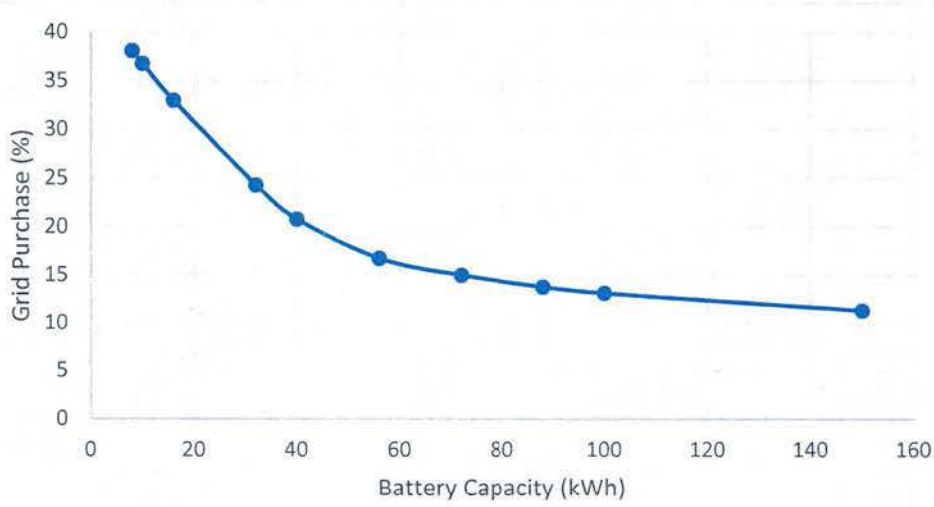

Figure 6.2.13: BESS sizes vs. grid energy purchase percentage (% of total consumption)

Figure 6.2.14 below, represents the selected energy profile for the planned microgrid with 31.2 kW (DC rating) of PV panels on the MMRP rooftop and a BESS capacity of 67 kWh. The color bands represent the energy from the different PV segments on the roof. Each segment was modeled as separate resources since the performance can vary significantly depending on the orientation of the panels. As can be seen from these results, the renewable percentage of this DC microgrid design would be about 91% for the modeled year. In months like May, June and July, the system would be nearly 100% renewable.

Production	kWh/yr	%
SP 327-COM-Seg4MM	16,505	28.70
SP 327-COM-Seg5MM	9,077	15.78
SP 327-COM-Seg6MM	5,868	10.20
SP 327-COM-Seg7MM	3,986	6.93
SP 327-COM-Seg8MM	3,986	6.93
SP 327-COM-Seg9MM	13,660	23.75
Grid Purchases	4,425	7.69
Total	57,506	100.00

Consumption	kWh/yr	%
AC Primary Load	23,908	50.14
DC Primary Load	23,773	49.86
Total	47,681	100.00

Quantity	kWh/yr	%
Excess Electricity	5,658.8	9.8
Unmet Electric Load	14.0	0.0
Capacity Shortage	41.0	0.1

Quantity	Value
Renewable Fraction	90.7
Max. Renew. Penetration	1,792.0

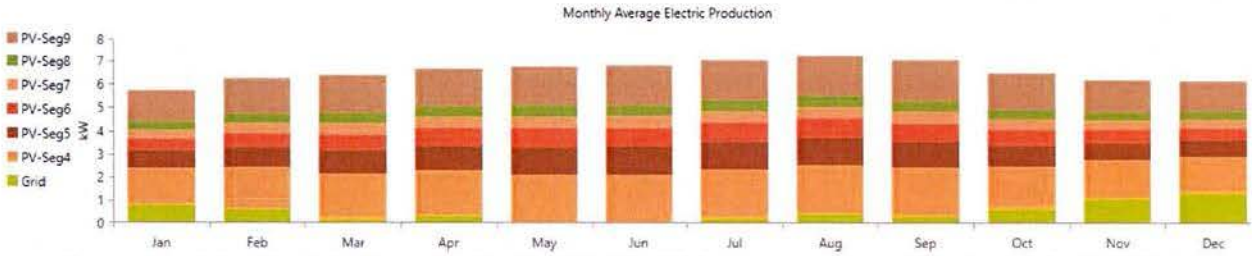

Figure 6.2.14: Electrical profile for HOMER PRO winning case (PV size: 31.3 kW DC)

C. New Energy and Industrial Technology Development Organization (NEDO) Smart Grid

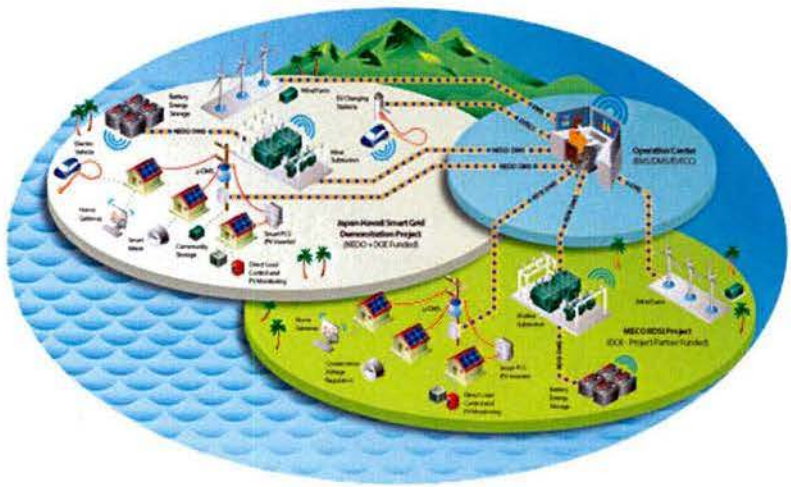

Figure 6.2.15: Schematic of the smart grid concept on Maui.

HNEI continued its support and collaboration with the NEDO smart grid project on Maui ("JUMPSmart Maui") under this award, which included the demonstration and evaluation of grid-to-vehicle (G2V) and vehicle-to-grid (V2G) electric vehicles (EVs). HNEI was one of the major stakeholders in the project that also included Hawaiian Electric, Maui Electric, the State of Hawaii, the County of Maui, and the Maui Economic Development Board. JUMPSmartMaui is designed to integrate distributed and central station renewable energy, EVs, energy storage, and controllable loads. Hierarchical levels of controls help manage the systems, which will ultimately enable functions including 1) the ability of batteries to discharge energy to the grid, or

store energy from the grid; 2) EVs as a demand response resource to the grid; and 3) EVs as a power source to homes (vehicle-to-home, V2H).

The project was implemented in two phases. Phase 1 included tests of EV load shifting, direct load control of water heaters, bulk battery operation, and power quality control of solar PV via smart inverters for a group of volunteer residential customers. Tools for visualization and control by operators were also demonstrated. Phase 2, called the Great Maui Project, expanded upon and optimized systems installed and demonstrated in Phase 1. Tasks in Phase 2 included a V2G/V2H demonstration, with EV charging and discharging to power homes and businesses; grid services using V2Gsystems and demand response; and greater use of renewable energy by aggregation of distributed energy resources for the best mix of power supply.

HNEI's role in the project was: 1) as a technical resource to develop, review and comment on project plans and results; and 2) as a public Hawaii entity to which NEDO would negotiate in good faith to transfer ownership of equipment at the conclusion of the project. HNEI personnel provided guidance and technical assistance throughout the project through its completion at the end of February 2017. As agreed in an MOU that was executed by the major stakeholders of the project on October 31 and November 1, 2011, HNEI negotiated and executed an Equipment Transfer Agreement with NEDO that resulted in HNEI acquiring a majority of the grid assets implemented in the project that were worth well in excess of $1 million. The equipment included distributed battery systems, micro-Digital Multiplex System (DMS) control units, medium voltage section switches and the computer server platform that was used to host the EV Energy Control System and Distribution Management System.

The project description and results from phase1 of the project were documented in an EPRI report as part of its Smart Grid Demonstration Initiative[1] and business case assessment and Case study of the project were provided by Mizuho Bank and Mitsubishi Inc., respectively, in a Hawaiian Electric filing to the State of Hawaii's Public Utilities Commission under Docket 2013-0046[2].

References

[1] *JUMPSmart Maui Demonstration Project Phase 1 Assessment*, Electric Power Research Institute, March 2016, https://www.epri.com/#/pages/product/3002007129/
[2] *For Approval of a License Agreement with AEC-USA, Inc., Decision and Order No. 32779 Compliance Filing*, Docket No. 2013-0046, State of Hawaii Public Utilities Commission, Filed August 8, 2017.

D. Okinawa Energy Demonstration Scoping Project

Subsequent to the proposal, HNEI obtained approval to expand the initial scope to conduct feasibility assessments at one or more locations within the Asia-Pacific region, including but not limited to current military bases and surrounding areas. One of the efforts under this expanded scope was to conduct a feasibility assessment to identify, evaluate and prioritize several candidate energy demonstration opportunities for the US Marine Corps (USMC) Okinawa. This had the additional benefit of leveraging HNEI's existing relationships within Okinawa that were

developed as part of the Hawaii-Okinawa Clean Energy Partnership established between the United States' Department of Energy, Japan's Ministry of Economy Trade and Industry, the Okinawa Provincial Government and the State of Hawaii.

Working with Marine Corps Installations Pacific – Marine Corps Base (MCIPAC-MCB) Camp Butler G-F's Energy Section, HNEI conducted feasibility assessments. The process was to identify, evaluate and prioritize several (up to five) candidate energy related demonstration project opportunities, identify the top two to three candidate demonstration projects to move forward for deeper feasibility assessment and scoping. Then down select the top one or two to develop and deliver a candidate project scope, budget and schedule that can be used by USMC Okinawa to pursue demonstration project implementation funding and action for project execution. The energy related demonstration projects were targeted to support one or more of the following USMC objectives: renewable energy integration, net zero energy, energy efficiency gains, electrical infrastructure reliability, resiliency, and/or energy security. In addition, the USMC Okinawa hoped to identify candidate demonstration projects that would enhance, where possible, the active working relationship with local Okinawan stakeholders.

Working with Energy Section personnel, a list of 15 potential project sites and associated demonstration objectives were developed and of those, five locations were selected for site assessments and data gathering. These were the Camp Courtney Barracks, Funtenma Air Base, Ie Shima Compound, Ie Shima Communications Tower, and the Jungle Warfare Training Center (JWTC). After the site assessments were completed, three locations were selected to move forward to a feasibility assessment, Camp Courtney (PV installation and limited emergency power), Ie Shima Main Compound (Microgrid PV installation with net zero capabilities and reduced fuel consumption during off-grid operation), and the JWTC (PV installation and networking of emergency generation for more efficient and extended off-grid operation during power interruptions). As the team discussed these potential demonstration scopes, the concept of Conservation Voltage Reduction (CVR) came up as something HNEI was working on and has shown to be of great value to smart grid implementations. The Energy Section and base command showed great interest in CVR and locations were selected for an assessment of their feasibility to host a CVR demonstration project.

After completing the feasibility studies for the selected sites above, two demonstration project locations and objectives were selected for scope, cost, and schedule development: 1) Camp Foster Plaza Housing (Conservation Voltage Reduction) and 2) the JWTC (Renewable energy / Microgrid). A budget, scope and schedule were developed to implement the CVR demonstration at Camp Foster Plaza Housing and a budget, scope and schedule were developed to complete a more detailed design of the demonstration project at the JWTC.

Following the presentation of the results of this Demonstration Scoping Project, the decision was made to move forward with the CVR demonstration at the Camp Foster Plaza Housing. The CVR demonstration project was initiated by HNEI under a separate funding source.

References

1. USMC Okinawa Energy Demonstration Scoping Project, Out Brief Presentation.

E. University of Hawaii

The University of Hawaii (UH) at Manoa campus is provided power by the local utility Hawaiian Electric Company, Inc. (HECO) through two 46kV substations. The power at the substations are stepped down to 12 kV before serving the UH owned distribution system. The annual electric bill for the Manoa campus is roughly $40 million (this is nearly 20% of the annual tuition revenue) with a campus peak demand of approximately 20 MW. Reducing the high cost of energy supply for the University microgrid is a high priority. There are near term plans to install on campus distributed solar photovoltaic (PV) renewable energy (RE) resources of approximately 1.5 MW and a desire to install significantly more at locations where opportunity exists. However, with the limited operational visibility of building and circuit loads on campus due to the existing metering infrastructure in place and the lack of a power system simulation model of the campus microgrid, an analytic evaluation of the impacts of high penetrations of distributed PV resources on distribution grid operations, delivered power quality and overall service reliability pose a present challenge.

The objective of this project is to support the development and implementation of RE resources on the Manoa campus microgrid, in turn allowing UH the opportunity for enhanced sustainability and reduced energy cost. This objective will be met through two key research and demonstration phased activities: (1) enablement of system monitoring and data analysis; and (2) development of a foundational analytic distribution system geospatial and electrical power flow model for the campus grid to assess the integration of renewable energy technologies.
APRISES11 encompassed Phase 1 and Phase 2a as outlined below. Per the knowledge gained under this APRISES11 effort, the remaining work is being continued under other funding.

Phase 1: System Monitoring and Data Analysis

a. Collect historical meter data from campus meters and from local utility
b. Support enablement of advanced metering capabilities on campus to secure access to key data going forward
c. Analyze the data collected

Phase 2: System Modeling and Assessment

a. Generate GIS database of the Manoa campus electrical infrastructure
b. Develop electrical power flow model
c. Conduct power system analytics

The results summarized in this section concludes all of Phase 1 and Phase 2a.

Phase 1: System Monitoring and Data Analysis

Work was completed to collect and assess existing data of the power service supplied to the overall Manoa campus from HECO. Power system data (i.e., kW and kVAR) is recorded by HECO at 15 minute intervals for the two substations feeding the UH campus. Figure 6.2.16 below provides a snapshot of the meter data of the totalized load (kW) of the two substations feeding UH Manoa for the year 2015. The HECO meter data provides insight into the total demand of the UH distribution network. This data is very useful to see the system power demand and energy use for the campus as a whole.

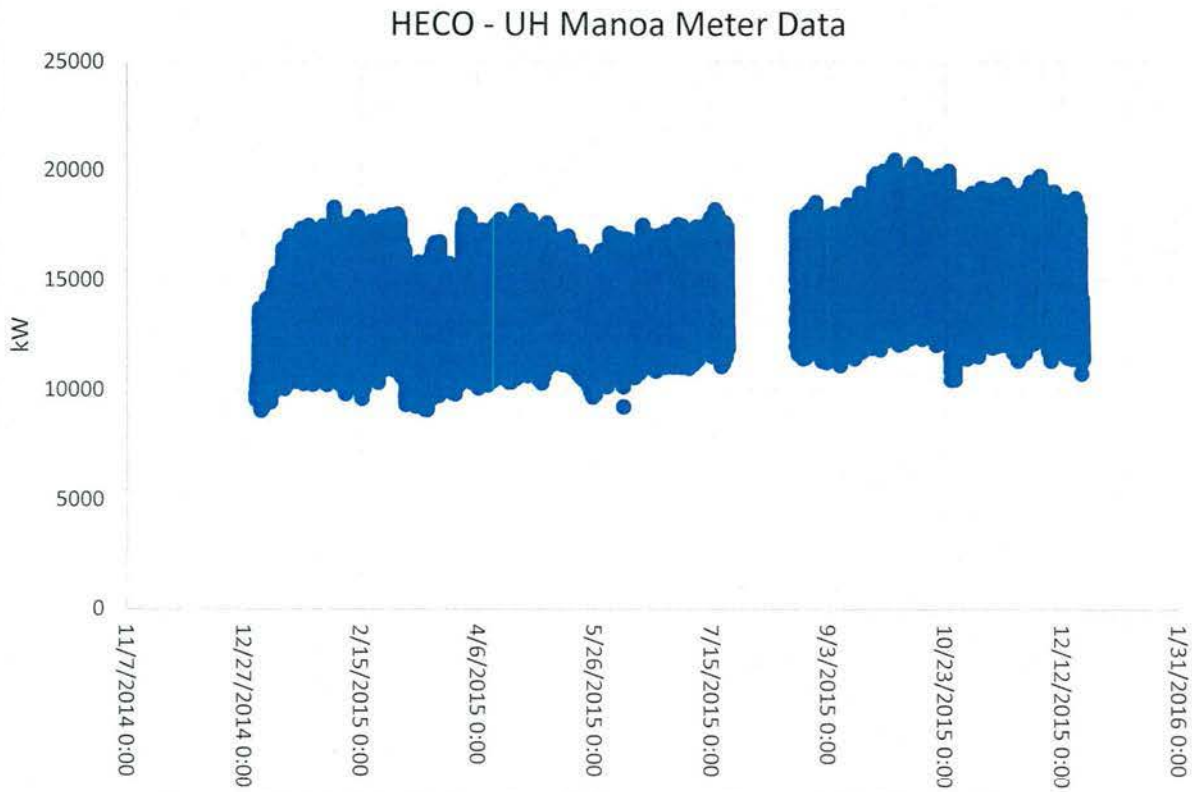

Figure 6.2.16: HECO Totalized Meter Data for the UH Manoa Campus

However, to conduct more refined power system studies foundational for the effective integration of distributed PV resources across campus, higher resolution data sensing, collection and analysis for specific distribution circuits serving locations on campus targeted for PV development is ultimately necessary. UH Manoa is currently in the process of installing high fidelity power quality meters at a majority of their buildings across campus. At the time of this work, approximately one-third of the total planned campus-wide meter deployment was completed. These meters offer the opportunity to collect highly valuable power system data with proper programming and data collection infrastructure in place. During Phase 1 of this project, HNEI assessed the meters installed on campus to date and determined that the meters were programmed at the time of install to capture only a limited set of energy use data. Action was then undertaken by HNEI to reprogram those meters to begin capturing the data required for further analysis and ultimate use in modeling and assessment of RE integration on the campus (e.g., power, voltage, current, and power factor). Table 6.2.1 below offers an example of the data points collected from a power quality meter that was reprogrammed to capture useful data for this study.

Table 6.2.1: UH Power Quality Meter Reprogrammed Data

Date & Time	Current : Ia (A)	Current : Ib (A)	Current : Ic (A)	Unbalance : Current (%)	Voltage : Van (V)	Voltage : Vbn (V)	Voltage : Vcn (V)	Voltage : Vab (V)	Voltage : Vbc (V)	Voltage : Vca (V)	Power : P3 (kW)	Power : Q3 (kvar)	Power Factor : PF3	Frequency (Hz)	Energy : +kWh (kWh)	Energy : +kvarh (kvarh)
2/16/2016 16:17:40	167	164	134	13.7	119	119	119	207	207	206	52.79	17.47	0.95	59.98	1169521	415024
2/16/2016 16:17:41	167	164	134	13.7	119	119	119	207	207	206	52.75	17.36	0.95	59.98	1169521	415024
2/16/2016 16:17:42	159	157	126	14.2	119	119	119	207	207	206	49.97	16.98	0.95	59.99	1169521	415024
2/16/2016 16:17:43	153	151	121	14.7	119	119	119	207	207	206	47.85	16.98	0.94	59.99	1169521	415024
2/16/2016 16:17:45	154	152	122	14.4	119	119	119	207	206	206	48.12	17.07	0.94	59.99	1169521	415024
2/16/2016 16:17:46	153	152	122	14.5	119	119	119	207	207	206	48.09	17.02	0.94	59.99	1169521	415024

Phase 2a: System Modeling and Assessment - Generate GIS database

In order to build an effective geospatial and electrical distribution power flow model of the UH microgrid, development of an accurate GIS database is first needed. This activity was an extensive effort using campus physical and electrical distribution maps, manhole diagrams, and single line diagrams of the UH campus distribution system to generate the GIS database of the physical locations of key reference points such as roads, buildings, and the relative location of electrical system components (i.e., cables, switches, transformers, etc.) installed in the field. See Figure 6.2.17 below for the GIS Map created.

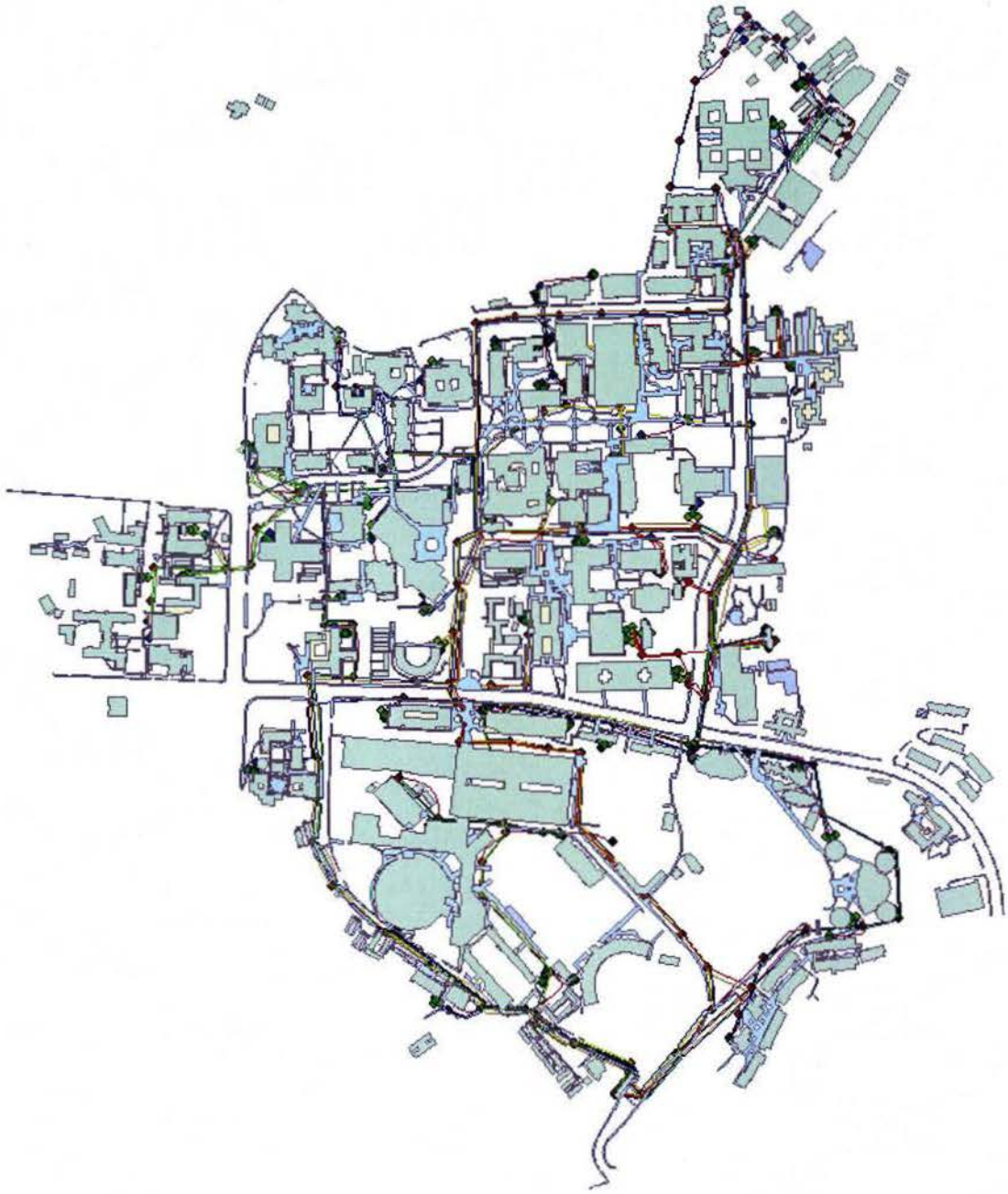

Figure 6.2.17: UH Manoa GIS Map

This completed APRISES11 efforts. However, the attributes of the electrical components (e.g., electrical cable size, transformer ratings and impedances, etc.) were not updated by the UH Facilities office and were thus unavailable at the time of this GIS development work. Thus, the ability to develop an effective electrical power flow model for the campus microgrid project was hampered. Fortunately, while our GIS work was underway, an effort managed by the UH Facilities office was launched to conduct an exhaustive field inspection based electrical system assessment study aimed to capture and update the "as-built" electrical infrastructure of the

campus distribution grid, which in turn would identify the electrical components attributes data needed to complete the electrical power flow model development (under other funding). This assessment study was only recently completed by the University, thus not allowing adequate time to complete all Phase 2 activities within the duration of the APRISES11 effort.

In conclusion, the ability to effectively achieve the broader project objectives of enhanced sustainability for the University of Hawaii and reducing its high cost of electricity through support for the development and implementation of renewable energy technologies on campus required this foundational work of understanding and gaining knowledge on the campus electrical system and the types of data available. After the development of the GIS database in Phase 2a, a gap in the required data for the continuation of this project was identified and the means to collect that data was only recently completed and made available by the University. Completion of the remaining Phase 2 activities is being assessed, and if deemed valuable will be conducted under other funding.

F. Maui Advanced Solar Initiative

The goal of the Maui Advanced Solar Initiative project was to use smart inverter functions such as Volt-Var (Volt-Ampere reactive) control to manage voltage and other power issues that occur in neighborhoods with high concentrations of solar PV. Initial hardware development and testing took place under US Department of Energy Award DE-EE0005338 "Development and Demonstration of Smart Grid Inverters for High -Penetration PV Applications. The final report for this project is available on the HNEI website. Under this award, additional testing of the hardware and field testing was conducted. HNEI recruited seventeen 17 residential volunteers in the Maui Meadows neighborhood of Kihei, Maui (Figure 6.2.18). The PV inverters at those residences are being monitored and controlled using software, hardware and robust communications systems that have been developed specifically for this purpose. In addition, there are several locations where house electrical loads and distribution service transformers in the neighborhood are being monitored, all at a one-second interval.

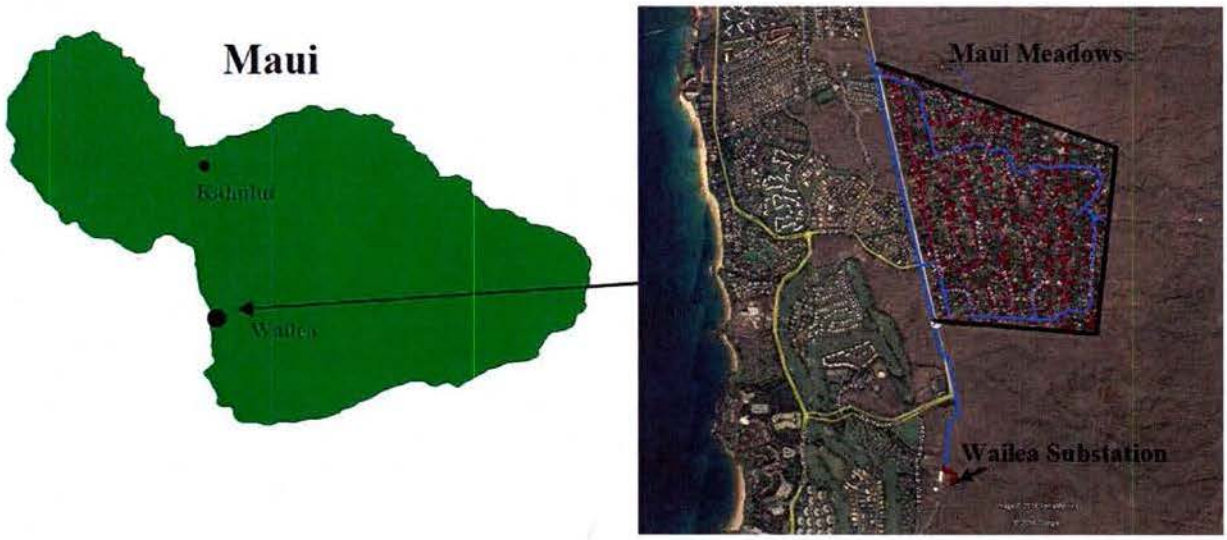

Figure 6.2.18: Project location

The Maui Meadows residential subdivision is served by distribution circuit 1517 originating from Wailea Substation. This subdivision consists of single phase residential loads and a single three phase load feeding the water supply pumps for the community. There are approximately 1,000 homes on circuit 1517 and more than 2 megawatts (MW) of nameplate distributed generation across 300 sites. The circuit's daytime minimum load (gross) is just under 1 MW.

Seventeen advanced inverters of various sizes and manufacturers were deployed at volunteers' homes throughout the Maui Meadows subdivision as shown in Figure 6.2.19 below. The distribution service transformers with data monitoring is circled in blue, green, or red ovals with the color indicating the phase of the transformer. Each monitored point has an assigned unique identification label (i.e. T115). The inverter identification labels are shown next to the red arrows (i.e I 039).

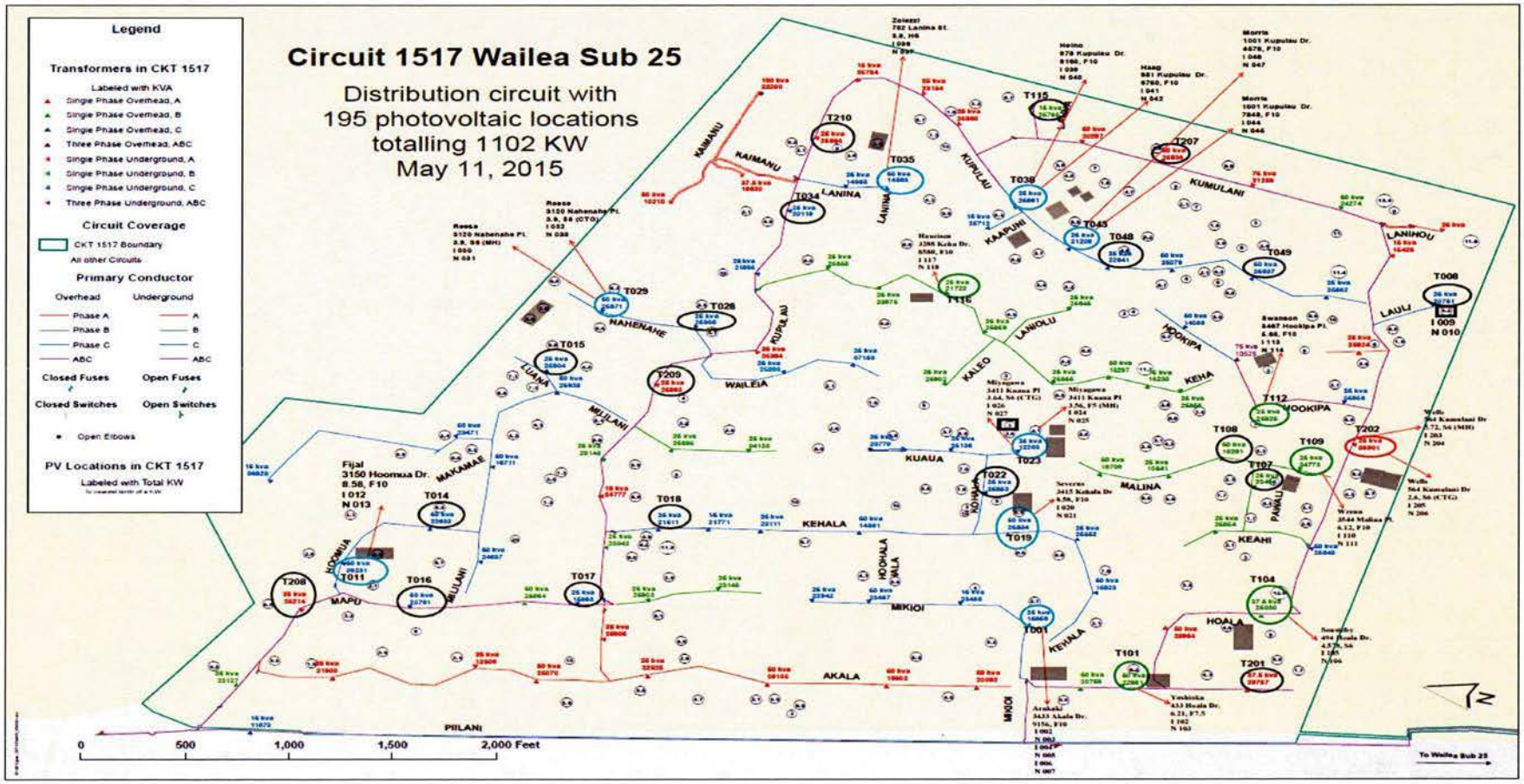

Figure 6.2.19: Map of advanced inverter location in Maui Meadows subdivision

An overview of the control and data monitoring system is shown in Figure 6.2.20. The inverter and service transformer power data are collected and remotely streamed to a server located at the University of Hawaii at Manoa campus via cellular network. The inverter control commands issued from a remote computer terminal uses the same communication path to communicate to the smart inverters.

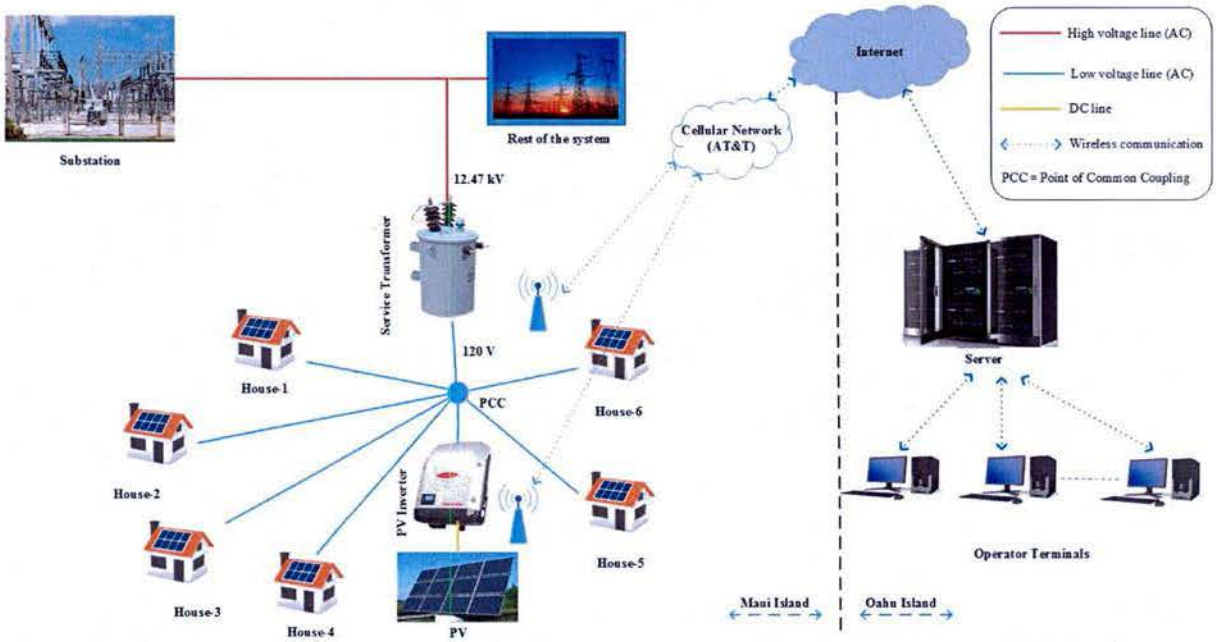

Figure 6.2.20: Data collection and control communication system

The power meter used within the data collection system is the E51 from Veris Industries. It was determined that the meter computes and provides non active power as its reactive power reading. Thus, the term non active power and reactive power are used interchangeably in the rest of this section.

Using advanced inverters to management voltage can be achieved by controlling the inverter's real and reactive power output. Three inverters of different manufacturers were used in this project: Hitachi, SMA, and Fronius. Due to the early stage of smart inverter technologies, there are many subtle but critical differences in the way smart functionality has been implemented by each inverter manufacturer. In the subsequent sections, the field testing results for each manufacturer is described in detail. The analysis of inverter control and its effect on local distribution voltage is discussed in the last section of the report.

Real Power Curtailment

Multiple curtailment commands of short duration were sent to the three inverters as illustrated in Figure 6.2. 21 below. The minimum real power output for each inverter is different. For the Hitachi, it maintains a minimum of 300 watts while the SMA and Fronius has a minimum of approximately 150 watts and 0 watts, respectively. While a curtailment command is in effect, the Fronius and Hitachi inverters are able to maintain a constant level of output power while the SMA inverter has some deviations around the curtailment set point.

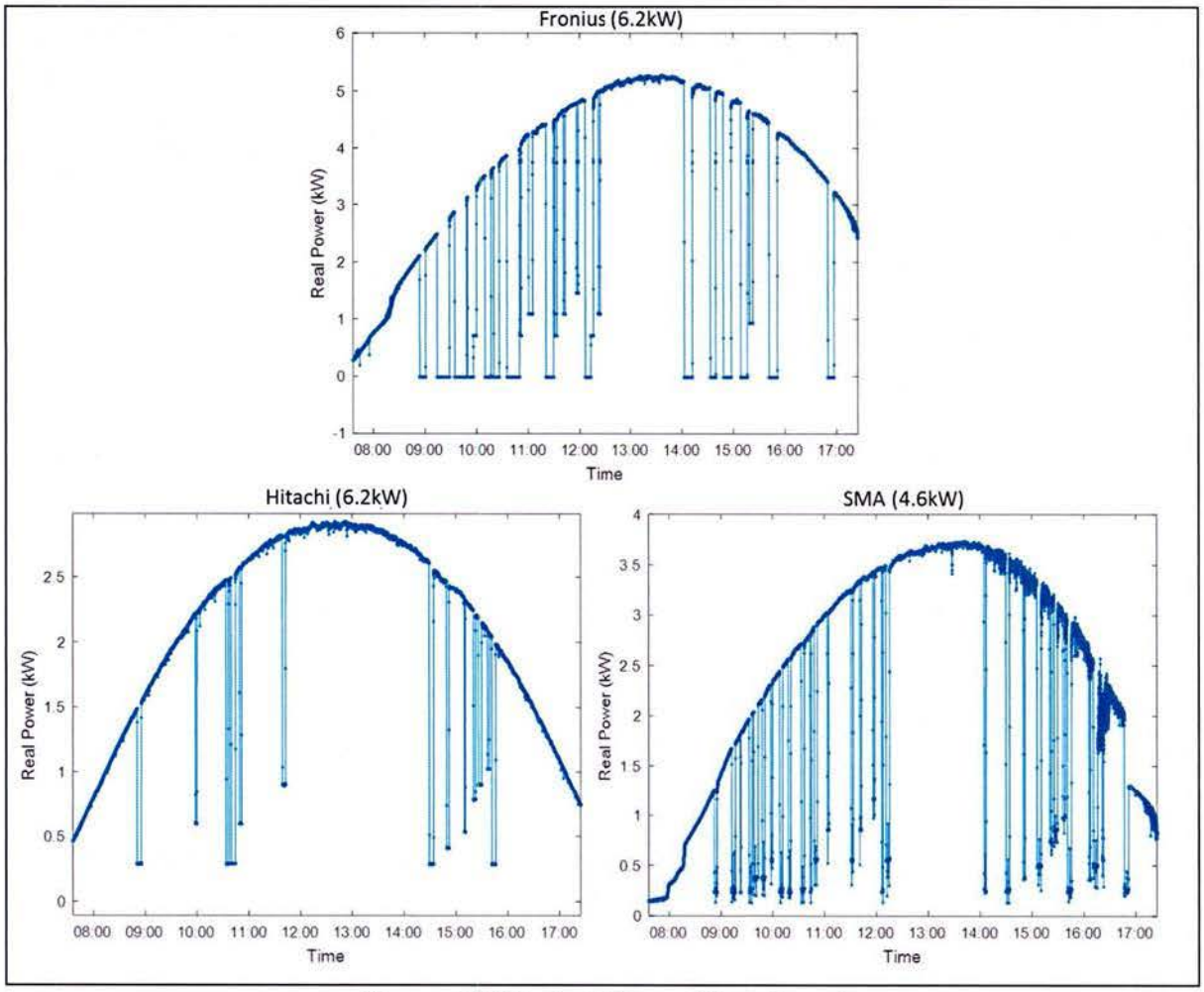

Figure 6.2.21: Real Power Curtailment

Volt-Var Control

The Volt-Var curve defines how dynamic reactive power is injected/absorbed through responses to the voltage at the terminals of the inverter. A Volt-Var curve can be divided into five regions as shown in Figure 6.2.22. Region-1 is the maximum generation of reactive power which is also known as the capacitive region. Region-2 is the variable region of reactive power generation. Region-3 is the zero reactive power generation or dead band. The variable reactive power absorption is in Region-4. Region-5 is the maximum absorption of reactive power which is also known as inductive region. The y-axis of Volt-Var control curves are typically specified in units of "% Available VARs." During lab testing of the inverters, it was determined that the slope of the Volt-Var curve in the variable region cannot be too steep. Since it was not possible to control the voltage of the field deployed inverters, the Volt-Var control testing was limited to Region-1 (capacitive) and Region-5 (inductive).

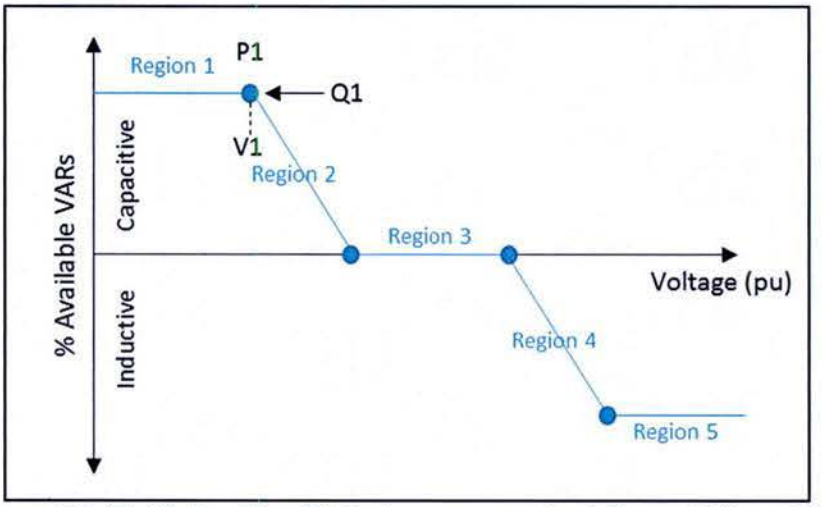

Figure 6.2.22: Volt – Var (Volt-Ampere reactive) Control Curve Regions

Volt-Var curves that will put the inverters in a capacitive mode i.e. generate reactive power were constructed based on the terminal voltage at each inverter location. Figure 6.2.23 are plots of reactive power as a function of time for each inverter. The red series is the constructed Volt-Var curve with the assumption that the inverter is capable of producing reactive power up to its rating. The inverters operated in a capacitive region during the test period as expected. However, the amount of reactive power available from each inverter is different and is typically not provided in the inverter manuals. The reactive power capability of the 7.5kVA Fronius is constrained to a power factor of 0.85 making it dependent on real power output. The Hitachi was able to produce up the 5.6kVAR or 93% of its rated KVA. The SMA inverter has a reactive power limit of 50% of its rated KVA which is 3 kVAR in this case.

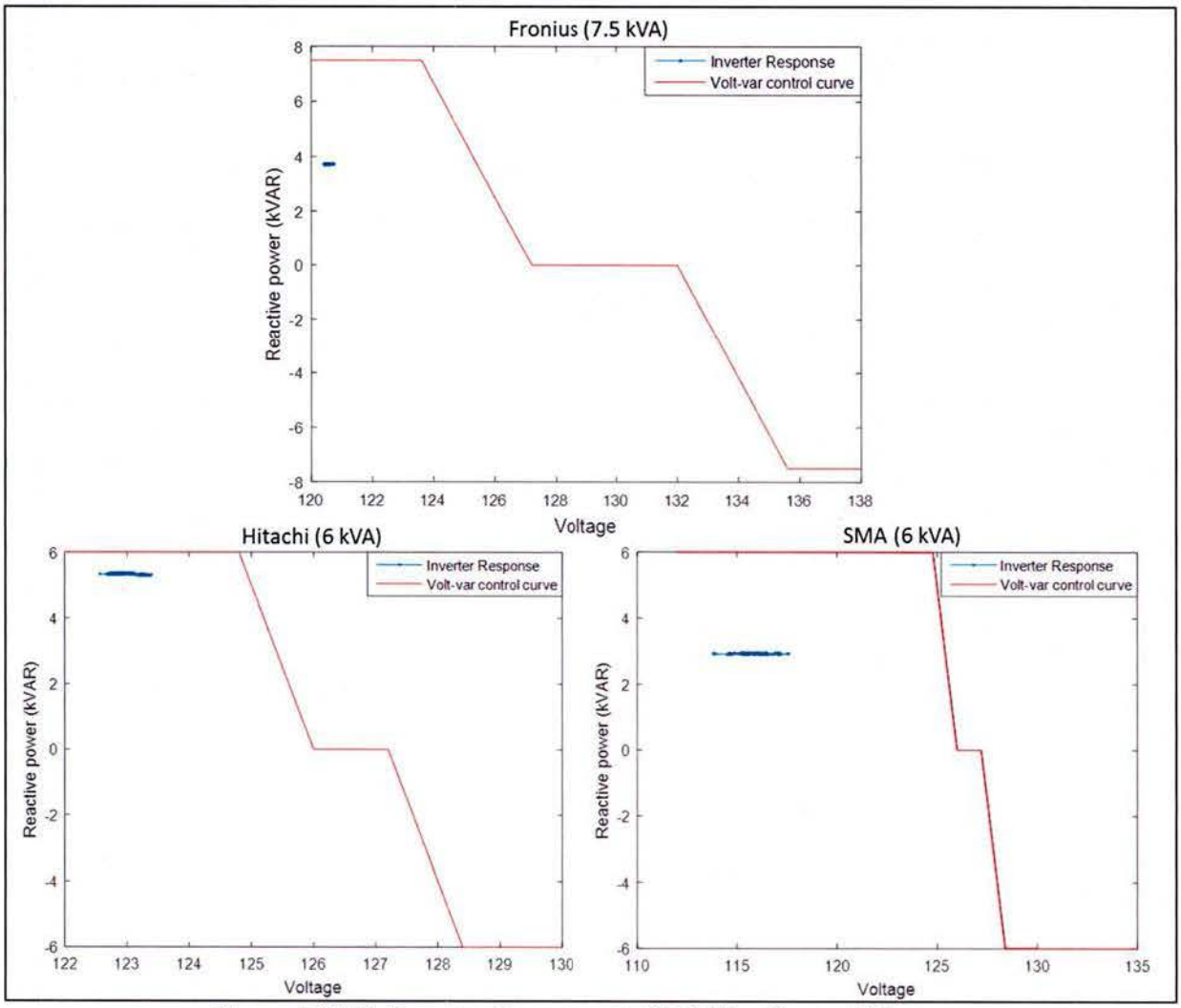

Figure 6.2.23: Inverter Response to Volt-Var Control Curve

Volt-Var curves that will put the inverters in an inductive mode i.e. increasing reactive load to the grid were constructed based on the terminal voltage at each inverter location. Figure 6.2.24 are plots of reactive power as a function of time for each inverter. The red series is the constructed Volt-Var curve with the assumption that the inverter is capable of absorbing reactive power up to its rating. The inverters operated in the inductive region during the test period as expected. However, the amount of reactive power absorbed from each inverter is different and is typically not provided in the inverter manuals. Comparing Figure 6.2.23 and 6.2.24, it can be seen that when inverters are absorbing reactive power, it is less consistent and does not always follow the input control curve as in the case of the Hitachi inverter.

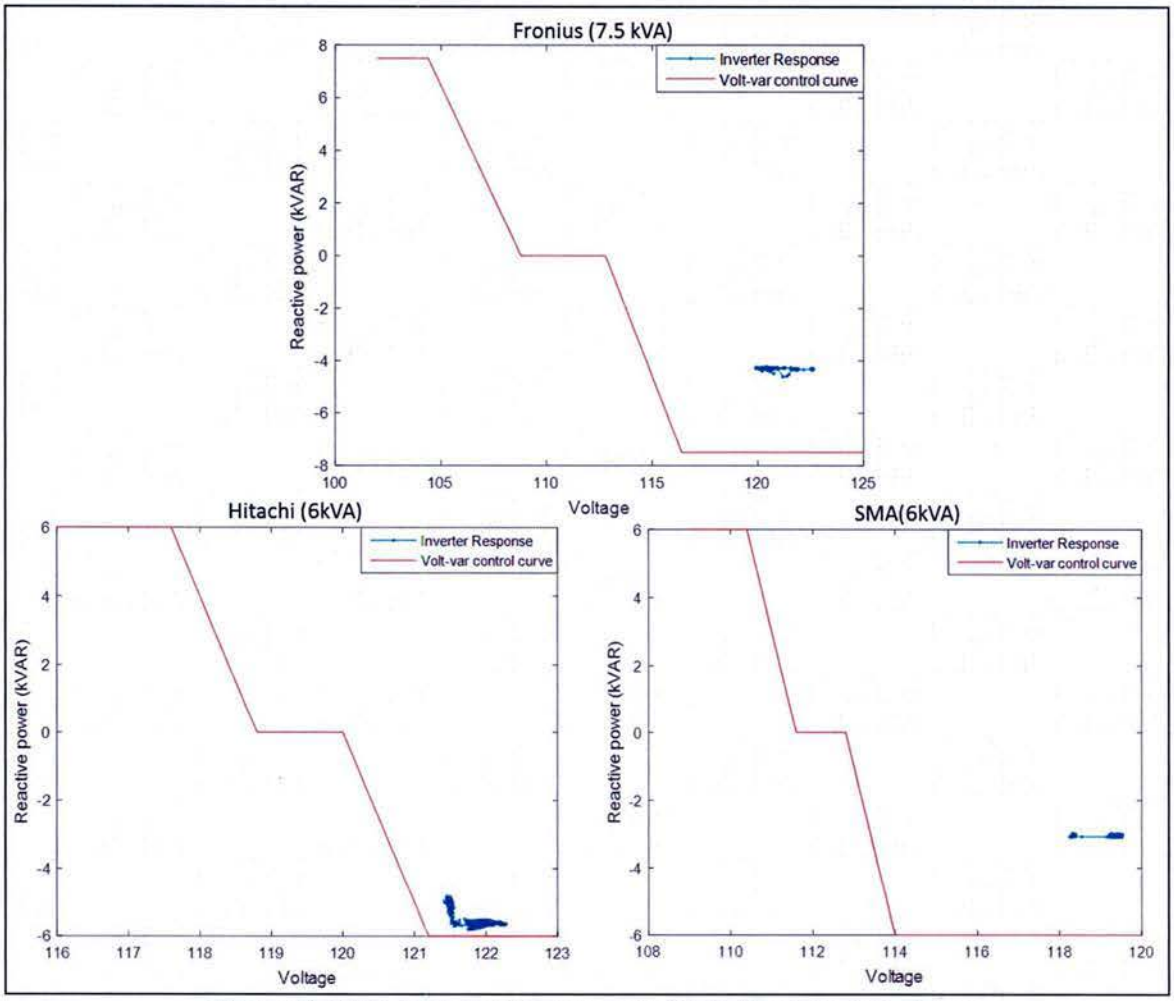

Figure 6.2.24: Inverter Response to Volt-Var Control Curve

In summary, Volt-Var control curves must be constructed so that the slope of the piecewise linear curve does not exceed the inverter manufacturer's expected amount. Additionally, the amount of available reactive power with respect to its rating is manufacturer specific.

Volt-Watt control

The Volt-Watt control provides a method to control output power based on the local voltage. A set of voltage levels (V1, V2, V3, and V4) and their corresponding power levels define the points on a piecewise linear curve as illustrated in Figure 6.2.25. The amount of real power being generated by the inverter is strictly dependent on the available input amount from its DC power source.

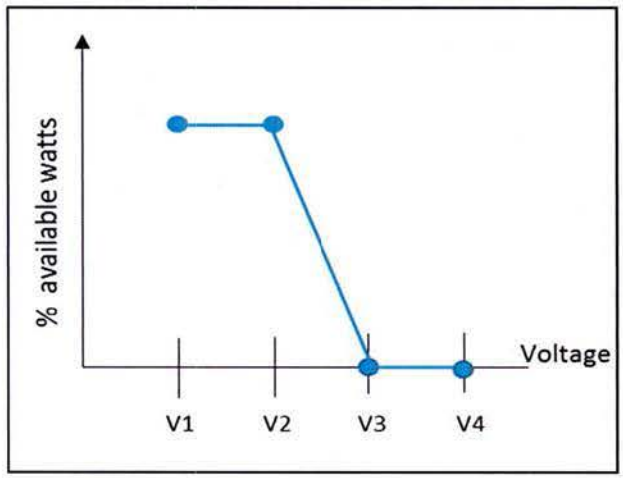

Figure 6.2.25: Volt-Watt Control Curve Regions

An evaluation of the effectiveness of the Volt-Watt command to curtail the real power output under an overvoltage condition was conducted.

A curve with set points shown in Figure 6.2.26 was used to validate the inverter's ability to curtail real power output.

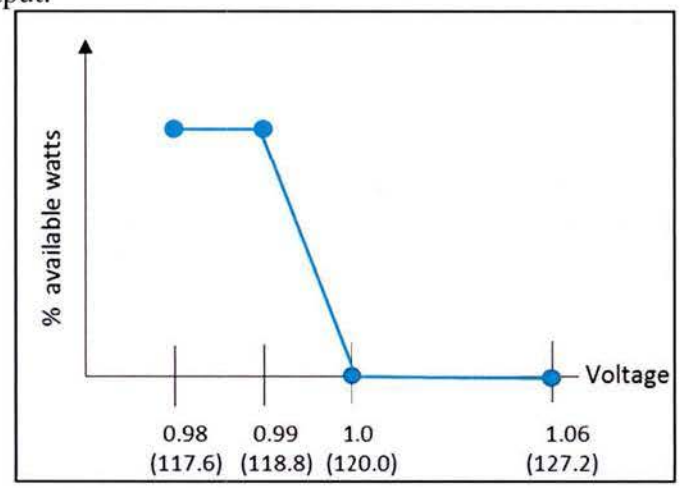

Figure 6.2.26: Input Volt-Watt Control Curve

The local voltage at the terminal of the inverters were above the V3 set point of 120V for the duration of this test. Therefore, the inverter was outputting close to zero watts of real power as shown below in Figure 6.2.27. It can be seen that the minimum output of the Volt-Watt command for the Hitachi inverter is about 350W while the SMA and Fronius inverter is able to output close to 0 watts. The results from the Volt-Watt control test are consistent with the active power curtailment test.

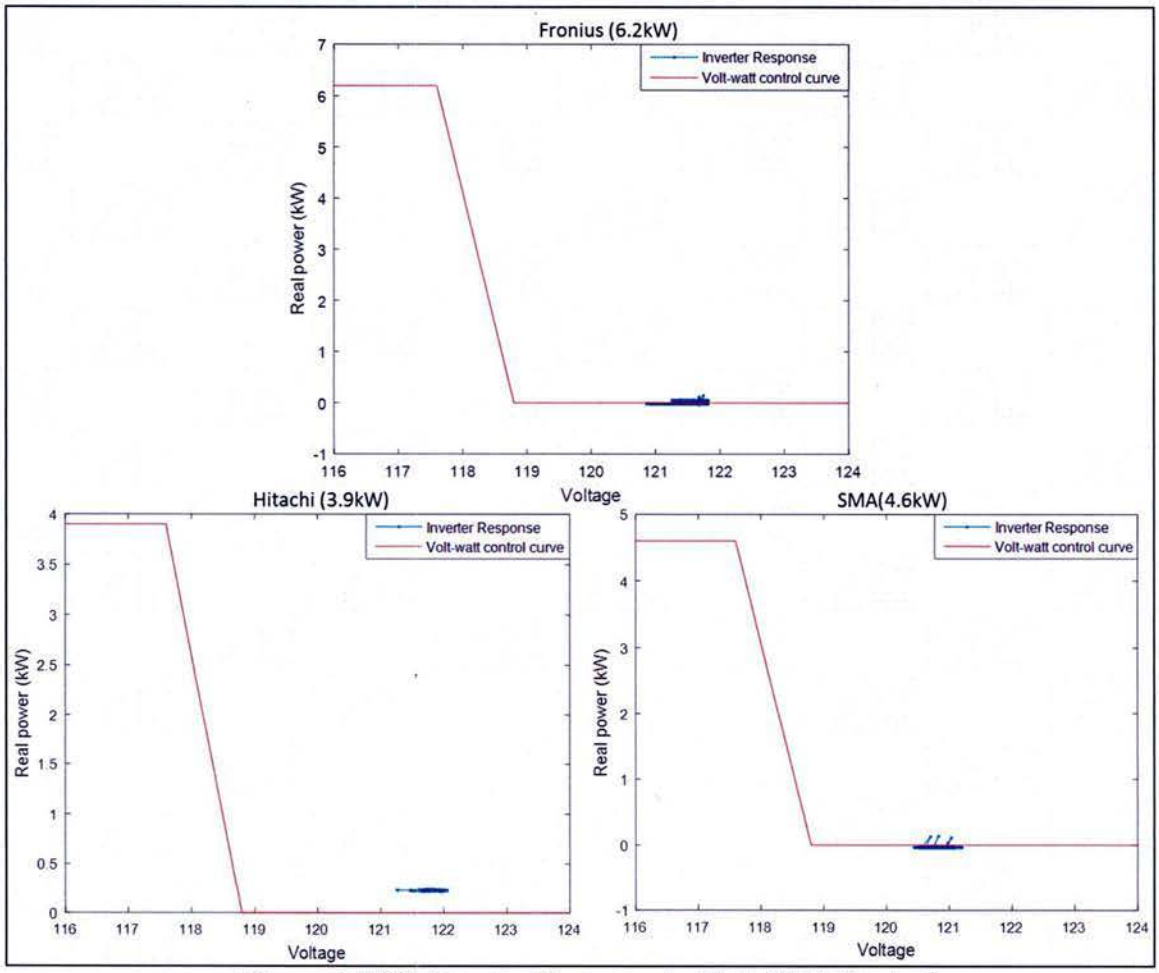

Figure 6.2.27: Inverter Response to Volt-Watt Control

Frequency-watt control

The SMA and Fronius inverters deployed for this project did not have the frequency-watt control functionality. Thus, the only inverter that will be analyzed in this section is the Hitachi inverter.

Frequency-watt control provides a mechanism to limit the real power generation when the grid frequency deviates from the nominal operating frequency by a specified amount. The method in which real power is controlled is through an input curve which consists of a set of points (P1-P7) defining a set of frequencies (f1-f5) and their watt levels as illustrated in Figure 6.2.28.

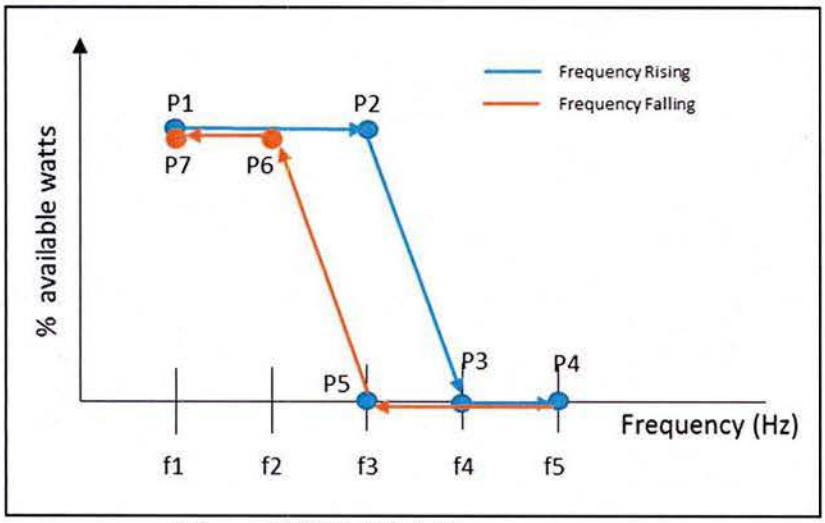

Figure 6.2.28: Watt-Frequency curve

The control curve also incorporates a hysteresis feature where the real power output ramps back up and returns to its prior production at a lower frequency. This is generally a common practice to prevent oscillation from occurring.

The frequency-watt control curve used to test the Hitachi inverter functionality is shown in Figure 6.2.29. As illustrated in the figure, the frequency set points are very tight since it is not possible to control grid frequency. As such, it is important to point out that this test is to simply test the functionality of this inverter control and not something that would be implemented in the field.

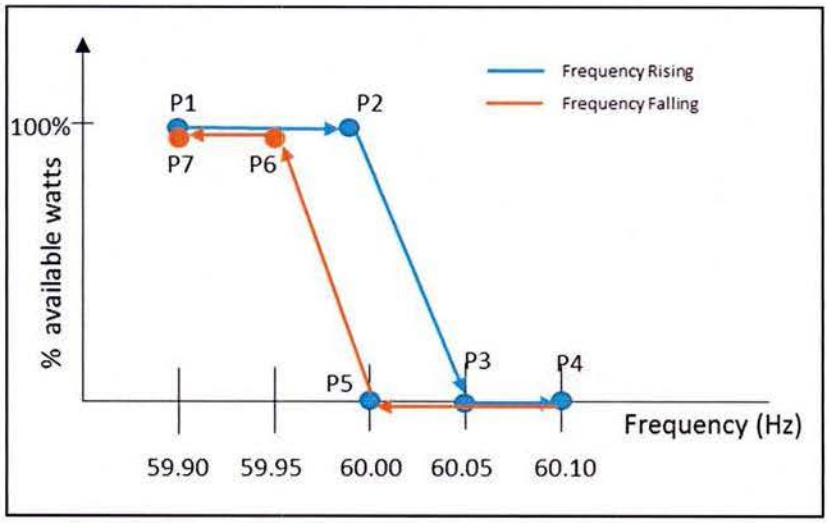

Figure 6.2.29: Watt-Frequency Control Curve

The command was sent at 9:00am to 11:00am and the results are shown in Figures 6.2.30 and 6.2.31 below.

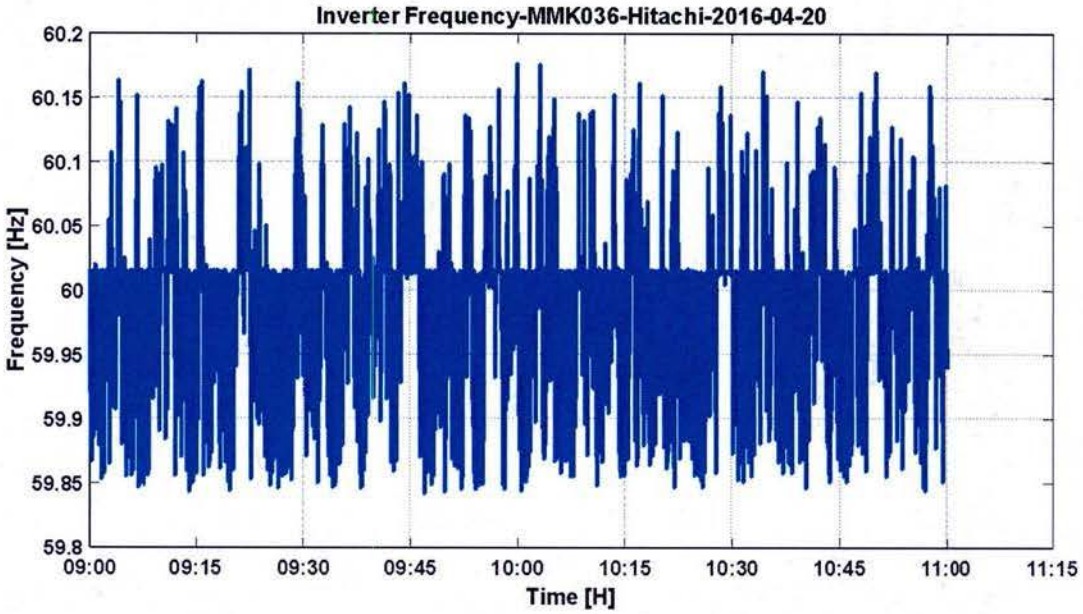

Figure 6.2.30: Inverter frequency

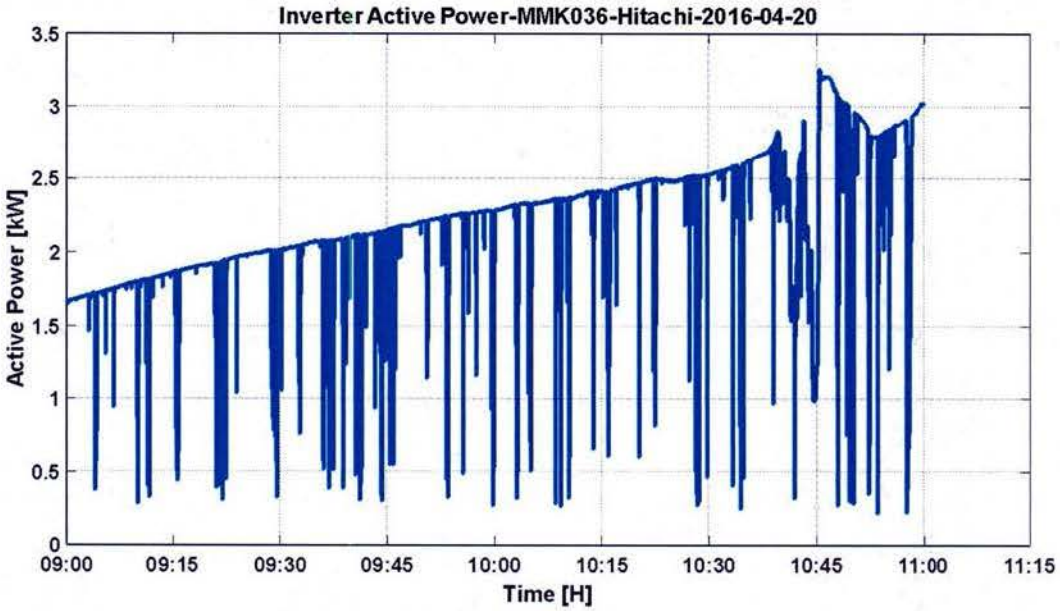

Figure 6.2.31: Inverter real power output

A magnified view of brief intervals from the above figures are shown below to visibly see the effectiveness of the command sent (see Figures 6.2.32, 6.2.33, and 6.2.34). The active power output of the inverter is represented by the blue line and the frequency is shown as the orange line. When the frequency exceeds 60.05Hz (green line), the real power output was curtailed until the frequency dropped below 60Hz (black line). In the three graphs, there seems to be a timing mismatch in the sensing of the grid frequency between the inverter and the data collection sensor and thus appears that the inverter is reacting before the grid frequency.

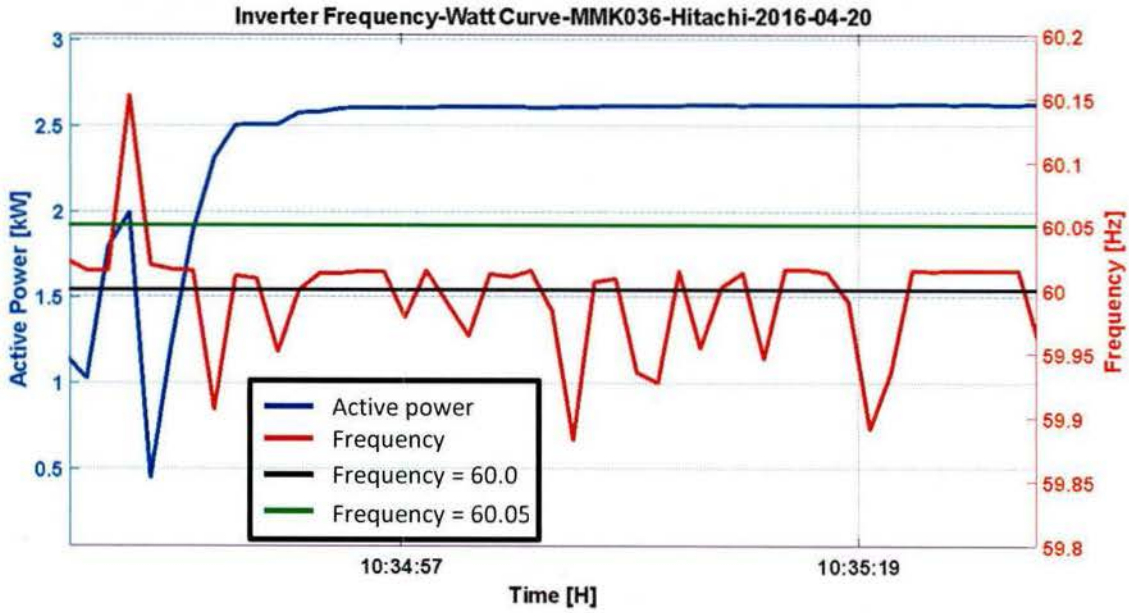

Figure 6.2.32: Inverter real power output versus frequency

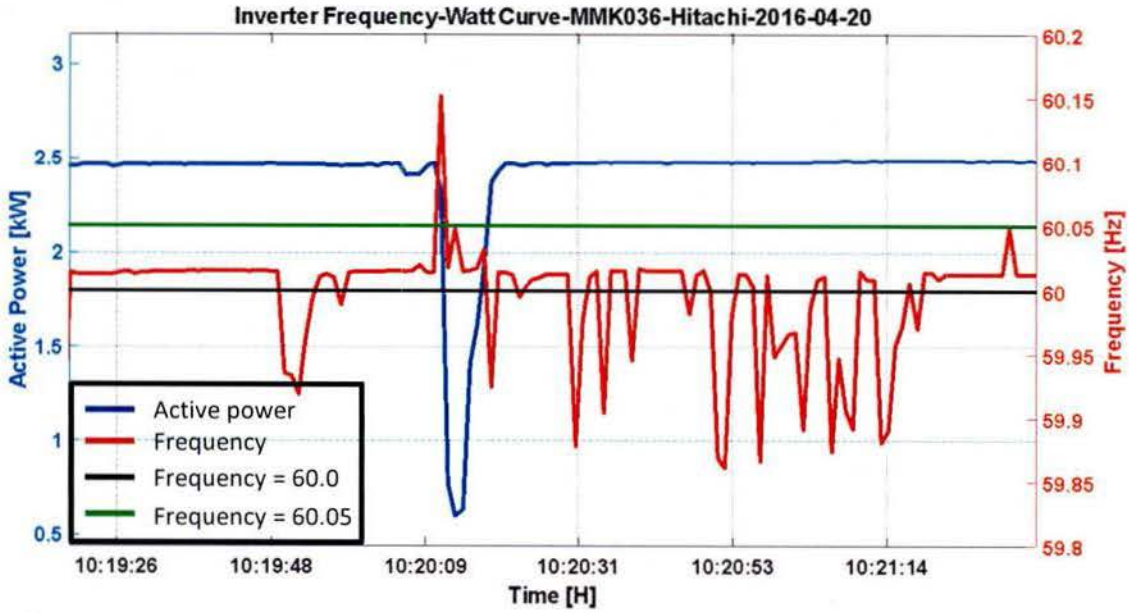

Figure 6.2.33: Inverter real power output versus frequency

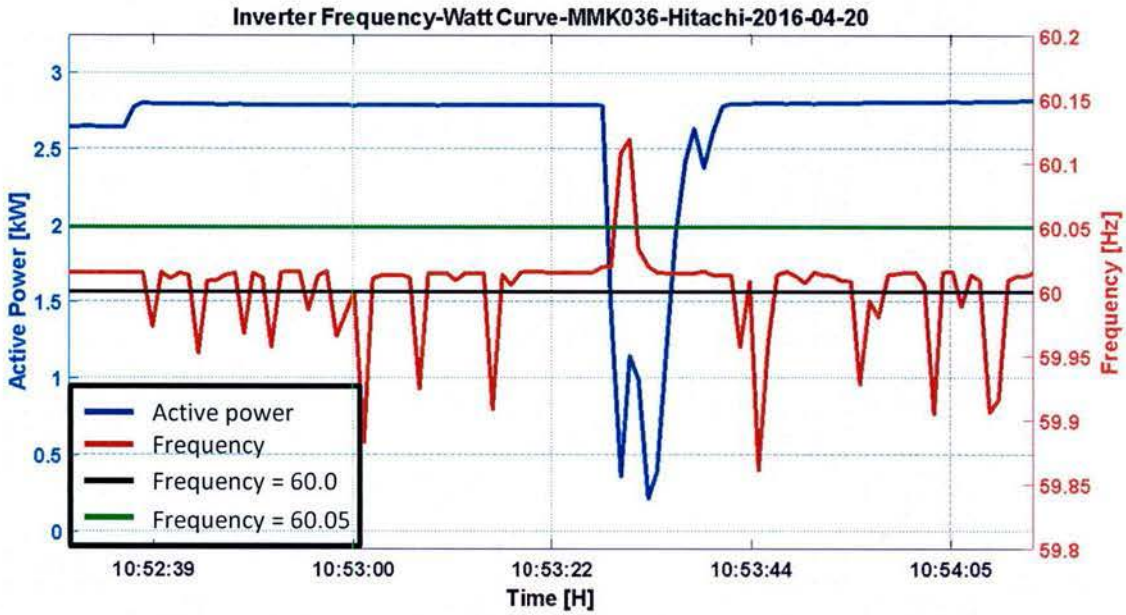

Figure 6.2.34: Inverter real power output versus frequency

Voltage impact of real power curtailment

The voltage at the inverter terminal is dependent on various factors. In this section of the report, the data from the upstream service transformer and the inverter is analyzed to illustrate how advanced inverter functions can be used to manage the local distribution voltage.

Curtailment commands in short duration were issued to an inverter as illustrated in Figure 6.2.35 below. The plot on the top is real active power with respect to time of the service transformer (in blue) and inverter (orange). The bottom plot is voltage as a function of time of the service transformer (in blue) and inverter (orange). During curtailment periods, the inverter voltage is lower in magnitude. Conversely, during periods of real power output the inverter terminal voltage is higher. In both scenarios, it is evident by looking at the voltage plot that the characteristic of the inverter follows that of the service transformer. It is evident that by controlling the inverter real power output, the inverter terminal voltage can be managed relative to the service transformer voltage.

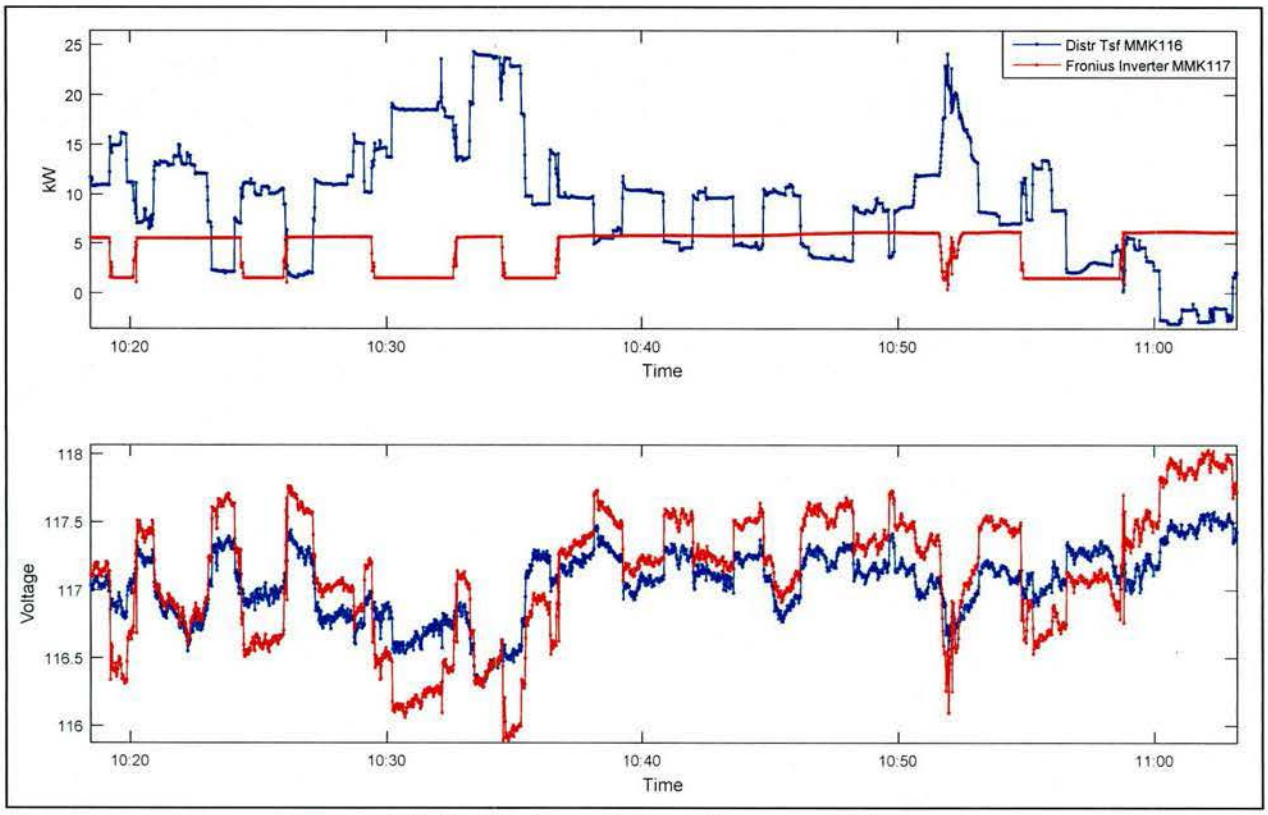

Figure 6.2.35: Real Power Curtailment and Voltage

Additional results of real power curtailment can be found in the internal report listed below.

Voltage impact using reactive power dispatch

Similarly, reactive power dispatch/absorption at the inverter affects voltage. As load demands are predominantly real power, voltage changes are dominated by the transformer real power changes and therefore must be considered when evaluating voltage effects due to reactive power. The impact to voltage at the inverter terminal and distribution service transformer due to reactive power is summarized in Figure 6.2.36 below.

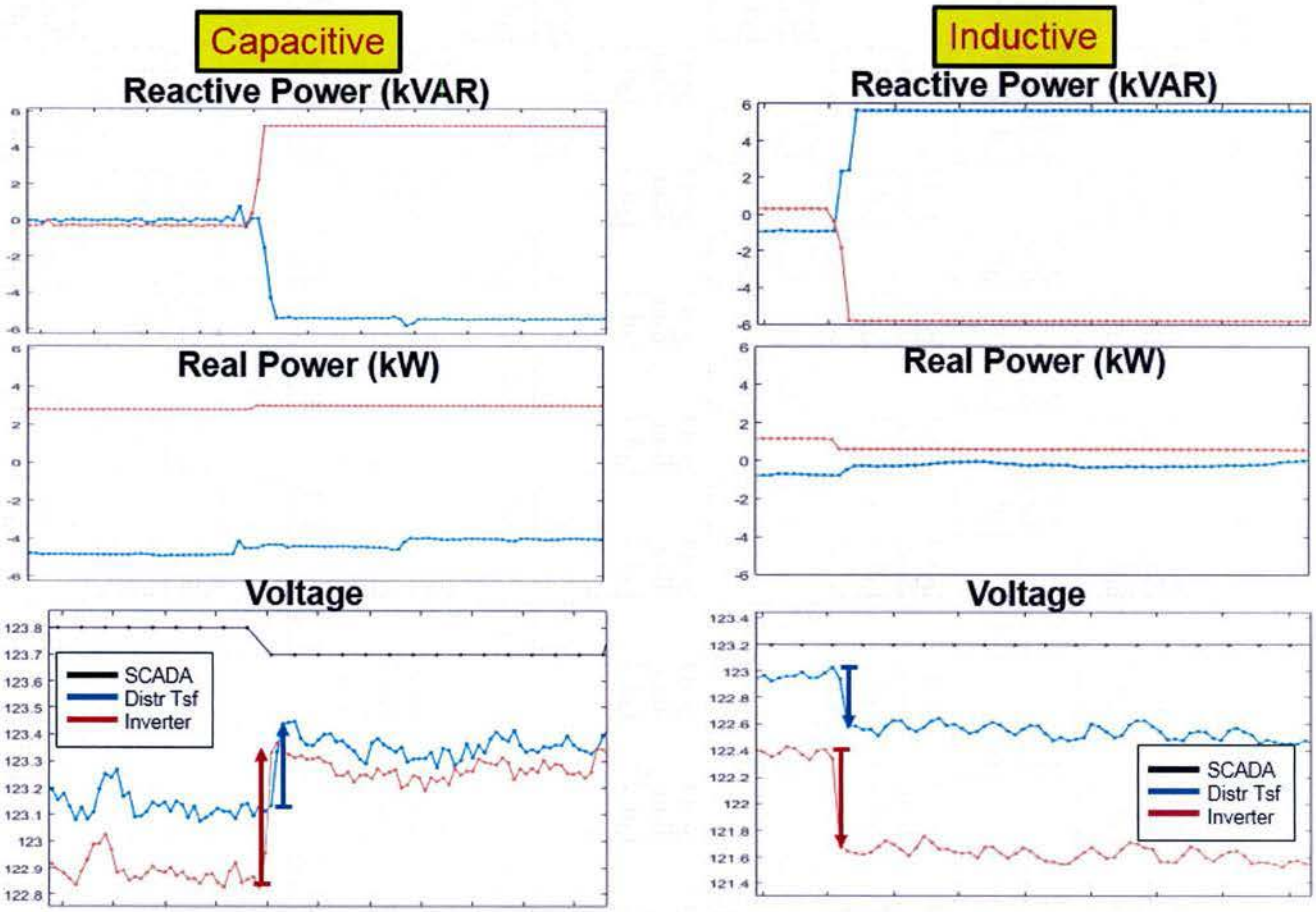

Figure 6.2.36: Voltage Impact due to Reactive Power

The set of plots illustrates clearly that by commanding the inverter to dispatch reactive power, it acts as a capacitor thereby increasing the voltage both at the service transformer and inverter terminal. Inverters can also be used to absorb reactive power which increases the reactive load relative to the distribution service transformer and as a result of that, it decreases the voltage at the inverter terminal and distribution service transformer.

The Maui Advanced Solar Initiative provided the opportunity for HNEI to field deploy remote data monitoring and an advanced inverter control system on the island of Maui. This project expanded the knowledge base of many members of the HNEI team in smart inverters and electrical power data analysis and equipment. During this funding period, we demonstrated that advanced inverters can be used to manage local distribution grid voltage by controlling the inverter real and reactive power output. However, standardization of how these functions are implemented across inverter manufacturers is necessary in order to utilize it in a real world scenario. The knowledge gained from this project led to the HNEI-CVR project.

Reports and Presentations Resulting from these Efforts

Reports

- SMA Inverter Lab Test Results

- Hitachi Inverter Lab Test Results
- Maui Advanced Solar Initiative Field Data & Results

Conference Presentations

- Dealing with High Penetration in Hawaii, S. Sadoyama, 7th International Conference on the Integration of Renewable and Distributed Energy Resources (IRED), Ontario, Canada, October 2016.

G. Conservation Voltage Reduction

Conservation voltage reduction (CVR) is a method to improve the efficiency of electric sources, such as the electric power grid, by optimizing voltage on the feeders that supply electricity to end-use devices (e.g., optimizing voltage on the feeders that run from substations to customers), thus reducing energy consumption. Traditional conservation of voltage methods within power grids have been performed by controlling a load tap changer (LTC) at the substation transformer (which in turn supplies energy to one or more connected distribution feeders and ultimately to downstream distribution service transformers and customers loads). The LTC shifts the voltage profile of the connected feeder(s) up or down, and is limited to lowering the voltage no lower than the lowest performing voltage point on the feeder(s). In particular, the voltage on a distribution feeder for a traditional utility power system is controlled by the LTC at the substation transformer, where the LTC shifts the voltage profile of the entire connected feeder(s) up or down. However, the LTC does not have the ability to manage individual low-voltage or high-voltage points along the path of the feeder. Thus, if the lowest performing voltage point on a distribution feeder is already near or at minus 5% of the nominal voltage, the opportunity to further lower the voltage across the entire feeder via traditional control of the substation transformer LTC is very limited or non-existent. While voltages at many or most other points along the controlled feeder may be operating at a higher voltage and could conceivably be lowered to reduce energy consumption, further voltage reduction by action of the LTC is constrained and not possible.

Traditionally, the power flow on the electric grid is unidirectional: the power flowed from the utility generators down to the homes and businesses. The voltage profile of distribution feeders in the traditional power system is illustrated in Figure 6.2.37.

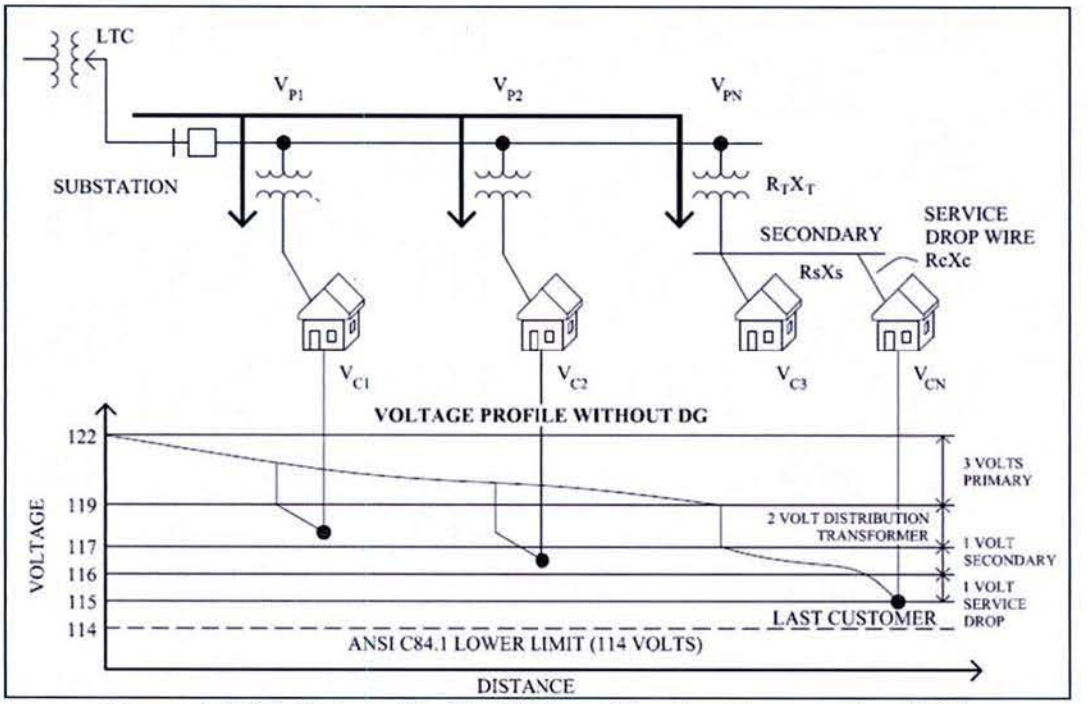

Figure 6.2.37: Voltage Profile Without Distributed generation (DG)

As shown, the voltage starts out high at the beginning of the feeder (substation transformer) and drops as power flows through cables, distribution transformers, and service wires before reaching its customers. With the advances in distributed generation (DG), e.g. solar rooftop photovoltaic (PV) systems, power generation at homes and businesses have become quite prevalent, causing the flow of power to be bidirectional. The location and size of these distributed resources contribute to the voltage profile; there may now be higher voltages at the end of the feeder than the start. Also, due to the variability of these distributed resources the voltages can be very erratic. For example, in the case of a feeder with solar PV there will be two very different voltage profiles: one profile during the day while the sun is shining and the other during the night when solar PV does not generate power. Further, with the addition of PV, feeder voltages can vary and shift in very short (seconds) and random time intervals during the day due to cloud shadows sweeping across PV arrays, in turn resulting in power production swings and erratic voltage fluctuations. As more distributed generation interconnects to the grid, it becomes increasingly difficult for utilities to effectively manage voltage variability and implement CVR with just the utility's LTC method of managing voltage.

In order to address the numerous issues noted above (e.g., variable loads in the grid, devices that produce power locally, lack of voltage control beyond the utility's LTC, etc.), an algorithm and corresponding system to control the voltage on the electrical power grid in real-time led to the invention of a new patent-pending technology. The concept of the technology is to reduce the voltage drop across each distribution transformer using reactive power.

HNEI Simulation Results

The field data and detailed electrical model developed under another APRISES11 project, the Maui Advanced Solar Initiative, were used to test the algorithm as shown in Figure 6.2.38 below.

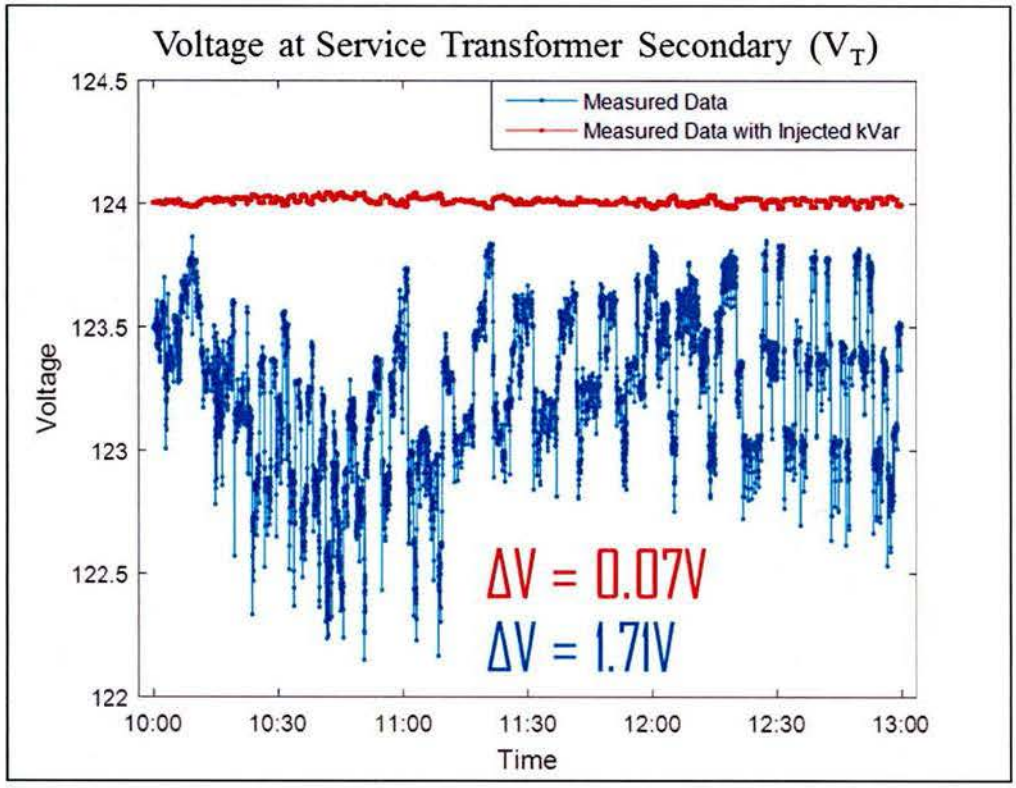

Figure 6.2.38: HNEI Conservation voltage reduction (CVR) Algorithm Simulation Result

The voltage fluctuation during this time period was about 1.7 volts with the algorithm turned off. With the HNEI-CVR algorithm, the voltage fluctuation was reduced to 0.07 volts. Various simulations were performed to ensure validity of results and details on the control and algorithms can be found in the patent application.

Maui Electric Algorithm Test Bed

To test the newly developed technology, we used commercial-off-the-shelf products to develop a prototype and worked with Maui Electric Company to setup a test bed at their facility. The electrical diagram and photos of the test bed are shown below in Figures 6.2.39 and 6.2.40, respectively.

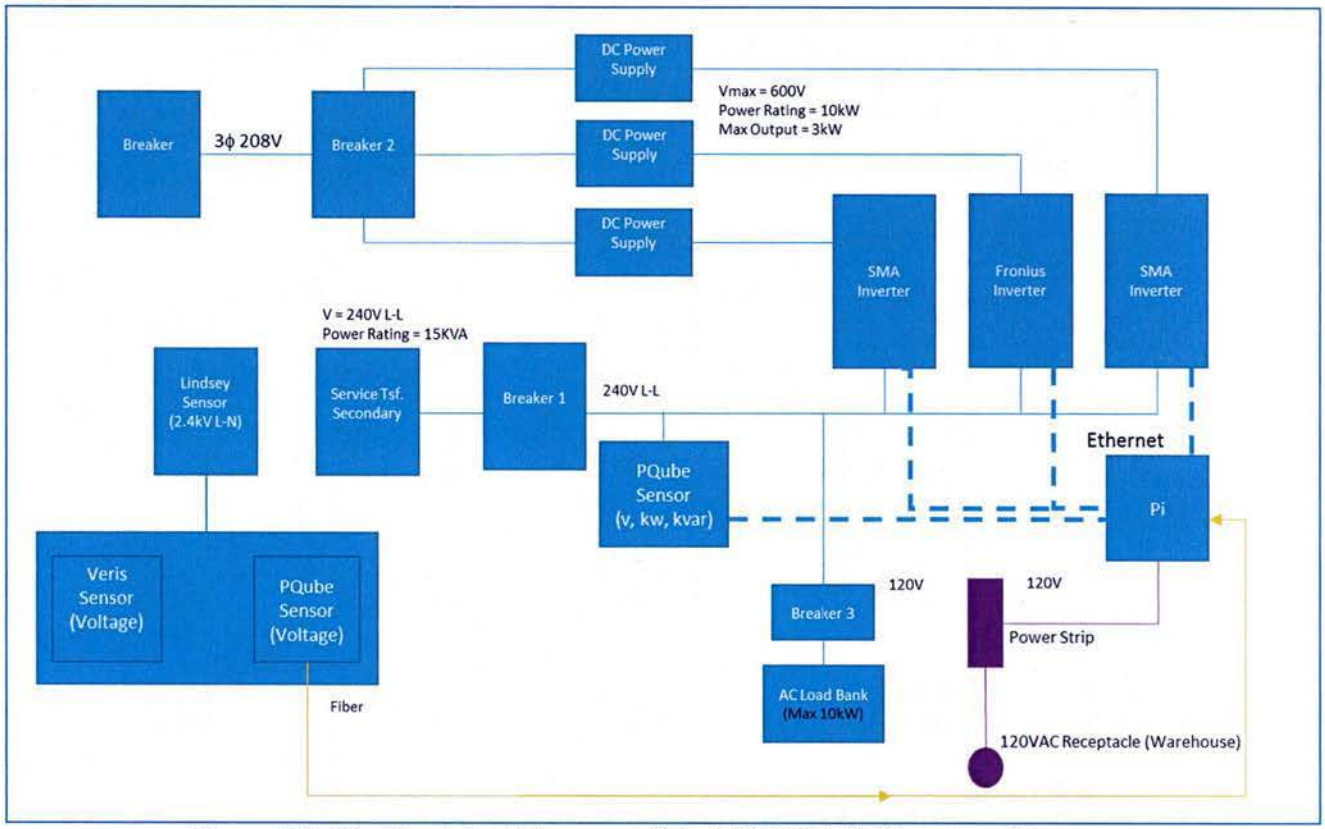

Figure 6.2.39: Electrical Diagram of the HNEI-CVR Prototype Test

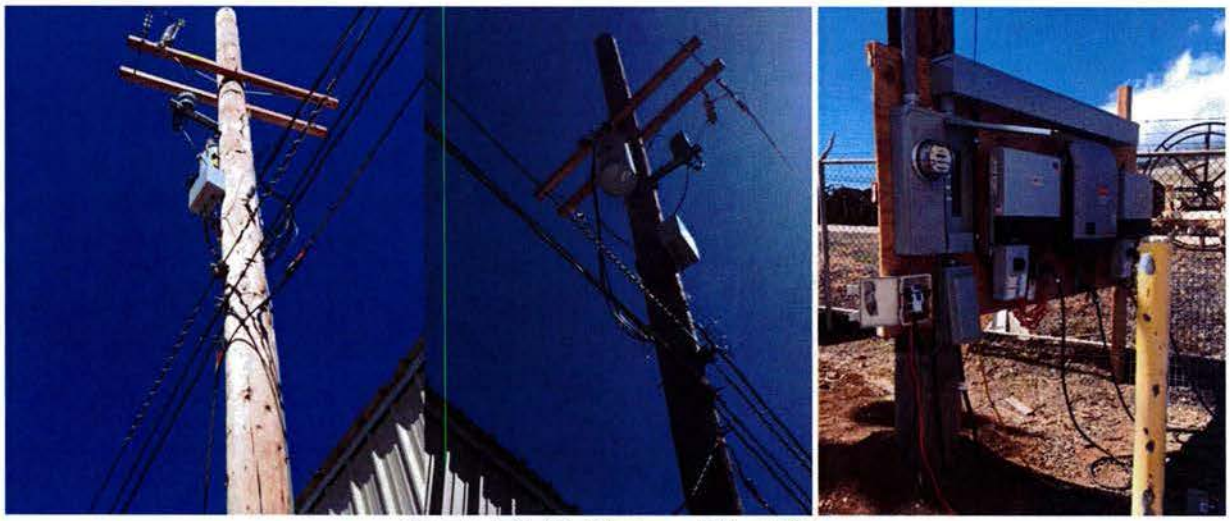

Figure 6.2.40: Photos of Test Site

Maui Electric Company setup a dedicated distribution service transformer for us to have full control over the load which consisted of a switchable resistor simulating real power load. In conjunction, a PV inverter was used to simulate variable real and reactive load via advanced inverter functions such as real power curtailment and reactive power dispatch. A primary voltage insulator was also installed to monitor the primary line voltage in order to validate the HNEI-

CVR algorithm which in effect reduces the voltage difference across the distribution service transformer.

HNEI-CVR Device Prototype Test

HNEI worked closely with two Japanese corporations; Hitachi and IKS to develop a prototype of the HNEI-CVR device. The device was shipped to Maui Electric Company for testing. The electrical schematic of the test setup and prototype device are shown in Figures 6.2.41 and 6.2.42, respectively.

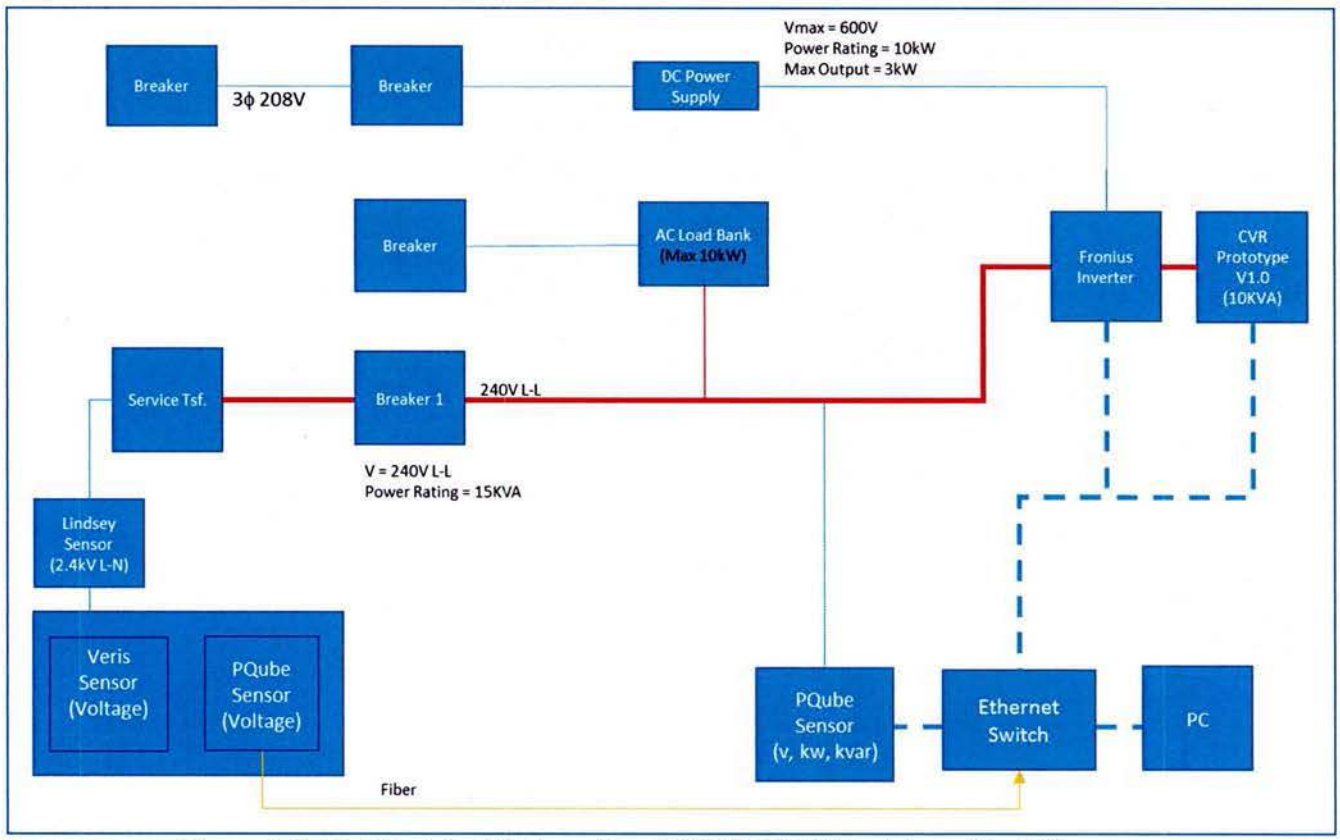

Figure 6.2.41: Electrical Schematic of HNEI-CVR Prototype Test Site

Figure 6.2.42: HNEI-CVR Prototype

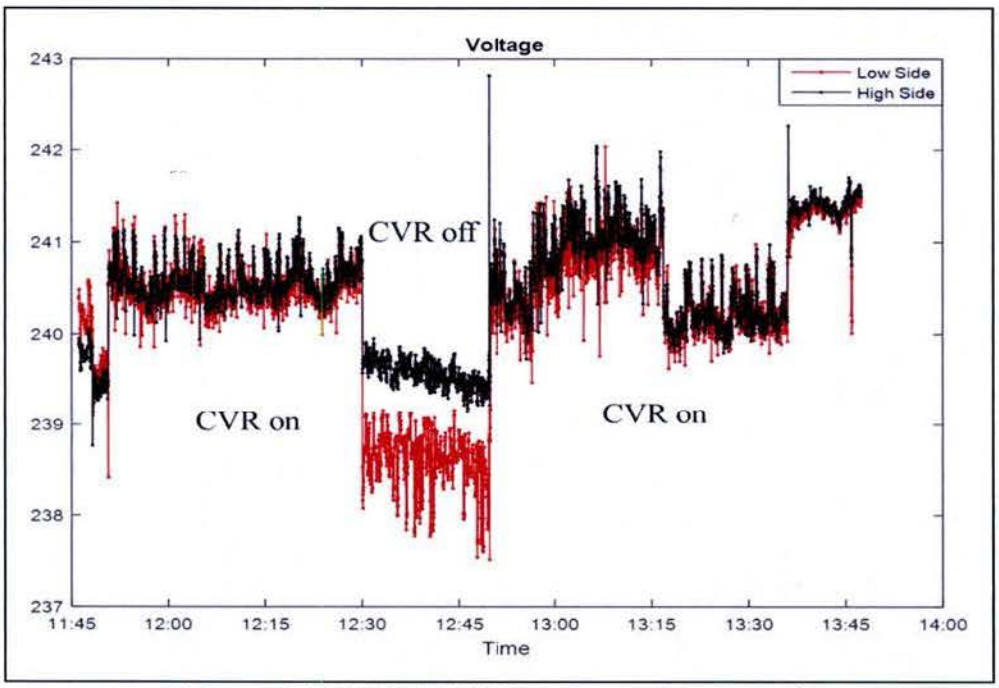

Figure 6.2.43: HNEI-CVR Prototype Test Result

One of the test scenario results is shown in Figure 6.2.43. The red and black series represents the voltage on the low and high side of the distribution service transformer, respectively. In this scenario, there are both real and reactive loads on the transformer and it is evident that when the device is turned on, the voltage difference across the transformer is reduced to a minimum.

A patent has been filed for the developed technology is currently in the patent-pending stage. HNEI is actively working closely with industry partners to perform a field demonstration and take the technology to market.

Patents

- Dynamic Reactive Power Compensation patent filed on 07/07/2017.

H. Grid-Scale Storage Testing

HNEI continued its testing and evaluation of grid-scale Battery Energy Storage Systems (BESS) under this award. To date, three grid-scale BESS have been procured and commissioned under prior funding. The 'Big Island' (Island of Hawaii) BESS has operated for over four years, in both a wind smoothing and frequency regulation mode. The Oahu BESS was commissioned in April of 2016, testing voltage regulation and power smoothing functions on a circuit with a high penetration level of distributed photovoltaic (PV) systems. The Molokai storage system was commissioned in June of 2016. Modification of the control system and algorithm development and testing were completed, under this award, in May 2017.

The island of Molokai currently has the highest installed capacity of distributed generation PV systems (DG PV) relative to the daytime power demand of the island's grid. Customers have installed 2,144 kW of DG PV and there is 133 kW of DG PV approved for interconnection to the Molokai grid. In addition, there is 665 kW of DG PV in an interconnection queue pending an increase in the hosting capacity of the grid. In total, there is 3,042 kW of DG installed, approved or in the queue for the Molokai system which has an average daytime load of roughly 4,500 kW.

The BESS on Molokai is intended to provide a high speed response to system disturbances such as the sudden loss of generation or load. Of the three BESS installations, the Molokai site provided the most challenges. The inertia (in essence, a resistance to change) of the Molokai grid is very low, such that relatively small imbalances between power generation and consumption can cause significant frequency deviations in millisecond (ms) timeframes. Technologies proposed to serve such a grid must be carefully vetted so that latent responses to these imbalances do not create instabilities in the system frequency. A 200ms delay between a loss of generation (or load) and realization of a real power correction from the BESS, can cause the entire grid to become unstable (that is, a latent correction can be worse than no correction at all if not done properly).

An investigation of the control system latencies associated with the Island of Hawaii BESS showed that the delay between a system frequency event and the response from the BESS varied

between 200 ms and 300 ms, which was sufficient for the Island of Hawaii system. The Molokai BESS as procured and installed utilized the same control scheme and would therefore have the same latency in its response. However, this response was found to be too slow for the Molokai power system. As a result, a control improvement project was initiated under this award to improve the response time of the Molokai BESS. The development and implementation of the improved control scheme was completed in May of 2017 and is currently undergoing field testing (which will be completed under other funding).

The control improvement project partners and their roles are shown in Table 6.2.2.

Table 6.2.2: Project team and roles.

Partners (Public and Private)	Role
Office of Naval Research (ONR)	Funding source
University of Hawaii (UH), Hawaii Natural Energy Institute (HNEI)	Project lead, technical oversight, coordination, planning, performance verification, analysis, and reporting
Maui Electric Company (MECO)	Utility grid owner, electrical design, planning, coordination, installation, communications design, safety, and metering design
Parker-Hannifin Inc.	Inverter manufacturer and testing
Integrated Dynamics Inc. (IDI)	Algorithm development, control system infrastructure redesign, software development, communications design, and simulations
Northern Plains Power Technologies (NPPT)	Grid simulations, inverter simulations, and algorithm development

The control improvement project was separated into two phases. Phase 1 was the investigation phase where the requirements for the inverter were developed and provided to the inverter manufacturer to prepare for Phase 2. Phase 2 was the implementation, testing and commissioning phase.

Phase I – Investigation

As part of their responsibilities as a partner in this BESS project, Maui Electric commissioned Northern Plains Power Technologies (NPPT) to conduct a study in collaboration with HNEI to develop an algorithm, and model the algorithm's performance and impact on the Molokai grid. In that effort, a multirate droop-based controller has been designed and it was determined that the BESS would need to respond within 50 ms to achieve its frequency stabilization objective.[1,2,3]

Integrated Dynamics Inc. (IDI), HNEI's consultant, analyzed and simulated the control algorithm specified by the NPPT study, separating it into an "inner loop", to be implemented in the Parker inverter control, and an "outer loop", to be implemented in a separate Site Dispatch Controller (SDC).[4]

The simulations showed a very substantial improvement in performance when an inner loop is used, and clearly inadequate performance without the inner loop. Further, adding synchrophasor sensing of frequency in the outer loop does not appreciably improve performance when an inner loop is used.

As a result of the Phase I analysis, IDI made the following recommendations for the implementation phase of the project, based on the response-time analysis:

(1a) All algorithms for the Molokai grid should use an inner / outer loop model; performance with outer loop alone is inadequate.
(1b) Implement NPPT's "sticky" controller.
(1c) The inner loop should use a single lookup table from frequency to watts; hysteresis not required; a new lookup table should be computed every 100 msec by the SDC and transferred to the Process Control System (PCS).
(1d) Use Parker's Low Voltage Ride Through (LVRT) mechanism to implement NPPT's voltage cutoff at 0.8 pu instantaneous trip.
(1e) Parker's default Phase-Locked Loop (PLL) has a settling time of 100 msec. This is too long to be useful for frequency control in this application. Change the PLL tuning to have a settling time of 40 msec or faster.

Additionally, during the course of the investigation, some implications of the NPPT algorithm were observed, which might cause undesirable consequences in certain transient conditions. As a result, the IDI team reviewed the performance of the NPPT algorithm and recommended that a more conventional control algorithm should also be considered as an alternative.

IDI made the following recommendations based on the additional work examining possible alternative algorithms:

(2a) The NPPT sticky algorithm's voltage cutoff logic is not robust to faults in which bus voltage remains above 0.8 pu; in such a case, the BESS could cause an overfrequency PV trip which would not otherwise occur.
(2b) Additionally implement the "Semi-Sticky" algorithm (enhanced Primary Frequency Response, with a sticky high-gain non-linearity) to improve transient response. (2b) Implement filtering of measured frequency in the inner loop (i.e. Parker inverter) to reduce effects of frequency noise on steady-state power variability.
(2c) Do not implement high-speed lead compensation, since the stability margin benefit is eliminated once noise sensitivity is taken into account.
(2d) The SDC / PCS interface should include feedback to the SDC of the range of powers and range of frequencies seen during a short period of time.
(2e) Set Parker's Undervoltage (UV) trip settings as low and long as possible when using Options #2, #3, or #4.
(2f) Analyze impact of PLL phase tracking errors during the implementation phase.

Using results of the analysis, IDI documented the inner loop PCS Control Requirements for implementation and testing by the inverter manufacturer, Parker Hannifin.[5]

Phase II – Implementation, Testing, and Commissioning

Following IDI's modeling and investigation in Phase I, IDI and Parker Hannifin implemented the inner iloop and outer loop control scheme, as well as the algorithms developed by IDI in Phase I, into a Parker 890GTB inverter installed at Parker Hannifin's test facility in North Carolina. The Unit Under Test (UUT) inverter at the test facility is identical to the one installed on Molokai. One 890GTB inverter was setup in island mode to provide the synchronizing frequency and voltage source, the other UUT inverter was configured with the inner loop and outer loop controls and algorithms as they would be implemented on Molokai. Figure 6.2.44 provides a schematic of the test configuration.

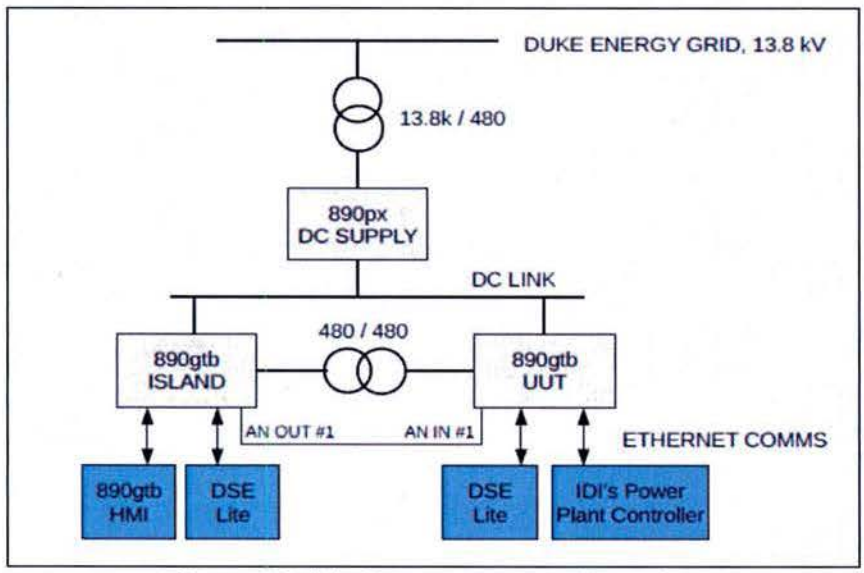

Figure 6.2.44 – Inverter test configuration

The Parker 890GTB's inverter was tested using an inner loop Frequency / Watt feedback. Functionality was as expected. Performance was not as good as desired, but will still be a significant improvement over a control system with only outer loop control.

The inverter drive is CPU limited. When Volt / VAR and Frequency / Watt inner loops are simultaneously enabled, Parker has determined that CPU speed limitations result in unacceptable slowdown of response time. Therefore, due to the CPU speed limitations, Parker disabled the Volt / VAR feedback logic; it was not available for testing. Also, our testing shows that computation time affects both average and worst-case Frequency / Watt response times.

The sync frequency, which is used for the inner loop Frequency / Watt feedback, has acceptable noise at most operating points. However, the noise level was problematic in testing at 60.7Hz. The root cause of the excessive noise scenario is not known at this time. However, it is expected that this problematic noise scenario will have minimal effect on overall performance in the field for the Molokai application, since the grid spends very little time at the problematic frequency.

After inverter performance testing was completed, IDI configured a hardware in the loop (HIL) simulation environment using the inverter test results to tune the simulation, to evaluate the control strategies. The NPPT and Adaptive Primary Frequency Response (PFR) control strategies were implemented and verified in the HIL simulation environment. The conclusions from this testing were:

- Performance of both NPPT and Adaptive PFR implementations are as expected when run with the inverter inner loop (Frequency / Watt curve) enabled.
- Both algorithms remain stable when applied with worst case inner loop controller delays, as measured at Parker Hannifin's test facility.
- Both algorithms are unstable when used without the inner loop, unless severely de-tuned to accommodate the much longer controller delays.

Once the HIL testing was completed, the inner and outer control loop and the NPPT and Adaptive PFR algorithms were implemented in the 890GTB inverter on Molokai. A test plan was developed in collaboration with the project stakeholders and commissioning tests were completed in May of 2017.

During the testing, the closed loop control system was enabled and a 'disturbance' was injected into the grid so that the BESS response could be evaluated. For repeatability, the BESS itself was used to inject the disturbance.

The SDC has a special test mode for injecting a disturbance. The test mode allows a P/Q offset to be added to the normal BESS commands for a specified period of time. This disturbance offset goes to the inverter directly, bypassing the limits the SDC normally enforces. For example, if the kW limit is configured for 100 kW, it is still possible to command a larger disturbance of 400 kW. In this way, it is possible to see what an authority-limited control system response will be to a larger disturbance.

A disturbance of -400 kW was used to temporarily increase load on the system, causing frequency to decrease momentarily until it is stabilized by the generator and BESS controls running in combination.

Two disturbance profiles were used for the commissioning test:

Disturbance Profile "STEP":

- P offset = -400 kW
- Q offset = 0 kVAR
- Duration = 30 seconds

Disturbance Profile "PULSE":

- P offset = -400 kW
- Q offset = 0 kVAR
- Duration = 0.5 seconds

A summary of the results of the commissioning test are provided below.

- The overall frequency excursions of the Molokai grid have clearly improved since commissioning the BESS (Figure 6.2.45).

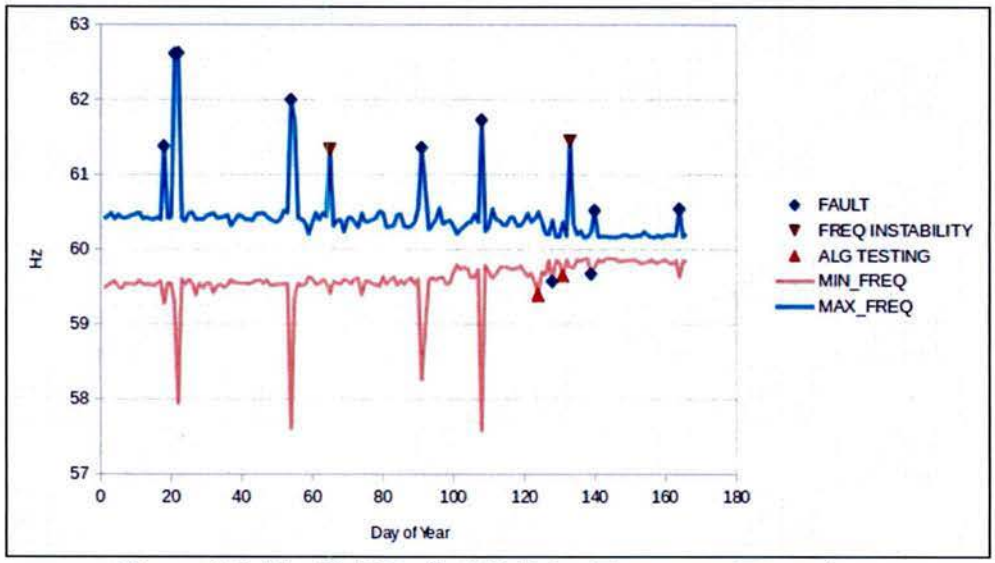

Figure 6.2.45 - 2017 Daily Min/Max Frequency Excursions

- Testing confirmed the necessity of the control system loop delay improvement project; when run as outer loop only, the BESS caused frequency instability and did not improve transient response (Figure 6.2.46).

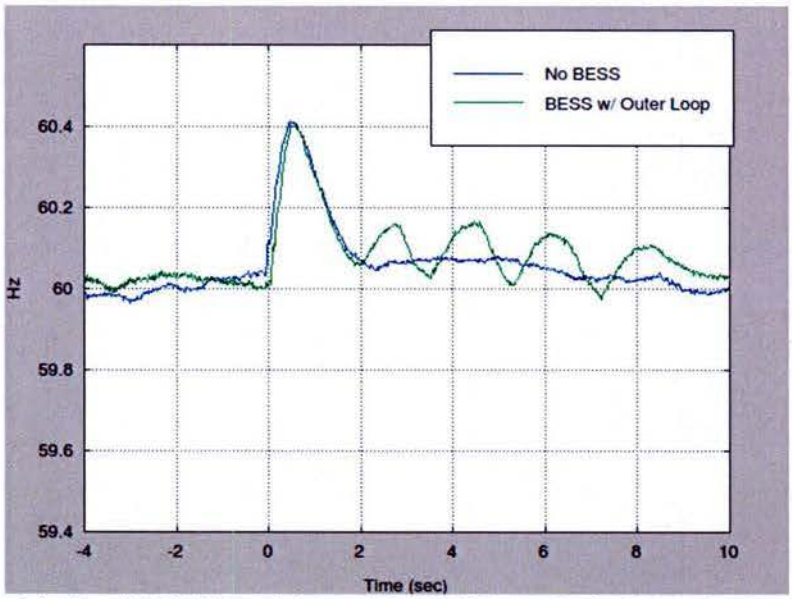

Figure 6.2.46 - 400KW load drop - No BESS vs. Only Outer Loop Control

- With 500 kW authority, the BESS reduces frequency excursion resulting from 400 kW step and pulse disturbances by half (Figures 6.2.47and 6.2.48).

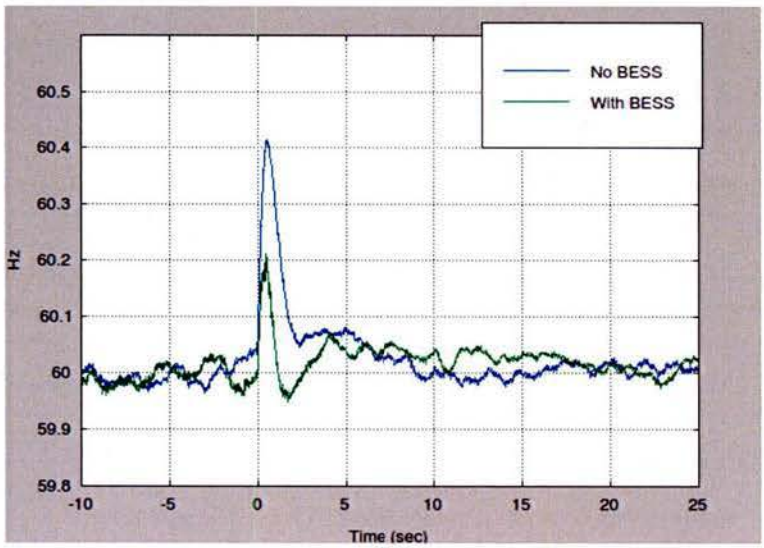

Figure 6.2.47 - 400 kW load drop, with and without BESS

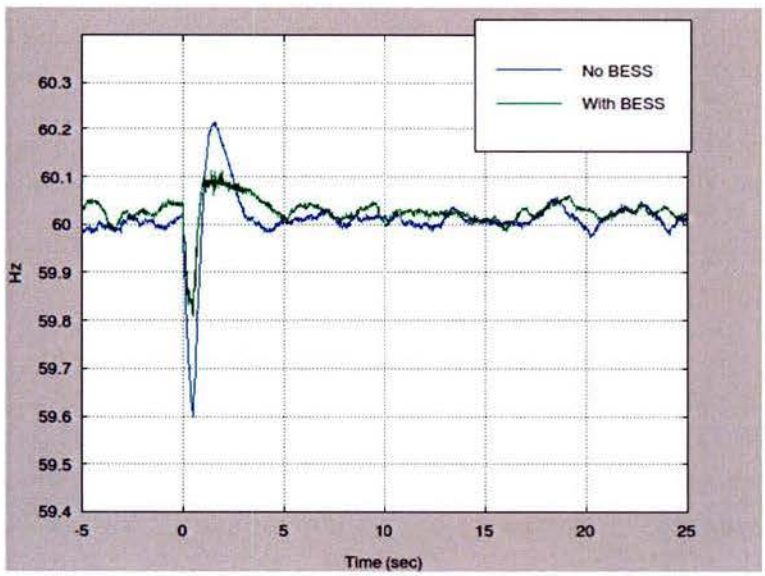

Figure 6.2.48 - 400 kW load pulse (0.5 sec), with and without BESS

- Frequency excursions are approximately the same between the Adaptive PFR and NPPT algorithms for step disturbances; Adaptive PFR is has lower overshoot for pulse disturbances.
- Inverter sync frequency in the field is significantly noisier than what was measured in the laboratory environment at Parker Hannifin in March 2017.

- The Adaptive PFR algorithm in its initial version showed excessive sensitivity to noise in the inverter's sync frequency. An upgrade to the algorithm was installed after the initial round of testing to reduce sensitivity to noise in the inverter's sync frequency.
- In one set of tests, the NPPT algorithm got 'stuck' in a mode where it continued charging the battery long after the event completed. A small modification to the NPPT algorithm was implemented to avoid getting stuck in this particular way.

Field Testing

Once the inner and outer loop control system and algorithms were commissioned, the project team decided to leave the BESS controls active using the Adaptive PFR algorithm with an authority limit of 500kW. Moving forward under other funding, the objective of the field test is to assess the performance of the BESS and the algorithm to actual system disturbances, such as generator trips, faults on the system (especially faults that cause very low voltages), or the switching of large pump loads on the systems. The switching of pump loads on the system happen daily, however the generator and fault events are not planned and happen somewhat randomly. As a result, it is expected that the BESS will need to be online for several months to capture its response to the larger system events. The evaluation of the BESS's response to these events and the associated improvements to the control system and/or algorithm will be completed under a separate award.

References

1. M. Ropp, "MECO BIS CONTROLLER FINAL REPORT" January 23, 2015.
2. M. Ropp, "Report on a proposed controller for a frequency-stabilizing battery inverter system for the Molokai power system", dated January 23, 2015.
3. M. Ropp, "Behavior of a proposed battery-inverter system on Molokai during faults", May 06, 2015.
4. K. Musser, "Molokai Algorithm Investigative Project Report", October, 5, 2015.
5. A. Mitchell, K. Musser, "Inner Loop PCS Control Requirements for Coastal 3 Altairnano BESS in Molokai", January, 2016.
6. K. Musser, "Parker Hannifin 890GTB Inverter, Frequency / Watt Performance Test Results", March 2017.
7. K. Musser, "Molokai BESS – Algorithm Ph2 Project, HIL Simulation verification Results", March 2017.
8. K. Musser, "Molokai BESS – Algorithm Ph 2 Project, Commissioning Test Report", June 2017.

I. Power Grid Monitoring

In order to improve the resiliency of the electric grid and allow high penetrations of distributed photovoltaics (PV), there is a need for better real-time situational awareness of the distribution circuit. On circuits with high penetration of PV, power sometimes backfeeds from residential customers to the grid. This can introduce issues such as overvoltage, violations of thermal limits on the electrical lines, and at a system level, the need to provide adequate operational reserves to

protect against transient cloud coverage. Under APRISES 11 funding, HNEI began to develop a low-cost real-time power monitor to help the utility identify and address these issues and ultimately operate the grid more reliably with large amounts of distributed PV.

HNEI previously deployed 60 distribution-level power monitoring devices under the US DOE-funded Maui Smart Grid Infrastructure project. This work showed that commercial power monitors are currently inadequate for system-wide deployment on the distribution grid. Some do not accurately measure reactive power under bi-directional active power flow, which is essential for advanced methods of voltage regulation. Others provide advanced measurement of reactive power, harmonics, and numerous other metrics, but are very expensive (~$3000/unit) and still require communications equipment with a commercial data plan (up to $100/mo), a power supply, and a weather resistant enclosure. These are designed primarily to record power quality data for post-processing and event detection rather than to stream the data required for real-time for controls and operation. A low-cost, integrated solution does not exist for circuit- or system-wide monitoring to address the specific needs of utility operations under high penetrations of PV.

Under this subtask, HNEI designed and built several prototypes of a custom real-time power monitor for use at the distribution level. This work indicates that the fully implemented system will be at least an order of magnitude cheaper than existing options. Software development is ongoing under other funding, and the device will be further tested, calibrated, and validated before field deployment. Installations are being planned for Maui Meadows (up to 100 units); Okinawa, Japan; and as a part of the instrumentation of HNEI's distribution systems lab.

An invention disclosure has been filed with University of Hawaii's Office of Technology Transfer (OTT) and the possibility of a provisional patent is being discussed. For this reason, the design and technical features of the device cannot be presented at this time. Details will be provided in a subsequent APRISES report.

In order to involve students in the development of the power monitor, HNEI conducted a semester-long electrical engineering project course for eight juniors at the UH at Manoa. The course included lectures and hands-on experience covering the fundamentals of AC power, lab safety, circuit board design and fabrication, programming, and communications. The course received excellent reviews, and a Senior Capstone Design course is currently being offered to four of the students, focusing on software development for this device.

HNEI established a Power Monitoring Lab within existing lab space for the development, assembly, soldering, and testing of these devices, with appropriate equipment, safety protocols, and training.

6.3 Grid Integration at Community College Sites

The objective was to analyze, and test the integration of promising green grid technologies and control systems to evaluate their performance in a variety of coastal island conditions. This evaluation was accomplished through deployment of the following technologies: integrated photovoltaic (PV) and on-site "neighborhood" (i.e. residential scale) storage systems; renewable

energy charging for electric vehicles (EVs); energy and CO_2 dashboards; distributed solar forecasting in combination with wind and solar sensors and measurement equipment; and database management capability to demonstrate and assess performance.

HNEI contracted this work to Maui College, to work with ONR, end-users, and technology providers. Maui College has utilized the college campus as a test bed for testing, measuring and analyzing promising technologies as follows:

A. Integrated PV and On-site Storage Systems: Two approaches to this task were used as work unfolded. Initially, the Sunverege Solar Integration System (SIS) was chosen as a neighborhood system. Additionally, a relatively large, canopied parking lot PV array was integrated with large batteries acquired through the NEDO funded Hitachi JumpSmart Maui project.
    a. SIS was installed at the UH Maui College Aquaponics facility. In addition to providing the opportunity to test a variety of SIS's software capabilities, such as programmable energy dispatch to optimize peak load and demand charge reduction, the Aquaponics facility has the compelling need to use an Uninterruptible Power Supply (UPS) system as fish in tanks will die in 20 minutes without pumped air, which would be the case with a grid power outage.
    b. Regrettably, the Schneider Electric XW+6848 inverter included with the system was removed from the HECO/MECO Qualified Grid Support Utility Interactive Inverters. Sunverge will be replacing the inverter with a HECO/MECO approved model when their new system is released in the 4th quarter of this year. Currently, the Sunverge SIS is programmed to utilize the UPS function in off-grid mode and serves reliably as a backup system in the event of grid failure. Additional grid support functions can be implemented after the inverter is replaced.
    c. Parking Lot PV Array with Hitachi Batteries: Over a period of several years, a 750 kW DC canopied array was installed in the main campus parking lot, with the PV acquired through a Power Purchase Agreement. During this period, two 460 kW DC battery systems were acquired through the NEDO / Hitachi JumpSmart Maui project. Over the past year, engineers from Hitachi and Johnson Controls, Inc. have been working to integrate control of the battery storage system into the Johnson Control Metasys Energy Management System (EMS). Integration has been largely successful and final testing of the system will soon be conducted under other funding.
    d. Currently, Metasys is programmed to discharge the battery system under two circumstances. Primarily, the system is designed to reduce campus peak load and subsequent demand charges. Additionally, the battery system is designed to absorb excess PV generation and prevent export of electricity to the Maui Electric grid. This circumstance typically arises during sunny summer weekends between semesters when generation is at a maximum and campus loads are reduced.
    e. As additional programs at the utility become available, such as demand response, frequency regulation and time-of-use metering, Metasys will be re-programmed to prioriotize battery discharge to minimize utility electricity bills.

B. Renewable Energy Charging for EVs: Although the main campus parking lot was chosen to develop the canopied PV array because of the size of the system it enabled, the choice of the parking lot array also supported the installation of eight ChargePoint Level 2 EV charging stations. Since trenching was necessary to land all AC and DC circuits for the PV array, there was minimal additional cost to run circuits for the charging stations.
    a. The solution of building Level 2 charging in with canopied parking worked quite well as it supported the perception that campus EVs were being powered by clean, renewable energy, leading to one of the highest adoptions of EVs and workplace charging utilization of any institution in the Maui Electric Company's service territory.

C. Energy and CO_2 Dashboards: The purpose of the energy and CO_2 dashboards is to communicate energy usage data on a building by building level to the campus and wider community. Five wall-mounted kiosks, three interactive and two with a fixed looped display were deployed around the campus. Interactive displays allow users to choose specific building data. Fixed loop displays run through a programmed loop which included building energy consumption data as well as additional campus energy-related video material.
    a. The main value of this task turned out to be the sub-metering required to provide the energy data to the displays. eGauge energy meters were deployed in every major campus building as well as the parking lot PV array. Once properly installed, the devices have proven to be accurate and reliable. The data is fed into the wall mounted displays via the campus computer network, which also allows for display of the data in other locations besides the kiosks. The actual energy use of campus buildings is displayed graphically in real time along with comparisons to the previous week.
    b. Although general interest in the displays is less than expected, the displays are useful for energy and sustainability classes. Future, possibly more flexible uses for the kiosks remains to be determined.

D. Distributed Solar Forecasting with Wind and Solar Sensors: A total sky imaging camera and data acquisition system for the purpose of short-term forecasting of solar irradiance data was obtained from Professor Jan Kleissl's UC San Diego Solar Forecasting Lab and deployed on the roof of the campus library. The system is connecteed to the UHMC network. Under APRISES12, images and data are being acquired and sent to San Diego for analysis.

E. Campus-wide Energy Management System: Sub-metering campus buildings energy meters deployed throughout the campus, as a result of the Energy and CO_2 dashboard efforts added to the data collected by the campus-wide energy management system. This system is a critical component of the demonstration project as it monitors and controls all building-related energy devices as well as the renewable energy generation and storage equipment. This enables key metrics for grid integration, namely demand side peak load and demand charge reduction, and the mitigation of unwanted export to the utility grid.

With an interest in obtaining feedback and additional ideas, a panel of community stakeholders was convened and project progress was presented. Further integration of campus assets through the energy management system is being developed under other funding. Additionally, efforts to utilize innovative grid support utility programs, such as load-side management and demand response are being carried out. As a result of this project, the 2017 UH President's Sustainability Leadership Award was presented to the UH Maui College Facilities Team for Clean Energy Solutions, (http://www.hawaii.edu/news/2017/03/22/uh-systemwide-sustainability-efforts-recognized/).

Task 7. ENERGY EFFICIENCY

Under Task 7,three projects relating to energy efficiency in buildings were completed: 1) four potentially zero energy research platforms and two other existing, conventional classrooms were instrumented and monitored to determine comparative performance in energy, indoor environmental quality, and comfort; 2) desiccant dehumidification was examined as a means to improve comfort at lower energy expense, and; 3) the applicability of ceiling fans to low energy thermal comfort was investigated.

A. Comparative Analysis of Test Platforms and Conventional Classrooms

HNEI and its subawardee, MKThink, conducted a comparative analysis of test platforms and conventional classrooms in Hawaii. Specifically, three zero energy research platforms, two conventional classrooms, and one net zero energy structure were instrumented with energy use, indoor environmental quality, and system operation sensors to compare their respective performance, as well as to compare their performance to predictive models, and to establish guidelines for building performance.

The three zero energy platforms, named Kawaikini East, Kawaikini West and Ilima (Figures 7.1 and 7.2), were designed and constructed by Project Frog between 2009-2013 (under previous ONR HEET10 funding, and summarized in the report available online, "Project Frog Test Platform Study at Kawaikini NCPS"). Two of these three platforms (Kawaikini East and Kawaikini West) were installed at the Kawaikini New Century Public Charter School in Lihue, on Kauai, and one (Ilima) was installed at Ilima Intermediate School in Ewa Beach, on Oahu. Two conventional classrooms also located in Ewa Beach on Oahu, (called Ewa P1 and Ewa D36) that are representative of a large sample of conventional Hawaii Department of Education (HIDOE) schools were also selected for comparison. A zero net energy classroom on Ewa Elementary campus (named Ewa P6), built as a result of a HIDOE design competition, was included in the comparative study (Figure 7.3).

Ilima FROG Classroom Information

CLASSROOM TYPE	Modular Portable FROG
PERFORMANCE	High Performance ZNE
DESIGNER	Project FROG
SIZE	1,280 NSF
YEAR BUILT	2010
ENCLOSURE TYPE	Insulated Foam Panels (R-24)
ROOF TYPE	Single Ply White Membrane & Insulation (R-22/R-30)
CLIMATE	Warm, dry, low cloud cover
ORIENTATION	South-facing
USE TYPE	Middle School Classroom

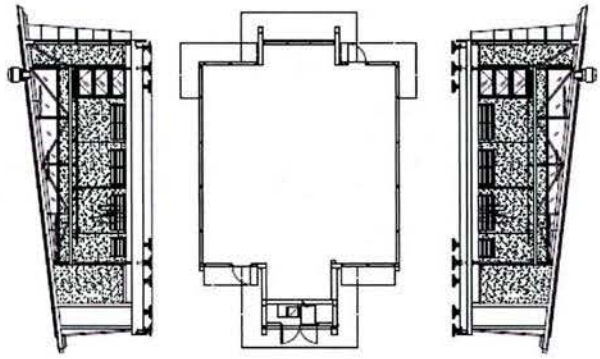

General Characteristics	
NSF	1,280 ft²
Length	42 ft
Width	31 ft
Ceiling Height	11'4" - 17'2"
Doors	2
Window Type	PPG Solarban 70 XL (0.26 U-Value, 0.27 SHGC)
Glazing Area	750 ft²
Louvers	Yes

Buildings Systems	
AC Type	Carrier Split System HVAC with underfloor air distribution
Set Point	65°F
Fans	9 variable speed 60" Hampton Bay ceiling fans
Lighting	Cerra Indirect/Direct (80/20), fluorescent lights (T-8)
Plugs	2 computers, printer

PV Systems	
System 1: thin-film panels	
System Size	2.64 kW
Modules	Solar Frontier SF-165-S (16 modules)
Inverter	SMA SB2500HF-US
System 2: traditional monocrystalline silicon	
System Size	2.6 kW
Modules	Mitsubishi PV-MLE260HD (10 modules)
Inverter	SMA SB2500HF-US

Figure 7.1: Details of the Frog Classroom (Kawaikini East, Kawaikini West, Ilima)

		Kawaikini East	Kawaikini West	Ilima
GENERAL	Location	Lihu'e, HI	Lihu'e, HI	Ewa Beach, HI
	School	Kawaikini New Country Public Charter School	Kawaikini New Country Public Charter School	Ilima Intermediate School
	Classroom Grade Level	7-12	7-12	7-8
	Classroom Type	Modular Portable FROG	Modular Portable FROG	Modular Portable FROG
	Year Built	2013	2013	2010
	Classroom Size (NSF)	1,280 ft²	1,280 ft²	1,280 ft²
BUILDING	Wall Assembly	Insulated Foam Panels (R-24)	Insulated Foam Panels (R-24)	Insulated Foam Panels (R-24)
	Roof Assembly	Insul + Single Ply (R-22/R-30)	Insul. + Single Ply (R-22/R-30)	Insul. + Single Ply (R-22/R-30)
	Primary Window Type	PPG Solarban 70 XL	PPG Solarban 70 XL	PPG Solarban 70 XL
SYSTEMS	AC Type	Mechanical Underfloor	Mechanical Underfloor	Mechanical Underfloor
	PV Type(s)	Thin film & Monocrystalline	Monocrystalline	Thin film & Monocrystalline
	PV System Size	5.24 kW	5.24 kW	5.24 kW
NOTES		Fan coil unit not working: 10/17/13 - 2/27/15. Classroom often had evening programs.		Air conditioning was used most of the time due to a bug and dust problem. Front windows were often covered for security concerns.

Figure 7.2: Frog Classroom Asset Summary (Kawaikini East, Kawaikini West, Ilima)

		Ewa P6	Ewa P1	Ewa D36
GENERAL	Location	Ewa Beach, HI	Ewa Beach, HI	Ewa Beach, HI
	School	Ewa Elementary School	Ewa Elementary School	Ewa Elementary School
	Classroom Grade Level	K-6	K-6	K-6
	Classroom Type[1]	Modular ZNE Portable	Traditional Portable	Traditional Masonry
	Year Built	2010	1996	1960
	Classroom Size (NSF)	1,176 ft²	840 ft²	900 ft²
BUILDING	Wall Assembly	Double wall metal cladding	Wood	Masonry
	Roof Assembly	Steel and rigid foam	Galvanized Steel	Wood
	Primary Window Type	Double Pane	Single Pane	Louvers with plexiglass
SYSTEMS	AC Type	None	Window AC Units	Window Units / Central
	PV Type(s)	mono & polycrystalline	N/A	N/A
	PV System Size	12.32 kW	N/A	N/A
NOTES		P6 was preinstalled with temperature, humidity and PV sensors. The installation of the lighting system prevented the operation of several windows.	P1 has insulated ceilings and walls. It also has vented windows with glass louvers and a wire mesh covering the windows on both sides of the structure.	Year 1 had a window AC unit. Year 2 had central AC. AC energy was extrapolated for 7/1/2014-6/30/2015 based on measured data from 11/12/15-11/20/15. The central AC runs from 6am to 6pm on weekdays.

Figure 7.3: Other Hawaiian Classroom Asset Summary (Ewa P6, Ewa P1, Ewa D36)

The results from this study are detailed the report "Test Platform Performance Comprehensive Analysis Phase 2 (MKThink, March 2016), available on the HNEI website. This report introduces the three key research questions used to conduct the study. Each question was partitioned into measurable metrics with criteria and sub-criteria developed for comparison:

1. How does Test Platform (FROGS) performance compare to traditional classrooms and each other?
2. Do Test Platforms perform as predicted by simulation models?
3. Do all classrooms perform within established guidelines (ASHRAE Adaptive comfort model, Indoor Air Quality, etc.)?

The criteria are described in Table 7.1.

Table 7.1: Criteria and sub-criteria

CRITERIA	SUB-CRITERIA	UNIT	DESCRIPTION
	Total Loads	kWh	All electrical load measured at the electrical panel
	Mechanical Cooling	kWh	Condensing Unit, Fan Coil Unit, and Exhaust Fan
	Ceiling Fans	kWh	Electrical energy use of ceiling fans
	Interior Lighting	kWh	Electrical energy use of primary classroom lighting
	Exterior Lighting	kWh	Outdoor lighting electrical energy use (where applicable)
	Plug Loads	kWh	Plug loads from in-classroom devices
	Thermal Comfort	PMV	ASHRAE Adaptive Comfort Model
	Air Quality	ppm	CO_2 concentration
	Lighting Quality	fc	Luminosity and glare ratio at work surface
	Air Supply	°F	Rise in temperature between supply and distribution
	Natural Daylighting	fc	Available daylight utilized without artificial lighting

Four additional exploratory questions were evaluated in this study as follows:

1. How well did Test Platforms achieve energy neutrality?
2. How do the classrooms compare in the use of natural daylighting?
3. How do local weather and differences in microclimates impact building operations and performance?
4. How do the classrooms compare against national averages for Energy Use Intensity (EUI)?

Major findings of the 2-year study are presented in a series of executive summary "dashboards" organized to support the study's primary and exploratory research questions. These dashboards provide a visual comparison of energy consumption, indoor environmental quality, and system performance for a selected 1-year period. The intent is to provide quick access to the most interesting results on the performance of these buildings.

Details of the building characteristics and system configurations are included in the report, including the general site information, general building and system information, and photovoltaic system information.

Weather and microclimate characteristics for the local sites were used to help determine the impact of location on performance. Modeling assumptions were made on details relative to the operational and behavioral parameters and were observed during the study. Classroom

performance was analyzed across the study criteria, annually, monthly, and daily as appropriate. Performance was also evaluated with respect to asset characteristics and behavior characteristics to determine which factors influenced performance. Findings, interpretation and future work for each of the research questions includes energy saving recommendations, for each classroom. The benchmarks, calculations, energy demand estimates, assumptions, limitations and references used to create the dashboard information are also presented in the report.

Results

The following dashboards provide a visual comparison of the results of energy consumption, indoor environmental quality, and system performance for a selected 1-year period, as follows :

- Annual energy and Indoor Environmental Quality (IEQ)
- Annual Indoor Environmental Quality and EUI
- Annual energy use - actual versus modeled
- Annual net zero energy-target and achieved
- Annual daylight analysis
- Annual EUI Benchmarked against national reporting

The dashboard in Figure 7.4 presents EUI, a measure of energy consumption per net square foot of floor area (kWh/sf/yr). The lower the EUI, the more efficiently the building is operating. These EUI are disaggregated by end uses: air conditioning, ceiling fans, plug loads, and interior lighting. IEQ comprises thermal comfort, in terms of percentage of time within ASHRAE defined comfort zone; air quality, in terms of percentage of time the CO_2 concentration exceeds the ASHRAE threshold of 1,100 ppm; illuminance, in percent of time wall illuminance is greater than 5 foot-candles (fc) and the illuminance ratio (wall illuminance to horizontal surface illuminance) is less than 5 fc.

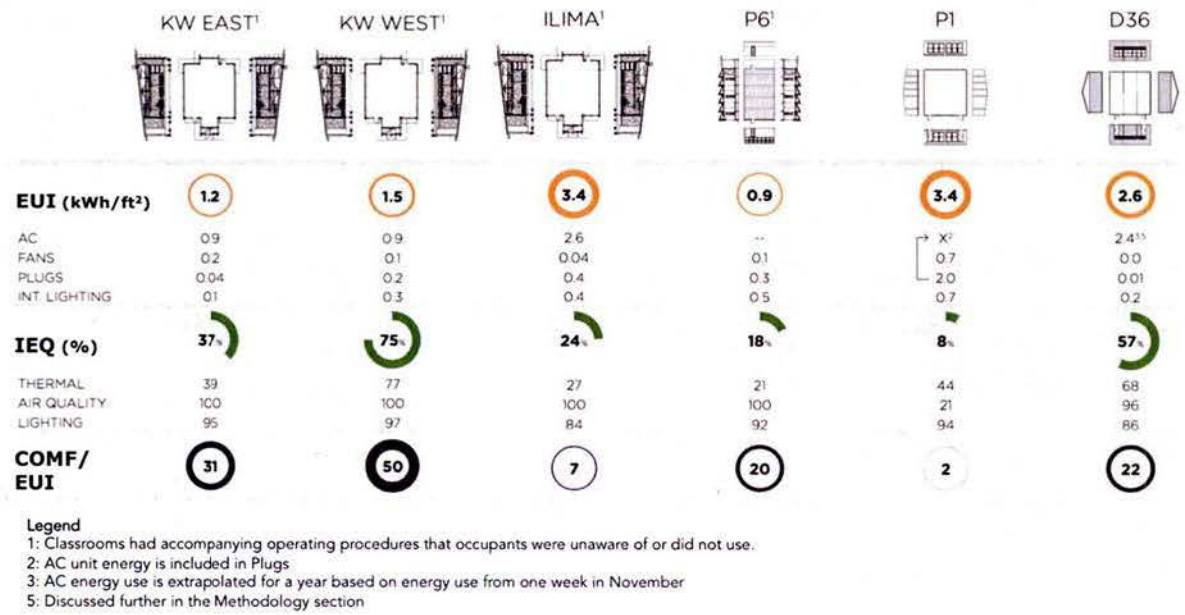

Figure 7.4 Annual Energy and Indoor Environmental Quality (IEQ) Classroom Comparison

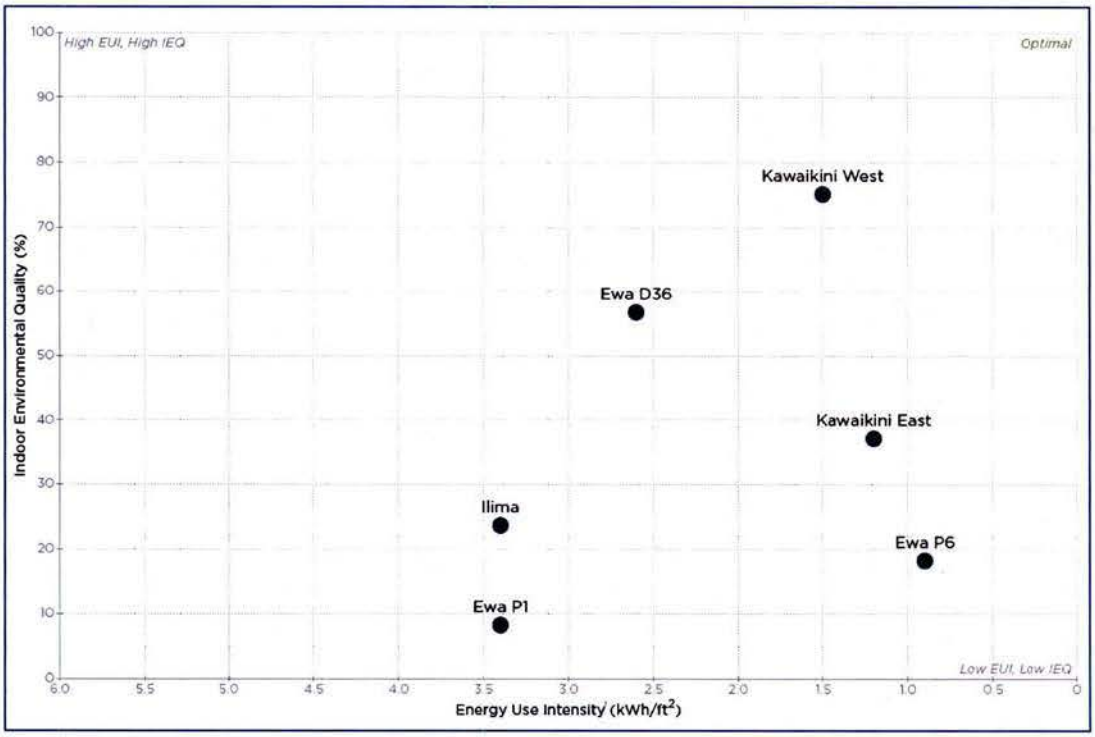

Figure 7.5: Annual IEQ / Energy Use Intensity (EUI)

The dashboard in Figure 7.5 compares classrooms on the basis of IEQ (%) per EUI (kWh/sf/yr). Kawaikini West delivered the highest level of IEQ index with the least amount of energy. Ewa P6, another net zero energy classroom, performed very well in terms of energy efficiency,

however, delivered a low IEQ score due to thermal, air quality, illuminance and comfort issues.

Kawaikini energy modeling used during the design phase of the project is compared to the actual performance in Figure 7.6. Three scenarios were modeled, *Optimal* (low energy), *Anticipated* (medium energy consumption), and *High* (highest consumption). Kawaikini East consumed 20% more than *anticipated*, while Kawaikini West consumed 19% less than *anticipated*. Kawaikini East used 37% more energy than the *high* modeling scenario. While this study did not evaluate the reasons for such energy variances, the data showed that Kawaikini East was used far more extensively than expected for such purposes as school administrative meetings, community meetings, and various after hour uses.

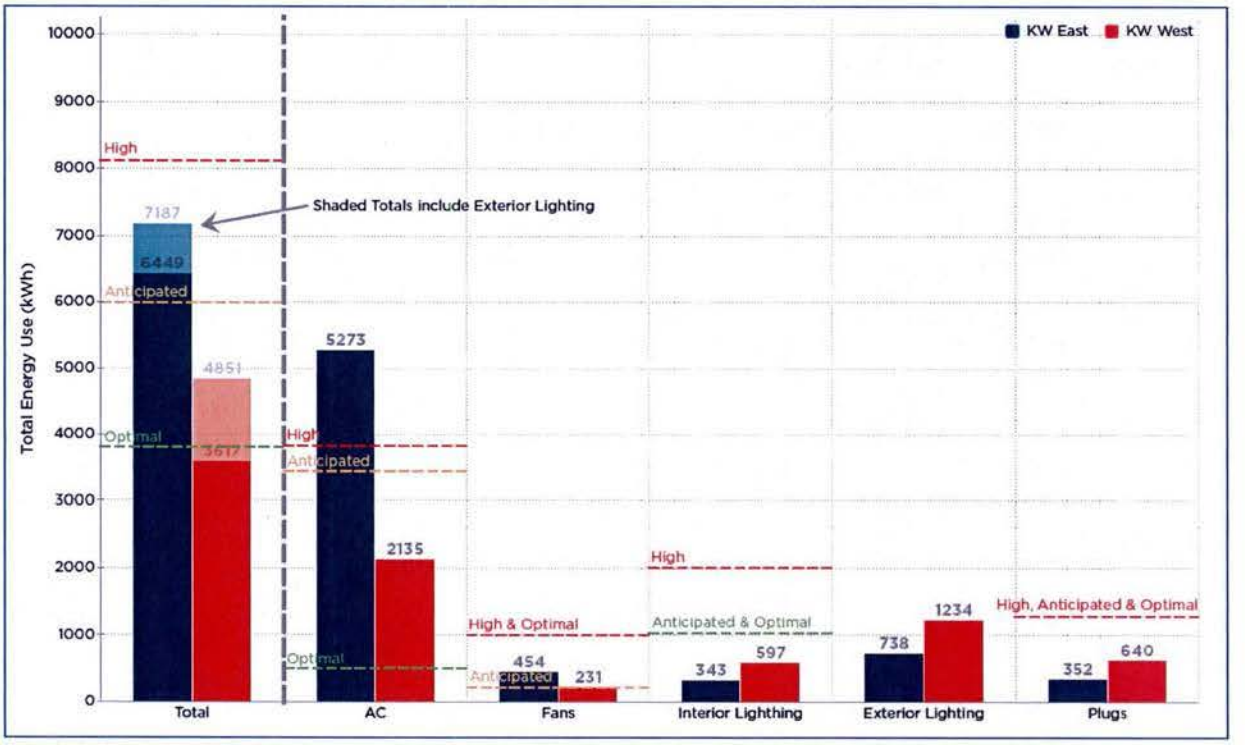

Figure 7.6: Total Energy Use- Actual versus Modeled in both Kawaikini school buildings

The Frog platforms, as well as classroom Ewa P6, were designed as net zero energy buildings. Figure 7.7 illustrates whether they met the goal of net zero energy. Both Kawaikini platforms generated more energy than they consumed. Classroom Ewa P6 generated nearly 5 times more energy than it used. Ilima, located in the hotter microclimate of Ewa Beach compared with both Kawaikini classrooms in Lihue, used about 7% more energy than it generated. The data showed an unprecedented spike in energy use during the final month of the data collection period. Anecdotally, this coincided with the school installing a computer server in the room, and running the air conditioning 24 hrs/day. If energy consumption remained average during the final month, Ilima would have met its net zero energy goal.

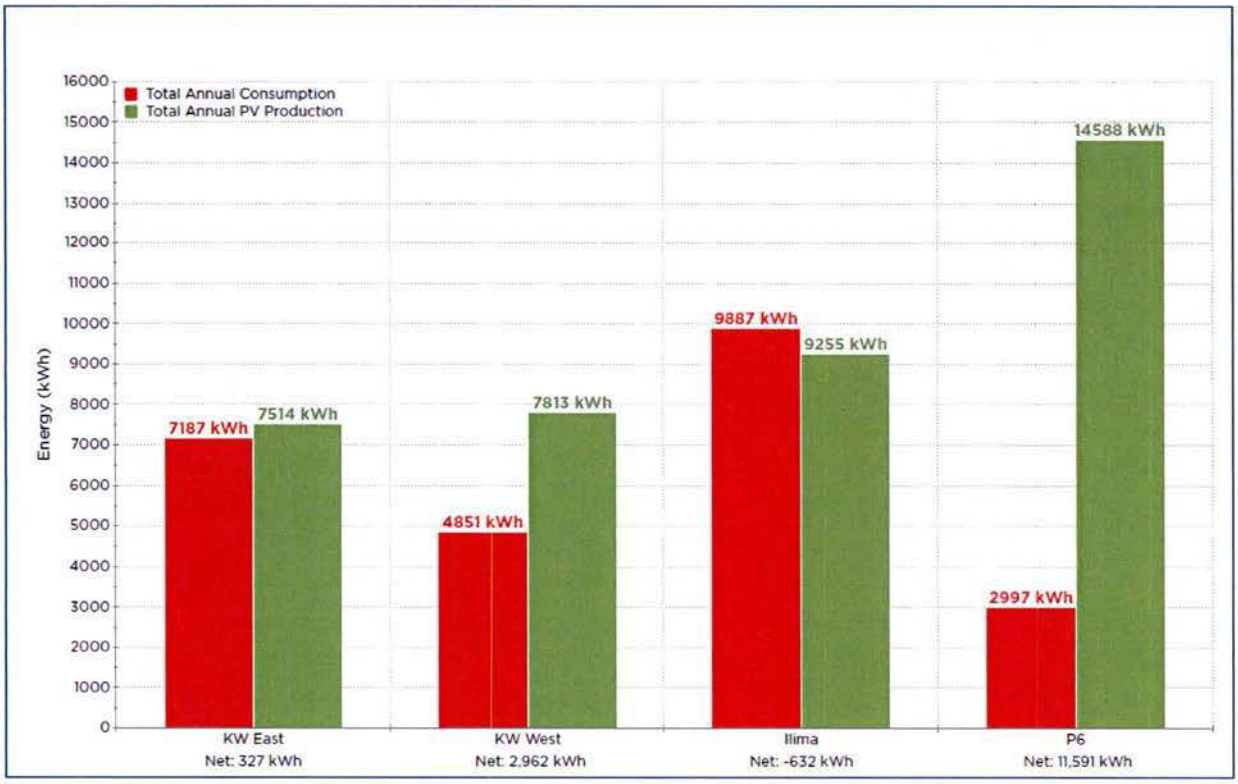

Figure 7.7: Kawaikini, Ilima and Ewa P6 Frog Annual Net Zero Energy Summary

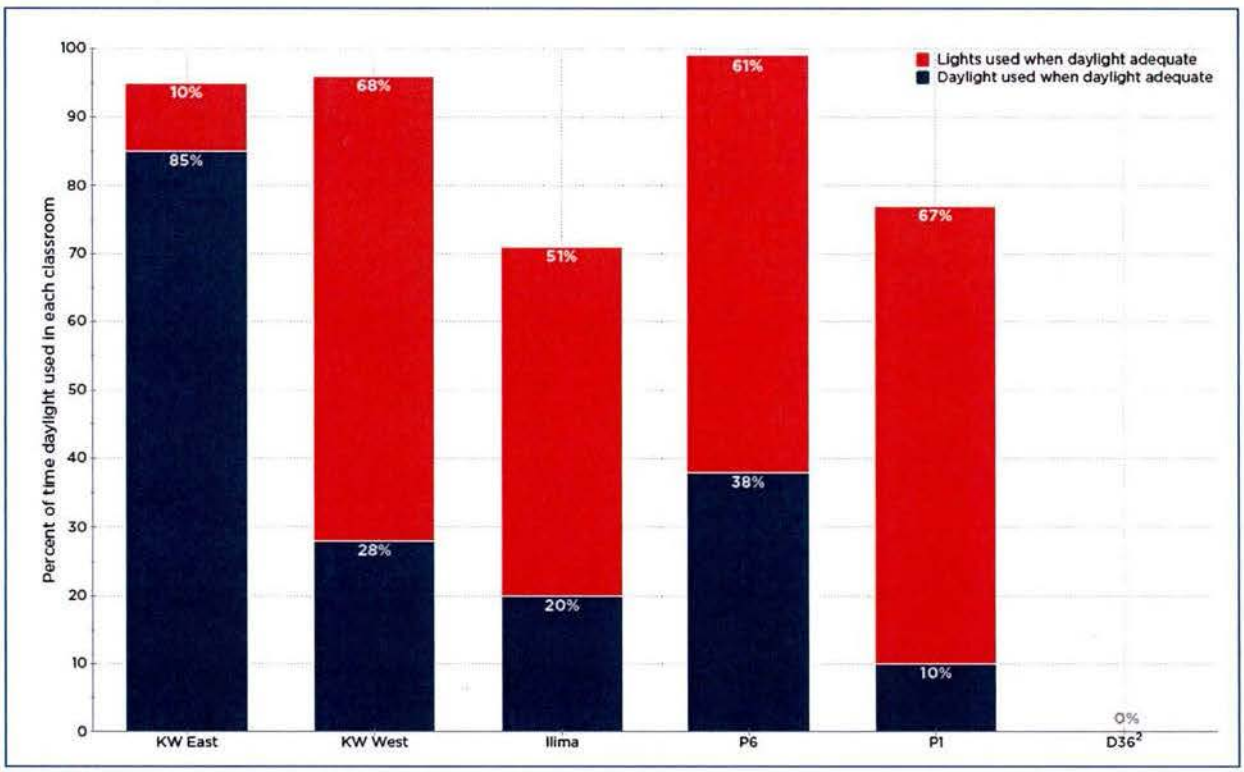

Figure 7.8: Annual Daylight Use vs Daylight Availability

One component of the IEQ metric is daylight illuminance. The study evaluated how these classrooms took advantage of natural daylight. Figure 7.8 compares the percentage of time that daylighting was used to the amount of time artificial lighting was used. Showing that use of daylighting can vary based on individual preference, Kawaikini East used natural daylight 85% of the time that adequate daylight was available, compared to Kawaikini West, where daylight was used on 28% of the time it was available. "Adequate" daylight is defined when average wall exceeds 5 footcandles and the wall-to-horizontal surface illuminance ratio is less than 5. The other classrooms used daylight between 10 to 38% of the time that adequate daylight was available.

An objective of this study was to determine how these classrooms compared to national averages. Figures 7.9 and 7.10 compare the 6 classrooms to national electricity consumption benchmarks, (described in more detail in the full MKThink report online). With the exception of Ilima, all classrooms fell within the top quartile of US K-12 schools, outperforming the national average.

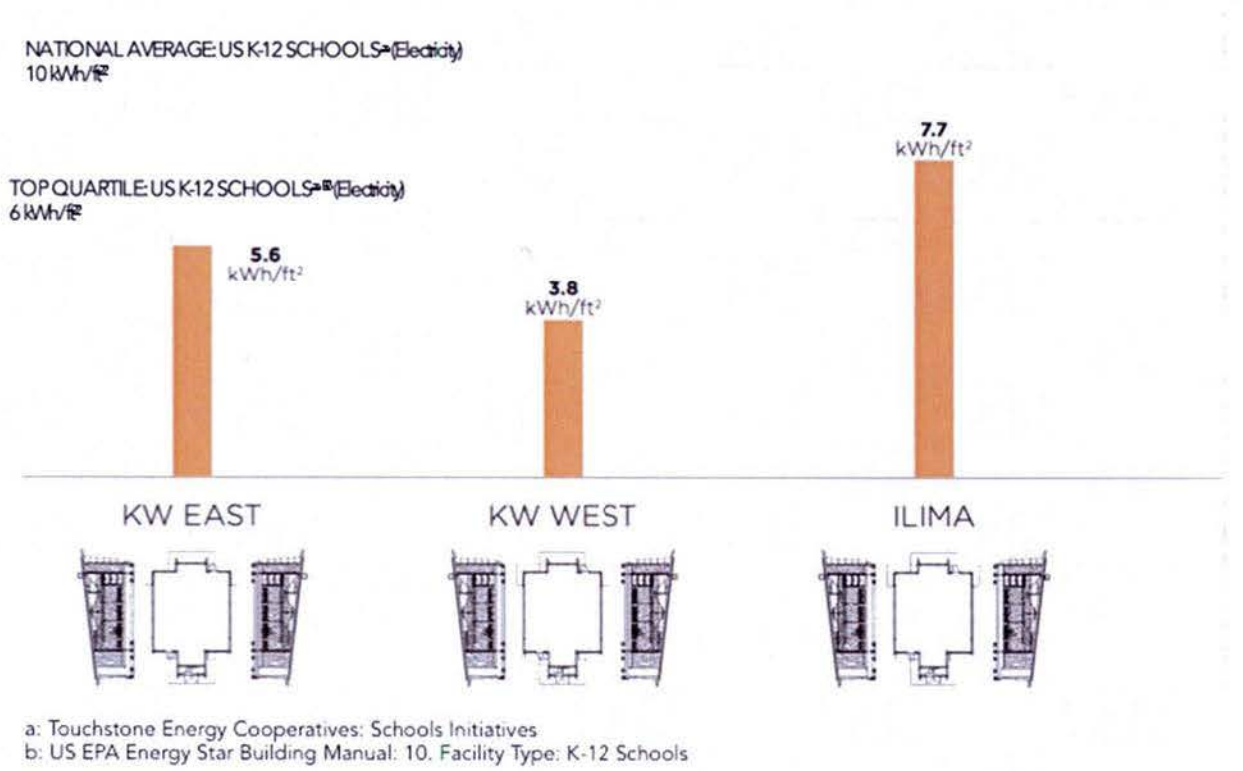

a: Touchstone Energy Cooperatives: Schools Initiatives
b: US EPA Energy Star Building Manual: 10. Facility Type: K-12 Schools

Figure 7.9: Annual EUI Benchmarked Against National Reporting: Frog buildings (Kawaikini East, Kawaikini West, Ilima)

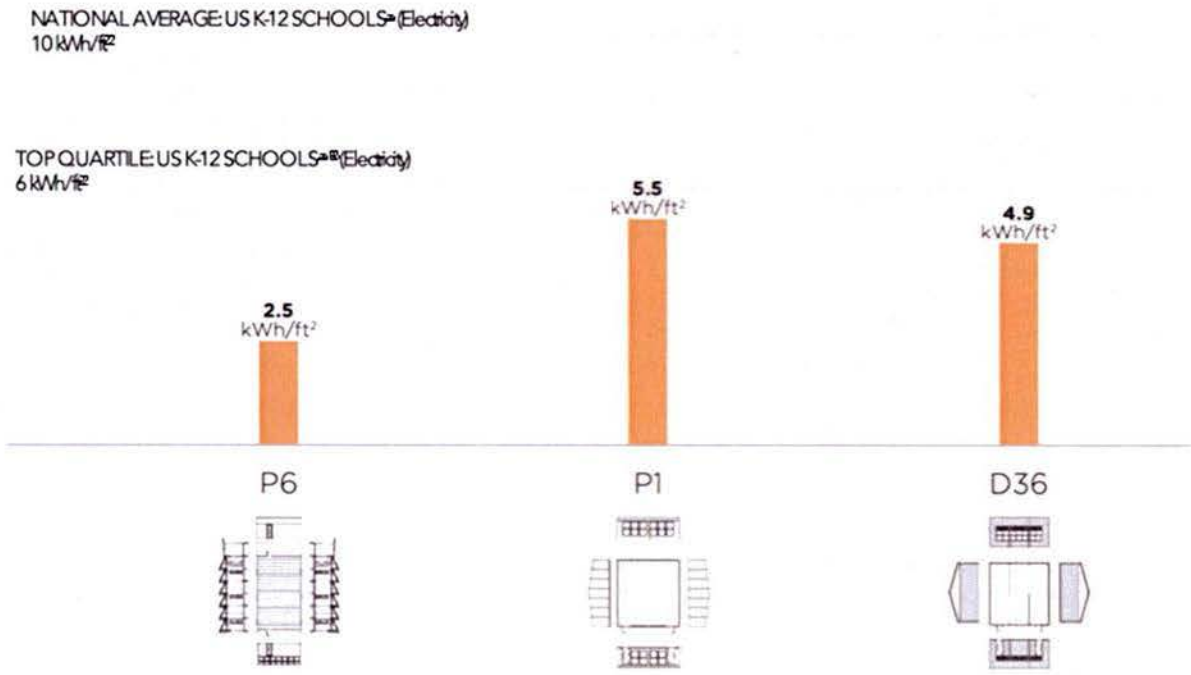

a: Touchstone Energy Cooperatives: Schools Initiatives
b: US EPA Energy Star Building Manual: 10. Facility Type: K-12 Schools

Figure 7.10: Annual Energy Use Intensity Benchmarked Against National Reporting: Ewa P6, Ewa P1, Ewa D36

Conclusions and Findings

The key findings of the main three questions addressed in this study were:

1. *How does Test Platform (FROGS) performance compare to traditional classrooms and each other?*

   Key Finding: On average, the test platforms used 40% less energy per square foot, had 6% more time with comfortable interior conditions and delivered 15% more comfort per energy unit consumed than traditional classrooms.

2. *Do Test Platforms perform as predicted by simulation models?*

   Key Finding: Compared to the "Anticipated" model scenario, Frog test platforms' total energy consumption varied from +20% to -19% overall, and by individual system from +77% to -72%. Additionally, 40% or less of Active Mode HVAC operations occurred during times recommended in the high-performance building operations guides.

3. *Do all classrooms perform within established guidelines (ASHRAE adaptive comfort model, indoor air quality, etc.)?*

   Key Finding: On average, test platforms had 15% less time within the thermal comfort zone, 41% more time with acceptable air quality and 2% more time with acceptable lighting conditions compared to traditional classrooms.

Key findings from the additional four questions were:

1. *How well did Test Platforms achieve energy neutrality?*
Key Finding: The three Project FROG net zero platforms achieved energy neutrality on an annualized basis.

2. *How do the classrooms compare in the use of natural daylighting?*
Key Finding: The three Project FROG platforms showed daylight capacity above 90%, but the existing HIDOE net zero energy classroom used artificial lighting more than 50% of the time.

3. *How do local weather and differences in microclimates impact building operations and performance?*
Key Finding: Differences in microclimate did not reveal statistically significant relationships with classroom performance. However, individual classrooms exhibited moderate weather related relationships.

4. *How do the classrooms compare against national averages for EUI?*
Five of six classrooms had lower EUIs than the top quartile of schools nationwide. Kawaikini west and Ewa P6 had EUIs 37% and 58% lower than national average, respectively.

The detailed report on Net Zero Energy and comparable classrooms entitled: "Test Platform Performance Analysis, Phase 2" is available on the HNEI website.

B. Desiccant Dehumidification

In the past several years there have been significant advances in the performance and reliability of desiccant dehumidification technology. When combined with newer air-management processes, these technologies offer significant cost savings, particularly in high temperature, high humidity areas characteristic of much of the Pacific region. In HEET10, HNEI conducted an evaluation of currently available and the most promising desiccant dehumidification technologies and air-management processes applicable to new building development and for the retrofit of existing structures. In this APRISES11 grant, HNEI expanded the research to include identification of a specific desiccant technology and a specific site in order to conduct a pilot installation with future funding.

HNEI contracted Manfred Zapka, PhD, P.E. of Sustainable Design and Consulting, LLC to conduct this second phase of the desiccant dehumidification research. The Contractor explored specific state-of-the-art liquid desiccant applications and determined availability and applicability of systems for installations (for a future pilot phase of the project), detailed as follows:

- Identify recent advancements in liquid desiccant technology that can be applied to space conditioning systems.

- Review commercially available liquid desiccant technologies.
- Identify and evaluate successful installation and state of technology maturity.
- Identify liquid desiccant technologies which will be adaptable to the Hawaii specific climate.
- Investigate different liquids desiccant flow systems and regeneration options.
- Evaluate projected costs of systems as new system or as retrofits.

The results from this study are summarized in the following report "Technology Review and Availability of Liquid Desiccant Systems" (March 2017), available online on the HNEI website.

This report provides an overview of important liquid desiccant processes and technologies which are the basis for the design of the planned pilot HVAC installation (under future funding) of a desiccant dehumidification and cooling system.

A discussion is provided in the detailed report of important basic aspects of dehumidification and a description of differences between technologies, including conventional cooling based dehumidification and solid and liquid desiccant dehumidification. Improving humidity control in buildings is gaining more importance. As the building envelope and the equipment inside the building become more energy efficient, the sensible thermal load is reduced and therefore that portion of the latent load increases. The conventional method of controlling HVAC is by temperature set-points, a method that only relies in the sensible load. In applications where the sensible heat index is small, latent load cannot be removed in an optimum manner. This requires a new approach to space conditioning where the control of sensible and latent loads must be separated so that they can be independently controlled.

While liquid desiccants are important for specific industrial processes, the use of liquid desiccants for the conditioning and/or cooling of buildings is not yet a widely-used technology in HVAC for buildings. Important design principles that have been under investigation and in active development for a longer time.

Shortcomings of conventional liquid desiccant dehumidification technology for their use in HVAC are discussed in the detailed report. Newer developments of liquid desiccant technologies are presented that include the so-called low flow technology. This newer technology avoids problems that "older" liquid desiccant technologies have regarding using liquid desiccant in HVAC. The improvements include simplifying the design, making operation of the liquid desiccant system more energy efficient, and solving major operational challenges. Further developing needs are identified to make liquid desiccants an even better fit for HVAC applications.

The liquid desiccant technologies and experiences of the seven candidate companies are also covered in the detailed report. The seven candidate companies were selected after an initial literature search (Table 7.2). One company of the seven initially selected candidate companies was found to have gone out of business recently. Each company had some unique liquid desiccant experience and proprietary technology that was deemed important for the planned pilot HVAC installation in Hawaii.

Table 7.2: Initial selection of candidate companies

No.	Company	Country	Type of Products	Status of Company
1	7 AC Technologies	US	Start-up company that develops membrane base liquid desiccant dehumidification; product is based on membrane technology developed by NREL	Start-up company, has been in business for less than 5 years
A	Advantix Systems	US	Innovative solutions for liquid desiccant products;	Company closed and went out of business
2	AIL Research	US	A wide range of liquid desiccant products and technologies	Company has been in business for more than 10 years and is a recognized leader in innovative technology development
3	Be Power tech	US	Start-up company that develops membrane base liquid desiccant dehumidification; product is based on membrane technology developed by NREL. Adds fuel cell as means to provide thermal energy for regeneration	Start-up company, has been in business for less than 5 years
4	Kathabar Dehumidification Systems, Inc	US	Large range of desiccant dehumidification products which are installed in various industrial dehumidification applications	US internationally active company that is in business for several decades
5	L-dcs	Germany	Providing integrated and energy saving HVAC solutions. Included are liquid desiccant technology	German company has been in business for more than 10 years and is a recognized leader in innovative technology development
6	Menerga Apparatebau, GmbH	Germany	Large range of HVAC technologies that provide advanced technology solution for building AC and comfort	German internationally active company that is in business for 30 years.

A systematic ranking of the candidate companies was developed. A two-tier ranking methodology was used to identify the prospect of a company to be a strong partner in the planned pilot HVAC project, with aspects considered including applicability and flexibility of their proprietary liquid desiccant technology, their experience in HVAC applications, their technical and design support potential and their willingness to make significant contributions to the project.

Results

The six candidate companies remaining in business were ranked using 14 criteria, which were grouped in the following four categories, where the four categories were given different weights:

- Technology maturity (overall weight 25%)

- Prior installation /application experience of technology (overall weight 20%)
- Technology flexibility / ability to implement pilot HVAC installation (overall weight 40%)
- Communication / willingness to cooperate substantially (overall weight 15%)

Companies were evaluated against each of the 14 ranking criteria. A ranking score point score, in percentage, was determined for each criterion and the sum of all score points determined the overall ranking of the company. The higher the total score, the better the company was considered ready to contribute to the planned pilot HVAC installation.

The result of the ranking is shown in Table 7.3.

Table 7.3: Total ranking scores of candidate companies

COMPANY	TOTAL SCORE	RANK
No. 2 – AIL Research Inc.	96%	1
No. 5 – L-dcs GmbH	90%	2
No. 1 – 7 AC Technologies	62%	3
No. 6 – Menerga Apparatebau, GmbH	60%	4
No. 4 – Kathabar Dehumidification System	56%	5
No. 3 – Be Power Tech	37%	6

AIL Research and L-dcs were found to be the two companies with the most promising liquid desiccant technology for the planned pilot HVAC installation.

Conclusions and Findings

The major findings of this report are as follows:

1. Improved humidity control in buildings becomes increasingly important as the typical thermal loads in buildings shift from predominately sensible to gradually more latent. The conventional HVAC technology uses temperature set points to control the total thermal load removal from the conditioned spaces. As the sensible thermal loads decrease due to more energy efficiency in envelope, lighting and equipment, more humidity enters and less humidity is rejected from the conditioned space. Humidity related indoor environmental impacts are logical consequences. Therefore, precise humidity control of conditioned spaces requires new HVAC approaches. Separate controls and rejection of sensible and latent loads is a key approach. Liquid desiccant dehumidification is a suitable technology for advanced humidity control and can provide more benefits as the conventional cooling based dehumidification.

2. Indoor comfort in the Hawaii environment does not require the cold temperatures that are common in conventional HVAC systems with cooling based dehumidification. This conventional HVAC method of reducing humidity from the indoor recirculated and fresh outside air is based on cooling the air below dew point temperature chilled coils and which causes condensation on the cooling coils. To avoid overcooling spaces, additional energy has to be used to reheat the supply air, a method that is very energy intensive. This has negative

occupant comfort implications. Since liquid desiccant dehumidification does not require cold process temperatures, overcooling can be avoided.

3. Conventional liquid desiccant technology has had a long and successful record of providing precise humidity control for specific industrial processes. All equipment and process issues that are part of these established liquid desiccant industrial applications have been thoroughly optimized.

4. Conventional liquid desiccant technology that was optimized for industrial applications does not automatically perform well in HVAC applications in commercial or residential buildings for several reasons. A major barrier to use liquid desiccant technologies for HVAC systems is the high maintenance requirement for industrial liquid desiccant units. Desiccant solutions are typically corrosive and can affect equipment, and droplets can be entrained into the process air flow if impacts are not mitigated. Liquid desiccant equipment that will be successfully used in HVAC applications must be corrosion resistant, and effective measures must be applied to avoid desiccant droplet carryover to the supply air stream. In addition, liquid desiccant technologies must be energy efficient and provide for low first and O&M costs.

5. Recent developments of the "low-flow" liquid desiccant technologies provide significant performance improvement that will make liquid desiccant technologies more suitable for building HVAC applications. Low-flow conditioners (e.g. liquid desiccant absorbers) avoid desiccant droplet entrainment into and conveyance by the supply air. Therefore low-flow conditioners can be regarded as "zero carry-over" equipment. In addition, low flow liquid desiccant technology keeps the desiccant flow rate low, thus avoiding large pumping power. Energy storage in form of a concentrated desiccant solution requires only a fraction of the required desiccant solution, in comparison to conventional high-flow liquid desiccant technology.

6. Low-flow technology requires internally cooled conditioners and internally heated regenerators. Recent development of internal cooled wicking plate conditioners and regenerators have solved desiccant distribution and wetting characteristics inside the conditioners and regenerator. The low-flow conditioner and regenerator are significantly smaller than the conventional packed bed (or column) process vessels, which are used for industrial liquid desiccant dehumidification. This results in smaller unit sizes which can be easier integrated into retrofitted HVAC systems.

7. Recent developments of liquid desiccant technology, such as low flow, reflect significant contributions that make liquid desiccant dehumidification and cooling a recognized and trusted component of energy efficient and high comfort HVAC applications. While current advances in liquid desiccant based HVAC technology are significant, several liquid desiccant technology innovations have been identified that will increase the performance further. Major identified innovations include advanced desiccants that are less corrosive and offer good flow and wetting characteristics, multiple-effect regenerators that will increase the coefficient of performance (COP) and improving the efficiency of using solar heat for liquid desiccant processes. Research needs are described in this report.

8. Seven companies with a strong knowledge base and previous track records of designing and manufacturing liquid desiccant systems for use in building HVAC applications were selected from an initially larger pool of possible companies. The initial selection of the seven companies was based on published technical papers as well as on online searches and research. Of the seven companies, one was found to have recently ceased business operations. For the remaining six companies a detailed analysis was conducted of their products, completed system installations and their willingness to cooperate on the pilot HVAC project in Hawaii. The results of the research and analysis of the seven companies are presented in this report.

9. For the remaining six companies, a ranking of their performance relative to a set of selection criteria was performed. The ranking utilized a two-tier methodology, where the first tier defines the relative importance of a selection criterion and the second tier assesses the degree to which the company satisfies the criteria statements. The scores for each selection criteria are added to yield the total score.

10. The results of the ranking indicate that two small engineering and technology companies have the highest scores. Both companies offer valuable flexibility in adapting their low-flow liquid desiccant technology to the requirements of the pilot HVAC installation. Both companies have the required design and manufacturing knowledge to provide the relatively small liquid desiccant system components for the pilot HVAC installation.

The detailed report "Technology Review and Availability of Liquid Desiccant Systems" is available on the HNEI website.

C. Ceiling Fan Evaluation

HNEI contracted with MKThink to conduct a literature review on ceiling fan technologies. This work will be completed under APRISES13, N00014-14-0054. Installation, testing and measurement of ceiling fans at a selected test site will also be conducted under future APRISES funding.

Organizations in Hawaii and in other tropical areas continue to seek innovative applications of technologies to improve thermal comfort. While ceiling fans have been used for centuries, there are few tools that allow designers and planners to make deliberate, conscious fan selection based on research, constraints of the space and the physical characteristics of the fans. In addition, newer algorithms have been identified that modulate and vary fan speed to create "random" cycles of air movement that interrupt a continuous, repetitive flow of air across the skin. This approach to reducing thermal boredom has been shown to increase the perception of comfort. The intent of this project is to evaluate fan typologies, control options, and operational characteristics and provide research-based design guidelines to assist in space planning, design and product selection.

The scope of this subtask was to:

- Define typologies of ceiling fan applications and a portfolio of existing and emerging fan technologies
- Develop metrics structure to evaluate the performance of the portfolio of fan technologies.
- Conduct literature survey of current fan technologies including fan blade design, motor design, controls, and CFD simulation techniques, and their applicability to quantifying performance of selected fan typologies.

Overall, these objectives, combined work under APRISES15 will result in a best practices primer targeting the education sector and other interested parties on the effective use and design of ceiling fan applications. This primer will cover ceiling fan controls, energy use, physical configuration, capital and operational costs and impact on thermal comfort.

This subtask examines the ceiling fan body of knowledge in detail in order to build on existing research and target gaps for further study. This literature review includes academic journals, industry journals, white papers, conference presentations and manufacturer information to name a few. First, the contractor investigated the ceiling fan industry by conducting ceiling fan market research summarizing industry publications (e.g. conferences, newsletters, manufacturer technical specs and collateral materials) to develop a high – level understanding of:

- Available and emerging technology (incl. motor, blade shape, smart sensing, etc.)
- Applications
    - Space type
    - HVAC type - mixed mode, natural ventilation
- Control strategies
- Energy use
- Cost-benefit analysis
    - Industry specific metrics including EPA Energy Star ceiling fan criteria
- Other focus areas (up to 2 additional) requested by HNEI
    - Design and/or market integration of lighting and ceiling fan systems

The contractor then conducted ceiling fan technical research summarizing academic and industry publications (e.g. Peer reviewed articles, industry specifications) specifically related to thermal comfort impacts by using ceiling fans. This research investigated:

- Control options
- Thermal comfort impacts
    - air flow
    - perceived comfort
- Energy use
- Other focus areas (up to 2 additional) requested by HNEI
    - CFD simulation techniques and their applicability to quantifying performance

The detailed report "Ceiling Fans: Literature Review and Market Report" is available on the HNEI website.

Reports Resulting from these Efforts

MKThink, *Net Zero Energy Test Platform Performance Comparative Analysis,* (March 2016).

Sustainable Design & Consulting LLC, and Hawaii Natural Energy Institute, *Technology Review and Availability of Liquid Desiccant Systems,* (June 2017).

MKThink, *Ceiling Fans: Literature Review and Market Report,* (September 2017).